CHEMICAL VAPOR DEPOSITION GROWTH AND COVALENT FUNCTIONALIZATION/INTERFACING OF 2D NANOMATERIALS FOR ELECTRONIC APPLICATIONS

by

PHONG NGUYEN

B.S., Emporia State University, 2010

AN ABSTRACT OF A DISSERTATION

submitted in partial fulfillment of the requirements for the degree

DOCTOR OF PHILOSOPHY

Department of Chemical Engineering
College of Engineering

KANSAS STATE UNIVERSITY
Manhattan, Kansas

2016

Abstract

The evolution of unique electrical, optical, thermal, mechanical, and chemical properties in two-dimensional (2D) nanomaterials due to the atomic confinement in the z-direction has ignited tremendous technology promises. With that promise comes a challenge of incorporating 2D nanomaterials into practical applications, enabling their large-area growth and using covalent or van der Waal bonding to extent and control their properties in electronic applications. This PhD thesis establishes the following results: (a) successfully developing of scalable processes for direct growth of large-area graphene, h-BN, and MoS_2-on-h-BN on SiO_2/Si substrate, (b) demonstrating an electronic sensor for the defection of molecular motion by covalently interfacing 2D nanomaterials with photo-mechanical molecules, and (c) establishing the modulation of structural, electrical, thermal properties of 2D nanomaterials by covalently interfacing metal nanoparticles with 2D nanomaterials.

A promising scalable route for large-area growth of 2D nanomaterial on a dielectric substrate is to perform chemical vapor deposition (CVD). *Via* two patented processes, we have synthesized graphene films directly on a SiO_2 substrate *via* carbon-diffusion through copper grains, and h-BN film on SiO_2 substrate *via* surface oxide assisted mechanism. The continuous graphene film grown with large coverage on SiO_2 substrate possessed a crystalline sp^2 domain size of 140 nm with low defect density (as indicated by low Raman I_D/I_G~0.1). The sheet resistance of this turbostratic stacking graphene was ~4 kΩ/sq, with a charge carrier mobility of ~250 $cm^2V^{-1}s^{-1}$. Unprecedented, large coverage of directly grown h-BN film on SiO_2 substrate was demonstrated. This h-BN film showed a 6-fold smoothness enhancement compared to that of SiO_2 substrate. Such smoothness and the nature of free dangling bond of h-BN film reduced Coulombic long range

scattering, leading to the 5-fold enhancement in the conductivity of the MoS_2, which is directly grown on the underlying h-BN platform.

The next-generation molecular electromechanical systems require controlled manipulation and detection of molecular motion to build systems which respond to molecular mechanics. To achieve this, we covalently interfaced photo-mechanical molecules (azobenzene) (density = 2.5 nm^{-2}) onto trilayer graphene (37.5% sp^2 coverage), where high sensitivity of this trilayer graphene due to high quantum capacitance (6.3 $\mu F/cm^2$) and carrier confinement was leveraged. This enabled graphene to sensitively detect azobenzene isomerization, where one hundred molecules generated one charged carriers in the graphenic platform (2.44 x 10^{12} holes/cm^2).

As mentioned before, surface modification of 2D nanomaterials opens an avenue to incorporate them into rational applications. We demonstrated the ability to interface noble metal nanoparticles (gold, silver) selectively onto a MoS_2 lattice (60° angular displacement) *via* both diffusion limited aggregation and instantaneous reaction arresting (using microwaves). Such gold nanoparticle interfaces allowed the modulation of electrical, and thermal properties, confirmed by Raman, electrical, and thermal studies. Consequently, a remarkably capacitive interaction between gold and thin MoS_2 sheet showed a 9-fold increase of effective gate capacitance with low Schottky barrier (14.52 meV), and a 1.5-fold increase in thermal conductivity with a low carrier-transport thermal-barrier (44.18 meV).

This long-term work has established the following points: 1) Scalable routes for the growth of 2D nanomaterials, which can be extended to synthesize complex hetero/lateral architectures for integrated thin film circuitries. Furthermore, 2) covalent functionalization of 2D nanomaterials with nanoparticles and molecular systems can futuristically develop rational interfaces with other 2D heterostructures, and molecular machines.

CHEMICAL VAPOR DEPOSITION GROWTH AND COVALENT FUNCTIONALIZATION/INTERFACING OF 2D NANOMATERIALS FOR ELECTRONIC APPLICATIONS

by

PHONG NGUYEN

B.S., Emporia State University, 2010

A DISSERTATION

submitted in partial fulfillment of the requirements for the degree

DOCTOR OF PHILOSOPHY

Department of Chemical Engineering
College of Engineering

KANSAS STATE UNIVERSITY
Manhattan, Kansas

2016

Approved by:
Co-Major Professor
Vikas Berry

Approved by:
Co-Major Professor
Placidus Amama

Copyright

PHONG NGUYEN

2016

Abstract

The evolution of unique electrical, optical, thermal, mechanical, and chemical properties in two-dimensional (2D) nanomaterials due to the atomic confinement in the z-direction has ignited tremendous technology promises. With that promise comes a challenge of incorporating 2D nanomaterials into practical applications, enabling their large-area growth and using covalent or van der Waal bonding to extent and control their properties in electronic applications. This PhD thesis establishes the following results: (a) successfully developing of scalable processes for direct growth of large-area graphene, h-BN, and MoS_2-on-h-BN on SiO_2/Si substrate, (b) demonstrating an electronic sensor for the defection of molecular motion by covalently interfacing 2D nanomaterials with photo-mechanical molecules, and (c) establishing the modulation of structural, electrical, thermal properties of 2D nanomaterials by covalently interfacing metal nanoparticles with 2D nanomaterials.

A promising scalable route for large-area growth of 2D nanomaterial on a dielectric substrate is to perform chemical vapor deposition (CVD). *Via* two patented processes, we have synthesized graphene films directly on a SiO_2 substrate *via* carbon-diffusion through copper grains, and h-BN film on SiO_2 substrate *via* surface oxide assisted mechanism. The continuous graphene film grown with large coverage on SiO_2 substrate possessed a crystalline sp^2 domain size of 140 nm with low defect density (as indicated by low Raman I_D/I_G~0.1). The sheet resistance of this turbostratic stacking graphene was ~4 kΩ/sq, with a charge carrier mobility of ~250 $cm^2V^{-1}s^{-1}$. Unprecedented, large coverage of directly grown h-BN film on SiO_2 substrate was demonstrated. This h-BN film showed a 6-fold smoothness enhancement compared to that of SiO_2 substrate. Such smoothness and the nature of free dangling bond of h-BN film reduced Coulombic long range

scattering, leading to the 5-fold enhancement in the conductivity of the MoS_2, which is directly grown on the underlying h-BN platform.

The next-generation molecular electromechanical systems require controlled manipulation and detection of molecular motion to build systems which respond to molecular mechanics. To achieve this, we covalently interfaced photo-mechanical molecules (azobenzene) (density = 2.5 nm^{-2}) onto trilayer graphene (37.5% sp^2 coverage), where high sensitivity of this trilayer graphene due to high quantum capacitance (6.3 $\mu F/cm^2$) and carrier confinement was leveraged. This enabled graphene to sensitively detect azobenzene isomerization, where one hundred molecules generated one charged carriers in the graphenic platform (2.44 x 10^{12} holes/cm^2).

As mentioned before, surface modification of 2D nanomaterials opens an avenue to incorporate them into rational applications. We demonstrated the ability to interface noble metal nanoparticles (gold, silver) selectively onto a MoS_2 lattice (60° angular displacement) *via* both diffusion limited aggregation and instantaneous reaction arresting (using microwaves). Such gold nanoparticle interfaces allowed the modulation of electrical, and thermal properties, confirmed by Raman, electrical, and thermal studies. Consequently, a remarkably capacitive interaction between gold and thin MoS_2 sheet showed a 9-fold increase of effective gate capacitance with low Schottky barrier (14.52 meV), and a 1.5-fold increase in thermal conductivity with a low carrier-transport thermal-barrier (44.18 meV).

This long-term work has established the following points: 1) Scalable routes for the growth of 2D nanomaterials, which can be extended to synthesize complex hetero/lateral architectures for integrated thin film circuitries. Furthermore, 2) covalent functionalization of 2D nanomaterials with nanoparticles and molecular systems can futuristically develop rational interfaces with other 2D heterostructures, and molecular machines.

Table of Contents

List of Figures xiii
List of Tables xxii
Acknowledgements xxiii
Dedication xxvi
Chapter 1 - The two-dimensional (2D) nanomaterial 1
Introduction 1
Graphene: The 2D carbon crystal 3
Molybdenum disulfide (MoS_2): Graphene's cousin 4
Hexagonal boron nitride (h-BN): Analog of graphene 6
The challenges in synthesizing and transferring of 2D nanomaterials into dielectric substrate for electronic applications 7
Mechanical exfoliation 7
Chemical top-down approach 8
Chemical vapor deposition (CVD) 11
CVD of graphene or h-BN on metals 11
CVD of MoS_2 on non-metallic substrate 13
Reference 15
Chapter 2 - Direct growth of thin layer graphene on SiO_2 via low pressure chemical vapor deposition (LPCVD) 25
Abstract 25
Introduction 25
Experimental Section 27
Procedure of multilayer graphene growth on SiO_2/Si substrate via LPCVD 27
Procedure to transfer graphene to SiO_2 for field effect transistor fabrication, and to TEM grid for selected area electron diffraction (SAED) characterization 29
Procedure to transfer graphene on top of Cu surface to SiO_2 for Raman characterization ... 31
Procedure of the thin graphene field effect transistor fabrication 32
Pre-treatment of GFET for electrical measurements 34

Instrumentations for chemical, physical and electrical characterization 34
Confocal Raman spectroscopy system.. 34
Field emission scanning electron microscope (FESEM) 35
Selected area electron diffraction (SAED) measurement via transmission electron microscope (TEM) 35
X-ray photoelectron spectroscopy (XPS) system 35
Cryostat electrical system 35
Results and Discussion 36
Physical characterization of thin graphene film.. 36
The growth mechanism of graphene at the interface 40
The influence of growth parameters on graphene quality.. 45
The electronic characterization of the thin graphene film 47
The f ield effect analysis of the thin graphene film 48
Charge transport mechanism of the thin graphene film... 51
Conclusion 53
Acknowledgements... 54
Reference 54
Chapter 3 - Direct growth of hexagonal boron nitride on SiO_2 via low pressure chemical vapor deposition (LPCVD) 62
Abstract 62
Introduction... 62
Experimental Section 64
Procedure of h-BN growth on SiO_2/Si substrate via LPCVD.. 64
Procedure of MoS_2 growth on h-BN via LPCVD.. 65
Procedure for the fabrication of MoS_2/h-BN sample for I-V measurement 66
Procedure to transfer hBN to TEM grid for selected area electron diffraction (SAED) characterization 66
Instrumentations for chemical, physical and electrical characterization 66
Confocal Raman spectroscopy system.. 66
Selected area electron diffraction (SAED) measurement via transmission electron microscope (TEM) 67

X-ray photoelectron spectroscopy (XPS) system 67
X-ray powder diffraction (XRD) system 67
UV-Vis system for optical band-gap characterization 67
Cryostat electrical system 68
Results and Discussion 69
H-BN growth mechanism 69
Growth of the h-BN film on Si (the control experiment) 72
Structural characterization of the h-BN film 73
Optical band gap analysis of the h-BN film 76
Structural characterization of the MoS_2 grown on h-BN film 78
Electrical analysis of the MoS_2 grown on h-BN film 81
Conclusion 83
Acknowledgements 83
References 84
Chapter 4 - Few layer graphene interfacing with reversible mechanical dipole-modulating molecules: A graphene interface-molecular machine 89
Abstract 89
Introduction 90
Experimental Section 91
Graphene oxide (GO) preparation 92
The ATG device fabrication 92
Amino azo benzene attachment 93
The reduction of GO to RGO via hydrazine treatment 94
Instrumentations for chemical, physical and electrical characterization 94
Raman spectroscopy system 94
X-ray photoelectron spectroscopy (XPS) system 94
Cryostat electrical system 94
Results and Discussion 95
Structural and chemical characterization of ATG 95
Opto-electronic characterization 98
Conclusion 105

Acknowledgements 105
References 105
Chapter 5 - Molybdenum disulfide (MoS_2) for metal-nanoparticles interfacing: An avenue for the modification electrical, thermal, and structural Properties 108
Abstract 108
Introduction 108
Experimental Section 110
MoS_2 incorporation with metal-nanoparticles via chemical route 110
Procedure for mechanical exfoliation MoS_2 110
Procedure for solution-based exfoliation MoS_2 110
MoS_2 incorporation with metal-nanoparticles via microwave route 111
MoS_2 incorporation with metal-nanoparticles via physical deposition (DC sputtering) 111
Instrumentations for chemical, physical and electrical characterization 111
Raman spectroscopy system 111
Thermal conductivity measurement set-up 112
Field emission scanning electron microscope (FESEM) 113
Transmission electron microscope (TEM) 113
Cryostat electrical system 113
Results and Discussion 114
The mechanism of Au incorporation into MoS_2 via chemical route functionalization and the corresponding structural characterization structural characterization 114
The mechanism of Au incorporation into MoS_2 via microwave route functionalization and the corresponding structural characterization 118
Raman characterization for metal-nanoparticles incorporated MoS_2 121
Electrical characterization for metal-nanoparticles incorporated MoS_2 123
The Schottky-barrier analysis 123
MoS_2 field effect mobility analysis 125
The enhancement in gate capacitance 127
The analysis of gate capacitance of Au deposition via functionalization route and one via physical deposition 128
The effect of loading density on the I-V behavior 129

The effect of the metal’s work function on the doping polarity on MoS_2 130

The effect of MoS_2 defects on the electrical behavior 131

The carrier transport mechanism in metal incorporated MoS2 device 133

The thermal conductivity analysis of MoS2 and metal incorporated MoS_2 134

Conclusion 138

Acknowledgements.. 138

References.. 139

Chapter 6 - Conclusion 143

Chapter 7 - Future outlook.. 146

List of Figures

Figure 1.1 a) Library of 2D nanomaterial discovered up-to-date [Figure adapted from Geim, A. K. et.al, "Van der Waals heterostructures.", Nature, 499, 419–425 (2013).] b) Presentation of 3D crystal, which composes by stacking of layers. Each of these monolayer is separated by weak van der Waals forces. 2

Figure 1.2 a) Top view of an artistic interpretation of monolayer graphene, b) Schematic diagram of graphene as a fundamental building block for 0D fullerenes, 1D nanotubes and 3D graphite [adapted from *Geim, A.K., Novoselov, K.S. "The Rise of Graphene." Nature Materials 6, 183-191 (2007)*] 4

Figure 1.4 a) Top view (top) and top view (bottom) of an artistic interpretation of monolayer MoS_2, b) Lattice interpretation of two polytypes of single layer MoS_2: trigonal prismatic (1H) and octahedral (1T) [Figure adapted from *G. Eda et al. "Photoluminescence from Chemically Exfoliated MoS_2." Nano Letters 11, 5111–5116 (2011).]* 5

Figure 1.5 a) Top view of an artistic interpretation of monolayer h-BN, b) Partially ionic due to the difference in electronegativity of B and N [Figure adapted from *A. Pakdel et al. "Nonwetting "White Graphene" Films." Acta Materialia 61, 1266–1273 (2013).*] 6

Figure 1.6 a) Optical image, and b) AFM scan of a mechanical exfoliated multi-layered graphene sheet (thickness ~ 3 nm. c) Schematic diagram of a Hall-bar graphene device [Figure adapted from *Novoselov, K. S. et al, "Electric Field Effect in Atomically Thin Carbon Films.", Science, 22, 666-669 (2004).*] 8

Figure 1.7 a) Schematic diagram showing the application of intercalation ion (ICs) in producing a stable dispersion of pristine 2D nanomaterials. b) Dispersion of exfoliated layered compounds [Figure adapted from *R. J. Smith et.al, "Large-Scale Exfoliation of Inorganic Layered Compounds in Aqueous Surfactant Solutions.", Advanced Materials 23, 3944 (2011).*] 10

Figure 1.8 The growth kinetic of graphene *via* CVD in case of CH_4, Cu, and Ni [Figure adapted from *Muñoz, R. et al, "Review of CVD Synthesis of Graphene.", Chemical Vapor Deposition 19, 297–3229 (2013).*] 12

Figure 1.9 a) The optical image of MoS_2 monolayer triangular grains grown by CVD on a 300 nm SiO_2/Si substrate. The dimension from tip to tip is 123 μm. b) The photoluminescence

of monolayer and bilayer MoS_2. [Figure adapted from *van der Zande, A et al, "Grains and Grain Boundaries in Highly Crystalline Monolayer Molybdenum Disulphide.", Nature Materials 12, 554–561 (2013).*] 14

Figure 2.1a) LPCVD set up for the growth of graphene on SiO_2/Si substrates, b) Graphene film on SiO_2/Si<111>. 28

Figure 2.2 The process of graphene synthesis on SiO_2/Si substrate 29

Figure 2.3: The transferring process of graphene to TEM grid. 30

Figure 2.4: The transferring process of graphene on top Cu surface to SiO_2/Si substrate. 31

Figure 2.5: The process of defining the geometry of the metal contact. 32

Figure 2.6: The process of defining the geometry of multilayer graphene. 33

Figure 2.7 : The set-up of back-gating measurement 36

Figure 2.8 Raman spectroscopy analysis of the grown graphene at the metal-oxide interface. Graphene shown here was synthesized with the following conditions: T = 900ºC, F_{H2}/F_{CH4}=1/5, and P_{Tot}= 2 Torr). a) the Raman spectra of multiple area corresponding to the optical image (inset), b-d) Raman mapping of G band, I_D/I_G ratio, and I_{2D}/I_G. The red, blue, and black circles correspond to the Raman spectra shown in a) 37

Figure 2.9 a) FESEM image of the grown graphene. b) The survey XPS scan of thin graphene. c) The high-resolution XPS spectrum of Cu $2p_{3/2}$. d) The high-resolution XPS spectrum of C 1s at high resolution and at room temperature. 38

Figure 2.10 a) A representative fit of the Raman 2D band. b) SAED of the majority region of the grown graphene. c) SAED of the A-B stacking region, and d) its line intensity profile. 40

Figure 2.11 a) Process involved during the synthesis of graphene at the interface of SiO_2 dielectric and Cu. b) The formation of the interface graphene at the edge of the grain boundaries, and the corresponding Raman G-band mapping (scale bar: 4 μm [red], and 10 μm [white]). c) G band mapping of an interface graphene island. d) the corresponding Raman spectra of circle and blue areas. 41

Figure 2.12 a) Raman G band mapping of the interface graphene, b) the corresponding Raman spectra to the red and black circle area on a). c) Raman G band mapping (Inverted color) of the interface graphene, d) the corresponding Raman spectra to the red and black circle area on c). 42

Figure 2.13 a) the G band mapping of interface graphene (300 nm Cu film). b) The coverage of interface graphene grown *via* 300 nm Cu, and 150 nm Cu. c) The growth rate of the interface graphene on SiO_2/Si<111> substrate and SiO_2/Si<100> substrate. d) X-ray diffraction of post-CVD Cu crystal lattice on SiO_2/Si<111> substrate and SiO_2/Si<100> substrate. 44
Figure 2.14 a) Raman mapping of I_D/I_G of interfaced graphene at different flow rate ratios (H_2/CH_4), and the corresponding average Raman spectra. c) Domain size (L_a) and I_D/I_G ratio with respected to flow rate ratio (H_2/CH_4). 46
Figure 2.15 a) Raman mapping of I_D/I_G of interfaced graphene (750-900^oC), b) and the corresponding average Raman spectra. c) Domain size (L_a) and I_D/I_G ratio with respected to reaction temperature. 47
Figure 2.16 a) Conductivity vs. carrier concentrations characteristics of the GFET at 10 K, inset: schematic of GFET (left) with the corresponding optical microscope image (right). b) Variation of field effect mobility with respect to carrier concentration for GFET at 10 K. c) The resistivity of GFET with respect to carrier concentration (10-140 K). d) The charge dependent mobility of hole with respect to temperature (10-140 K), inset: The charge dependent mobility of electron with respect to temperature (10-140 K). 49
Figure 2.17 a) Normalized background conductivity vs. temperature. b) The band structure of thin graphene film, where the simple two band (STB) model of the grown graphene is suitable for energies near the Fermi level (E_F), and as the energies is far from the EF, the dispersion curve behaves like a Dirac cone (DC) as for single-layer graphene. c) The STB model fit for background resistivity as respected to temperature of GFET (10-140K). d) Arrhenius model fit for GFET transport (40-160 K) with inset of variable range hopping (VHR) model fit for GFET transport (40-160 K). 52
Figure 3.1 a) LPCVD set up for the growth of h-BN on SiO_2/Si substrates, b) The processing conditions for the growth of h-BN. 64
Figure 3.2 The LPCVD set-up for direct growth of MoS_2 on h-BN/SiO_2/Si substrates. 65
Figure 3.3 The schematic for a home-built UV-Vis system 68
Figure 3.4 Processes involved during h-BN synthesis on SiO_2/Si substrates using LPCVD 70
Figure 3.5 XPS spectroscopic analysis. (a) B 1s, O 1s, and (c) N 1s 72

Figure 3.6 Raman spectroscopic analysis of post h-BN growth Si surface. (a) Optical microscopic view of the Si surface and (b) Raman spectra corresponding to different regions marked blue, red and black color. 73
Figure 3.7 a) The Raman spectra of E_{2g} peak, inset: The optical microscopy image of h-BN film. b) Scanning Raman intensity mapping of E_{2g} peak. c) Scanning Raman position mapping of E_{2g} peak. The colored circles at different areas of a), b) and (c) correspond to the Raman spectrum in a). d) AFM topography and the corresponding line scan for thin h-BN film for 1 min growth. 74
Figure 3.8 a) AFM measurement of surface of SiO_2/Si before and after h-BN growth and (b) surface roughness histogram of the height distribution measured *via* AFM for SiO_2/Si (blue diamonds) and h-BN (black circles) with Gaussian fit to the distribution (red solid lines). 75
Figure 3.9 a) SAED of h-BN film transferred onto TEM grids. b) XRD analysis of h-BN film on SiO_2/Si surfaces. 76
Figure 3.10 a) h-BN film grown on quartz substrate (2 cm x 1.5 cm area). b) Raman spectrum of the corresponding h-BN films on quartz substrate. c) UV-vis absorbance spectra (room temperature). d) Tauc plot corresponds to the optical band gap of 5.51 eV. 77
Figure 3.11 MoS_2:h-BN heterostructure: a) the Raman spectrum corresponds to E^1_{2g} and A_{1g} peaks the Raman E_{2g} phonon mode of underneath h-BN. Inset: (left) Raman vibrational modes for MoS_2 in-plane E^1_{2g} and out-plane A_{1g} modes, (right) Optical image of MoS_2:h-BN heterostructure. c-d) The Raman intensity mapping for (b) MoS_2 (E'_{2g}), (c) MoS_2 (A_{1g}) 79
Figure 3.12 XPS analysis of MoS_2:h-BN heterostructure: a) Mo 3d and b) S 2p. 80
Figure 3.13 a) PL spectrum of the direct grown MoS_2 on SiO_2 sample at room temperature. b) PL spectrum of the direct grown MoS_2 on h-BN sample at room temperature. b) I-V characteristic of MoS_2/h-BN vs. MoS_2/SiO_2 samples. 82
Figure 4.1 Representative model showing azobenzene molecules covalently bonded on the sp^3 regime of functionalized graphene. The azobenzene-group changes its configuration on graphene (trilayer) when exposed to UV (cis) and blue light (trans). This mechanical motion of azobenzene modulates the density of holes in ATG. (Bottom-right) The optical image of ATG device between the gold electrodes 20 μm apart. The Raman spectrum of the ATG sheet shows the D and G peak representing the graphenic backbone. Since graphene is

functionalized, the Raman spectrum shows a D peak at 1350 cm^{-1}. No appreciable 2D peak was observed. 91

Figure 4.2 ATG device's chemical construct 92

Figure 4.3 (a) AFM image (1.7 µm X 1 µm) of a typical ATG sheet shows a height of 3.6 nm high. Subtracting the height of the azobenezene and oxy groups, the underlying graphene is 3 sheets (including the two oxidized sheets). (b) The XPS spectrum of the ATG sheet shows the presence of the azo-group. The peak at 400.5 eV corresponds -(C-N)- and (N=N) in azobenzene. (c) The XPS (N 1s) of the TLG sheet shows the presence of the peak for the amide linkage with silica appears at around 401.5 eV. (d) The XPS (the C 1s and N 1s) shows the position and the intensity of the nitrogen peak and carbon peak of ATG. The atomic ratio of these two peaks is found to be 1:16 (N: C) 96

Figure 4.4 a) The figure shows the response of the ATG device (under 19 psia pure He environment at room temperature) exposed to UV, Blue and Dark for 90 sec each at 100 mV source-drain voltage. b) The same response (as (a)) is measured at 10 mV source-drain voltage. The current axis has been rescaled to better represent the change. Also, the azobenzene's trans configuration can be achieved *via* blue light exposure and temperature. Since, the rate of decrease of conductivity was not significantly more than that in dark environment; the room temperature is high enough to favor the trans state in the absence of UV. Further, it is known that the azobenzene could readily fluctuate between cis and trans configuration[22], leading to fluctuation in current as observed in electrical measurements. c) The response in conductivity of the functionalized TLG (without azobenzene attachment) on 300 nm silica substrate exposed to UV and Dark for 100 sec each at 100 mV source-drain voltage is shown as control sample. 100

Figure 4.5 a) A schematic of the back gating measurement setup on device consisting of an ATG sheet spanning gold electrodes spaced 20 µm apart. The silica substrate, 300 nm, acted as a gate oxide, and heavily doped silicon acts as gate electrode. b) The gating study, conducted at 10 mV drain voltage, showed that the ATG device is p-type with a hole mobility of 0.195 $cm^2/V/s$. The measurement was made for the cis-configuration of azobeneze in ATG. 102

Figure 4.6 Graphical analysis of V_G determination 104

Figure 5.1 a) Schematic depicting the anchoring of gold nanoparticles on MoS_2 *via* chemical reduction strategy. b) TEM image of MoS_2 before functionalization. c) FESEM image of

Au-MoS_2 NP hybrid. d-f) Time-dependent images of the hybrid at different stages of functionalization. d and e) FESEM images of the hybrid after 2 h and 24 h of reaction respectively. f) TEM image after 6 h of reaction. g and h) FESEM and TEM image of the nanoparticle formed on MoS_2 sheet. 115

Figure 5.2 a) FESEM images of multilayered MoS_2 preferentially functionalized at the edges during the initial phases of the chemical reduction reaction. b-d) FESEM images of Au-MoS_2 composite prepared using chemical reduction route done at different temperatures, b) 4 °C, c) 25 °C and d) 60 °C. e) FESEM images of Ag-MoS_2 composite prepared using chemical reduction route. 117

Figure 5.3 EDS spectrum and elemental maps of Au-MoS_2 hybrids produced by chemical reduction. The corresponding electron microscope image also can be seen. All scale bars are 10 μm. 118

Figure 5.4 a) Schematic depicting the anchoring of gold nanoparticles on MoS_2 *via* MW irradiation. b) and c) large area and higher magnification FESEM image of Au-MoS_2 NP hybrid. d-f) Time-dependent images of the hybrid at different stages of functionalization. d) 2 s, and e) 5 s and f) 10 s of MW irradiation. (g) FESEM images showing the preferential edge and/or defect functionalization of gold nanoparticles on turbostatic multilayer MoS_2. A large number of gold nanoparticles formed in lines indicating the presence of edges or defects. Scale bar 30 μm. 119

Figure 5.5 FESEM images of multilayered MoS_2 preferentially functionalized at the edges during the initial phases of microwave irradiation. 120

Figure 5.6 TEM images showing the high selectivity of Au NPs at the edge, and indicating the intimate contact between MoS_2 and Au NPs. 121

Figure 5.7 Raman spectrum of Au-MoS_2 hybrid prepared *via* (a) chemical reduction and (b) Microwave irradiation. The Raman spectra of the bulk MoS_2 sheet showing the E^1_{2g} (~385 cm^{-1}, in plane vibration) and A_{1g} (~410 cm^{-1}, out of plane vibration) peaks (a). The Δ represents the difference between the Raman peak positions (i.e. $A_{1g} - E^1_{2g}$), and is used to determine the number of MoS_2 layers. For Δ ~23 cm^{-1}, the number of layers was estimated to be three. After gold deposition, the A_{1g} and E^1_{2g} peaks up-shift by ~ 1 cm^{-1} (in a), which implied p-doping. In the case of microwave irradiation (b) a downshift of features can be observed, implying n-doping. (c) Illustration of relevant modes of vibration in MoS_2. 122

Figure 5.8 a) MoS_2 device, 25 nm thick, is extracted using scotch tape-base micromechanical cleavage. Inset shows the AFM imaging of MoS_2. b) I_{DS}-V_{DS} curves recorded for MoS_2 device at various temperatures from 80 K to 180 K. It shows as source-drain bias voltage increases the hopping tendency is significantly increased in the reverse side than forward side. c) at 160 K a) logarithmic plot of total current *I* as a function of reverse bias V_{DS} shows an estimation of Schottky barrier E_o = 14.80 eV and b) logarithmic plot of total current *I* as a function of forward bias V_{DS} shows an estimation of Schottky barrier E_o = 14.45 eV. 124

Figure 5.9 a) At 80 K the conductivity of MoS_2 device is increased 10^3 folds after gold functionalization (Au-MoS_2). The inset shows an enlarged view of I_{DS} versus V_{DS} response for MoS_2 at 80 K. b) Back-gating characteristics (160 K with V_{DS} = 0.5 V) of MoS_2 and Au-MoS_2 FETs are shown. The top inset shows capacitance circuitry of the Au-MoS_2 device. Bottom-left inset shows the structure of MoS_2 FET with electrical connections used to characterize the device. Au-MoS_2 device shows ~9 fold increase in effective gate capacitance. Bottom-right inset shows an FESEM micrograph of gold nanoparticles on MoS_2. (Bar = 10 μm). c) Log scale of drain current versus back gate. Subthreshold-Swing measurement is made for currents increasing from 1 nA to 10 nA. The insets show the zoomed in graph for both MoS_2 (black curve) and Au-functionalized MoS_2 (red curve). The gate voltage increases from 2.7 to 3.725 V for MoS_2 and from -11.375 to -7.375 V for Au-MoS_2. 126

Figure 5.10 Back gating scans of MoS_2 before and after 2 and 4 seconds Au/Pd sputtering. The mobility increases progressively from2.3 $cm^2V^{-1}s^{-1}$ to 4.6, and11 $cm^2V^{-1}s^{-1}$. The inlet shows the back gating schematic of Au sputtered MoS_2. 128

Figure 5.11 (Top panel) FESEM images of gold NPs with different loading densities deposited on MoS_2 device. At high loading, a percolating connection is formed between gold nanoparticles between electrodes. (Bottom panel) I-V respond of different Au NP loaded device (left) low loading non bridged gold channel, (middle) high loading non bridged gold channel, (right) bridged gold channel (short-circuit). 129

Figure 5.12 Raman spectra of MoS_2 before (black) and after (red) Au NP functionalization. a) MoS_2 on SiO_2, and b) MoS_2 on gold electrodes. 131

Figure 5.13 a) Room-temperature current versus voltage (IV) curves (V_G = 0V) for before and after MoS_2 device in water for 24 hrs. b) Room-temperature gating scans (V_{DS} = 1V) for before and after MoS_2 device in water for 24 hrs The conductivity of the device decreases after water interaction. The mobility of the device decreases after water interaction 132
Figure 5.14 Room-temperature current versus voltage (IV) curves (V_G = 0V) before and after MoS_2 device in water exposed to microwave for 5 s. and (b) Room-temperature gating scans (V_{DS} = 1V) before and after MoS_2 device in water exposed to microwave for 5 s. 133
Figure 5.15 a) The gating characteristic (I_{DS} versus V_{BG}) for Au-MoS_2 FET between 80 K and 180 K with 0.5 V applied bias voltage (V_{DS}). b) The Arrhenius thermal activation fit for MoS2, and Au-MoS_2. Inset: The Variable range hopping model fit for Au-MoS_2 device at the studied temperature range. 134
Figure 5.16 a) Schematic of thermal conductivity experiment showing the 532 nm laser focused on supported MoS_2 sheet. The focus laser generates local hot spot which radially dissipate over MoS_2 sheet. b) Raman spectrum of control MoS2 sample before (black) and after 15 S exposure under maximum laser power showing no shift in Raman features..................... 135
Figure 5.17 Raman spectra at different temperatures and the gradient of E^1_{2g}, and A_{1g} peaks positions with temperature $\left(\frac{\delta\omega_{E^1_{2g}}}{\delta T}\right)$ and $\left(\frac{\delta\omega_{A_{1g}}}{\delta T}\right)$ for MoS_2 (a) and Au-MoS_2 (d). Shifts in A_{1g} peak (b), and E^1_{2g} peak (c) of Raman spectrum versus temperature in MoS_2. Shift in A_{1g} peak (e), and E^1_{2g} peak of Raman spectrum versus temperature in Au-MoS_2.................... 136
Figure 5.18 Raman spectra at different temperatures and the gradient of E^1_{2g}, and A_{1g} peaks positions with temperature $\left(\frac{\delta\omega_{E^1_{2g}}}{\delta T}\right)$ and $\left(\frac{\delta\omega_{A_{1g}}}{\delta T}\right)$ for MoS_2 (a) and Au-MoS_2 (d). Shifts in A_{1g} peak (b), and E^1_{2g} peak (c) of Raman spectrum versus temperature in MoS_2. Shift in A_{1g} peak (e), and E^1_{2g} peak of Raman spectrum versus temperature in Au-MoS_2.................... 136
Figure 5.19 Raman spectra at different power and the gradient of E^1_{2g} and A_{1g} peaks positions with the reflected power $\left(\frac{\delta\omega_{E^1_{2g}}}{\delta P}\right)$, and $\left(\frac{\delta\omega_{A_{1g}}}{\delta P}\right)$ for MoS_2 (a) and Au-MoS_2 (d). b-c) Shift in

A_{1g}, and E^1_{2g} peak region of Raman spectrum versus the reflected power in MoS_2. e-f) Shift in A_{1g}, and E^1_{2g} peak region of Raman spectrum versus the reflected power in Au-MoS_2 137

List of Tables

Table 2.1: The oxidizing impurities are associated with CH_4 and H_2 in our study. 28

Acknowledgements

When I joined Dr. Vikas Berry's lab in January 2011, I aimed for a Master degree in Chemical Engineering. My whole attitude towards research changed after working for six months with Dr. Berry. His inner fire for research passed down to me to such a degree that I went on to achieve my PhD degree. His patience, attitudes, encouragement, and guidance have aided me in conquering the challenges, and the opportunities during my research years. The 5-year experience in working with Dr. Berry has shaped my intellect, and my professional carrier path. I would like to thank him for his guidance, patience, encouragement, supports, attitude, and so much more. It has been a wonderful and fun adventure working as a team with him in advancing, and exploring the frontier of 2D nanomaterial science.

I would like to extend my special thanks to SunEdison for the financial support, and for providing me an opportunity to collaborate with industrial partner.

I would like to thank Dr. James H Edgar, Dr. Placidus Amana, Dr. Keith Hohn, and Dr. Andrew Rys for serving in my PhD committees, and for their guidance, and their constructive inputs to make this dissertation a reality. They also have always been patient, and collaborative of my endeavors. I would like to extend my thanks to Mr. Michael R. Searcist for his positive, and valuable supports to my research, and to my lab. Furthermore, I would like to thank the late Dr. L.T. Fan, who was always curious and excited about my works.

During my time in the Berry research lab, I have been very fortunate to have excellent colleagues, post-docs, graduate students, and undergraduate students, including Dr. Nihar Monhanty, Dr. Kabeer Jasuaja, Joshua Podrebarac, Balabalaji Padavala (Bala), Quanxing Zheng, Dr. Sreeprasad Sreenivasan (Prasad), the late Dr. Vasanta Pallem, Cody Fager, Namhoon Kim, Deven Moris, Shikai Deng, Donovan Briggs, Songwei Che, Rousan Debbarma, Bijentimala

Keisham (Nicky), Dr. Sanjay Behura, Kai-Chih Chang, Yu Wen (Daniel), Xin Yu (Rex), Deisy Arrington, Muna Sabor, and Alexander Crocker (in chronological order). When I joined the group, I met two of my seniors, Nihar and Kabeer, who shared the passions with Dr. Berry toward research. They passed it down to me along with their valuable experience, creativity, and knowledge. Together with Dr. Berry, they paved a smooth entrance for my PhD path. I would like to thank Dr. Sreenivasan, the late Dr. Pallem, and Dr. Behura for their professional collaborations, their extensive knowledge in nanomaterial, and their helps in editing my papers. I would also like to thank Shikai, and Donovan for being great co-workers, and fantastic roommates. I would like to thank Rousan Debbarma for his entertaining attitude, and his deep knowledge in science and engineering in various projects. I will always enjoy exchanging my knowledge, sharing a laugh, watching the movies, and having new cuisine with him. I would like to thank Nicky and Songwei for their enthusiasm toward research. It was enjoyable to work and to exchange knowledge with them in CVD engineering, and Raman spectroscopy. I would like to thank Bala, Zheng, Kai-Chih, Daniel, Deisy, Rex in discussing their projects and exchanging their knowledge. I would like to thank Cody for his engineering skills in calibrating many lab-built systems. I would like to thank Alex for his engineering skills in the set-ups of chemical vapor deposition systems in our lab. I would like also to thank Joshua, Namhoon, Muna, and Deven for their helps, and their discussions during several project.

Outside our group, I would like to thank Myles Ikenberry for all the hours he spends on my XPS samples. I would like to thank Clint Frye for countless hours in discussing in crystal growth, and CVD engineering. I would also like to thank all the members of the chemical engineering department of Kansas State University and of University of Illinois at Chicago for their supports and in making the 5 years one of the best periods in my life.

Outside the department I would like to thank Dr. Dan Boyle for the help with FESEM, TEM, and E-Beam lithography training. I would like to thank all the members of NCF at University of Illinois at Chicago for training me on various instruments in clean room. I would also like extend my thanks to Dr. Seyoung An for his extensive training in oxidation furnace, RIE system, and Karl Suss MA6 Mask Aligner system.

Furthermore, I would like to have another special thanks for Dr. Berry for giving me the opportunity to attend to NSF-I-Corps program, where I gained tremendous confidence. I would like to show my special appreciation to Dr. Melbs LeMieux, who showed me great passions towards entrepreneurship and guided me through the I-Corps program. Dr. Berry and Dr LeMieux showed me that if I can find joy in my works, I will able to learn and to conquer many obstacles.

I would like to thank Mr. Jim Braun for his supports at the beginning of my PhD journey. I would like to thank Mr. Mike Morgan, and Mr. Pat Ruffin to their constant supports to my PhD journey. Also I would like to thank Mrs. Crystal Aceves, Dr. Peter Smooker, and Dr. Bert Wiswell for helping proofread my thesis.

Last but not least, I would like to show my tremendous thanks to Dr. Berry's family, especially to his wife, Namrita, who has been very kind to my group members. No matter where I am either at small town of Manhattan, or at big city of Chicago, she has always made me feel like home.

Dedication

I would like to dedicate this thesis to my parents, Mr. Canh Nguyen, and Mrs. Muoi Nguyen and to my brother, Mr. Vu Nguyen, who is thousand miles away. They have been supported in every aspect of my life, and I owe it to them for what I am today. I also would like to dedicate this work to my brother family including his wife, Uyen Nguyen, and their daughter, Sophie Nhi Nguyen (Ruby). Also I would like to dedicate this thesis to fiancée (and soon to be wife) Ms. Phuong Ngoc Minh Tran, who has been always showing patience, believing in me, and supporting me to achieve my goals. I would also like to dedicate this thesis to my advisor, Dr. Vikas Berry, for believing in me, and for helping me get my confidence. I would like to dedicate this to my friends including Hien Minh Ngo, Nam Quoc Pham, and Thanh Duy Tran who have always supported me since I moved to Kansas even though they are half-way around the world. In addition, I would like to dedicate this thesis to Mr. Mike Morgan, Mr. Pat Ruffin, and Mr. Randy Colemen for always been there since the beginning of my Ph.D journey. Last but not least, I would like to specially dedicate this thesis to the late Mr. John Andrew Weber Jr. He was a kind person, who helped my family when we were in struggle. He was not only a friend, but also a mentor who showed patience, and taught me so many valuable lessons in life when I first came to the U.S. I owe him so much for that.

Chapter 1 - The two-dimensional (2D) nanomaterial

Introduction

New materials with a collection of unique and extraordinary properties have led to great technological advances for humankind. The ability of manipulating matter at atomic/molecular level has facilitated discovery, control, and synthesis of these novel materials. Such ability, first envisioned by Dr. Richard P. Feynman in during his famous lecture "*There's Plenty of Room at the Bottom*" in 1959, is the central heart of nanotechnology.

Over the past thirty years, by practicing Feynman's idea, material engineers, and scientists including physicists, chemists, and biologists have reached to a point in the development of state-of-the-art techniques where we have instruments to tackle the challenges offered by the emerging frontiers of nanotechnology. Since then, it has been conceivable to sculpt materials at their tiniest scale to a level at which, in essence, a complete miniaturized analytical laboratory can be realized on a single hand-held chip[1]. Furthermore, the discovery, and synthesis of low dimensional nanomaterials including quantum dots and nanoparticles (0-dimensional [0D] class)[2–4], nanotubes and nanowires (1-dimensional [1D] class)[5–7], and graphene and atomically thin materials (2-dimensional [2D] class)[8–10] have distinguished the development of nanotechnology.

Over the past decade, the wondrous 2D class has grown extensively[8,11–13] (**Figure 1.1a**). These 2D nanomaterials are covalently bonded atomic layers. *Via* weak van der Waals force, these layers are appended to each other to generate their 3D bulk crystalline structures [12,13] (**Figure 1.1b**). In contrast of their bulk layered counterpart, these 2D nanomaterials offer a set of novel physical-chemical-electrical properties, which enable to tremendous possibilities that will revolutionize several key applications, including miniaturization of semiconductors[9,14], drug

delivery[15–17], medical diagnosis[18–20], eco-friendly chemical ingredients[21,22], and clean energy generation[23,24] and storage[25–27].

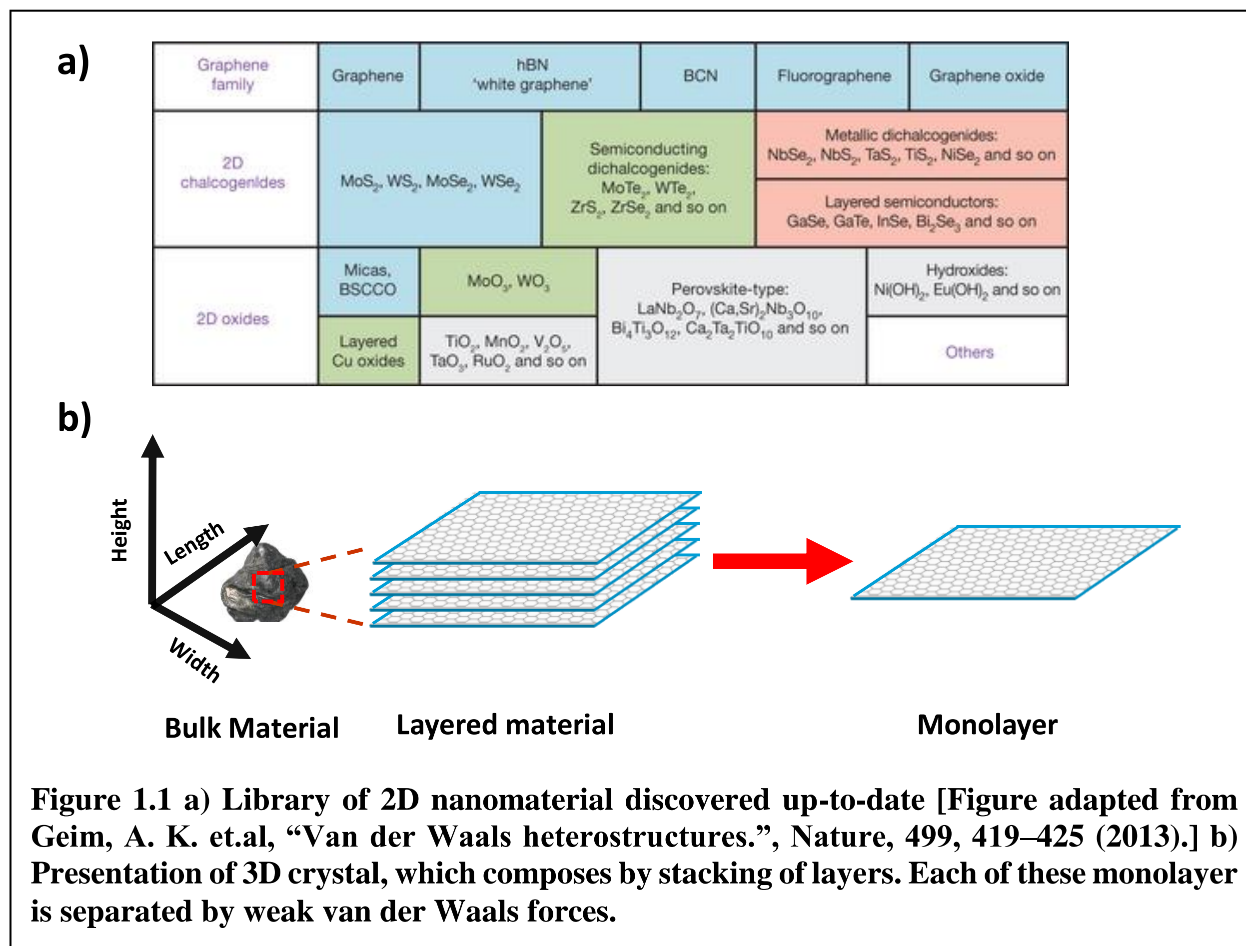

Figure 1.1 a) Library of 2D nanomaterial discovered up-to-date [Figure adapted from Geim, A. K. et.al, "Van der Waals heterostructures.", Nature, 499, 419–425 (2013).] b) Presentation of 3D crystal, which composes by stacking of layers. Each of these monolayer is separated by weak van der Waals forces.

In order to enhance practices in applied researches and applications of 2D nanomaterials, the ability to facilely synthesize large-area, and high-quality 2D nanomaterials is essential. Furthermore, the incorporation of these 2D nanomaterials with other class of nanomaterials and molecules provides avenues to penetrate into the new world of nano-structure. This leads to the comprehension of the synergy between 2D nanomaterials with mechanical actuating molecules, and the control of their fundamental properties at the nanoscale. Thus, the grand purposes of this thesis are simplified as following: (a) To understand the science of the large-area growth of these 2D nanomaterials *via* a readily available technology i.e. chemical vapor deposition technique. (b)

A demonstration of the covalent bonding between 2D nanomaterials with mechanical actuating molecules assists the study of robust detection of molecular motions on the surface of 2D nanomaterial platform. Furthermore, (c) novel developments in interfacing routes of 2D nanomaterials with other nano-systems aids in the modulation of the structural, electrical, and thermal properties of 2D nanomaterials.

Graphene: The 2D carbon crystal

The first isolated 2D crystalline material, graphene, is a single-layer of sp^2 bonded carbon atoms arranged in a hexagonal lattice. This material, a long-term "academic material" and previously theorized not to exist, was discovered by Konstantin Novoselov and Andre Geim in 2004, which led them to win the Nobel Prize in 2010[8,28–30]. Graphene is a fundamental building block for a range of well-known carbon materials such as 3D graphite (layer by layer stacking of graphene), 1D carbon nanotube (rolled up graphene), and (OD) fullerene (spherical wrap of graphene with additional pentagons for curvature defects)[31] (**Figure 1.2**). Furthermore, graphene possesses a superior thermal conductivity (~5,000 W/mK)[32] ,exceptional mechanical strength (a Young Modulus [stiffness] of 1 TPa)[33], high optical transparency (2.3% white light absorption)[34], high chemical and thermal stability (~500°C)[35]. Remarkably, graphene is an atomically thin semi metal exhibiting ballistic transport of its charge carriers at room temperature (200,000 $cm^2V^{-1}s^{-1}$)[8,29,36], high quantum capacitance[37], and carrier confinement. Owing to these properties, graphene is ultra-sensitive electronic platform for single-molecule detectors[38,39] and electronic nano-mechanical systems[40,41]. This will be further demonstrated in chapter 3, where graphene was utilized for the study of the robust detection of molecular motions on its surface. In addition, graphene can be applied in several unique electronic applications, including ultrafast nanoelectronic devices[29,30], ultracapacitors[42], and optoelectronics[43].

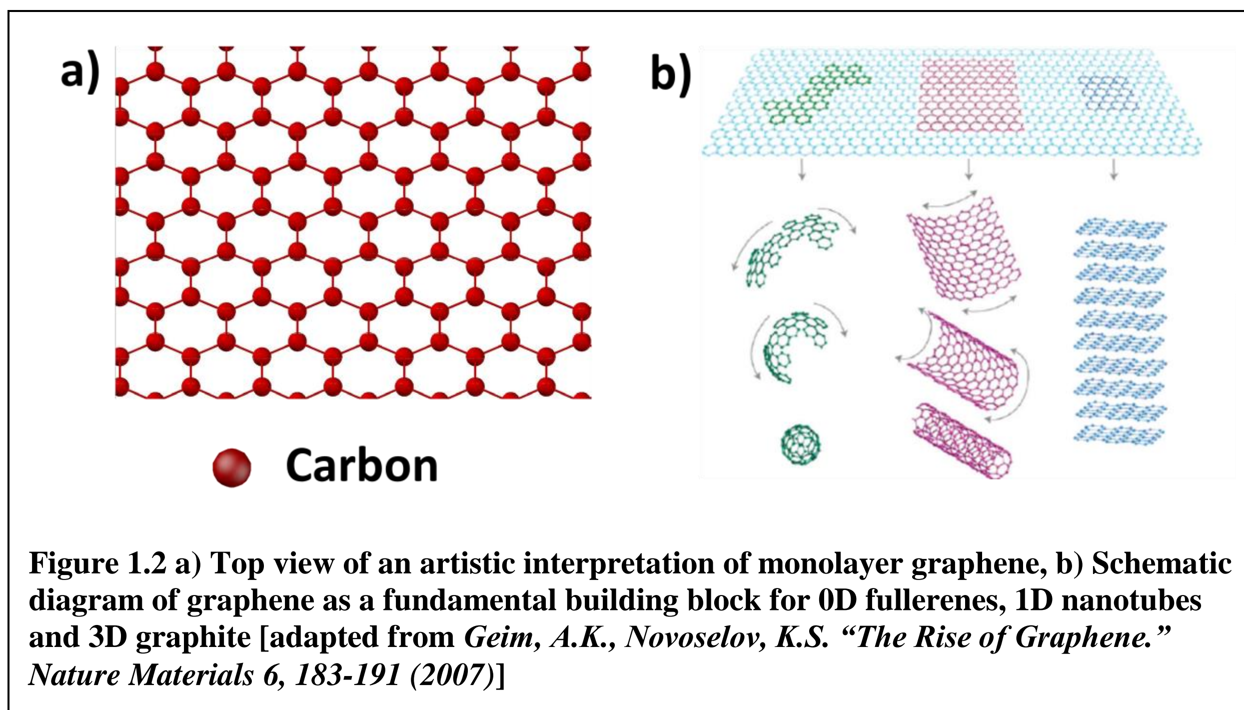

Figure 1.2 a) Top view of an artistic interpretation of monolayer graphene, b) Schematic diagram of graphene as a fundamental building block for 0D fullerenes, 1D nanotubes and 3D graphite [adapted from *Geim, A.K., Novoselov, K.S. "The Rise of Graphene." Nature Materials 6, 183-191 (2007)*]

Molybdenum disulfide (MoS_2): Graphene's cousin

Monolayer MoS_2 is a representative of the 2D transition-metal dichalcogenide (TMDs) class. As shown in **Figure 1.3** It is a three-atom-thick layer, composed of a stratum of molybdenum atoms sandwiched between two layers of sulfur atoms in a trigonal prismatic lattice, referred to as 2H or semiconducting MoS_2. On the other hand, Mo and S atoms are arranged in antiprismatic lattice and referred to as 1T or metallic MoS_2[44]. The relatively weak interlayer interaction between the MoS_2 sheet allows their monolayer crystals (thickness 0.65 nm) to be cleaved mechanically and chemically[45]. Furthermore, MoS_2 is mechanically flexible with a Young's modulus of 0.33 TPa[46]. Interestingly, the electrical and optical properties of MoS_2 changes dramatically with number of layers: bulk MoS_2 exhibits an indirect band-gap of 1.2 eV, while monolayer MoS_2 has a direct band-gap of ~1.8 eV[47] with enhanced photoluminescence[48]. A single layer MoS_2 field effect transistor (FET) exhibits an electron mobility of 0.5 – 15 $cm^2/(V.s)$

with a high on/off current ratio (10^3 to 10^8)[9]. Recent studies show that MoS_2 can be applied effectively in sensing[49,50], energy harvesting[51], and photo-electronic applications[52].

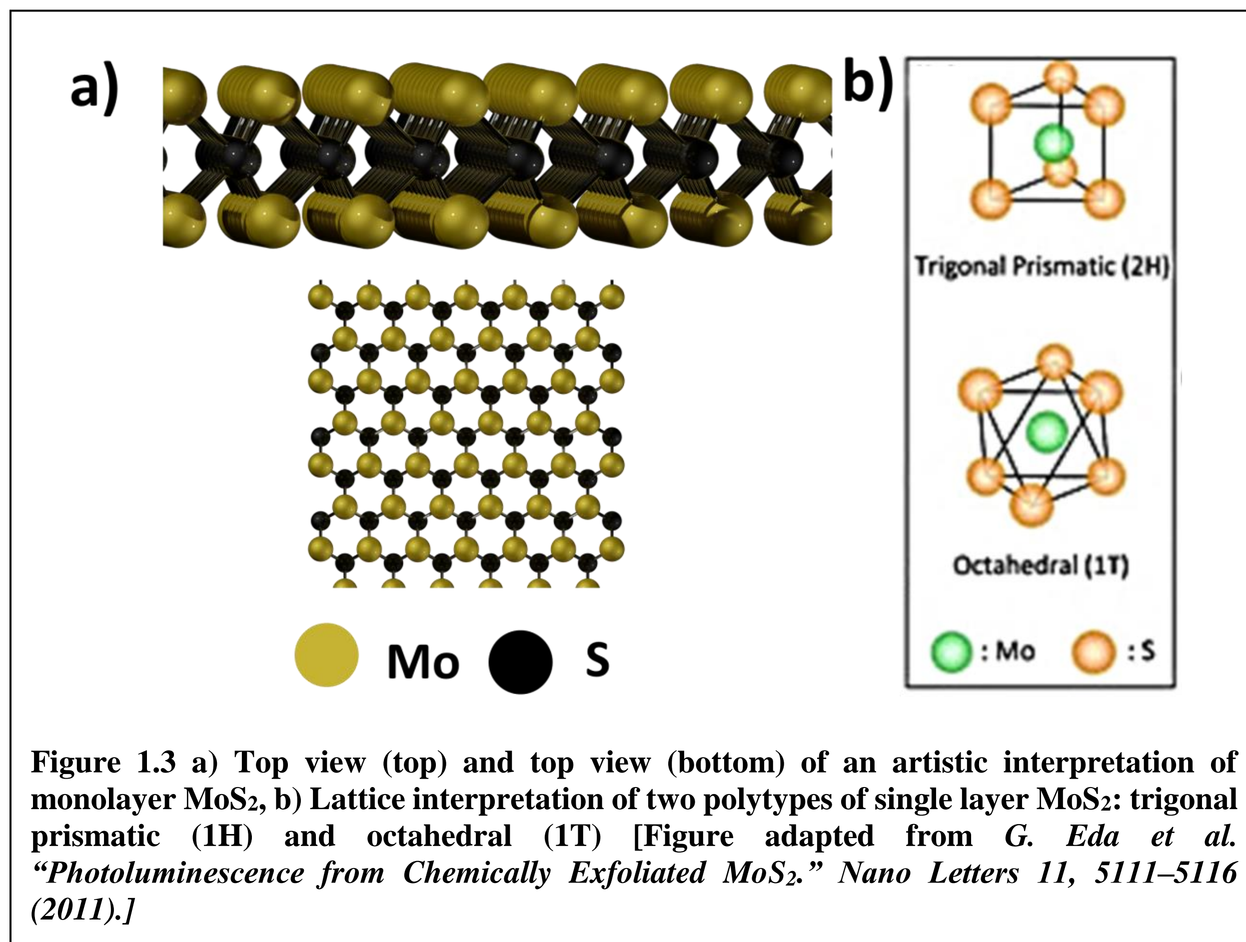

Figure 1.3 a) Top view (top) and top view (bottom) of an artistic interpretation of monolayer MoS_2, b) Lattice interpretation of two polytypes of single layer MoS_2: trigonal prismatic (1H) and octahedral (1T) [Figure adapted from *G. Eda et al. "Photoluminescence from Chemically Exfoliated MoS_2." Nano Letters 11, 5111–5116 (2011).]*

Due to its inert nature, it is challenging to broaden the applications of MoS_2. Modifying the surface of MoS_2 is critical to enable its incorporation into practical applications. In chapter 4, the successful leveraging of stable sulfur-metal binding to incorporate highly-capacitive metal nanoparticles onto MoS_2 was described *via* two different methods: (1) the solution functionalization route and (2) the microwave assisted functionalization route. Such interfacing of nanostructures was extensively studied to comprehend the new enhanced structural, electrical, and thermal properties of the metal nanoparticle-MoS_2 heterostructure.

Hexagonal boron nitride (h-BN): Analog of graphene

Hexagonal boron nitride (h-BN) is a single-atom-thick two-dimensional sheet of sp^2 hybridized alternating boron and nitrogen atoms in a honeycomb lattice. It is an electronic insulator with a large direct band gap (5.97 eV)[53] and a low dielectric constant (~ 4)[54] (**Figure 1.4**). In contrast to graphene, due to the difference in electronegativity of B and N atoms, the B−N bonds in BN materials becomes partially ionic, leading to the "lip−lip" interactions between adjacent layers in BN nanostructures[55,56]. Consequently, h-BN possesses a uniform thickness and

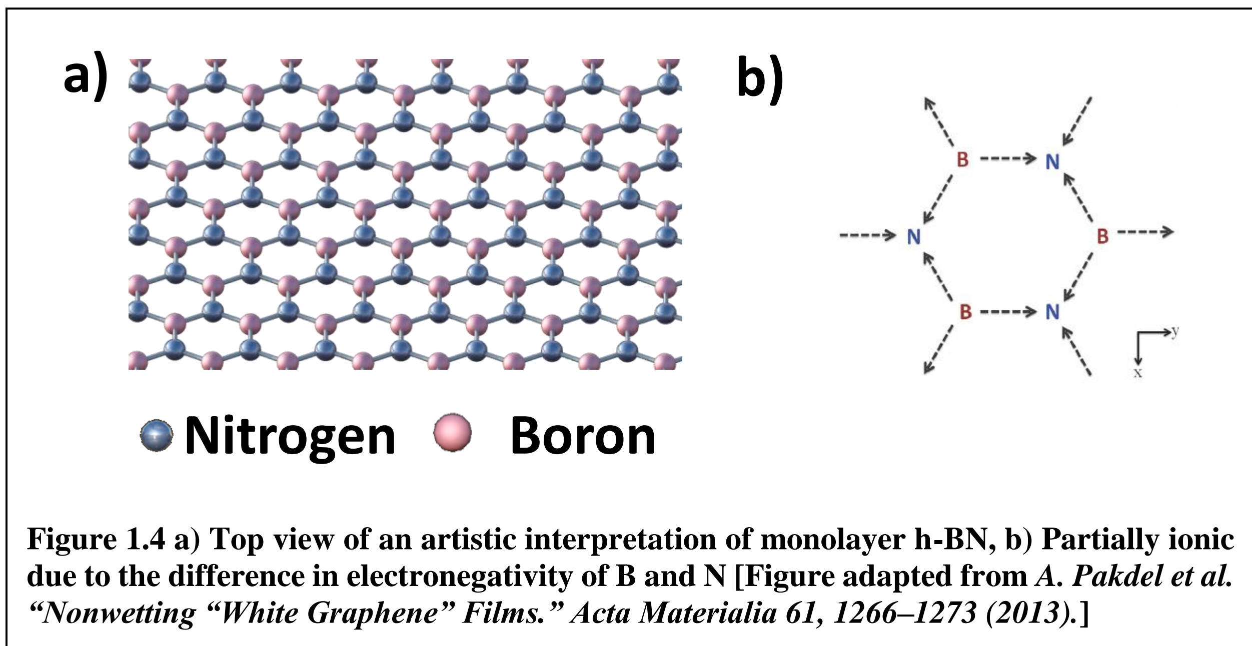

Figure 1.4 a) Top view of an artistic interpretation of monolayer h-BN, b) Partially ionic due to the difference in electronegativity of B and N [Figure adapted from *A. Pakdel et al. "Nonwetting "White Graphene" Films." Acta Materialia 61, 1266–1273 (2013).*]

atomically flat surface free of dangling bonds, which effectively reduces electron and phonon scattering effects[57–59] Furthermore, this material offers other superior properties: high thermal conductivity (2,000 W/mK)[60], large mechanical strength[61], high optical transparency[62], high chemical/temperature stability (up to 1000 °C)[63–65], deep ultraviolet emission[53], and thinnest tunneling junction[66]. Owing to these properties, h-BN can be used as an ultra-smooth, and clean (no dangling bond) dielectric, which further enhances the electrical performance in graphene and other 2D semiconductor electronics[12,59,67]. This will be further discussed in chapter 5. In addition,

h-BN can be applied in a range of applications such as, a deep ultra-violet emission device[53], the world's thinnest tunneling junction[66], a proton exchange membrane[68], and a highly chemically tolerant film for protective coatings[65].

The challenges in synthesizing and transferring of 2D nanomaterials into dielectric substrate for electronic applications

Driven by their fascinating properties and promising applications, 2D nanomaterials have been explored extensively for their novel properties, function, and practical applications. Hence, it is crucial to develop a reliable, robust, facile methods to produce ultrathin 2D nanomaterials. To date, many reliable synthetic strategies have been proposed to produce high quality, large area, and ultrathin 2D nanomaterials: mechanical exfoliation, chemical top-down approach, and chemical vapor deposition.

Mechanical exfoliation

This method was first used to isolate graphene in 2004 by Novoselov and Geim (**Figure 1.5**). In a typical process, the surface of the bulk 3D crystal is adhered onto one of a piece of Scotch tape, while the other surface is attached to another piece of Scotch-tape. Then the two pieces of Scotch-tape are separated to produce thin layer sheets. The process is repeated until thin flakes are produced, which are transferred onto a host substrate, typically silicon dioxide on silicon (SiO_2/Si), by placing the Scotch-tape side with the adhered thin flakes. Finally, the Scotch tape is peeled off from the substrate. The single- or few-layer flakes are easily found on the substrate using either an optical microscope, atomic force microscope, or Raman spectroscopy. *Via* this described method, most of the 2D nanomaterials, shown in **Figure 1.1**, have been exfoliated successfully to produce ultra-thin 2D flakes from their 3D counterpart, such as h-BN, MoS_2, WS_2, black phosphorus,

etc[8,30,69,70]. Since these thin 2D flakes are exfoliated by a mechanical process, they possess not only the pristine structure of their 3D layered structure, but also the highest crystal quality with few defects. Hence, the mechanical exfoliation technique is ideal for the fundamental study of 2D nanomaterials' intrinsic properties. However, this process has extremely low-yield and produces 2D materials of micro-scale dimensions, which demands precise handling.

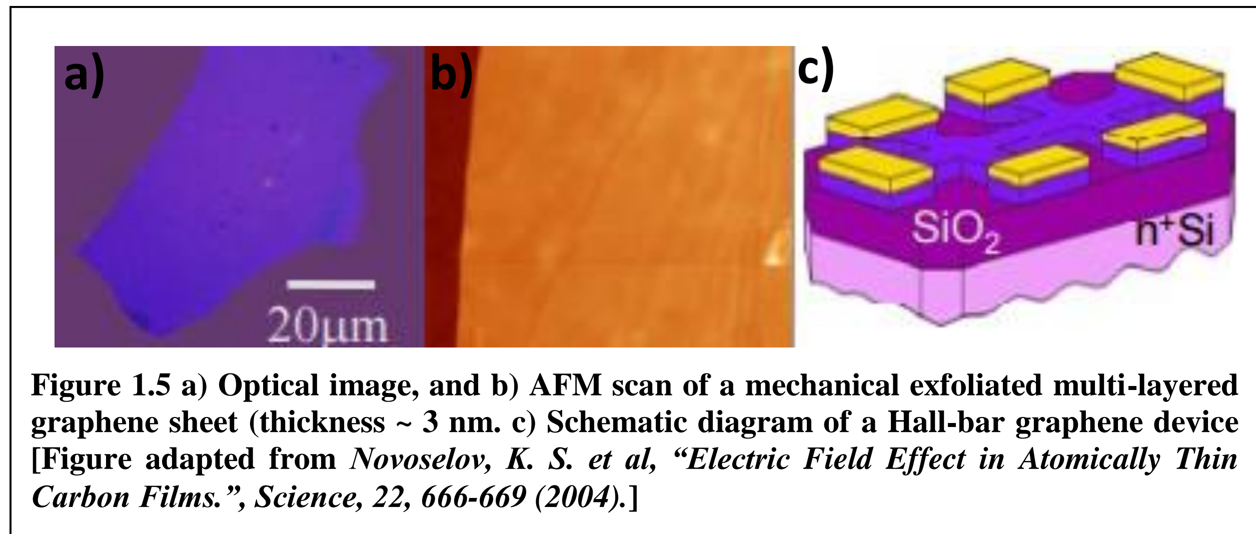

Figure 1.5 a) Optical image, and b) AFM scan of a mechanical exfoliated multi-layered graphene sheet (thickness ~ 3 nm. c) Schematic diagram of a Hall-bar graphene device [Figure adapted from *Novoselov, K. S. et al, "Electric Field Effect in Atomically Thin Carbon Films.", Science, 22, 666-669 (2004).*]

Chemical top-down approach

This approach exfoliates the ultrathin 2D nano-sheets from their 3D source and stabilize them in solution[45,71–76]. Typically, this liquid exfoliation method exfoliates bulk layered crystals directly in solvents, such as N-methylpyrrolidone (NMP), *via* sonication for a long period of time[45,76] (2 hours-24 hours). The main key for exfoliation *via* solvents is to match surface tension between the layered crystal and the solvent; this is the key factor in minimizing the energy and increasing the efficiency of exfoliation[72]. In this process, sonication can separate the layers by breaking weak van der Waals interactions, but cannot break the in-plane covalent bonding. However, most of the efficient solvents are organic-based liquids, not water. The addition of surfactant solution or aqueous polymer is found to be effective in stabilizing the nano-sheets[55].

Another top down approach is exfoliation *via* ion-intercalation (**Figure 1.6**). This technique is dependent on the intercalation of ions (Li, K, Na) into the interlayer spacing of layered bulk crystals to weaken the van de Waals interlayer-interaction. Subsequently, the intercalated 3D crystal undergoes a shorter period of sonication to exfoliate ultrathin nanosheets in water, or ethanol [77–80]. This method has an additional advantage in monitoring the phase transformation from semiconducting 2H phase to metallic 1T phase of TMDs[77,80].

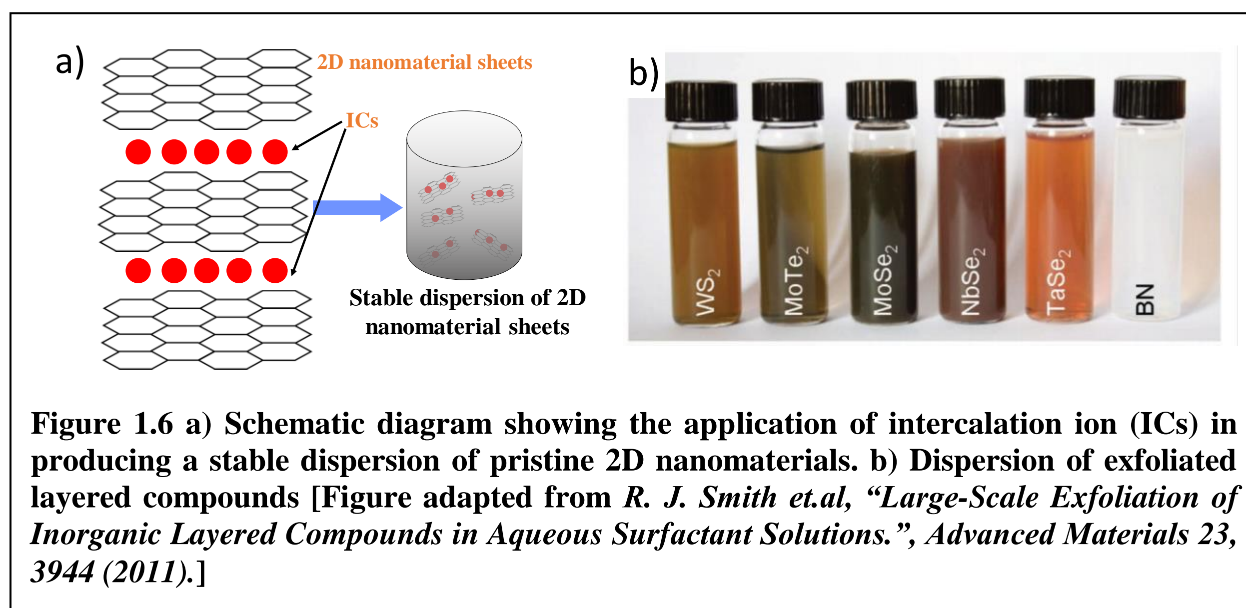

Figure 1.6 a) Schematic diagram showing the application of intercalation ion (ICs) in producing a stable dispersion of pristine 2D nanomaterials. b) Dispersion of exfoliated layered compounds [Figure adapted from *R. J. Smith et.al, "Large-Scale Exfoliation of Inorganic Layered Compounds in Aqueous Surfactant Solutions.", Advanced Materials 23, 3944 (2011).*]

In addition to the above discussed liquid exfoliation, 2D nanomaterials, especially graphene, can be exfoliated in aqueous solution by introducing oxygen functional groups into the lattice, which provides repulsion force and expands the spacing of the interlayers[81–85]. The ultrathin graphene oxide (GO) nanosheets are then exfoliated from the expanded structures under sonication. The oxygen functional groups, such as carboxyl (-COOH), epoxy (-O-), and hydroxyl (-OH) groups, are at the edge, and the basal plane of GO[82,85]. These oxygen functional groups bind to sp^3 islands on the sp^2 graphenic structure ensue an overall negative charge on the sheets which aids in exfoliation and subsequent stabilization in solution. Furthermore, the GO sheets can easily

be partially transformed into reduced graphene oxide (rGO) sheets by the reduction of most of the oxygen functional groups on their surface [82,86–88].

These chemical top down aproaches provide high-yield mass-production (milliliters to hundreds of liters)[75] of ultrathin 2D nanosheets in solution. However, the yield of single-layer sheets obtained is still quite low, and the lateral dimensions of the sheets are in micrometer size, which requires precise handling. Furthermore, the additional external moieties (intercalated metals, and oxygen functional groups) degrade or alter the electrical performance of the exfoliated 2D materials in comparison to those produced by mechanical exfoliation[44,77,80,89–91].

Chemical vapor deposition (CVD)

Large area and high quality with low structural defects of thin 2D nanomaterials are required for most practical applications conceived for 2D nanomaterials, including microelectronics, sensor, thermionic devices, flexible devices, and optoelectronics. Such quality of 2D nanomaterials cannot be met by mechanical exfoliation or the chemical top down approach, due to the small lateral size of the sheets, and the precise handling requirements. Another technique chemical vapor deposition (CVD) may solve these challenges[92–96].

CVD of graphene or h-BN on metals

Due to their high catalytic activity, high quality graphene has been grown on transitional metals such as nickel (Ni), copper (Cu), ruthenium (Ru), platinum (Pt), cobalt (Co), iridium (Ir), etc. Furthermore, Ni and Cu metals are currently the two major substrates to produce graphene with large grain, and high quality. The growth mechanisms of graphene on Ni (as well as on Co, Ru, Ir), and Cu are different, mainly due to the carbon solubility in the metals (**Figure 1.7**).

In the case of high carbon solubility such as Ni, ~ 1.2 atomic % at 900 ^{o}C[95], the growth includes two elementary steps: (1) carbon dissolution into the metal from hydrocarbon gas (CH_4),

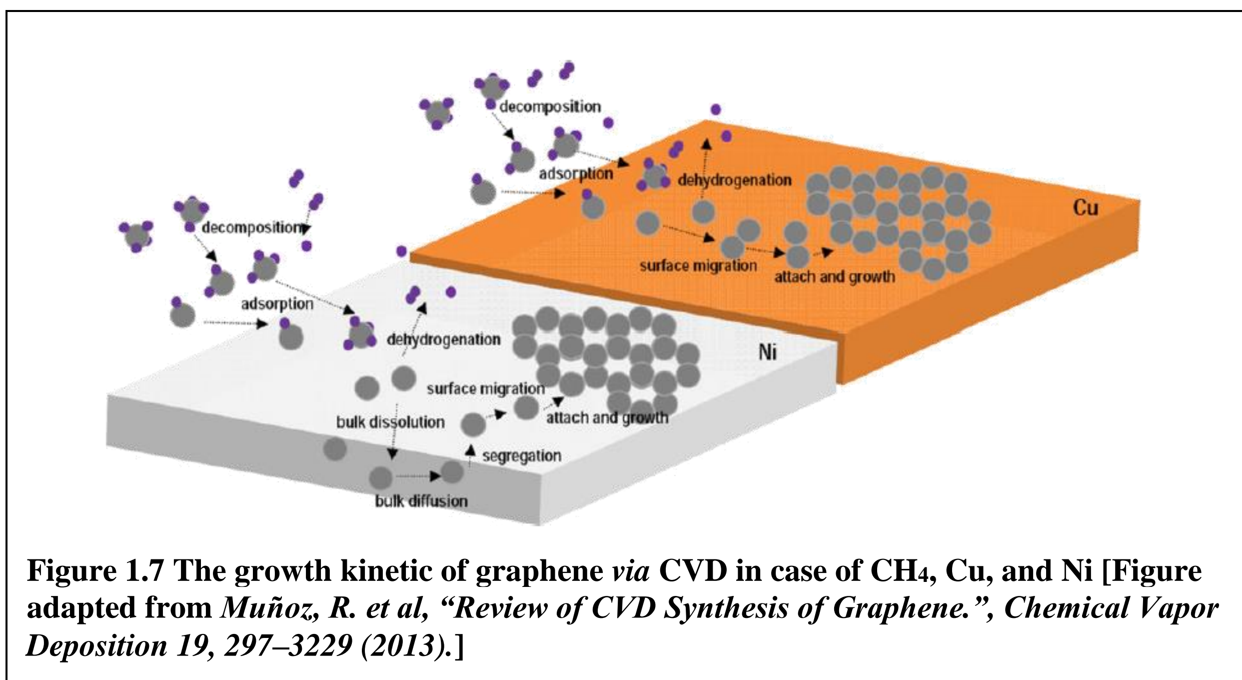

Figure 1.7 The growth kinetic of graphene *via* CVD in case of CH_4, Cu, and Ni [Figure adapted from *Muñoz, R. et al, "Review of CVD Synthesis of Graphene.", Chemical Vapor Deposition 19, 297–3229 (2013).*]

or solid at an elevated temperature, and (2) carbon precipitation to form graphene at the surface upon cooling. Furthermore, the grown graphene depends on the kinetic parameters selected for the synthesis. Among all process parameters, a fast cooling rate seems to be a critical factor in suppressing the formation of multiple graphene layers[95,97].

On the other hand, in the case of metal with low carbon solubility in metal such as Cu (~0% at 1000°C)[94], the growth of graphene is described in the following elementary steps: 1) hydrocarbon gas (CH_4) and reducing gas (H_2) transport through boundary layers, and adsorb on the surface. 2) Thermal catalytic decomposition of methane occurs on Cu to form carbon radicals, 3) which diffuse on the surface catalyst. 5) At local supersaturation, these carbon radicals nucleate to form graphene nuclei, which further form graphene islands. Finally 6) if the carbon radical attachment rate is faster than the carbon radical removing rate, a full coverage graphene sheet is synthesized. Consequently, graphene grown over Cu substrate can be considered as self-limiting. This mechanism is similar to thermal catalytic CVD, in which the film grows over metal, and causes a reduction in catalytic activity due to catalyst poisoning. Depending on the process

parameters (reaction temperature, flow rate, pressure), the growth could be either mass transport limited, or surface reaction limited[98].

Similar to graphene, large area, and high quality h-BN are also grown on transition metals such as Cu, Pt, Ni, etc[10,53,99–101]. Due to the solubility of B radical, and N radical in the metals, the growth mechanism of h-BN film can also be classified as either 1) surface-mediated growth, or 2) precipitation/segregation.

Even though the CVD technique provides large area, and high quality graphene, and h-BN film, the major challenges are in the additional transferring step of these 2D nanomaterials onto the desired substrate, typically (SiO_2/Si) in order to utilize them in electronic applications. Such a wet/dry transfer method includes: 1) a 2D material on metal is supported by a sacrificial polymer layer, followed by metal etching step. 2) Subsequently, polymer/2D material transfer to the target substrates, followed by the removal of the polymer either by organic solvent, or by ultra-high vacuum annealing. Such additional transfer process plays a critical role in limiting the electrical performance of graphene applications, due to tears, folds, wrinkles, and external impurities[102,103]. Many studies have focused on improving the quality of graphene and h-BN on the substrate *via* transfer[104–109]. Recently, other groups have been developed alternative transfer-free methods for the growth of high quality graphene or h-BN film on the selected non catalyst substrate[110–123]. Hence, in accordance with the aim of enhancing the coverage and the quality of graphene and h-BN films on dielectric substrates, this thesis offers two detailed studies on the direct growth of graphene (chapter 1), and of h-BN (chapter 2) on SiO_2/Si substrate.

CVD of MoS_2 on non-metallic substrate

In contrast to the growth of graphene, and that of h-BN, high quality, and large area MoS_2 can be grown directly on dielectric substrate such as SiO_2, Al_2O_3, etc[124–131]. Furthermore, the

precursors commonly used are molybdenum trioxide (MoO_3), and sulfur (S) or hydrogen sulfide (H_2S) gas. The growth of MoS_2 can be classified as a catalyst free vapor solid growth mechanism. 1) At elevated temperature (~650ºC), MoO_3 is reduced by sulfur vapor to form volatile suboxide MoO_{3-x}[124]. 2) These volatile substances transport through the boundary layer, 3) get adsorbed to the substrate, and furthermore 4) get sulfonated by adsorbed S to form oxisulfides $MoOS_2$, and nucleate into MoS_2 islands. 5) Finally, these MoS_2 islands expand, and connect to others to form a continuous sheet of MoS_2 (**Figure 1.8**). In this growth mechanism, the limiting step is the diffusion of vapor phase MoO_{3-x}[125]. Even if the sulfur is depleted, the $MoOS_2$ continues to grow into a uniform film of MoS_2 film.

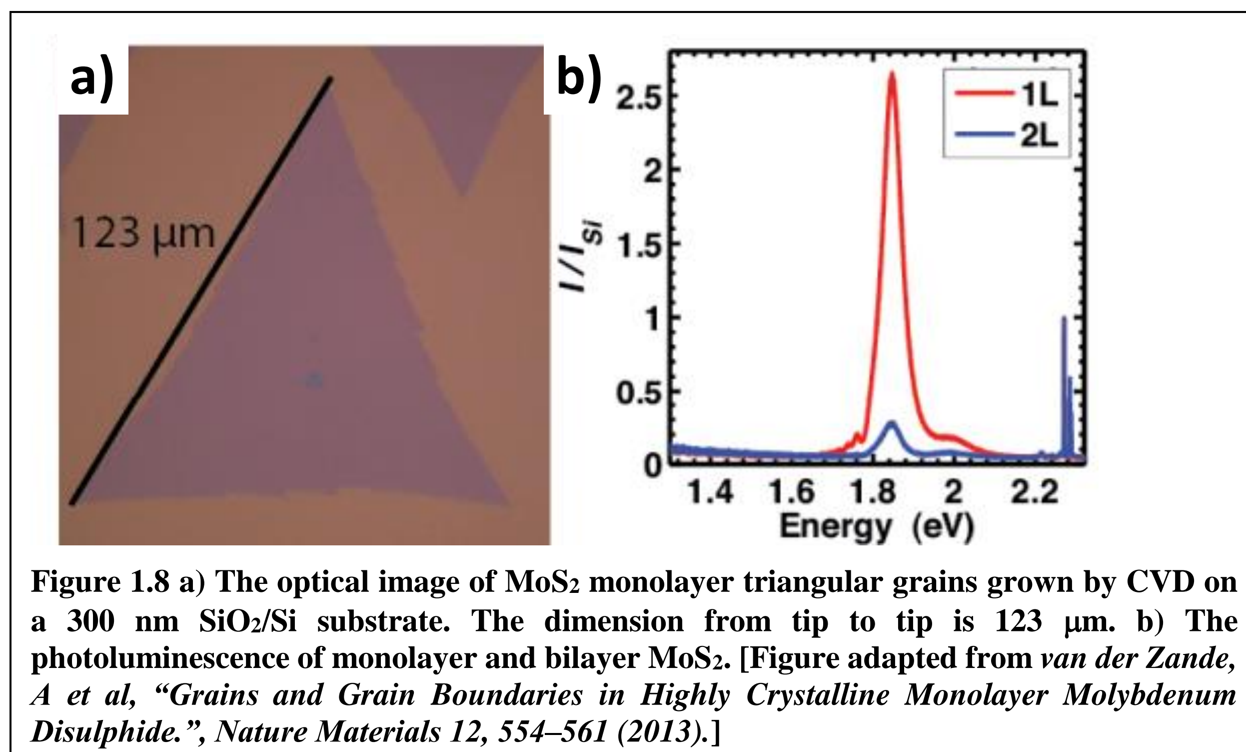

Figure 1.8 a) The optical image of MoS_2 monolayer triangular grains grown by CVD on a 300 nm SiO_2/Si substrate. The dimension from tip to tip is 123 μm. b) The photoluminescence of monolayer and bilayer MoS_2. [Figure adapted from *van der Zande, A et al, "Grains and Grain Boundaries in Highly Crystalline Monolayer Molybdenum Disulphide.", Nature Materials 12, 554–561 (2013).*]

The challenge of utilizing CVD grown MoS_2 in electronic applications depends on the quality of post-CVD underlying dielectric. Currently, SiO_2/Si substrate, a common platform for MoS_2 growth exhibits high surface roughness, high density of surface impurities, and surface electronic puddles. These lead in high Coulombic scattering, which limits the charge mobility in

MoS_2 sample. The heterostructure growth of MoS_2 on smooth, and dangling bond free h-BN film with low surface impurity density These challenges are addressed in the electronic performance of direct grown MoS_2 on h-BN film in chapter 2.

Reference

1. Daw, R. et al. Lab On A Chip. Nature 442, 367–367 (2006).
2. Tyagi, P. et al. Controlling Piezoelectric Response In Semiconductor Quantum Dots Via Impulsive Charge Localization. Nano Letters 10, 3062–3067 (2010).
3. Colvin, V. L. et al. Light-Emitting Diodes Made From Cadmium Selenide Nanocrystals And A Semiconducting Polymer. Nature 370, 354–357 (1994).
4. Hamilton, J. F. et al. Catalysis by Small Metal Clusters. Science 205, (1979).
5. Gudiksen, M. S. et al. Growth Of Nanowire Superlattice Structures For Nanoscale Photonics And Electronics. Nature 415, 617–620 (2002).
6. Chopra, N. G. et al. Boron Nitride Nanotubes. Science 269, (1995).
7. Iijima, S. Helical Microtubules Of Graphitic Carbon. Nature 354, 56–58 (1991).
8. Novoselov, K. S. et al. Electric Field Effect In Atomically Thin Carbon Films. Science 306, 666–9 (2004).
9. Radisavljevic, B. et al. Single Layer MoS_2 Transistors. Nature Nanotechnology. 6, 147–150 (2011).
10. Kim, S. M. et al. Synthesis Of Large-Area Multilayer Hexagonal Boron Nitride For High Material Performance. Nature Communications 6, 8662 (2015).
11. Butler, S. Z. et al. Progress, Challenges, And Opportunities In Two-Dimensional Materials Beyond Graphene. ACS Nano 7, 2898–2926 (2013).
12. Geim, A. K. & Grigorieva, I. V. Van der Waals Heterostructures. Nature 499, 419–425 (2013).
13. Zhang, H. Ultrathin Two-Dimensional Nanomaterials. ACS Nano 9, 9451–9469 (2015).
14. Geim Yin, Z. et al. Single-layer MoS_2 phototransistors. ACS Nano 6, 74–80 (2012).
15. Liu, Z., et al. Pegylated Nanographene Oxide For Delivery Of Water-Insoluble Cancer Drugs. Journal Of The American Chemical Society 130, 10876–10877 (2008).

16. Kim, H. et al. Photothermally Triggered Cytosolic Drug Delivery Via Endosome Disruption Using A Functionalized Reduced Graphene Oxide. Acs Nano 7, 6735–6746 (2013).
17. Goenka, S. et al. Graphene-Based Nanomaterials For Drug Delivery And Tissue Engineering. Journal Of Controlled Release 173, 75–88 (2014).
18. Mohanty, N. et al. Graphene-Based Single-Bacterium Resolution Biodevice And DNA Transistor: Interfacing Graphene Derivatives With Nanoscale And Microscale Biocomponents. Nano Letters 8, 4469–4476 (2008).
19. Yang, Y. et al. Graphene Based Materials For Biomedical Applications. Materials Today 16, 365–373 (2013).
20. Cruz, S. Et Al. Graphene: The Missing Piece For Cancer Diagnosis? Sensors 16, 137 (2016).
21. Patchkovskii, S. et al. Graphene Nanostructures As Tunable Storage Media For Molecular Hydrogen. Proceedings Of The National Academy Of Sciences Of The United States Of America 102, 10439–44 (2005).
22. Xie, J. et al. Defect-Rich MoS_2 Ultrathin Nanosheets With Additional Active Edge Sites For Enhanced Electrocatalytic Hydrogen Evolution. Advanced Materials 25, 5807–5813 (2013).
23. Tsai, M.L. et al. Monolayer MoS_2 Heterojunction Solar Cells. ACS Nano 8, 8317–8322 (2014).
24. Bernardi, M. et al. Extraordinary Sunlight Absorption And One Nanometer Thick Photovoltaics Using Two-Dimensional Monolayer Materials. Nano Letters 13, 3664–3670 (2013).
25. Mendoza-Sánchez, B. et al. Synthesis Of Two-Dimensional Materials For Capacitive Energy Storage. Advanced Materials 28, 6104–6135 (2016).
26. Pumera, M. et al. Graphene-Based Nanomaterials For Energy Storage. Energy Environ Sci 4, 668–674 (2011).
27. Dai, L., et al. Carbon Nanomaterials For Advanced Energy Conversion And Storage. Small 8, 1130–1166 (2012).
28. Geim, A. K. et al. Graphene: Status And Prospects. Science 324, 1530–4 (2009).

29. Novoselov, K. S. et al. Two-Dimensional Gas Of Massless Dirac Fermions In Graphene. Nature 438, 197–200 (2005).
30. Novoselov, K. S. et al. Two-Dimensional Atomic Crystals. Proceedings Of The National Academy Of Sciences 102, 10451–10453 (2005).
31. Geim, A. K. et al. The Rise Of Graphene. Nature Materials. 6, 183–191 (2007).
32. Balandin, A. A. et al. Superior Thermal Conductivity Of Single-Layer Graphene. Nano Letters 8, 902–907 (2008).
33. Lee, C. et al. Measurement Of The Elastic Properties And Intrinsic Strength Of Monolayer Graphene. Science 321, 385–388 (2008).
34. Nair, R. R. et al. Fine Structure Constant Defines Visual Transparency Of Graphene. Science 320, 1308 LP-1308 (2008).
35. Nan, H. Y. et al. The Thermal Stability Of Graphene In Air Investigated By Raman Spectroscopy. Journal Of Raman Spectroscopy 44, 1018–1021 (2013).
36. Zhou, S. Y. et al. First Direct Observation Of Dirac Fermions In Graphite. Nature Physics 2, 595–599 (2006).
37. Xia, J. et al. Measurement Of The Quantum Capacitance Of Graphene. Nature Nanotechnology 4, 505–509 (2009).
38. Schedin, F. et al. Detection Of Individual Gas Molecules Adsorbed On Graphene. Nature Materials 6, 652–655 (2007).
39. Kulkarni, G. S. et al. Graphene Nanoelectronic Heterodyne Sensor For Rapid And Sensitive Vapour Detection. Nature Communications 5, (2014).
40. Bunch, J. S. et al. Electromechanical Resonators From Graphene Sheets. Science 315, 490–3 (2007).
41. Poot, M. et al. Nanomechanical Properties Of Few-Layer Graphene Membranes. Applied Physics Letters 92, (2008)
42. Stoller, M. D. et al. Graphene-Based Ultracapacitors. Nano Letters. 8, 3498–3502 (2008).
43. Liu, Q. et al. Organic Photovoltaic Cells Based On An Acceptor Of Soluble Graphene. Applied Physics Letters 92, (2008).
44. Eda, G. et al. Photoluminescence From Chemically Exfoliated MoS_2. Nano Lett. 11, 5111–5116 (2011).

45. Coleman, J. N. et al. Two-Dimensional Nanosheets Produced By Liquid Exfoliation Of Layered Materials. Science 331, 568–71 (2011).
46. Akinwande, D. et al. Two-Dimensional Flexible Nanoelectronics. Nature Communications. 5, 5678 (2014).
47. Mak, K. F. et al. Atomically Thin MoS_2: A New Direct-Gap Semiconductor. Physical Review Letters 105, 136805 (2010).
48. Splendiani, A. et al. Emerging Photoluminescence In Monolayer MoS_2. Nano Letters 10, 1271–1275 (2010).
49. Li, H. et al. Fabrication Of Single- And Multilayer MoS_2 Film-Based Field-Effect Transistors For Sensing NO At Room Temperature. Small 8, 63–67 (2012).
50. Perkins, F. K. et al. Chemical Vapor Sensing With Monolayer MoS_2 .Nano Letters 13, 668–673 (2013).
51. Gourmelon, E. et al. MS_2 (M = W, Mo) Photosensitive Thin Films For Solar Cells. Solar Energy Materials and Solar Cells 46, 115–121 (1997).
52. Buscema, M. et al. Large And Tunable Photothermoelectric Effect In Single-Layer MoS_2. Nano Letters 13, 358–363 (2013).
53. Kubota, Y. et al. Deep Ultraviolet Light-Emitting Hexagonal Boron Nitride Synthesized At Atmospheric Pressure. Science. 317, 932–934 (2007).
54. Kim, K. K. et al. Synthesis And Characterization Of Hexagonal Boron Nitride Film As A Dielectric Layer For Graphene Devices. ACS Nano 6, 8583–8590 (2012).
55. Blase, X. et al. Frustration Effects And Microscopic Growth Mechanisms For BN Nanotubes. Physical Review Letters 80, 1666–1669 (1998).
56. Buongiorno Nardelli, M. et al. Lip-Lip Interactions And The Growth Of Multiwalled Carbon Nanotubes. Physical Review Letters 80, 313–316 (1998).
57. Kim, E. et al. Chemical Vapor Deposition-Assembled Graphene Field-Effect Transistor On Hexagonal Boron Nitride. Applied Physics Letters 98, 262103 (2011).
58. Bresnehan, M. S. et al. Integration Of Hexagonal Boron Nitride With Quasi-Freestanding Epitaxial Graphene: Toward Wafer-Scale, High-Performance Devices. ACS Nano 6, 5234–5241 (2012).
59. Dean, C. R. et al. Boron Nitride Substrates For High-Quality Graphene Electronics. Nature Nanotechnology 5, 722–726 (2010).

60. Tao, O. et al. Thermal Transport In Hexagonal Boron Nitride Nanoribbons. Nanotechnology 21, 245701 (2010).
61. Zhi, C., et al. Large-Scale Fabrication Of Boron Nitride Nanosheets And Their Utilization In Polymeric Composites With Improved Thermal And Mechanical Properties. Advanced Materials 21, 2889–2893 (2009).
62. Tamor, M. A. et al. Method Of Making Hard, Transparent Amorphous Hydrogenated Boron Nitride Films. U.S Patent 5518780 A (1996).
63. Chen, Y. et al. Boron Nitride Nanotubes: Pronounced Resistance To Oxidation. Applied Physics Letters 84, 2430–2432 (2004).
64. Liu, Z. et al. Ultrathin High-Temperature Oxidation-Resistant Coatings Of Hexagonal Boron Nitride. Nature Communications. 4, (2013).
65. Li, L. H. et al. Strong Oxidation Resistance Of Atomically Thin Boron Nitride Nanosheets. ACS Nano 8, 1457–1462 (2014).
66. Britnell, L. et al. Electron Tunneling Through Ultrathin Boron Nitride Crystalline Barriers. Nano Letters. 12, 1707–1710 (2012).
67. Lee, G. H. et al. Flexible And Transparent MoS_2 Field-Effect Transistors On Hexagonal Boron Nitride-Graphene Heterostructures. ACS Nano 7, 7931–7936 (2013).
68. Hu, S. et al. Proton Transport Through One-Atom-Thick Crystals. Nature 516, 227–230 (2014).
69. Li, H. et al. Preparation And Applications Of Mechanically Exfoliated Single-Layer And Multilayer MoS_2 And WSe_2 Nanosheets. Accounts of Chemical Research 47, 1067–1075 (2014).
70. Castellanos-Gomez, A. et al. Isolation And Characterization Of Few-Layer Black Phosphorus. 2D Materials 1, 025001 (2014).
71. Brent, J. R. et al. Production Of Few-Layer Phosphorene By Liquid Exfoliation Of Black Phosphorus. Chemical Communications 50, 13338–13341 (2014).
72. Hernandez, Y. et al. High-Yield Production Of Graphene By Liquid-Phase Exfoliation Of Graphite. Nature Nanotechnology 3, 563–568 (2008).
73. Khan, U. et al. Polymer Reinforcement Using Liquid-Exfoliated Boron Nitride Nanosheets. Nanoscale 5, 581–587 (2013).

74. Liang, L. et al. Vacancy Associates-Rich Ultrathin Nanosheets For High Performance And Flexible Nonvolatile Memory Device. Journal of the American Chemical Society 137, 3102–3108 (2015).
75. Paton, K. R. et al. Scalable Production Of Large Quantities Of Defect-Free Few-Layer Graphene By Shear Exfoliation In Liquids. Nature Materials 13, 624–630 (2014).
76. Nicolosi, V. et al. Liquid Exfoliation Of Layered Materials. Science. 340, 1226419 (2013).
77. Dines, M. B. Lithium Intercalation *Via* N-Butyllithium Of The Layered Transition Metal Dichalcogenides. Materials Research Bulletin 10, 287–291 (1975).
78. Parvez, K. et al. Exfoliation Of Graphite Into Graphene In Aqueous Solutions Of Inorganic Salts. Journal of the American Chemical Society 136, 6083–6091 (2014).
79. Zeng, Z. et al. Single-Layer Semiconducting Nanosheets: High-Yield Preparation And Device Fabrication. Angewandte Chemie International Edition 50, 11093–11097 (2011).
80. Zheng, J. et al. High Yield Exfoliation Of Two-Dimensional Chalcogenides Using Sodium Naphthalenide. Nature Communications 5, 699–712 (2014).
81. Allen, M. J. et al. Honeycomb Carbon: A Review Of Graphene. Chemical Reviews 110, 132–145 (2010).
82. Dreyer, D.R. The Chemistry Of Graphene Oxide. Chemical Society Reviews 39, 228-240 (2010)
83. Hummers, W. S. et al. Preparation Of Graphitic Oxide. Journal Of The American Chemical Society 80, 1339–1339 (1958).
84. Stankovich, S. et al. Synthesis Of Graphene-Based Nanosheets *Via* Chemical Reduction Of Exfoliated Graphite Oxide. Carbon 45, 1558–1565 (2007).
85. Zhu, Y. et al. Graphene And Graphene Oxide: Synthesis, Properties, And Applications. Advanced Materials 22, 3906–3924 (2010).
86. Gao, X. et al. Hydrazine And Thermal Reduction Of Graphene Oxide: Reaction Mechanisms, Product Structures, And Reaction Design. Journal Of Physical Chemistry C 114, 832–842 (2010).
87. Mohanty, N. et al. High-Throughput, Ultrafast Synthesis of Solution- Dispersed Graphene *Via* A Facile Hydride Chemistry. Small 6, 226–231 (2010).
88. Park, S. et al. Chemical Structures Of Hydrazine-Treated Graphene Oxide And Generation Of Aromatic Nitrogen Doping. Nature Communications 3, 638 (2012).

89. Gao, W., et al. New Insights Into The Structure And Reduction Of Graphite Oxide. Nature Chemistry 1, 403–408 (2009).
90. Schwamb, T. et al. An Electrical Method For The Measurement Of The Thermal And Electrical Conductivity Of Reduced Graphene Oxide Nanostructures. Nanotechnology 20, 405704 (2009).
91. Stankovich, S. et al. Stable Aqueous Dispersions Of Graphitic Nanoplatelets *Via* The Reduction Of Exfoliated Graphite Oxide In The Presence Of Poly(Sodium 4-Styrenesulfonate). J Mater Chem 16, 155–158 (2006).
92. De Arco, L. G. et al. Synthesis, Transfer, And Devices Of Single- And Few-Layer Graphene By Chemical Vapor Deposition. Ieee Transactions On Nanotechnology 8, 135–138 (2009).
93. Kim, K. S. K. S. et al. Large-Scale Pattern Growth Of Graphene Films For Stretchable Transparent Electrodes. Nature 457, 706–10 (2009).
94. Li, X. et al. Large Area Synthesis Of High Quality And Uniform Graphene Films On Copper Foils. Science 324, 1312–1314 (2009).
95. Reina, A. et al. Large Area, Few-Layer Graphene Films On Arbitrary Substrates By Chemical Vapor Deposition. Nano Letters 9, 30–35 (2009).
96. Yu, Q. et al. Graphene Segregated On Ni Surfaces And Transferred To Insulators. Applied Physics Letters 93, 113103 (2008).
97. Chen, Z. et al. Three-Dimensional Flexible And Conductive Interconnected Graphene Networks Grown By Chemical Vapour Deposition. Nature Materials 10, 424–428 (2011).
98. Bhaviripudi, S. et al. Role Of Kinetic Factors In Chemical Vapor Deposition Synthesis Of Uniform Large Area Graphene Using Copper Catalyst. Nano Letters 10, 4128–4133 (2010).
99. Park, J.H. et al. Large-Area Monolayer Hexagonal Boron Nitride On Pt Foil. ACS Nano 8, 8520–8528 (2014).
100. Stehle, Y. et al. Synthesis Of Hexagonal Boron Nitride Monolayer: Control Of Nucleation And Crystal Morphology. Chemistry Of Materials 27, 8041–8047 (2015).
101. Zhang, C. et al. Controllable Co-Segregation Synthesis Of Wafer-Scale Hexagonal Boron Nitride Thin Films. Advanced Materials 26, 1776–1781 (2014).

102. Chen, Y. et al. Progress And Challenges In Transfer Of Large-Area Graphene Films. Advanced Science 3, 8 (2016).
103. Lin, Y. C. et al. Graphene Annealing: How Clean Can It Be? Nano Letters 12, 414–419 (2012).
104. Barin, G. B. et al. Optimized Graphene Transfer: Influence Of Polymethylmethacrylate (PMMA) Layer Concentration And Baking Time On Grapheme Final Performance. Carbon 84, 82–90 (2015).
105. Deng, W. et al. A High-Yield Two-Step Transfer Printing Method For Large-Scale Fabrication Of Organic Single-Crystal Devices On Arbitrary Substrates. Scientific Reports 4, 5358 (2014).
106. Li, X. et al. Transfer Of Large-Area Graphene Films For High-Performance Transparent Conductive Electrodes. Nano Letters 9, 4359–4363 (2009).
107. Na, S. R. et al. Clean Graphene Interfaces By Selective Dry Transfer For Large Area Silicon Integration. Nanoscale 8, 7523–7533 (2016).
108. Wang, B. et al. Support-Free Transfer Of Ultrasmooth Graphene Films Facilitated By Self-Assembled Monolayers For Electronic Devices And Patterns. Acs Nano 10, 1404–1410 (2016).
109. Zhang, G. et al. Versatile Polymer-Free Graphene Transfer Method And Applications. Acs Applied Materials & Interfaces 8, 8008–8016 (2016).
110. Behura, S. K. et al. Vertically Oriented Few-Layer Graphene As An Electron Field-Emitter. Physica Status Solidi (A) Applications And Materials Science 210, 1817–1821 (2013).
111. Behura, S. K. et al. Electrical Characteristics Of Horizontally And Vertically Oriented Few-Layer Graphene On Si-Based Dielectrics. Ingenta Connect 16, 6246-6251 (2016).
112. Chen, J. et al. Near-Equilibrium Chemical Vapor Deposition Of High-Quality Single-Crystal Graphene Directly On Various Dielectric Substrates. Advanced Materials 26, 1348–1353 (2014).
113. Chen, J. et al. Two-Stage Metal-Catalyst-Free Growth Of High-Quality Polycrystalline Graphene Films On Silicon Nitride Substrates. Advanced Materials 25, 992–997 (2013).
114. Chen, J. et al. Oxygen-Aided Synthesis Of Polycrystalline Graphene On Silicon Dioxide Substrates. Journal Of The American Chemical Society 133, 17548–17551 (2011).

115. Kim, K. B., Lee, C. M. & Choi, J. Catalyst-Free Direct Growth Of Triangular Nano-Graphene On All Substrates. Journal Of Physical Chemistry C 115, 14488–14493 (2011).
116. Russo, P., Hu, A. & Compagnini, G. Synthesis, Properties and Potential Applications of Porous Graphene: A Review. Nano-Micro Letters, 5, 260–273 (2013).
117. Hwang, J. et al. Van Der Waals Epitaxial Growth Of Graphene On Sapphire By Chemical Vapor Deposition Without A Metal Catalyst. ACS Nano 7, 385–395 (2013).
118. Song, H. J. et al. Large Scale Metal-Free Synthesis Of Graphene On Sapphire And Transfer-Free Device Fabrication. Nanoscale 4, 3050 (2012).
119. Sun, J. et al. Direct Growth Of High-Quality Graphene On High-K Dielectric $SrTiO_3$ Substrates. Journal Of The American Chemical Society 136, 6574–6577 (2014).
120. Gao, T. et al. Temperature-Triggered Chemical Switching Growth Of In-Plane And Vertically Stacked Graphene-Boron Nitride Heterostructures. Nature Communications 6, 6835 (2015).
121. Wang, M. et al. A Platform For Large-Scale Graphene Electronics – CVD Growth Of Single-Layer Graphene On CVD-Grown Hexagonal Boron Nitride. Advanced Materials 25, 2746–2752 (2013).
122. Yang, W. et al. Epitaxial Growth Of Single-Domain Graphene On Hexagonal Boron Nitride. Nature Materials 12, 792–797 (2013).
123. Zhang, C. et al. Direct Growth Of Large-Area Graphene And Boron Nitride Heterostructures By A Co-Segregation Method. Nature Communications 6, 6519 (2015).
124. Weber, T. et al. Basic Reaction Steps In The Sulfidation Of Crystalline MoO_3 To MoS_2 , As Studied By X-Ray Photoelectron And Infrared Emission Spectroscopy. The Journal Of Physical Chemistry 100, 14144–14150 (1996).
125. Najmaei, S. et al. Vapour Phase Growth And Grain Boundary Structure Of Molybdenum Disulphide Atomic Layers. Nature Materials 12, 754–759 (2013).
126. Feldman, Y. et al. Gas-Phase Growth Of Mos2 Nested Inorganic Fullerenes And Nanotubes. Science (New York, NY) 267, 222–225 (1995).
127. Lee, Y. H. et al. Synthesis Of Large-Area MoS_2 Atomic Layers With Chemical Vapor Deposition. Advanced Materials 24, 2320–2325 (2012).
128. Margulis, L. et al. Nested fullerene-like structures. Nature 365, 113–114 (1993).

129. van der Zande, A. M. et al. Grains And Grain Boundaries In Highly Crystalline Monolayer Molybdenum Disulphide. Nature Materials 12, 554–561 (2013).
130. Wu, S. et al. Vapor–Solid Growth Of High Optical Quality MoS_2 Monolayers With Near-Unity Valley Polarization. ACS Nano 7, 2768–2772 (2013).
131. Zhan, Y. et al. Large-Area Vapor-Phase Growth And Characterization Of MoS_2 Atomic Layers On A SiO_2 Substrate. Small 8, 966–971 (2012).

Chapter 2 - Direct growth of thin layer graphene on SiO_2 via low pressure chemical vapor deposition (LPCVD)

Abstract

This chapter presents a chemistry for the transfer-free growth of graphene *via* chemical vapor deposition. The process relies on diffusion of carbon radicals through copper (Cu) grain boundary and crystallization at copper and silicon based dielectrics. The graphene developed by this method exhibits low defect (L_a~140 nm) multilayer domains with turbostratic structure. The growth of graphene is two-fold faster at the interface between Cu and SiO_2/Si<111> substrate than that of Cu and SiO_2/<100> Si substrate. Furthermore, process parameters such as growth temperature, and gas composition (H_2/CH_4 flowrate ratio) play a critical role in formation of high quality graphene films. The low temperature back-gating transport measurements of the interfacial graphene show the carrier mobility (277 $cm^2V^{-1}s^{-1}$, and 233 $cm^2V^{-1}s^{-1}$ for holes and electrons respectively). Furthermore, the study of electronic transport at various temperature reveals a dominant Coulombic scattering, a thermal activation energy (2.0±0.2 meV), and 2-D hopping conduction in the thin graphene film-field effect transistor. A band overlapping energy (2.3±0.4 meV) is also estimated by utilizing the simple two band model.

Introduction

Graphene, conclusively isolated in 2004, is a monolayer (thinnest material ~ 0.34 nm) of sp^2 bonded carbon atoms arranged in a two-dimensional (2D) honeycomb lattice and is the primary building block of all the carbonaceous materials of all other dimensions such as: graphite (3D), carbon nanotubes (1D) and fullerene (0D)[1]. Graphene possesses a plethora of extraordinary properties, such as ballistic electronic transport over 0.4 μm with high charge carrier mobility

(2,00,000 cm^2/Vs at 300 K)[2], superior thermal conductivity (5,000 W/mK)[3], room temperature quantum Hall effect[4], a chemically[5,6] and geometrically[7] controllable band gap and megahertz characteristic frequency[8]. According to the International Technology Roadmap for Semiconductors (ITRS)[9,10], due to graphene's exceptional electronic and thermal properties, it is being considered for post-silicon (Si) electronics. Furthermore, graphene's strong interaction with photons and high electrochemical stability could enumerate advanced functions to Si-based CMOS devices, such as radio-frequency switches and photonic modulators.

Recently, high-quality and large-area graphene has been successfully produced on various metal catalytic substrates *via* chemical vapor deposition (CVD)[11–19]. In order to characterize graphene, it is essential to transfer the as-grown graphene onto selected dielectric surfaces. However, in such wet/dry transfer process, graphene is supported by a sacrificial polymer layer followed by etching of metal layer. Subsequently, the polymer/graphene is transferred to a desired substrate, and the supporting polymer is either etched by dissolving in acetone or released by thermal treatment. In addition, this added step consistently degrades graphene's electronic properties due to tear, fold, wrinkles, and external impurities. Graphene produced *via* these transfer steps is unfavorable for industrial applications as the produced graphene film still contains polymeric and metallic impurities further deteriorating the intrinsic properties.

To date, the growth of graphene *via* catalyst-free CVD methods have been developed on various substrates such as Si-based dielectric substrate[20–25], Al_2O_3[26,27], $SrTiO_3$[28], and h-BN[29–32]. Such techniques require high growth temperature, longer growth time, or additional modification of CVD setup. Incorporating thin catalytic transition metal films (copper (Cu), and nickel (Ni)) onto desired dielectric substrates helps in reduction in the growth temperature, reaction time, and defects enabling synthesis of high quality graphene films. In case of Ni, the formation of graphene

at the interface of substrate and catalytic film is due to segregation of carbon atoms from the Ni layer (carbon solubility in Ni is ~ 1.2 atomic % at 900 ºC)[15]. Owing this non-equilibrium process, the production of uniform, and low-defect density of graphene films requires a precise control of the cooling rates. In contrast, Cu catalyzes low-defect density graphene films due to surface adsorption mechanism[33,34]. Yet, the formation of graphene at the interface of Cu and SiO_2 substrate is not well understood. Furthermore, Ismach et al. showed that a continuous graphene can be directly transferred on SiO_2 substrate during the growth by evaporating sacrificial Cu film with an extended period of thermal treatment[35]. This transfer technique may result in unwanted Cu particles trap between continuous graphene film and SiO_2 dielectric substrate.

Herein, the process of direct formation of thin film graphene directly on SiO_2/Si substrates was described. Furthermore, this chapter shows a complete mechanism of directly grown graphene at the interface of SiO_2 and Cu, where Cu was used as a catalyst. In addition to the detailed structural characteristics including Raman spectroscopy and selective area electron diffraction (SAED) pattern analysis, low-temperature electrical transport properties of the interfacial graphene layer were measured. This work may stimulate further developments in utilizing direct graphene developed here for silicon-wafer compatible industrial productions.

Experimental Section

Procedure of multilayer graphene growth on SiO_2/Si substrate *via* LPCVD

A thin film of Cu (~150 nm) was thermally evaporated from Cu pellets (99.999% purity, Kurt.J.Lesker) on selected substrates such as: SiO_2/ <100> Si, and SiO_2/ <111> Si (**Figure 2.1b**). The substrate was then placed in the center heating zone of a quartz tube (ϕ=1”), which is in a split MTI-OTF-1200X furnace designed low pressure CVD system (LPCVD) as shown in **Figure 2.1a**. Methane, CH_4 (99.999% purity, Praxair) was the precursor gas, and hydrogen, H_2

(99.9999%, Praxair) was the reducing gas were used. The oxidizing impurities in these gases are shown in the **Table 2.1**.

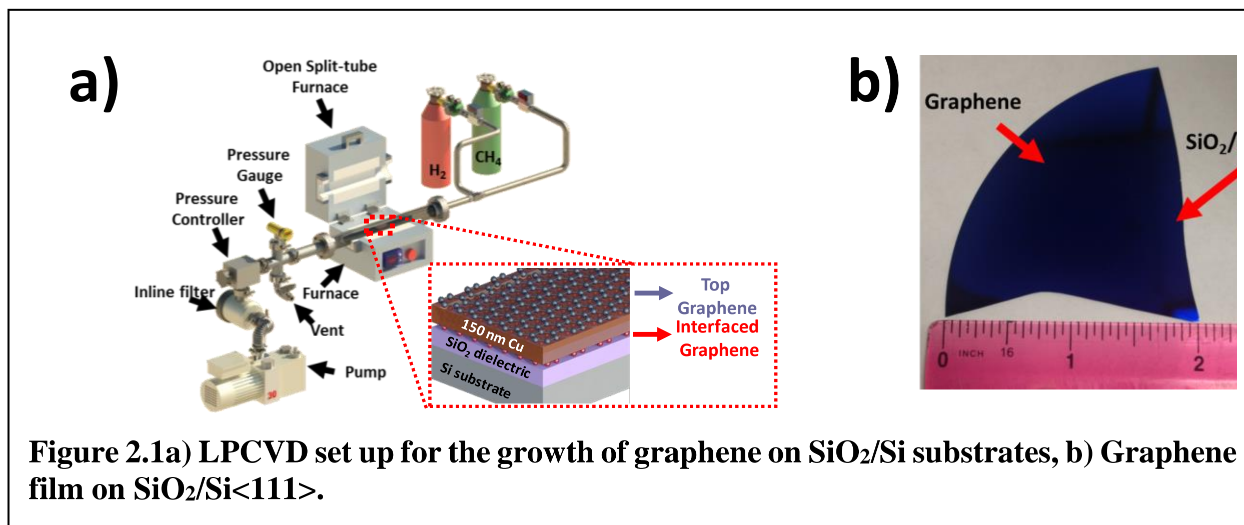

Figure 2.1a) LPCVD set up for the growth of graphene on SiO_2/Si substrates, b) Graphene film on SiO_2/Si<111>.

	CH_4 (99.999% purity, Praxair)	H_2 (99.9999%, Praxair)
O_2	< 1 ppm	< 0.2 ppm
H_2O	< 1 ppm	< 0.2 ppm
CO_2	< 3 ppm	< 0.1 ppm
CO	< 1 ppm	< 0.1 ppm

Table 2.1: The oxidizing impurities are associated with CH_4 and H_2 in our study.

To synthesize a thin film of graphene directly on these substrates, the growth was typically conducted *via* following steps: (1) thermal annealing at 750 °C with 15 sccm of H_2 (P_{Tot} = 80 mTorr, t_{aneal}= 25 minutes), (2) growth of graphene in the temperature range 750 °C-900 °C with different ratio of CH_4:H_2 (P_{Tot} = 2 Torr), and (3) cooing the slowly (20 °C/min) to 700 °C, and then cooling it by simply opening the furnace lid. After the synthesis process, graphene was formed on both sides of the copper layer (top graphene, and interfaced graphene). The top graphene film and the copper layer were subsequently removed *via* oxygen plasma etching, and wet-chemical etching

with $Fe(NO_3)_3$ solution (0.6 mg/mL), respectively. **Figure 2.2** shows the overall process of graphene synthesis on SiO_2/Si substrate.

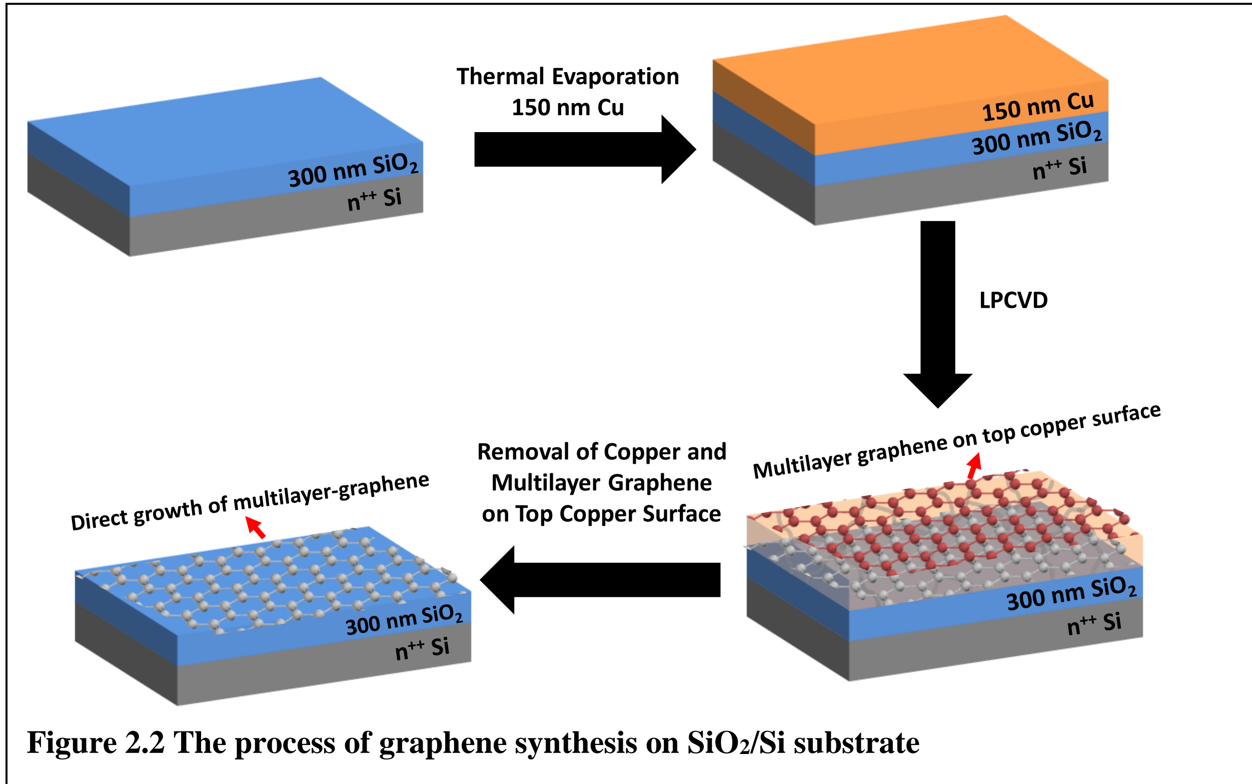

Figure 2.2 The process of graphene synthesis on SiO_2/Si substrate

Procedure to transfer graphene to SiO_2 for field effect transistor fabrication, and to TEM grid for selected area electron diffraction (SAED) characterization

Since graphene, and underlying substrate went through high temperature process, the interfaced graphene could be further doped by the substrate (as shown in the later discussion). This could lead to the non-ambipolar behavior in the graphene transistor, which provided challenges in determine the correct electronic performance of the graphene transistor. Hence, as shown in **Figure 2.3,** graphene grown on SiO_2/Si substrate was required to transferred to 300 nm $SiO_2/n^{++}Si$ substrate or TEM grid by the following steps: First, 25 mg/mL of poly(methyl methacrylate) (PMMA) (MW 996,000, Sigma Aldrich) in anisole (99% purity, Acros Organics) was spin-coated onto graphene/ SiO_2/Si substrate at (i) pre-spin: at 500 RPM for 5 sec (500 RPM/sec ramp rate)

and (ii) full-spin: at 4,000 RPM for 30 sec (1,000 RPM/sec ramp rate). The PMMA-coated graphene/SiO_2/Si sample was then air dried for 5 minutes, followed by etching the SiO_2/Si substrate with 1% of HF for 8 h at room temperature. The floating PMMA/graphene sample was

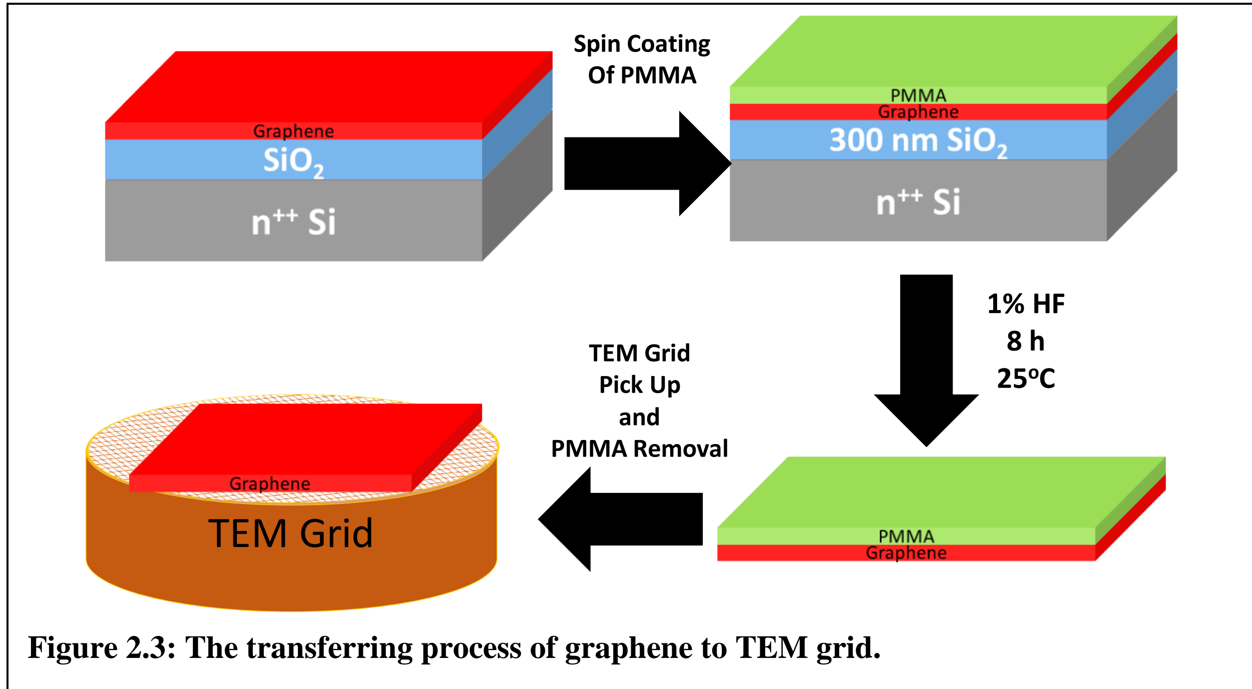

Figure 2.3: The transferring process of graphene to TEM grid.

picked up by submerging a clean metal spoon into the solution, and lifting up at 40° angle to the surface of etchant solution. Immediately, it was transferred onto DI water at the same manner as previous picking up step (repeated three times). Similarly, the subsequent substrates (300 nm $SiO_2/n^{++}Si$) or TEM grid (Formvar on 300 mesh copper grid) were then used to pick up the PMMA/graphene samples and then dried overnight in the air. To remove the PMMA, these samples were submerged into acetone for 5 min at room temperature, followed by washing with copious amount of acetone and IPA, and water (in the sequential order) and dried with purified air flow for 2 min.

Procedure to transfer graphene on top of Cu surface to SiO_2 for Raman characterization

The graphene grown on top copper surface was transferred to 300 nm SiO2/n++Si by the following steps (**Figure 2.5**): First, 25 mg/mL of poly(methyl methacrylate) (PMMA) (MW 996,000, Sigma Aldrich) in anisole (99% purity, Acros Organics) was spin-coated onto the

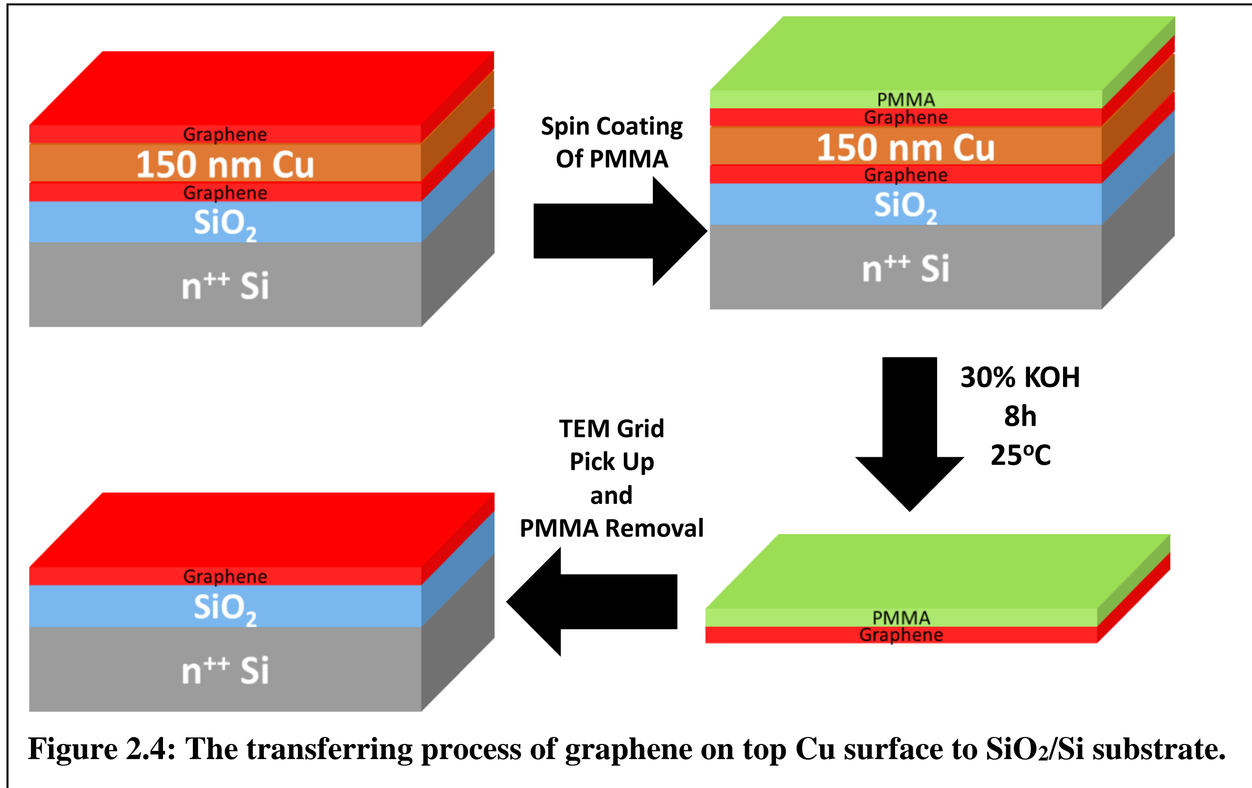

Figure 2.4: The transferring process of graphene on top Cu surface to SiO_2/Si substrate.

graphene/ SiO2/Si substrate at (i) pre-spin: at 500 RPM for 5 sec (500 RPM/sec ramp rate) and (ii) full-spin: at 4,000 RPM for 30 sec (1,000 RPM/sec ramp rate). The PMMA-coated graphene/Cu foil was then air dried for 5 minutes, followed by etching the SiO_2/Si substrate with 30% of KOH for 8 h. The floating PMMA/graphene sample was picked up by submerging a clean metal spoon into the solution, and lifting up at 40° angle to the surface of etchant solution. Immediately, it was transferred onto DI water at the same manner as previous picking up step (repeated three times). Similarly, the subsequent substrates (300 nm SiO2/n^{++}Si) were then used to pick up the

PMMA/graphene samples and then dried overnight in the air. To remove the PMMA, these samples were submerged into acetone for 5 min at room temperature, followed by washing with copious amount of acetone and IPA, and water (in the sequential order) and dried with purified air flow for 2 min.

Procedure of the thin graphene field effect transistor fabrication

We used etching procedure to fabricate the graphene field effect transistor (GFET). This procedure includes two major steps: 1) defining the geometry of metal contact (**Figure 2.5**), and 2) defining the geometry of transistor (**Figure 2.6**).

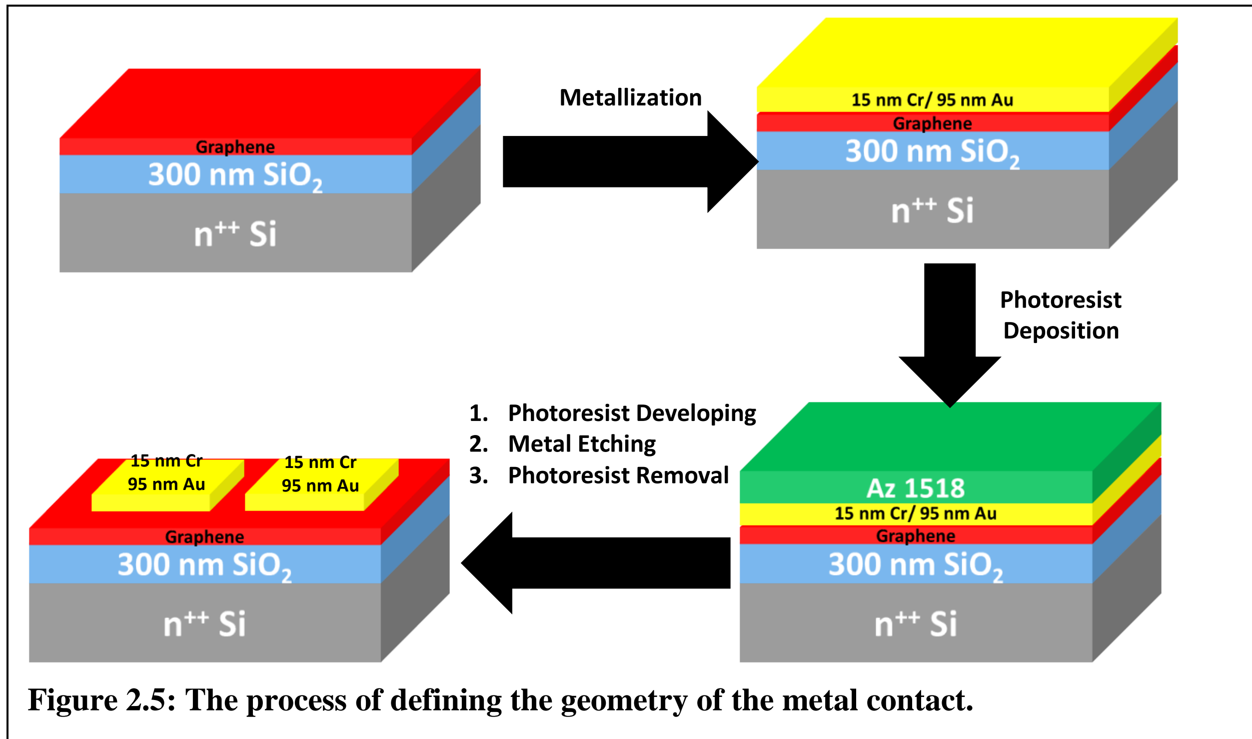

Figure 2.5: The process of defining the geometry of the metal contact.

First, graphene transferred on SiO_2/Si were deposited with Cr/Au (15 nm/95 nm) layers. A positive photoresist (AZ 1518) was spin-coated onto the samples at 4000 RPM for 45 sec. The samples were then baked on the hot plate at 110 °C for 1 min. Subsequently, a dose of UV light (365 nm and lamp power of 900 W) was introduced into the samples with aligned mask for 12 sec

using Karl Suss MA6 mask aligner. Then samples were developed in a solution of 3:1 (DI water: AZ 340) for 18 sec to form the pattern of the source-drain contact. The un-protected Cr/Au area was etched by Au etchant (36 seconds, room temperature), submerged in the flowing water (2 min), and etched by Cr etchant (12 seconds, room temperature), submerged in the flowing water (2 min). The electrode contacts were then revealed. Subsequently, in order to remove the remaining photoresist, the sample was washed with copious amount of acetone and IPA, and water (in the sequential order) and dried with purified air flow for 2 min.

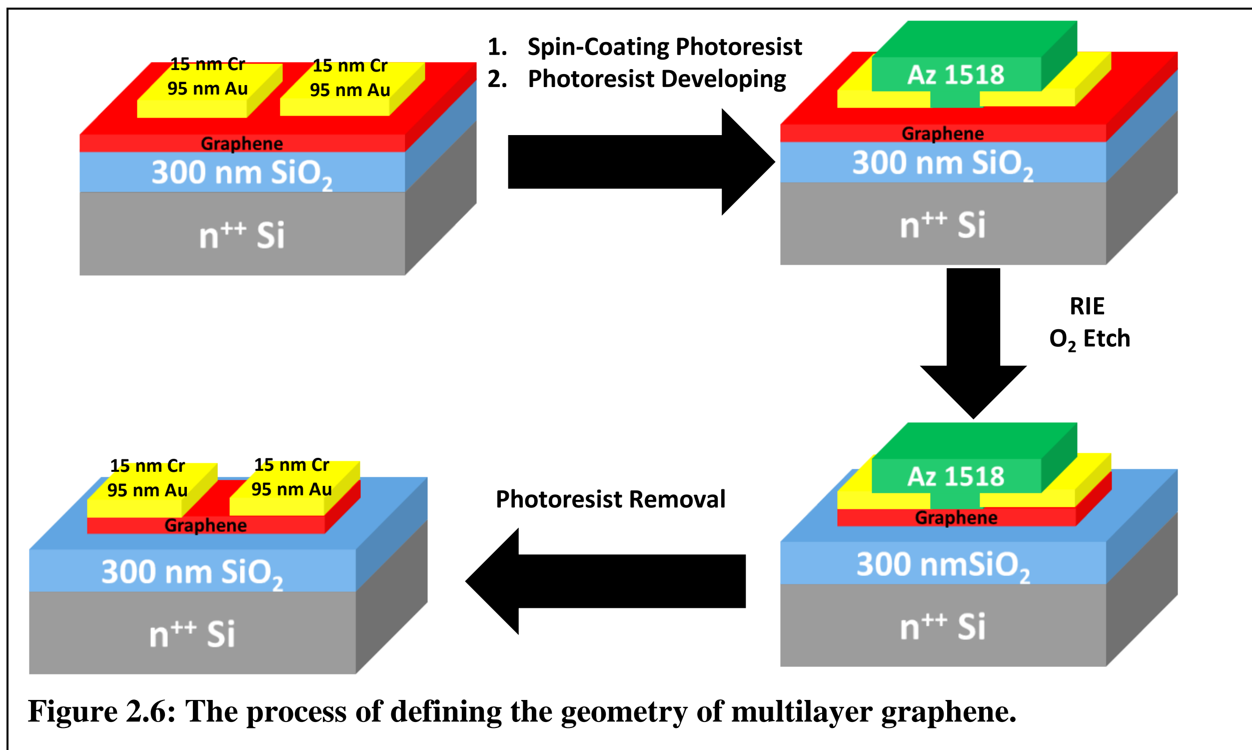

Figure 2.6: The process of defining the geometry of multilayer graphene.

After defining the metal contacts, the bar structure with a channel length of 25 µm and channel width of 12.5 µm was fabricated by repeating previous steps with another layer of positive photoresist with similar procedure (described above). After developing to form a protected pattern of graphene bar, the un-wanted graphene region was etch *via* Oxford reactive ion etching oxygen plasma (10 W power, 45 sec exposure, 535-550 V peak to peak voltage, and 260 V bias voltage). Subsequently, the photoresists were stripped off by submerging the sample into two consecutive

baths of AZ 351 solution (5 min, then 3 min), and into IPA solution for 5 min. Finally, the sample was washed with copious amount of acetone and IPA (in the sequential order), and dried with purified air flow for 2 min.

Pre-treatment of GFET for electrical measurements

Prior to electrical transport measurements, the sample was placed into a clean 4" quartz tube in a split furnace. The chamber was evacuated to ~10^{-6} Torr in 20 min by roughing pump, and turbo-molecular pump. The system was stabilized for an addition 10 min. The furnace temperature was increased to 200 ºC in 20 min, and annealed for 2 hours to remove absorbed impurities such as water, photoresists. After cooling down to room temperature, the samples were immediately placed inside the ARS cryostat system for electrical transport characterization.

Instrumentations for chemical, physical and electrical characterization

Confocal Raman spectroscopy system

The data for Raman spectroscopy was obtained using WITEC Confocal Raman Alpha 300-RA system, with a laser excitation wavelength of 532 nm (power of 17 mW). A thermoelectrically cooled CCD Camera (ANDOR iDUS DV401A-BV-352) (-65ºC) was used to detect Raman signal. The focal length of UHTS 300 VIS spectrometer is 300 mm. The pinhole size (100 µm) is the core diameter of the multi-mode fiber for the highest detection signal. The 100X objective, and 600 l/mm grating were used to examine all the graphene samples. The laser spot size (360 nm) was determined using the equation:

$$Spot\ size = \frac{0.61\lambda}{NA}$$

where λ (532 nm) is the wavelength of the laser and NA (0.9) is the numerical aperture. The SiO_2/Si substrate (~520 cm^{-1}) was used as a reference to calibrate the Raman instrument. The

intensity mapping was collected with the resolution of 512x512 (pixel x pixel), and the integration time of 0.5 s/pixel.

Field emission scanning electron microscope (FESEM)

The FESEM image was collected using FEI Company Nova NanoSEM 430. The acceleration voltage was used as 5 kV with vCD detector, and spot size of 3.

Selected area electron diffraction (SAED) measurement *via* transmission electron microscope (TEM)

The SAED pattern was collected using FEI-CM100 TEM. The acceleration voltage (100 kV) was used with camera length of 25 cm.

X-ray photoelectron spectroscopy (XPS) system

XPS data were recorded with a Kratos AXIS-165 spectrometer using acrochromatic Al Kα radiation (1486.6 eV). Analysis was carried out under a vacuum less than 5×10^{-10} Torr. The XPS binding energies were measured with a precision of 0.1 eV. The analyzer pass energy was set to 80 eV. The contact time was 500 ms, and the area scanned was 5 mm^2. Spectra were referenced to C1s peak at 284.5 eV.

Cryostat electrical system

The electrical measurements of multilayer graphene samples were carried out in ARS closed cycle cryogenic probe station, connecting to Edwards E2M5 rotary vane pump to provide high vacuum ($<5 \times 10^{-6}$ Torr). Lakeshore temperature controller (model 336) control the temperature of the samples.

Figure 2.7 shows the set-up for the back gating measurement, which was performed by keeping the source-drain voltage constant and measuring the change in conductivity with the gate

voltage, which was applied to the heavy-doped silicon. The Keithley 2612 dual-channel system source meter connected to a computer *via* a GPIB/IEEE-488 interface card.

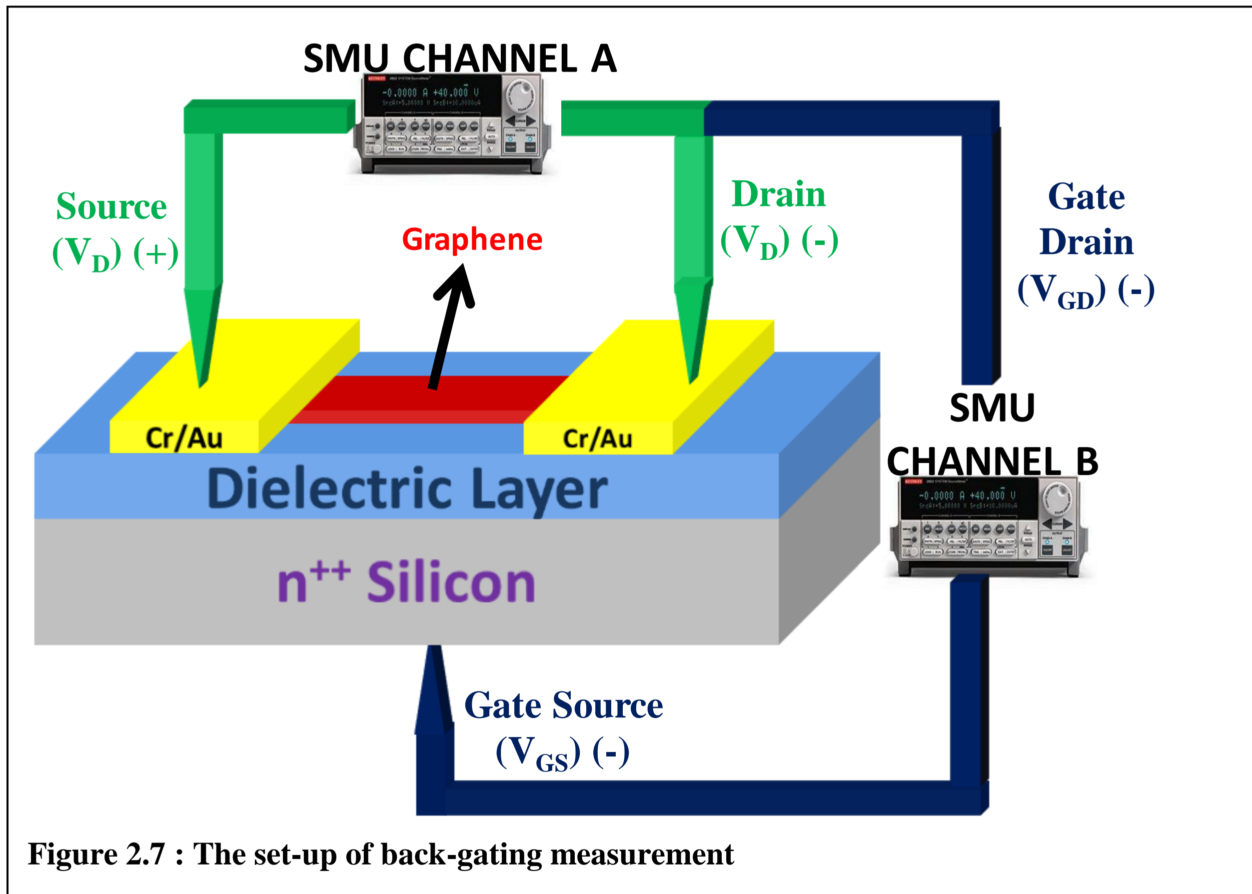

Figure 2.7 : The set-up of back-gating measurement

Results and Discussion

Physical characterization of thin graphene film

Raman spectroscopy is a versatile vibrational technique, and can be employed to qualify the doping, strain, stress, and defects in the lattice of two-dimensional nanomaterials including graphene[36–39]. As shown in **Figure 2.8a**, a typical Raman spectra of the grown thin graphene film consists of the following prominent features: D band (~1350 cm^{-1}), G band (~1580 cm^{-1}), and 2D band (~2700 cm^{-1}). The Raman spectral intensity mapping of G band, I_D/I_G ratio, and I_{2D}/I_G ratio presented in **Figure 2.8b** with the regions marked blue, red and black circle corresponds to Raman

spectra in **Figure 2.8a** show high coverage of graphene film (>90%). The inhomogeneous contrast of the G mapping indicates the non-uniformity of graphene film. The relative intensity of D band over G band (I_D/I_G) can be used to probe the defects in the film, which is in the range of 0.1-0.4 as shown in **Figure 2.8c** indicating a relatively low defect polycrystalline graphene. Furthermore, the relative intensity of 2D band over G band (I_{2D}/I_G) suggests a relatively high doping in graphene[36] (which will be further confirmed in a later section).

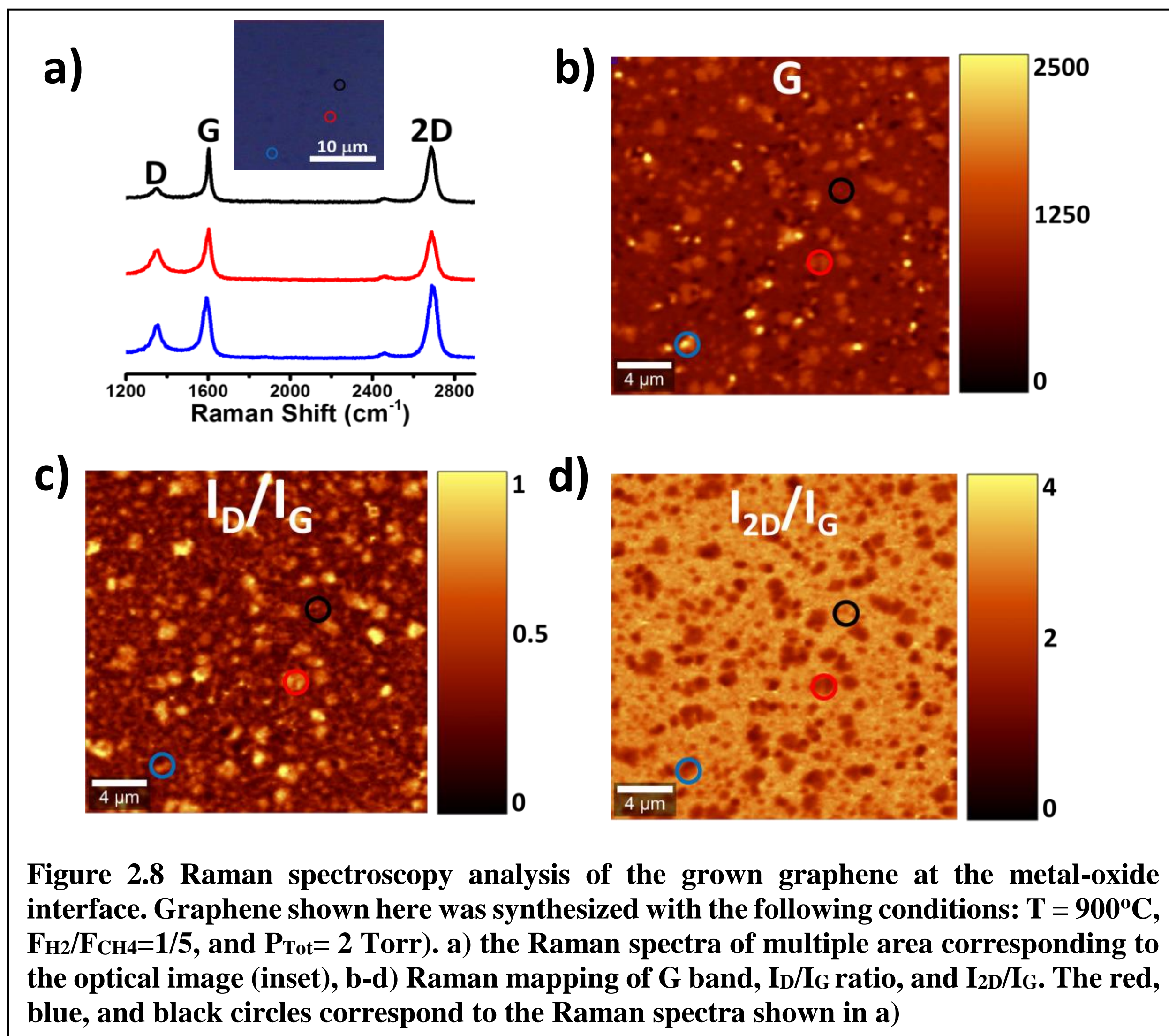

Figure 2.8 Raman spectroscopy analysis of the grown graphene at the metal-oxide interface. Graphene shown here was synthesized with the following conditions: T = 900°C, F_{H2}/F_{CH4}=1/5, and P_{Tot}= 2 Torr). a) the Raman spectra of multiple area corresponding to the optical image (inset), b-d) Raman mapping of G band, I_D/I_G ratio, and I_{2D}/I_G. The red, blue, and black circles correspond to the Raman spectra shown in a)

Surface of continuous thin graphene film is non uniform, which consists multilayer domains as shown in field emission scanning electron microscope (FESEM) image in **Figure**

2.9a. Despite the growth under low pressure condition, this evidence implies that the interfaced graphene growth is not controlled by surface reaction step[40]. The details of the growth mechanism and consequences are discussed in the latter sections. In addition, the quality of graphene film is analyzed by X-ray photoelectron spectroscopy (XPS, Kratos AXIS-165). **Figure 2.9b-c** show no presence of metallic elements, arising from the Cu catalyst and $Fe(NO_3)$ etchant, which have binding energy of Cu $2p_{3/2}$ at 933 eV, and that of Fe $2p_{3/2}$ at 710 eV.

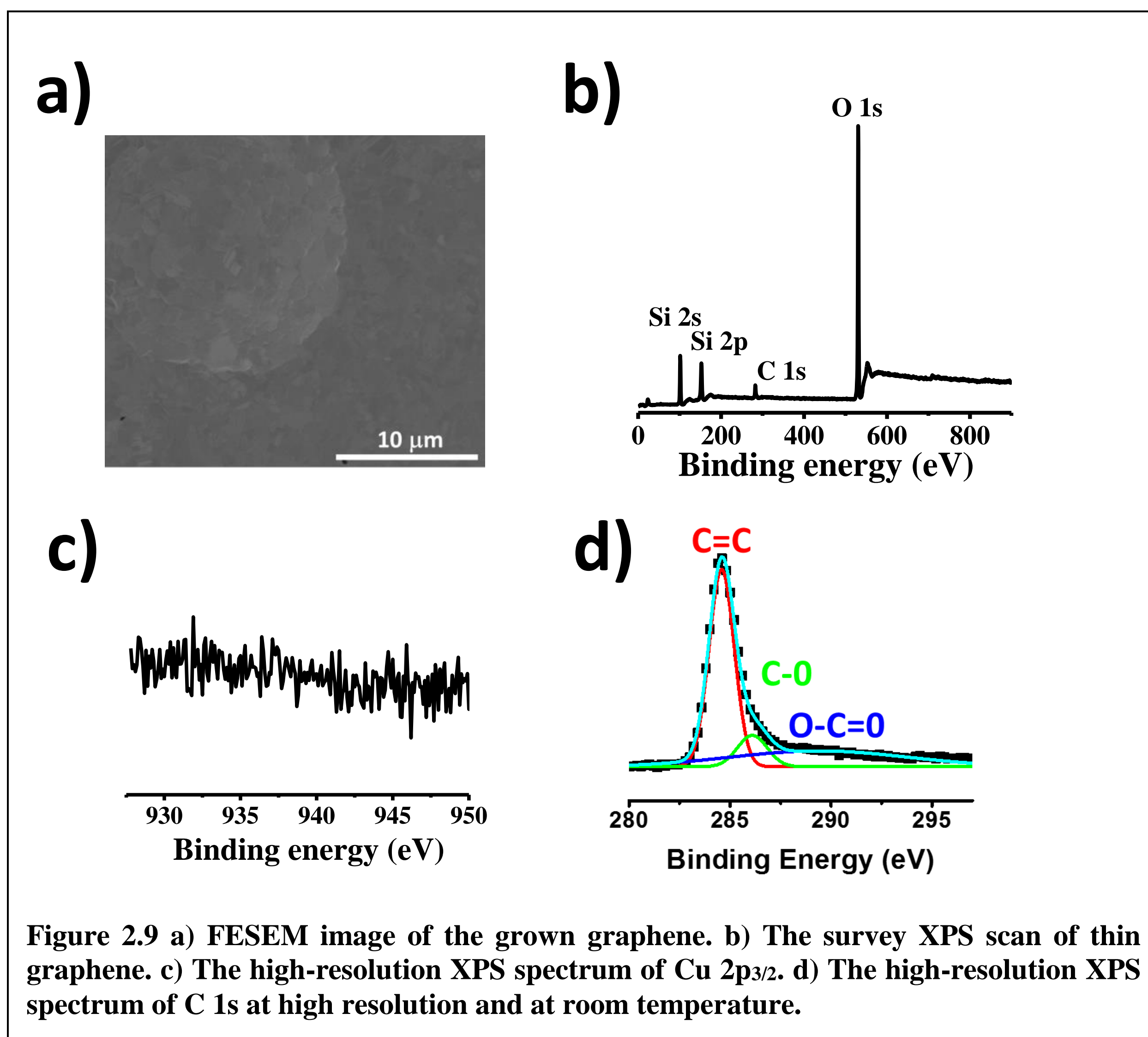

Figure 2.9 a) FESEM image of the grown graphene. b) The survey XPS scan of thin graphene. c) The high-resolution XPS spectrum of Cu $2p_{3/2}$. d) The high-resolution XPS spectrum of C 1s at high resolution and at room temperature.

In addition, the presence of graphene is confirmed by the characteristic sp^2 C=C peak at 284.5 eV as shown in **Figure 2.9d**. Furthermore, the deconvolution of the C 1s peak shows the

presence of defects in graphene domain, which are from sp^3 carbon components, C-O, and O-C=O peaks at 286.1 eV and 289.4 eV, respectively[41,42]. The sp^3 carbon components may originate from two sources: (1) adventitious carbon in the XPS instrument, and (2) defects in the synthesized thin graphene domains, which is confirmed through the Raman data presented in following sections.

Furthermore, the shape of 2D band is important to identify the stacking order of the multilayer graphene[43–45]. The obtained 2D bands of multiple graphene areas are symmetric. A representative fitting of the 2D Raman spectrum is shown on the **Figure 2.10a**, showing a single Lorentzian fit, with an average FWHM (~40 cm^{-1}). These findings suggest a dominant misoriented stacking in our grown graphene[44–48], which is further confirmed in SAED measurement.

The selective area electron diffraction (SAED) is employed to observe the interfaced graphene's crystalline structure, and its rotation angle. As suggested above, a mixture of A-B stacked layers and turbostratic arranged layers were observed in the synthesized graphene film. The six-fold hexagonal symmetry is clearly found in **Figure 2.10b-c**, indicating crystalline nature of the domain, and the Bravais-Miller (hkil) indices were used to label the diffraction peaks as shown in right side of **Figure 2.10c**. The lattice spacing has been calculated as 2.4 Å, which further confirms the graphenic structure[49,50]. Furthermore, the intensity of the inner peaks from the equivalent planes {1100} are always lower than the outer peaks from {2100}. The intensity ratio of I_{-1-120}/I_{-1010} and I_{1-210}/I_{-1100} are greater than 2, and 3 respectively, as shown in the **Figure 2.10d**, indicating the non-twisted A-B stacking structure (0° rotation) of the interfaced graphene in an average[29-31]. In the other hand, turbostatic graphene region is confirmed by the presence of 12 diffraction spots. The rotation between layers are estimated to be 25°, suggesting non A-A stack or A-B stacked thin layer graphene. The observed results agree well with the results of graphene produced *via* CVD method[46,51].

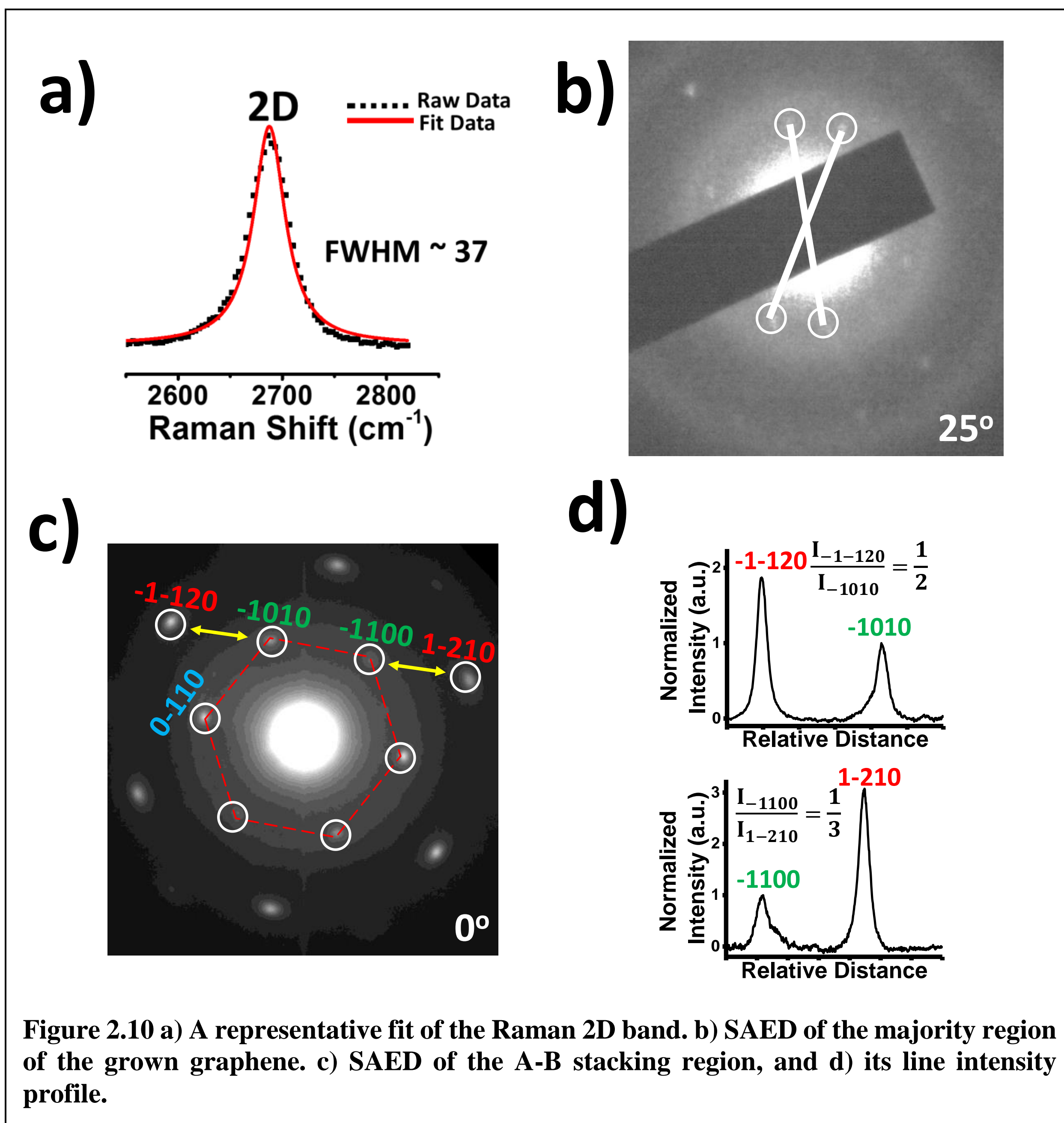

Figure 2.10 a) A representative fit of the Raman 2D band. b) SAED of the majority region of the grown graphene. c) SAED of the A-B stacking region, and d) its line intensity profile.

The growth mechanism of graphene at the interface

The main objective of this work is to provide the growth mechanism of the interfaced graphene, which are described in the following elementary steps as shown in **Figure 2.11a**. (1) The precursors, CH_4 and H_2 transport through the bulk boundary layer, and absorb on the surface of Cu. (2) Furthermore, the catalytic decomposition of CH_4 precursor by Cu generate mobile

intermediate carbon radicals C_xH_y (e.g., CH_3, CH_2, CH, C*, C_2H_y, etc,) which are growth precursors for the multilayer graphene in our study[52,53]. Furthermore, the exothermic reaction of the carbon dimerization $2C^*(s) \rightarrow C_2$ is spontaneous on the surface of Cu[54–56]. Hence, the major constituent of the carbon radicals is expected to be dimer and monomer species[57].

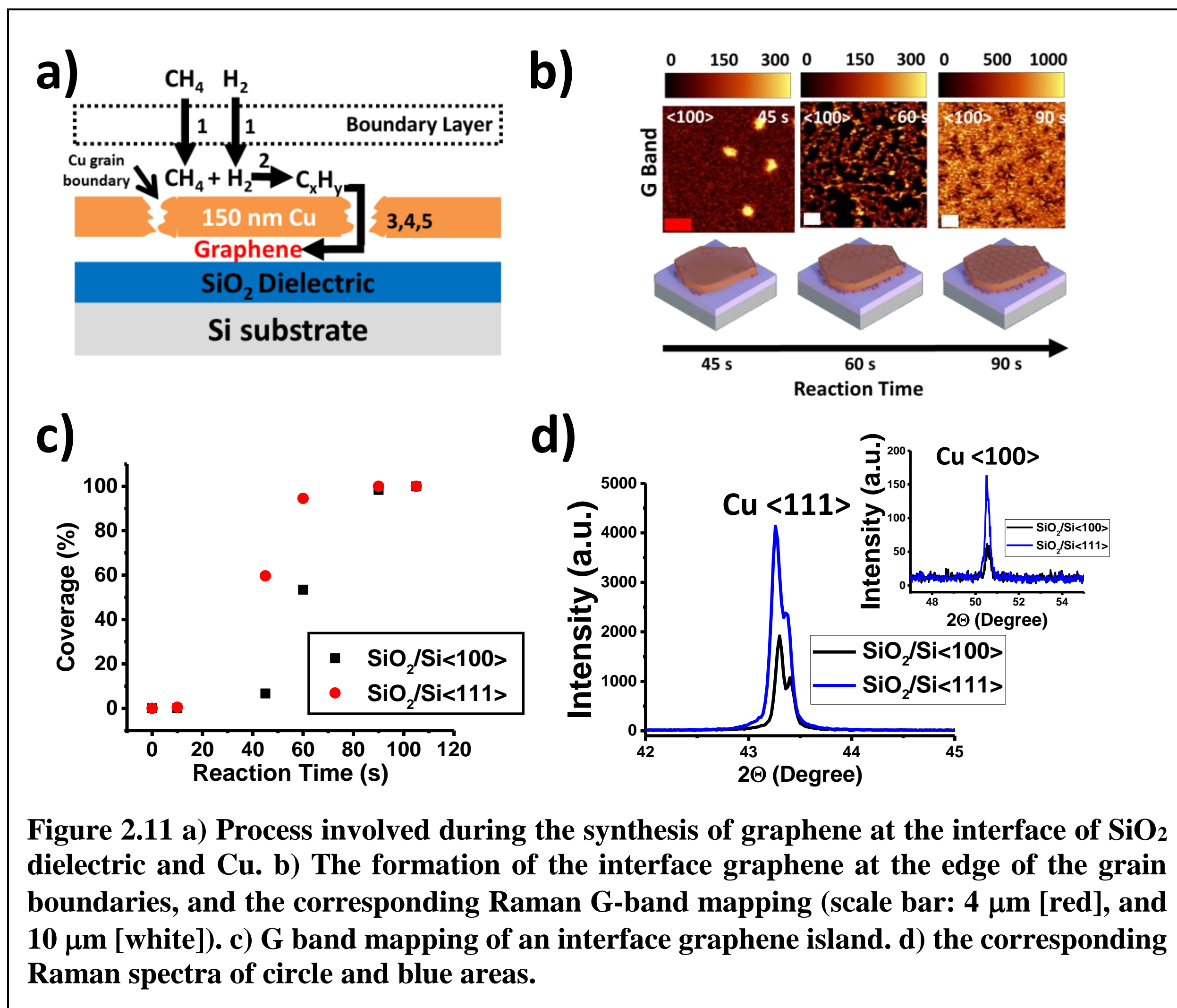

Figure 2.11 a) Process involved during the synthesis of graphene at the interface of SiO_2 dielectric and Cu. b) The formation of the interface graphene at the edge of the grain boundaries, and the corresponding Raman G-band mapping (scale bar: 4 μm [red], and 10 μm [white]). c) G band mapping of an interface graphene island. d) the corresponding Raman spectra of circle and blue areas.

Subsequently, (3) the carbon radical further mobilized on the surface of Cu, transported through copper grain boundary to the interface of Cu and SiO_2/Si[33,58]. (4) The G band mapping shown **Figure 2.11b** indicates the formation of graphene at the interface with respected to the reaction time at 850°C. Since carbon concentration reaches a critical value[59], a series of multilayer

graphene islands, 400 nm in diameter are nucleated and connect to each other to form strings of graphene in the spider-web fashion as confirmed by Raman mapping of G band, and the representative Raman spectra as shown in **Figure 2.11b-d** and **Figure 2.12a**. (5) Subsequently, as the carbon radical continues to replenish, these graphene strings continues to expand inside the interface, and form a continuous film.

The growth formation here is in contrast to that of graphene on the top surface of Cu film. Here, the intensity mapping of Raman G band was utilized for the analysis of graphene formation at the interface, and that on the top surface of Cu film, which was transferred to SiO_2 substrate. The green and red circle represents graphene area, and non-graphene area respectively. As shown

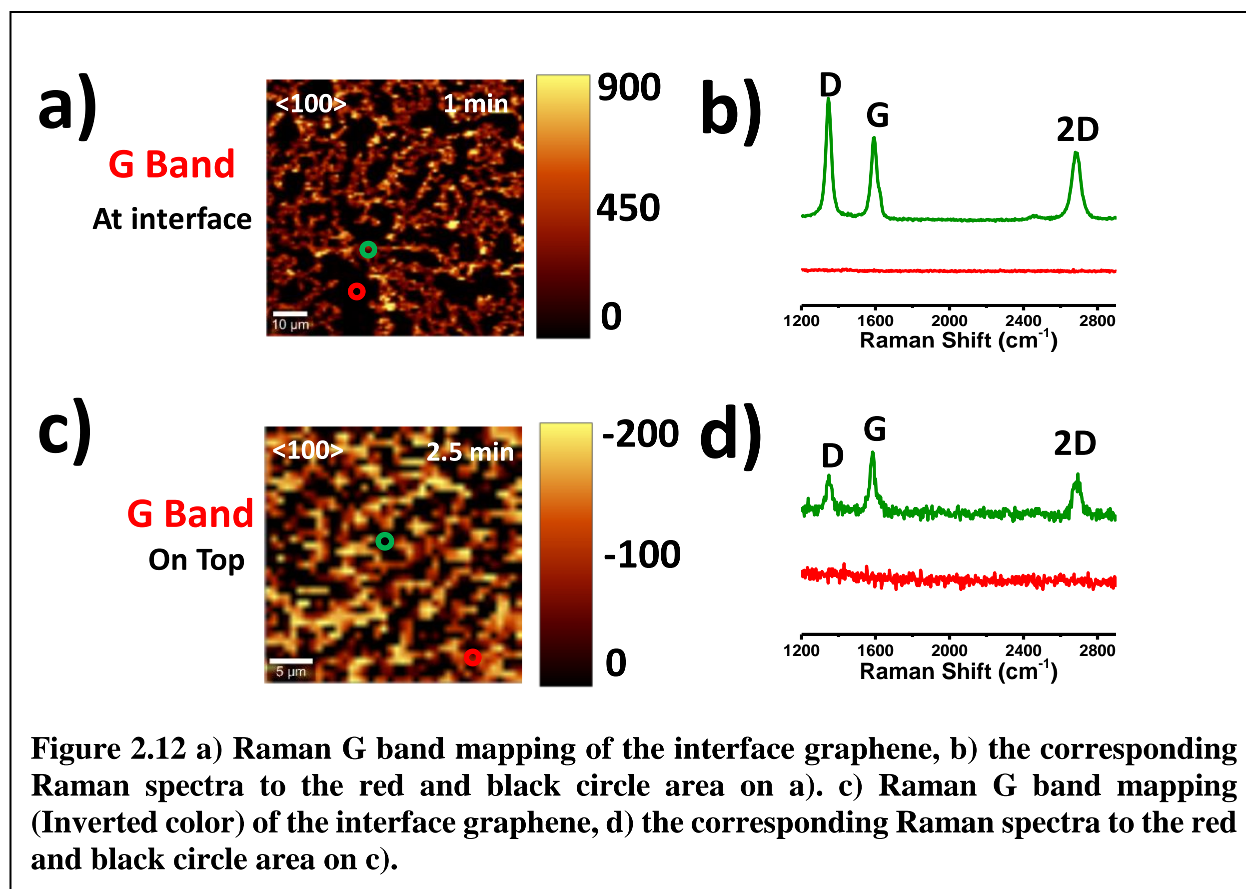

Figure 2.12 a) Raman G band mapping of the interface graphene, b) the corresponding Raman spectra to the red and black circle area on a). c) Raman G band mapping (Inverted color) of the interface graphene, d) the corresponding Raman spectra to the red and black circle area on c).

in **Figure 2.12 a-d**, the darker regions of the Raman G mapping represent the non-graphene area at the interface, while the its brighter regions show the presence of interface graphene. The color

contrast of the Raman G mapping of the interface graphene is, in fact, similar to one of the inverted color of one of graphene grown on top Cu as shown in **Figure 2.12 c-d**. This indicates that on top surface of copper film, graphene islands nucleate, and expand outward (in every direction). Furthermore, the ImageJ color contrast analysis suggests that the coverage rate of graphene on top copper surface is slower than that at the interface.

The next interesting question is which step is the limiting step in our proposed growth mechanism. In case of the growth mechanism of graphene on Cu *via* LPCVD, the limiting step is the surface reaction or surface adsorption[40,60], in which the surface morphology of graphene is uniform, which is different in the observed surface of graphene thin film. Furthermore, the mobility of the carbon radical on copper surface is relatively fast[61]. These evidences suggest that the limiting step should be the grain boundary diffusion of carbon radicals. Since the diffusion rate depends on the thickness of the deposited Cu, a control experiment of graphene growth is carried out with 300 nm Cu on SiO_2/Si<100> (sample A), and 150 nm Cu on SiO_2/Si<100> (sample B). **Figure 2.13a** shows the G mapping of the interface graphene of the sample A. Both sample A, and sample B were placed side by side in the CVD furnace, and underwent 90 second growth. The interfaced coverage, obtained *via* the imageJ color contrast analysis, shows a much lower interface graphene's coverage (70%) in sample A than one in sample B (90%) **(Figure 2.13b**). This result supports our confirmation of the limiting step, grain boundary diffusion.

Figure 2.13c shows the growth rate of the interface graphene on SiO_2/Si<100> and SiO_2/Si<111> surfaces. Initially during growth, the carbon radical's concentration has to reach the critical values in order to compete with desorption, hence there is a delay time in the growth data. Furthermore, we have also observed that the growth of graphene at the interface of SiO_2/Si<111> takes places 2 fold faster than that of graphene at the interface of SiO_2/Si<100>. This phenomenon

was investigated further by obtaining the XRD pattern of Cu on SiO_2/Si<111>, and of Cu on SiO_2/Si<100> as shown in **Figure 2.13d**, which exhibits a dominant Cu<111> over Cu<100> in

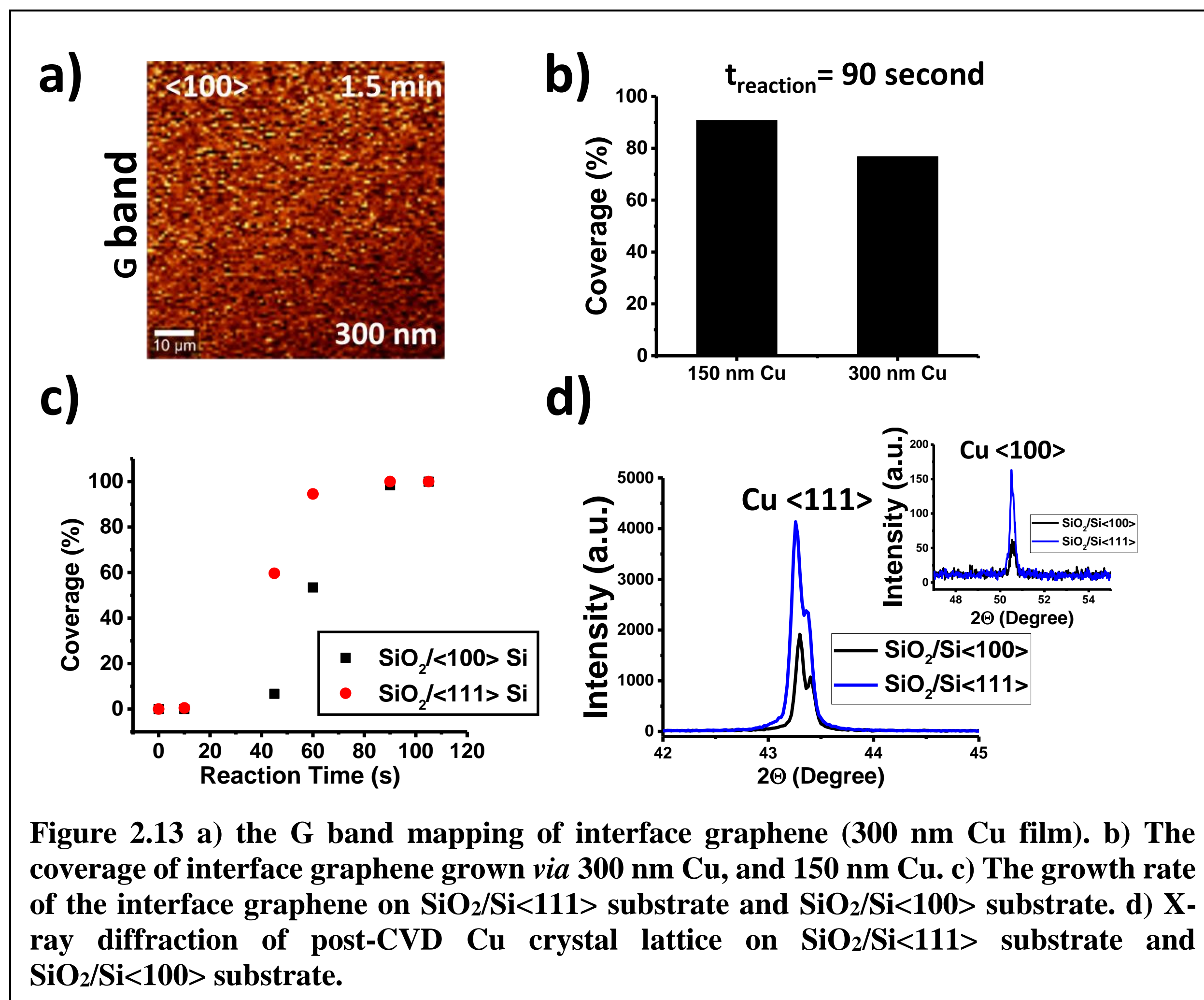

Figure 2.13 a) the G band mapping of interface graphene (300 nm Cu film). b) The coverage of interface graphene grown *via* 300 nm Cu, and 150 nm Cu. c) The growth rate of the interface graphene on SiO_2/Si<111> substrate and SiO_2/Si<100> substrate. d) X-ray diffraction of post-CVD Cu crystal lattice on SiO_2/Si<111> substrate and SiO_2/Si<100> substrate.

both the samples. Furthermore, the intensity of both Cu <111> and Cu<100> are higher in SiO_2/Si<111> substrate than in SiO_2/Si<100>, which indicates a higher density of both Cu crystalline in SiO_2/Si<111>. Furthermore, the growth of multilayer graphene is favored to growth on Cu<111> compared to Cu<100> due to its lower adsorption energy, and lower diffusion energy[48,62,63]. In addition, the growth of interface graphene is facilitated by the close lattice match between hexagonal graphene (lattice constant 0.246 nm) and hexagonal Cu <111> (lattice constant 0.256 nm)[60,64,65].

The influence of growth parameters on graphene quality

During the graphene CVD process, the oxidizing impurities-which arise from gas feed stock, air leakage, and copper substrate[66]-can significantly impact the growth conditions by altering the balance between etching, and growth[67,68]. The solution to this challenge is to vary the flowrate ratio of H_2 and CH_4 (F_{H2}/F_{CH4}), which can compensate these impurities (O_2, H_2O, CO, and CO_2 in our study as shown in **Table 2.1**), hence enhances the graphene quality[69–71]. In the absence of hydrogen ($F_{H2}/F_{CH4} = 0$), due to high oxidizing impurities in CH_4, and air-leakage, the thin graphene film can be etched or converted into oxidized graphene (sp^3 carbon)[67,68,72,73] which leads to the formation of multilayer graphene patches as shown in shown in the Raman intensity I_D/I_G ratio mapping of **Figure** and to poor graphene crystallization (presence of D' peak [~1626 cm^{-1}]) as shown in **Figure 2.14b**. This evidence suggests the introduction of hydrogen would benefit the formation of graphene. On the other hand, if hydrogen exceeds the desired value, it inhibits the adsorption of CH_4, which reduces the rate of the dehydrogenation of CH_4, and affects the crystallization of the graphene[60]. Furthermore, hydrogen can create point defects, which consist of hybridized sp^3 C-H bonds[74], which leads to the increase in the Raman intensity I_D/I_G, and the presence of D' band ($F_{H2}/F_{CH4} = 2/1$) as shown in **Figure 2.14a-b**. The optimal F_{H2}/F_{CH4} can be determined *via* Tuinstra and Koenig relationship[75]:

$$\boldsymbol{L_a\ (nm) = (2.4 \times 10^{-10})\lambda^4 \left(\frac{I_D}{I_G}\right)^{-1}} \quad \textbf{Equation 2.1}$$

where, λ (nm) is the laser wavelength, L_a (nm) in-plane crystallite size, and I_D/I_G is the intensity ratio of D band and G band. Hence, the optimized ratio F_{H2}/F_{CH4} (1/5) corresponds to the highest L_a value (~90 nm) in our case as shown in **Figure 2.14c**.

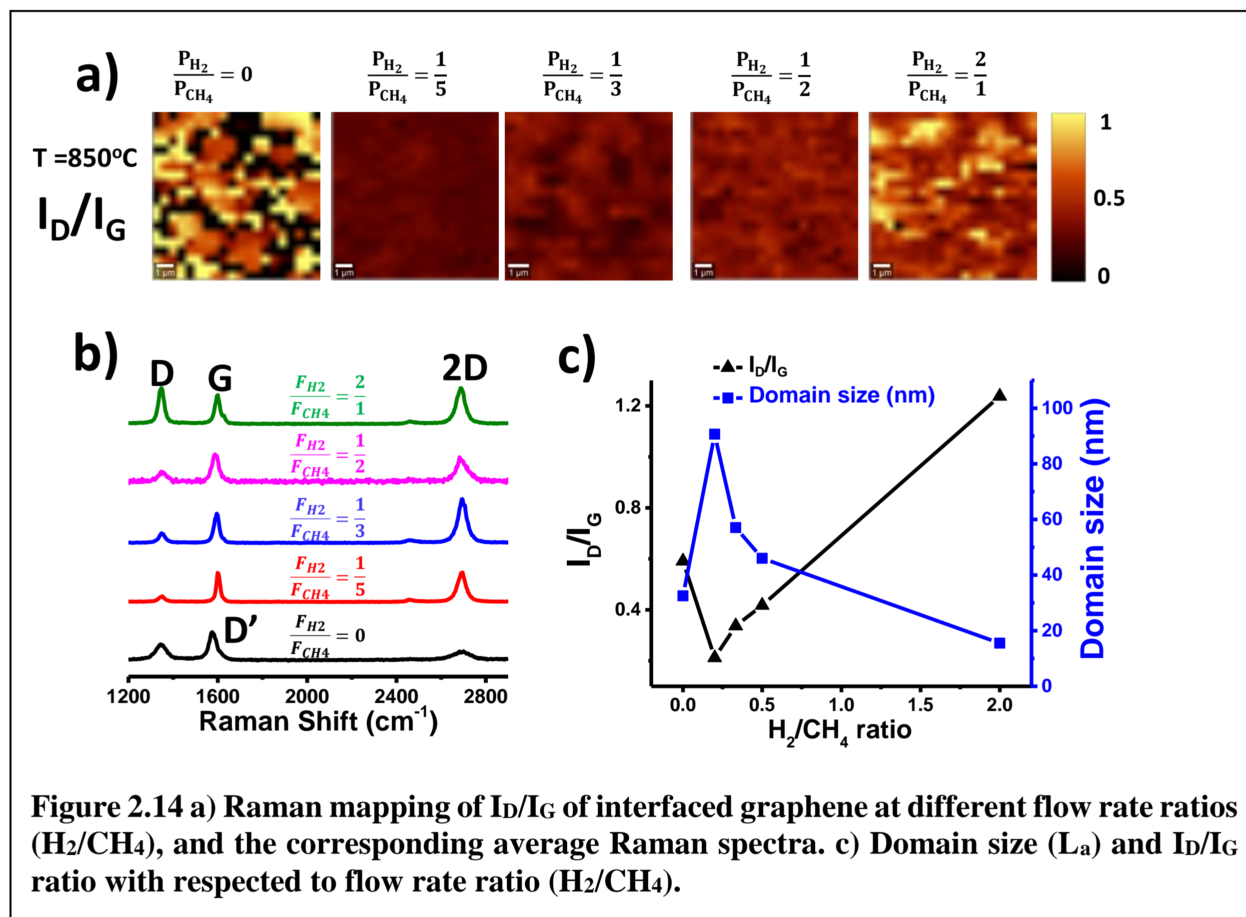

Figure 2.14 a) Raman mapping of I_D/I_G of interfaced graphene at different flow rate ratios (H_2/CH_4), and the corresponding average Raman spectra. c) Domain size (L_a) and I_D/I_G ratio with respected to flow rate ratio (H_2/CH_4).

Since temperature plays an important role in graphene synthesis, **Figure 2.15a** shows the Raman I_D/I_G mapping of the grown graphene at various temperature (750°C -900°C). At low temperature such as 750°C, a high D band intensity and the presence of D' band (~1626 cm^{-1}) indicates a poor graphitization[76,77] as shown in **Figure 2.15b**, and the presence of high density of sp^3 carbon. Due to endothermic dehydrogenation of CH_4 reaction, as the temperature increases, the G peak becomes sharper ($\Delta FWHM_G$ =10 cm^{-1}) with the disappearing of D' peak, indicating an increase in the crystallization of graphene film. **Figure 2.15c** shows the in-plane crystallite size (L_a) and the I_D/I_G ratio as respect with reaction temperature. The estimated L_a (nm) is 140 nm, which further illustrates that 900°C is the optimized reaction temperature in our CVD setup. At

950°C, copper starts to evaporate strongly, which leads to non-continuous and high defect graphene.

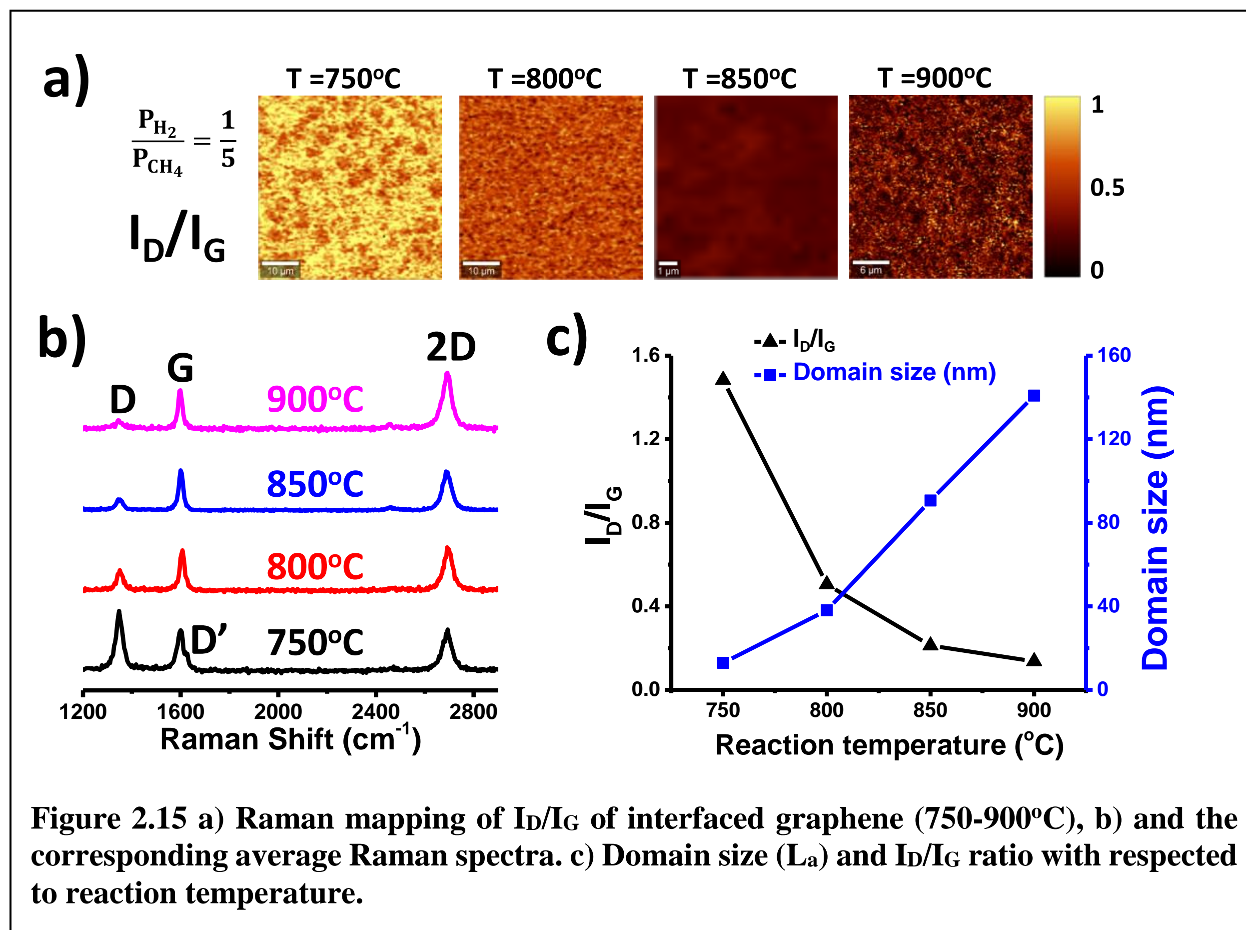

Figure 2.15 a) Raman mapping of I_D/I_G of interfaced graphene (750-900°C), b) and the corresponding average Raman spectra. c) Domain size (L_a) and I_D/I_G ratio with respected to reaction temperature.

Furthermore, the G band downshifts (~8 cm^{-1}) as the reaction temperature increases from 800°C to 900°C, which is attributed notably to a reduction of thermal induced hole doping[78]. Due to a reduction of the I_D/I_G ratio, the defect density also decreases, leading to the reduction of oxygen adsorption (p-doping) on graphene surface after removing from the furnace[78,79]. After CVD process, the N_2 gas in the atmosphere shows no influence on the position of G peak[78].

The electronic characterization of the thin graphene film

It is important to understand the electronic properties of the grown thin graphene film, which was transferred to a clean substrate of 300 nm SiO_2 on n^{++} Si. The optical image of typical

back-gate GFET is shown in the right inset of **Figure 2.16a** with the dimensions (12.5 µm x 25 µm, L/W ~ 2). The GFET uses Cr/Au film (15/95 nm) as the source and drain contacts, and n^{++} Si as the gate source (as shown in left inset of **Figure 2.16a**). In order to minimize the external doping, all the measurements were carried out under high vacuum conditions (<1 x 10^{-7} Torr) in a ARS cryostat.

The field effect analysis of the thin graphene film

Figure 2.16a shows that the conductivity as a function of carrier density, at which the resistivity transform from sublinear behavior into linear behavior as carrier concentration is away from the charge neutrality point (CNP). This indicates a transition from low carrier densities, where charge transport is dominated by Coulombic impurities, to large carrier densities, where short-range scatterers dominate[80]. Furthermore, the I_{on}/I_{off} ratio for the GFET is ~ 1.7. Because the length of the fabricated transistor is much larger the mean free path of graphene (L>>λ), an equation for the diffusive transport should be acquired in order to fit the experimental data.

$$(\sigma)^{-1} = (ne\mu_C + \sigma_G)^{-1} + \rho_S \quad \textbf{Equation 2.2}$$

where σ is the measured conductivity, μ_C is density-independent mobility due to charged-impurity Coulomb (long-range) scattering, ρ_S is the contribution to resistivity from short-range scattering, and σ_G is the background conductivity at the charge neutrality point[81–83]. Consequently, the equation yields μ_C of 277 $cm^2V^{-1}s^{-1}$, and 233 $cm^2V^{-1}s^{-1}$ for p-type and n-type conduction respectively. The μ_C is limited due to two possible mechanisms: (1) Coulomb scattering near CNP, and (2) electron-phonon scattering at high carrier density. In the first mechanism, the long ranged charge scatterers arise from the charge impurities from the surface of SiO_2 i.e. electron-hole puddles[84–86]. In the latter mechanism, the short range resistivity (ρ_S), which is estimated to be ~3.8

kΩ/sq, can help explain the low value of μ_C in the GFET transistor. Despite being debated, the origin of short range resistivity can be attributed to (1) the flexural (out of plane) phonons that are excited inside the ripples of graphene[87,88], (2) the surface polar optical phonon of underlying substrates[89–91], (3) lattice defects or point defects on graphene film[92], and (4) contact resistance[93]. In the first two phenomena, phonon scatterers are screened from the outer few layers of graphene

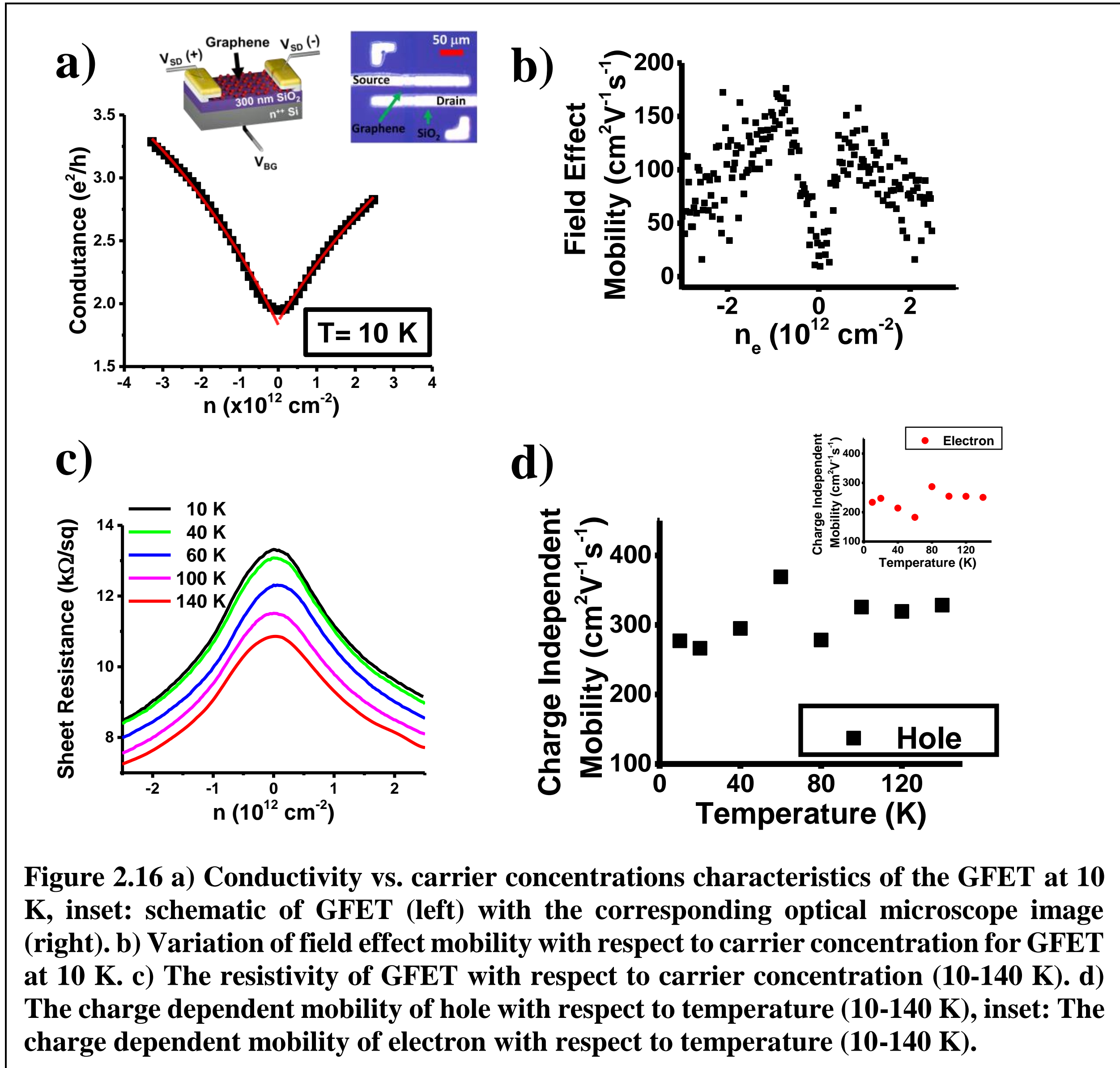

Figure 2.16 a) Conductivity vs. carrier concentrations characteristics of the GFET at 10 K, inset: schematic of GFET (left) with the corresponding optical microscope image (right). b) Variation of field effect mobility with respect to carrier concentration for GFET at 10 K. c) The resistivity of GFET with respect to carrier concentration (10-140 K). d) The charge dependent mobility of hole with respect to temperature (10-140 K), inset: The charge dependent mobility of electron with respect to temperature (10-140 K).

thin film, suggesting the negligible effect of electron-phonon scattering mechanism in our GFET. In addition, typical values for the resistivity of SiO_2 surface polar optical were low as shown in

previous report (30-500 Ω)[89]. The minor role of phonon scattering on the mobility of the thin film graphene is further confirmed later. On the other hand, as shown in our above Raman data, the I_D/I_G ratio is noticeable, indicating a smaller the crystalline graphene domain size than the channel length of the fabricated transistor. Consequently, the high density of defects in graphene grain boundaries contribute largely in short range scattering transport[92]. Furthermore, in contrast of the contact resistance of graphene monolayer, the one of graphene thin film is independent of carrier concentration due to the lack of charge depletion region near the contact[83,94]. The magnitude of the contact resistance is highly dependent in fabrication techniques. Therefore, it leads to a confirmation that the majority of the short range scattering in our GFET are lattice or point defects, and contact resistance. Furthermore, in the literature, the field effect mobility (μ_{FE}) is defined as the derivative of the Drude formula, $\mu_{FE} = (\frac{1}{C})(\frac{d\sigma}{dV_{BG}})$, which evaluates the μ_{FE} varies from ~75 $cm^2V^{-1}s^{-1}$ at high carrier density, to ~175 $cm^2V^{-1}s^{-1}$ near the CNP (as shown in **Figure 2.16b**).

The temperature dependence of the GFET's sheet resistivity as a function of carrier density is shown in **Figure 2.16c**. The GFET exhibits ambipolar conductivity over the entire temperature range (10 K-140 K). In the absence of back gate voltage, the transport in the GFET is hole dominant. As the temperature increases, in all high/low density regime, the GFET has pronouncedly non-metallic behavior ($d\rho/dT<0$). This is an important difference between monolayer graphene FET and other exfoliated bilayer graphene FET [88,95,96], which possesses the consistence of the resistivity away from the charge neutrality point as the temperature changes. In addition, the equation (1) is used to evaluate the density-independent mobility (μ_C) (hole) with respect to temperature, which is shown in **Figure 2.16d**. The density-independent mobility for electrons with respect to temperature is shown in the inset of **Figure 2.16d**. The slow decrease of μ_C with decreasing the temperature indicates the Coulomb scattering transport in our thin film

GFET is dominant[97] over electron-phonon scattering. Furthermore, since the magnitude of the electron-phonon scattering mobility is much greater than Coulomb scattering mobility and short-range scattering mobility, it is neglected in our thin GFET transport[91,98].

Charge transport mechanism of the thin graphene film

Figure 2.17a shows the increase of background conductivity with respect to temperature. This semiconductor-like behavior can be explained by simple two band (STB) model[83,99–101]. In contrast to Dirac cone linear dispersion in graphene monolayer, the interaction between layers in graphite results in the parabolic dispersion relation. Since our thin graphene film is few layer thickness, the band structure behaves in a way that the parabolic dispersion relationship occurs at the energies near Fermi level (E_F), and the linear dispersion, occurs at higher energy range. Furthermore, the valence and the conduction bands overlap with an energy $\Delta=2E_o$ as shown in inset of **Figure 2.17b**. The temperature behavior of the GFET is evaluated through the resistivity at the CNP with the following expression.

$$(\sigma_G)^{-1} = \frac{1}{e\mu(T)n(T)} = \left(\frac{1}{e}\right)\left(\frac{1}{\mu_C} + A_oT\right)\left(2C_ok_BTln\left[1 + e^{\left\{E_o/k_BT\right\}}\right]\right)^{-1}$$ **Equation 2.3**

where μ_C is density-independent mobility due to charged-impurity Coulomb (long-range) scattering, σ_G is the background conductivity at the charge neutrality point, k_B is Boltzmann constant, A_o is constant dependent on electron-phonon scattering in GFET, $C_o$is constant dependent on effective mass of the charge carriers, T is temperature, and E_o is the half band overlap. The back ground resistivity is fitted to equation 4.2 with free parameter of $\mu_C A_o$, $\mu_C C_o$, and E_o as shown in **Figure 2.17c**. The overlapping band is estimated to be 2.3±0.4 meV, which is expected to thin graphene film.

As shown in **Figure 2.17d**, the magnitude of the decrease in GFET's resistivity (dρ/dT) is not the same in the range (T>40 K), which suggests an activation energy over energy gap (E_A) of charge transport. To further understand this transport mechanism of GFET in the absence of back gate voltage (V_{BG}= 0 V), a series of I-V measurements were carried out in the temperature

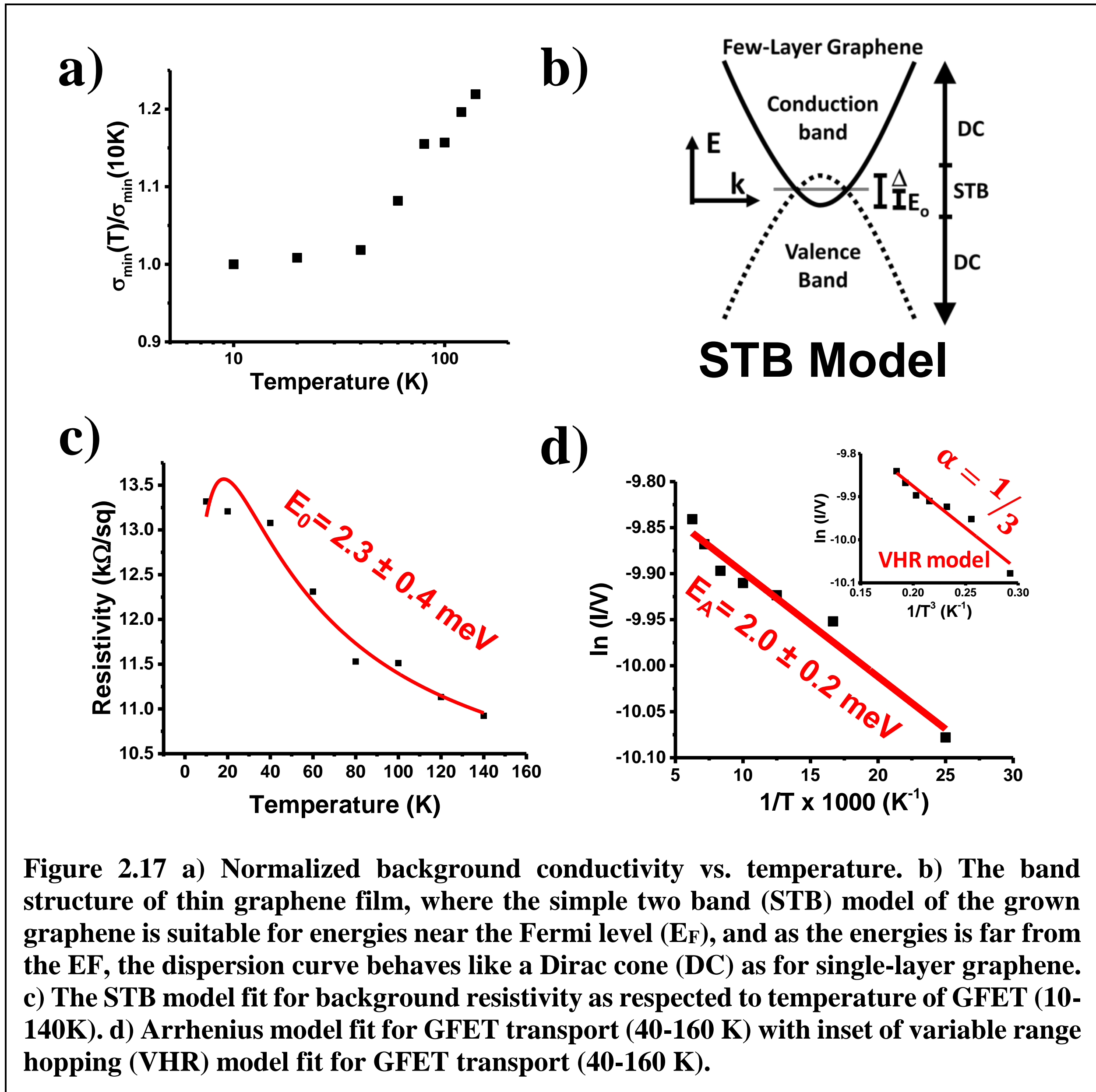

Figure 2.17 a) Normalized background conductivity vs. temperature. b) The band structure of thin graphene film, where the simple two band (STB) model of the grown graphene is suitable for energies near the Fermi level (E_F), and as the energies is far from the EF, the dispersion curve behaves like a Dirac cone (DC) as for single-layer graphene. c) The STB model fit for background resistivity as respected to temperature of GFET (10-140K). d) Arrhenius model fit for GFET transport (40-160 K) with inset of variable range hopping (VHR) model fit for GFET transport (40-160 K).

range (40-160 K). The transport can be elucidated by two common mechanisms: 1) Arrhenius thermal activation model as shown $\left(\frac{I}{V}\right) \propto \exp\left[{}^{-E_A}/_{2k_BT}\right]$ (**Equation 2.4**), and 2) the variable

range hopping (VHR) model[102,103] as shown: $\left(\frac{I}{V}\right) \propto \exp\left[-\left({}^{T_o}/_{T}\right)^{\alpha}\right]$ **(Equation 2.5).** The two equations (3) and (4) yield the thermal energy barrier of 2.0±0.2 meV (from equation 2.4), and α~1/3 (from equation 2.5), which suggests the hopping in 2 dimensions, in-plane and through multiple layers of GFET.

Conclusion

In summary, this chapter demonstrated the mechanism of thin graphene film on the interface of SiO_2/Si substrate and thin copper film (~150 nm) *via* LPCVD. Graphene nucleates at the grain boundaries at the interface of Cu and SiO_2/Si. The growth is grain boundary diffusion limited. Excitingly, SiO_2/Si<111> substrate enhances the crystallization of Cu<111> and Cu<100>. Furthermore, the optimized growth parameters such as temperature, and flow rate ratio of methane gas and hydrogen gas, were found as 900°C, and F_{H2}/F_{CH4}~1/5. The turbostratic stacking thin graphene film is found to be low defect (L_a~140 nm), with field effect mobility of 277 $cm^2V^{-1}s^{-1}$, and 233 $cm^2V^{-1}s^{-1}$ for hole and electron respectively. In addition, the various temperature electronic transport studies reveal that the thin graphene film exhibits a dominant Coulombic scattering, an overlapping band of 2.3±0.4 meV, a thermal activation energy of 2.0±0.2 meV, and 2-D hopping conduction. We envisioned that our work will generate interest in scalable direct growth of large-area, contamination free, transfer/unloading free thin layer graphene, which is vital for graphene electronics, and graphene-platform 2D heterostructures applications ranging from nano-scale electronics to energy conversion and optoelectronics.

Acknowledgements

The financial support from SunEdison Semiconductor, USA was acknowledged. This work made use of instruments in the Electron Microscopy Service (Research Resources Center, UIC) and Nanotechnology Core Facility of University of Illinois at Chicago.

Reference

1. Geim, A. K. et al. The Rise Of Graphene. Nature Materials 6, 183–191 (2007).
2. Novoselov, K. S. et al. Electric Field Effect In Atomically Thin Carbon Films. Science 306, 666–669 (2004).
3. Balandin, A. A. et al. Superior Thermal Conductivity of Single-Layer Graphene. Nano Letters 8, 902–907 (2008).
4. Novoselov, K. S. et al. Room-Temperature Quantum Hall Effect In Graphene. Science 315, 1379–1379 (2007).
5. Gilje, S. et al. A Chemical Route To Graphene For Device Applications. Nano Letters 7, 3394–3398 (2007).
6. Gómez-Navarro, C. et al. Electronic Transport Properties Of Individual Chemically Reduced Graphene Oxide Sheets. Nano Letters 7, 3499–3503 (2007).
7. Barone, V. et al. Electronic Structure And Stability Of Semiconducting Graphene Nanoribbons. Nano Letters 6, 2748–2754 (2006).
8. Bunch, J. S. et al. Electromechanical Resonators From Graphene Sheets. Science 315, 490–3 (2007).
9. Diebold, A. C. The ITRS Metrology Roadmap. he Institute of Electrical and Electronics Engineers, 1–2 (2009)
10. Novoselov, K. S. et al. A Roadmap For Graphene. Nature 490, 192–200 (2012).
11. Grüneis, A. et al. Dynamics Of Graphene Growth On A Metal Surface: A Time-Dependent Photoemission Study. New Journal of Physics 11, 73050 (2009).
12. Li, X. et al. Large Area Synthesis Of High Quality And Uniform Graphene Films On Copper Foils. Science 324, 1312–1314 (2009).
13. Kim, Y. et al. Synthesis Of Graphene On Various Copper Foils By Chemical Vapor

Deposition. Journal of Ceramic Processing Research 15, 269–272 (2014).

14. McCarty, K. F., et al. Kinetics And Thermodynamics Of Carbon Segregation And Graphene Growth On Ru(0001). Carbon 47, 1806–1813 (2009).
15. Reina, A. et al. Large Area, Few-Layer Graphene Films on Arbitrary Substrates By Chemical Vapor Deposition. Nano Letters 9, 30–35 (2009).
16. Sutter, P., et al. Graphene On Pt(111): Growth And Substrate Interaction. Physical Review B 80, 245411 (2009).
17. Varykhalov, A. et al. Graphene Grown On Co(0001) Films And Islands: Electronic Structure And Its Precise Magnetization Dependence. Physical Review B 80, 35437 (2009).
18. Vinogradov, N. A. et al. Formation and Structure of Graphene Waves on Fe(110). Physical Review Letters 109, 26101 (2012).
19. Yu, Q. et al. Graphene Segregated On Ni Surfaces And Transferred To Insulators. Applied Physics Letters 93, 113103 (2008).
20. Behura, S. K., et al. Vertically Oriented Few-Layer Graphene As An Electron Field-Emitter. Physica Status Solidi (A) Applications and Materials Science 210, 1817–1821 (2013).
21. Chen, J. et al. Near-Equilibrium Chemical Vapor Deposition Of High-Quality Single-Crystal Graphene Directly On Various Dielectric Substrates. Advanced Materials 26, 1348–1353 (2014).
22. Chen, J. et al. Two-Stage Metal-Catalyst-Free Growth Of High-Quality Polycrystalline Graphene Films On Silicon Nitride Substrates. Advanced Materials 25, 992–997 (2013).
23. Chen, J. et al. Oxygen-Aided Synthesis Of Polycrystalline Graphene On Silicon Dioxide Substrates. Journal Of The American Chemical Society 133, 17548–17551 (2011).
24. Kim, K. B. et al. Catalyst-Free Direct Growth Of Triangular Nano-Graphene On All Substrates. Journal of Physical Chemistry C 115, 14488–14493 (2011).
25. Behura, S. K. et al. Electrical Characteristics of Horizontally and Vertically Oriented Few-Layer Graphene on Si-Based Dielectrics. Journal of Nanoscience and Nanotechnology 16, 6246–6251 (2016).
26. Hwang, J. et al. Van Der Waals Epitaxial Growth Of Graphene On Sapphire By Chemical Vapor Deposition Without A Metal Catalyst. ACS Nano 7, 385–395 (2013).
27. Song, H. J. et al. Large Scale Metal-Free Synthesis Of Graphene On Sapphire And Transfer-Free Device Fabrication. Nanoscale 4, 3050 (2012).

28. Sun, J. et al. Direct Growth Of High-Quality Graphene On High-K Dielectric Srtio 3 Substrates. Journal Of The American Chemical Society 136, 6574–6577 (2014).
29. Gao, T. et al. Temperature-Triggered Chemical Switching Growth Of In-Plane And Vertically Stacked Graphene-Boron Nitride Heterostructures. Nature Communications 6, 6835 (2015).
30. Wang, M. et al. A Platform For Large-Scale Graphene Electronics – CVD Growth Of Single-Layer Graphene On CVD-Grown Hexagonal Boron Nitride. Advanced Materials 25, 2746–2752 (2013).
31. Yang, W. et al. Epitaxial Growth Of Single-Domain Graphene On Hexagonal Boron Nitride. Nature Materials 12, 792–797 (2013).
32. Zhang, C. et al. Direct Growth Of Large-Area Graphene And Boron Nitride Heterostructures By A Co-Segregation Method. Nature Communications 6, 6519 (2015).
33. Su, C.-Y. et al. Direct Formation Of Wafer Scale Graphene Thin Layers On Insulating Substrates By Chemical Vapor Deposition. Nano Letters 11, 3612–3616 (2011).
34. Sun, Z. et al. Growth Of Graphene From Solid Carbon Sources. Nature 468, 549–552 (2010).
35. Ismach, A. et al. Direct Chemical Vapor Deposition Of Graphene On Dielectric Surfaces. Nano Letters 10, 1542–1548 (2010).
36. Das, A. et al. Monitoring Dopants By Raman Scattering In An Electrochemically Top-Gated Graphene Transistor. Nature nanotechnology 3, 210–5 (2008).
37. Dresselhaus, M. S. et al. Perspectives On Carbon Nanotubes And Graphene Raman Spectroscopy. Nano Letters 10, 751–758 (2010).
38. Ferrari, A. C. Raman Spectroscopy Of Graphene And Graphite: Disorder, Electron–Phonon Coupling, Doping And Nonadiabatic Effects. Solid State Communications 143, 47–57 (2007).
39. Ferrari, A. C. A. et al. Raman Spectroscopy As A Versatile Tool For Studying The Properties Of Graphene. Nature Nanotechnology 8, 235–46 (2013).
40. Bhaviripudi, S. et al. Role Of Kinetic Factors In Chemical Vapor Deposition Synthesis Of Uniform Large Area Graphene Using Copper Catalyst. Nano Letters 10, 4128–4133 (2010).
41. Debbarma, R. et al. Electrical Transport And Network Percolation In Graphene And Boron Nitride Mixed-Platelet Structures. ACS Applied Materials & Interfaces 8, 8721–8727

(2016).

42. Park, S. et al. Graphene Oxide Papers Modified By Divalent Ions—Enhancing Mechanical Properties *Via* Chemical Cross-Linking. ACS Nano 2, 572–578 (2008).
43. Cançado, L. G. G. et al. Measuring The Degree Of Stacking Order In Graphite By Raman Spectroscopy. Carbon 46, 272–275 (2008).
44. Lenski, D. R. et al. Raman And Optical Characterization Of Multilayer Turbostratic Graphene Grown *Via* Chemical Vapor Deposition. Journal Of Applied Physics 110, 13720 (2011).
45. Ferrari, A. C. et al. Raman Spectrum Of Graphene And Graphene Layers. Physical Review Letters 97, 187401 (2006).
46. Park, H. J. et al. Growth And Properties Of Few-Layer Graphene Prepared By Chemical Vapor Deposition. Carbon 48, 1088–1094 (2010).
47. Pimenta, M. A. et al. Studying Disorder In Graphite-Based Systems By Raman Spectroscopy. Physical Chemistry Chemical Physics 9, 1276–1290 (2007).
48. Wood, J. D. et al. Effects Of Polycrystalline Cu Substrate On Graphene Growth By Chemical Vapor Deposition. Nano Letters 11, 4547–4554 (2011).
49. Meyer, J. C. et al. On The Roughness Of Single- And Bi-Layer Graphene Membranes. Solid State Communications 143, 101–109 (2007).
50. Ohta, T. et al. Controlling The Electronic Structure Of Bilayer Graphene. Science 313, 951–4 (2006).
51. Liu, L. et al. High-Yield Chemical Vapor Deposition Growth Of High-Quality Large-Area AB-Stacked Bilayer Graphene. ACS Nano 6, 8241–8249 (2012).
52. Li, Q. et al. Growth Of Adlayer Graphene On Cu Studied By Carbon Isotope Labeling. Nano Letters 13, 486–490 (2013).
53. Zhang, W. et al. First-Principles Thermodynamics Of Graphene Growth On Cu Surfaces. The Journal Of Physical Chemistry C 115, 17782–17787 (2011).
54. Gajewski, G. et al. Ab Initio Calculations Of The Reaction Pathways For Methane Decomposition Over The Cu (111) Surface. The Journal Of Chemical Physics 135, 64707 (2011).
55. Riikonen, S. et al. The Role Of Stable And Mobile Carbon Adspecies In Copper-Promoted Graphene Growth. The Journal Of Physical Chemistry C 116, 5802–5809 (2012).

56. Yazyev, O. V. et al. Effect Of Metal Elements In Catalytic Growth Of Carbon Nanotubes. Physical Review Letters 100, 156102 (2008).
57. Hayashi, K. et al. Selective Graphene Formation On Copper Twin Crystals. Journal Of The American Chemical Society 134, 12492–12498 (2012).
58. Fang, W. et al. Asymmetric Growth Of Bilayer Graphene On Copper Enclosures Using Low-Pressure Chemical Vapor Deposition. ACS Nano 8, 6491–6499 (2014).
59. Kim, H. et al. Activation Energy Paths For Graphene Nucleation And Growth On Cu. ACS Nano 6, 3614–3623 (2012).
60. Tao, L. et al. Synthesis Of High Quality Monolayer Graphene At Reduced Temperature On Hydrogen-Enriched Evaporated Copper (111) Films. ACS Nano 6, 2319–2325 (2012).
61. Wu, P. et al. Bilayer Graphene Growth *Via* A Penetration Mechanism. The Journal Of Physical Chemistry C 118, 6201–6206 (2014).
62. Ishihara, M. et al. Direct Evidence Of Advantage Of Cu(111) For Graphene Synthesis By Using Raman Mapping And Electron Backscatter Diffraction. Materials Letters 65, (2011).
63. Vlassiouk, I. et al. Graphene Nucleation Density On Copper: Fundamental Role Of Background Pressure. The Journal Of Physical Chemistry C 117, 18919–18926 (2013).
64. Gao, L. et al. Epitaxial Graphene On Cu(111). Nano Letters 10, 3512–3516 (2010).
65. Hu, B. et al. Epitaxial Growth Of Large-Area Single-Layer Graphene Over Cu(111)/Sapphire By Atmospheric Pressure CVD. Carbon 50, 57–65 (2012).
66. Hao, Y. et al. The Role Of Surface Oxygen In The Growth Of Large Single-Crystal Graphene On Copper. Science 342, (2013).
67. Choubak, S. et al. No Graphene Etching In Purified Hydrogen. The Journal Of Physical Chemistry Letters 4, 1100–1103 (2013).
68. Reckinger, N. et al. The Influence Of Residual Oxidizing Impurities On The Synthesis Of Graphene By Atmospheric Pressure Chemical Vapor Deposition. Carbon 63, 84–91 (2013).
69. Jacobberger, R. M. et al. Graphene Growth Dynamics On Epitaxial Copper Thin Films. Chemistry Of Materials 25, 871–877 (2013).
70. Zhang, Y. et al. Vapor Trapping Growth Of Single-Crystalline Graphene Flowers: Synthesis, Morphology, And Electronic Properties. Nano Letters 12, 2810–2816 (2012).
71. Liu, L. et al. A Systematic Study Of Atmospheric Pressure Chemical Vapor Deposition Growth Of Large-Area Monolayer Graphene. J Mater Chem 22, 1498–1503 (2012).

72. Strudwick, A. J. et al. Chemical Vapor Deposition Of High Quality Graphene Films From Carbon Dioxide Atmospheres. ACS Nano 9, 31–42 (2015).
73. Choubak, S. et al. Graphene CVD: Interplay Between Growth And Etching On Morphology And Stacking By Hydrogen And Oxidizing Impurities. The Journal Of Physical Chemistry C 118, 21532–21540 (2014).
74. Losurdo, M. et al. Graphene CVD Growth On Copper And Nickel: Role Of Hydrogen In Kinetics And Structure. Physical Chemistry Chemical Physics 13, 20836 (2011).
75. Cançado, L. G. et al. General Equation For The Determination Of The Crystallite Size La Of Nanographite By Raman Spectroscopy. Applied Physics Letters 88, 163106 (2006).
76. Elias, D. C. et al. Control Of Graphene's Properties By Reversible Hydrogenation: Evidence For Graphane. Science 323, 610–3 (2009).
77. Liu, L. et al. Graphene Oxidation: Thickness-Dependent Etching And Strong Chemical Doping. Nano Letters 8, 1965–1970 (2008).
78. Ryu, S. et al. Atmospheric Oxygen Binding And Hole Doping In Deformed Graphene On A Sio_2 Substrate. Nano Letters 10, 4944–4951 (2010).
79. Mehmood, F. et al. Adsorption And Diffusion Of Oxygen On Single-Layer Graphene With Topological Defects. The Journal Of Physical Chemistry C 117, 10366–10374 (2013).
80. Nomura, K. et al. Quantum Transport Of Massless Dirac Fermions. Physical Review Letters 98, 76602 (2007).
81. Adam, S. et al. Boltzmann Transport And Residual Conductivity In Bilayer Graphene. Physical Review B - Condensed Matter And Materials Physics 77, 115436 (2008).
82. Hwang, E. H. et al. Carrier Transport In Two-Dimensional Graphene Layers. Physical Review Letters 98, 186806 (2007).
83. Nezich, D. et al. Electrical Characterization Of Graphene Synthesized By Chemical Vapor Deposition Using Ni Substrate. Nanotechnology 23, 15701 (2012).
84. Deshpande, A. et al. Spatially Resolved Spectroscopy Of Monolayer Graphene On Sio2. Physical Review B 79, 205411 (2009).
85. Martin, J. et al. Observation Of Electron-Hole Puddles In Graphene Using A Scanning Single Electron Transistor. Nature Physics 4, 13 (2007).
86. Zhang, Y. et al. Origin Of Spatial Charge Inhomogeneity In Graphene. Nature Physics 5, 722–726 (2009).

87. Ishigami, M. et al. Atomic Structure Of Graphene On SiO_2. Nano Letters 7, 1643–1648 (2007).
88. Morozov, S. V. et al. Giant Intrinsic Carrier Mobilities In Graphene And Its Bilayer. Physical Review Letters 100, 16602 (2008).
89. Chen, J-H. et al. Intrinsic And Extrinsic Performance Limits Of Graphene Devices On SiO_2. Nature Nanotechnology 3, 206–9 (2008).
90. Fratini, S. et al. Substrate-Limited Electron Dynamics In Graphene. Physical Review B - Condensed Matter And Materials Physics 77, 195415 (2008).
91. Hwang, E. H. et al. Acoustic Phonon Scattering Limited Carrier Mobility In Two-Dimensional Extrinsic Graphene. Physical Review B - Condensed Matter And Materials Physics 77, 115449 (2008).
92. Vasko, F. T. et al., Voltage And Temperature Dependencies Of Conductivity In Gated Graphene. Physical Review B 76, 233404 (2007).
93. Kim, S. et al. Realization Of A High Mobility Dual-Gated Graphene Field-Effect Transistor With Al_2O_3 Dielectric. Applied Physics Letters 94, 62107 (2009).
94. Blake, P. et al. Influence Of Metal Contacts And Charge Inhomogeneity On Transport Properties Of Graphene Near The Neutrality Point. Solid State Communications 149, 1068–1071 (2009).
95. Bolotin, K. I. et al. Temperature-Dependent Transport In Suspended Graphene. Physical Review Letters 101, 96802 (2008).
96. Tan, Y.-W., et al. Temperature Dependent Electron Transport In Graphene. The European Physical Journal Special Topics 148, 15–18 (2007).
97. Zhu, W. et al. Carrier Scattering, Mobilities, And Electrostatic Potential In Monolayer, Bilayer, And Trilayer Graphene. Physical Review B 80, 235402 (2009).
98. Du, X. et al. Approaching Ballistic Transport In Suspended Graphene. Nature Nanotechnology 3, 491–5 (2008).
99. Kelly, B. T. T. Physics of Graphite. Journal of Nuclear Materials 114, 1983 (1983).
100. Du, X. et al. Metal-Insulator-Like Behavior In Semimetallic Bismuth And Graphite. Physical Review Letters 94, (2005).
101. Zhang, Y. et al. Fabrication And Electric-Field-Dependent Transport Measurements Of Mesoscopic Graphite Devices. Applied Physics Letters 86, 73104 (2005).

102. Joung, D. et al. Efros-Shklovskii Variable-Range Hopping In Reduced Graphene Oxide Sheets Of Varying Carbon Sp^2 Fraction. Physical Review B - Condensed Matter And Materials Physics 86, 235423 (2012).

103. Mohanty, N. et al. Nanotomy-Based Production Of Transferable And Dispersible Graphene Nanostructures Of Controlled Shape And Size. Nature Communications 3, 844 (2012).

Chapter 3 - Direct growth of hexagonal boron nitride on SiO_2 *via* low pressure chemical vapor deposition (LPCVD)

Abstract

Here, this chapter shows high quality, wafer-scale and uniform thin h-BN film synthesized directly on oxidized substrates *via* a novel boron-oxygen chemistry route for oxide-assisted nucleation (B/N atomic ratio = 1:1.16±0.03 and optical band gap = 5.51 eV). Due to low pressure (10 Torr), and high elevated temperature (1100°C), the h-BN growth is surface reaction limited, leading to the increase in ~6-fold smoothness in SiO_2/Si substrate, which underwent the same CVD condition. This study provides a route to realize van der Waals heterostructures based on h-BN dielectrics and their fundamental investigations. The heterostructures are devoid of wrinkles and adsorbates, which is critical for 2D nanoelectronics, as verified by the increase in electrical conductivity (5 times for MoS_2/h-BN). This versatile process provides an avenue to a variety of heterostructures with complex sandwiched 2D electronic circuitry.

Introduction

To enhance the intrinsic characteristics of van der Waals heterostructures for 2D nanoelectronics and thermionics, large-area, planar, dielectric substrate with ultra-flat, smooth surface, lateral continuity, and a structure free of dangling bonds and surface traps[1–3] are required. The ideal candidate, the hexagonal boron nitride (h-BN), possesses not only these properties, but also other superior properties: high thermal conductivity (2,000 W/mK)[4], large mechanical strength[5], high optical transparency[6], high chemical/temperature stability (up to 1000 °C)[7–9], deep ultraviolet emission[10], and thinnest tunneling junction[11]. H-BN, which is a single-atom-thick two-dimensional sheet of sp^2 hybridized boron and nitrogen atoms with a honeycomb lattice, is an

electronic insulator with large direct band gap (5.97 eV)[10] and a low dielectric constant (~ 4)[12]. A vast study has been made to synthesize h-BN on various metal catalytic surfaces (Cu[13], Ni[14], Co[15], Pt[16] and Cu-Ni alloy[17]) *via* chemical vapor deposition (CVD). However, these techniques require substrate unloading and additional wet/dry transfer processes; for example, a sacrificial polymer layer supports the h-BN film on metal, followed by metal etching and polymer/h-BN transfer to arbitrarily substrates. Due to the formation of tears, folds, wrinkles, and adsorption of polymeric impurities[18] , such transfer process is neither robust, nor reliable, and consistently degrades h-BN's structural properties

Here, we introduce a novel technique, which is an oxide-assisted growth of direct formation of large-area, continuous thin films of h-BN on Si-based dielectric (SiO_2 and Quartz) substrates *via* leveraging the boron/oxygen bond. This eliminates the need for a metal catalyst, substrate unloading from CVD, post-synthesis transfer steps, and the resultant polymer contamination. Furthermore, the grown h-BN substrates can be directly applied for realizing van der Waals heterostructures with transition metal dichalcogenides (TMDs), especially MoS_2. This intimately interfaced, van der Waal heterostructures (MoS_2/h-BN) fabricated through an all-CVD growth process benefits from: 1) ~6-fold reduction in roughness of h-BN film in comparison to SiO_2 substrate, 2) the absence of the external adsorbates at the surface and at the interface. Subsequently, these will lead to reduction in surface roughness scattering and charged impurity scattering, enhancing of intrinsic charge carrier mobility for MoS_2-hBN heterostructures, which is also critical for other 2D nanoelectronics, thermionics, and photonic applications. Therefore, the proposed versatile process can potentially be extrapolated to realize a variety of heterostructures with well-defined stacking for complex sandwiched 2D electronic circuitry.

Experimental Section

Procedure of h-BN growth on SiO_2/Si substrate *via* LPCVD

A low-pressure CVD (LPCVD) system was modified to adapt the solid vapor growth. Here the substrate was placed in a fused quartz tube (outside diameter of 1 inch), which is placed inside a split tube furnace. A separate heated chamber was connected to the inlet of the LPCVD, and employed for h-BN precursors: solid ammonia-borane (AB) (NH_3-BH_3) complex (**Figure 3.1a**). The substrates (SiO_2/Si and quartz) were cleaned using piranha solution for 2 hours (a volumetric mixture of 3:1 of 98% H_2SO_4 to 35% H_2O_2). After the piranha treatment, as shown in **Figure 3.1b** the treated substrates were directly placed in the center of quartz tube's heating zone and ramped to 1100 °C in 10 sccm H_2 (P_{Tot}=200 mtorr) to restrict further oxidation. After reaching 1100°C, the

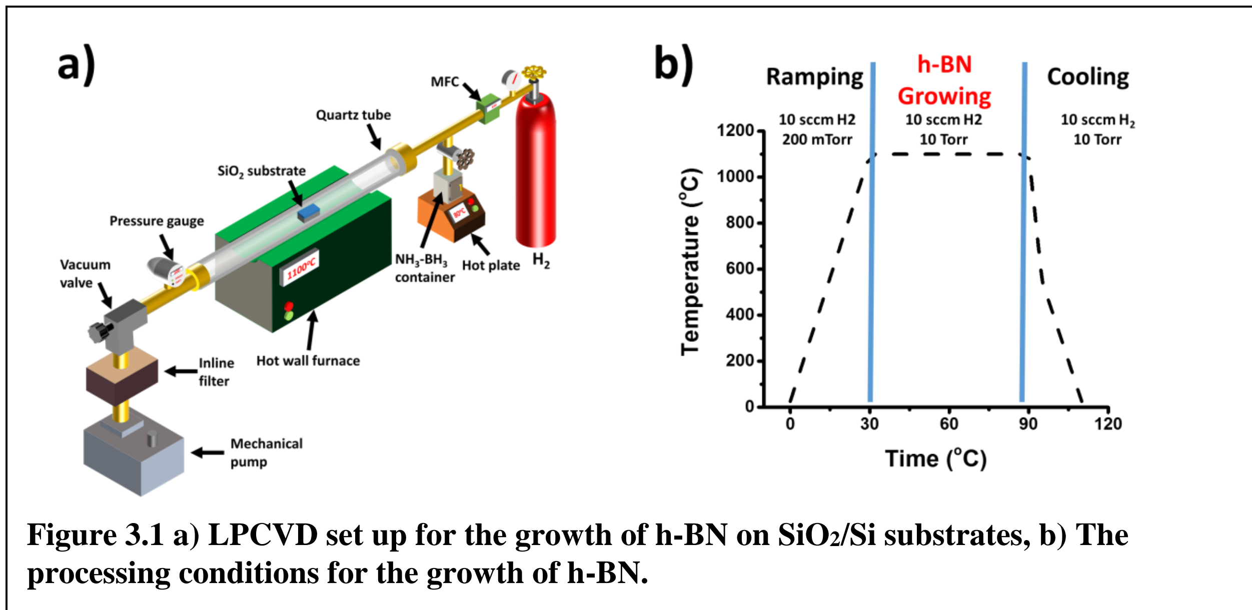

Figure 3.1 a) LPCVD set up for the growth of h-BN on SiO_2/Si substrates, b) The processing conditions for the growth of h-BN.

chamber containing AB was heated at ~ 100 °C to thermally decompose into H_2 gas, monomeric aminoborane (BH_2NH_2) and borazine ($(HBNH)_3$).[13] The gas mixture was transported to the chamber containing the substrate *via* supplied H_2 carrier gas. The h-BN synthesis takes place at a

pressure of 10 Torr and the reaction time was varied from 10 sec to 60 min followed by fast cooling (opening the furnace, ≈ 100 ^{0}C/min). Finally, the h-BN film is ready for further characterization.

Procedure of MoS_2 growth on h-BN *via* LPCVD

The split-tube 3-zone CVD furnace (MTI Corporation) was used for the synthesis of h-BN and large-area heterostructured films with MoS_2. The carrier gas is H_2 or Ar, or a combination of

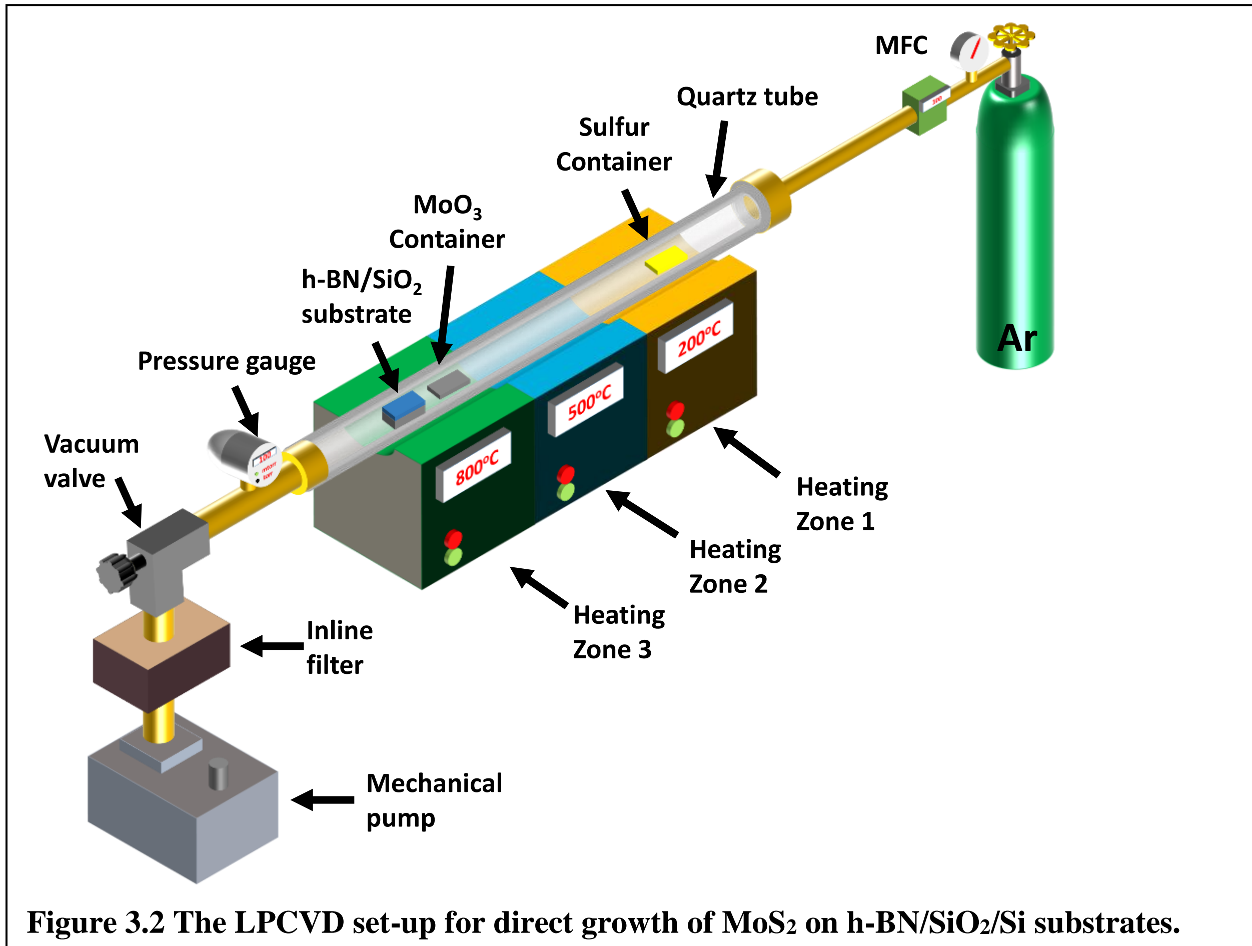

Figure 3.2 The LPCVD set-up for direct growth of MoS_2 on h-BN/SiO_2/Si substrates.

both. As shown in **Figure 3.2** the substrate (i.e. h-BN/SiO_2/Si and SiO_2/Si) is placed in the 3rd zone near the molybdenum oxide (MoO_3) powder. During the sulfurization process, samples were kept at 800 ^{o}C for 30 - 60 min under argon and/or hydrogen flow and maintaining a vacuum of 10 Torr. Sulfur (S) vapors were generated from S powders placed up-stream in a lower temperature region (250 ^{o}C) (the 1st zone). Finally, the MoS_2 film on hBN is ready for characterization.

Procedure for the fabrication of MoS_2/h-BN sample for I-V measurement

Similar to the fabrication of graphene field effect transistor described in chapter 2 (experimental section), the fabrication process is simplified as follows: After the synthesis of MoS_2 on SiO_2/Si or quartz substrates with and without h-BN, metal contact electrodes (Cr (15 nm)/Au (95 nm)) were deposited using e-beam evaporator. Then positive photoresist was spun onto the film, and developed. A metal etching procedure was performed to create the pattern.

Procedure to transfer hBN to TEM grid for selected area electron diffraction (SAED) characterization

The procedure here is similar to the transfer procedure described in chapter 2 (experimental section), which can be simplified as followed: After the synthesis of h-BN film on SiO_2/Si substrate, a layer of PMMA was spun onto the film *via* spin-coating. The underlying SiO_2/Si substrate can be etched either by 1% HF or 30% KOH for 8 h at room temperature. The PMMA/h-BN was picked up by the TEM grid from the water solution. After being dried overnight, the sample was drop-casted acetone, IPA for serval times to remove PMMA layers.

Instrumentations for chemical, physical and electrical characterization

Confocal Raman spectroscopy system

The data for Raman spectroscopy was obtained using WITEC Confocal Raman Alpha 300-RA, with a laser excitation wavelength of 532 nm (power of 17 mW), a laser spot size of 360 nm, and a pinhole of 100 μm. A thermoelectrically cooled CCD Camera (ANDOR iDUS DV401A-BV-352) (-65°C) was used to detect Raman signal. The focal length of UHTS 300 VIS spectrometer is 300 mm. The 100X objective (NA =0.9), and 600 l/mm grating were used to examine all h-BN and MoS_2 samples. The SiO_2/Si substrate (~520 cm^{-1}) was used as a reference

to calibrate the Raman instrument. The intensity mapping was collected with the resolution of 512x512 (pixel x pixel), and the integration time of 0.5 s/pixel.

Selected area electron diffraction (SAED) measurement *via* transmission electron microscope (TEM)

The SAED pattern was collected using JEOL JEM-3010 TEM. The acceleration voltage (300 kV) was generated from LaB6 electron source. Images were collected using a Gatan Orius SC200 CCD camera, which is connected to a computer running Digital Micrograph software.

X-ray photoelectron spectroscopy (XPS) system

XPS data were recorded with a Kratos AXIS-165 spectrometer using acrochromatic Al Kα radiation (1486.6 eV). Analysis was carried out under a vacuum less than 5×10^{-10} Torr. The XPS binding energies were measured with a precision of 0.1 eV. The analyzer pass energy was set to 80 eV. Furthermore the contact time was 500 ms, and the area scanned was 5 mm^2. Spectra were referenced to C1s peak at 284.5 eV.

X-ray powder diffraction (XRD) system

The h-BN/SiO_2 sample was placed on standard holder inside Siemens / Bruker D5000 powder diffractometer, which is a wild angle XRD (20°-90°). The X-ray source is Cu K-alpha (λ=0.154 nm).

UV-Vis system for optical band-gap characterization

The h-BN/quartz sample was placed on the sample holder as shown in **Figure 3.3.** The absorbance data was recorded using Newport 818-UV calibrated photodiode sensor (range of detection is 200 nm to 300 nm), which was connected to Keithley 2612 dual-channel system. A monochromator (Oriel Cornerstone 130 1/8 m) and Keithley 26112 dual-channel system were

connected to computer *via* a GPIB/IEEE-488 interface card. The absorbance (α) was calculated using the following expression:

$$\alpha = \left|\frac{I_{h-BN}-I_{quartz}}{I_{quartz}}\right| \quad \textbf{Equation 3.1}$$

where $I_{h\text{-}BN}$ is the measured current of h-BN/quartz sample and I_{quartz} is the measured current of reference sample, i.e. quartz substrate.

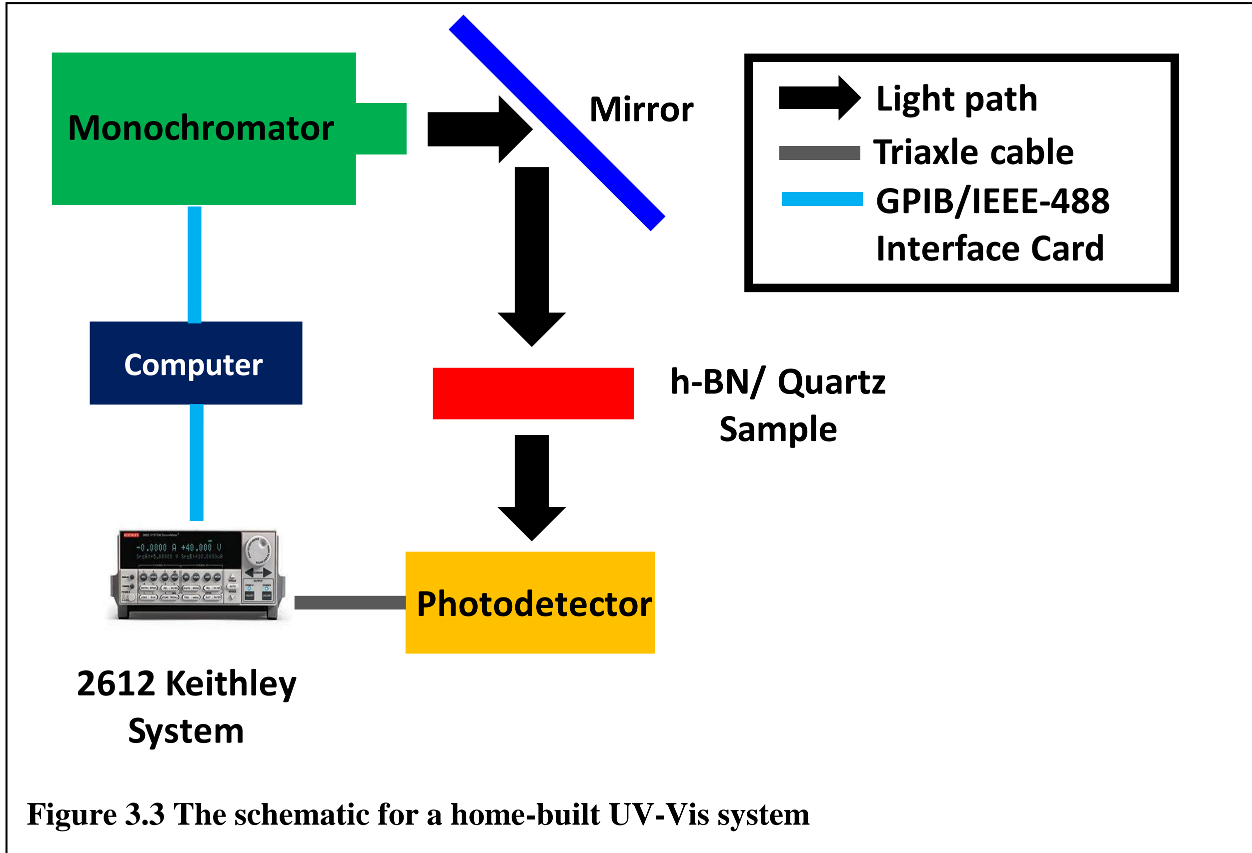

Figure 3.3 The schematic for a home-built UV-Vis system

Cryostat electrical system

The electrical measurements of MoS_2/h-BN and MoS2/SiO_2 samples were carried out in ARS closed cycle cryogenic probe station, which can provide high vacuum (<5 × 10^{-6} Torr). Lakeshore temperature controller (model 336) control the temperature of the samples. The I-V measurement was performed by varying the voltage source and measuring the change in

conductivity. The Keithley 2612 dual-channel system source meter connected to a computer *via* a GPIB/IEEE-488 interface card.

Results and Discussion

H-BN growth mechanism

As shown in **Figure 3.4**, the growth of h-BN can be described by following seven elementary steps: (1) At 100 ^{o}C, the solid AB complex is sublimed into gaseous phase and carried into reaction zone by H_2 gas. (2) Before reaching the 1100 ^{o}C zone, the AB complex is thermally decomposed into H_2, aminoborane (BH_2NH_2) and borazine ($B_3H_6N_3$)[19,20].(3) At a temperature of 1100 °C, ($B_3H_6N_3$) and (BH_2NH_2) molecules further dissociate into $(BN)_xH_y$ radicals, which (4) adsorb and diffuse along the SiO_2 surface). (5) The $(BN)_xH_y$ starts the nucleation of h-BN domain by binding at the oxygen dangling bond of SiO_2. (6) If the rate of attachment of $(BN)_xH_y$ radicals at the edge of h-BN domain is higher than the rate of their detachments, then the h-BN domains start to expand into continuous h-BN sheet. (7) The byproduct H_2 is desorbed from the surface of h-BN, and transported to the bulk gas.

The formation mechanism of the h-BN films on SiO_2/Si substrates can be understood *via* vapor-solid-solid growth mechanism[21,22]. Furthermore, CVD growth of h-BN is influenced by the role of kinetic factors i.e. the relative magnitude of the mass transport coefficients (h_g) and surface reaction constants (K_s)[22,23]. Hence the process can be classified into two regimes: mass transport region, which involves diffusion through boundary layers, and surface reaction step. These two types of fluxes co-exist in series:

(1) Flux of the radicals through boundary layer,

$$F_{mass\ transport} = h_g (C_g - C_S) \quad \textbf{Equation 3.2}$$

where h_g is mass transfer coefficient, C_g is the concentration of gas in the bulk, and C_S is the concentration of the radicals at the surface.

(2) Flux of consuming radicals at the surface.

$$F_{Surface\ reaction} = K_S C_S^n \quad \text{Equation 3.3}$$

where K_S is surface reaction constant and n is the order of reaction (assuming to be 1). The slower flux will be considered as rate limiting step. At steady state, the total flux F_{Total} equals to $F_{mass\ transport}$, and also equals to $F_{Surface\ reaction}$. The growth of h-BN film with a uniform thickness occurs when $h_g >> K_s$ (surface reaction controlled region), while the growth of thickness non-uniform thick film occurs when $h_g << K_s$ (mass transport limited region).

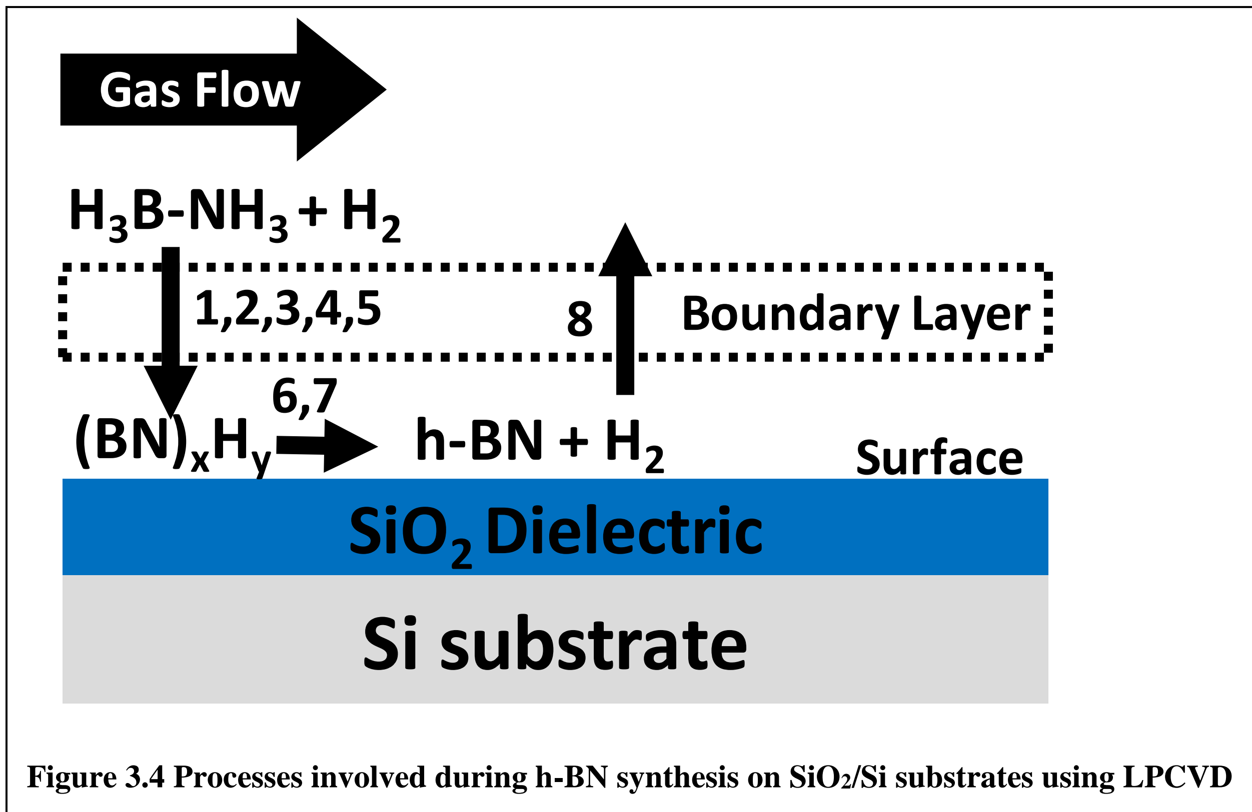

Figure 3.4 Processes involved during h-BN synthesis on SiO_2/Si substrates using LPCVD

In our proposed growth, the rate limiting step is the surface reaction step, due to these following evidence. (1) The grown h-BN film is uniform and smooth (as shown later in **Figure 3.8**). (2) Surface oxygen in Cu favors the h-BN growth as it facilitates dissociation of the precursor

gas and enhances the dehydrogenation process along the edges of the h-BN domains[24]. (3) Furthermore, for carbon nanotube and graphene synthesis the oxygen-aided growth is a surface deposition process with a low reaction rate[21,22]. (4) The SiO_2/Si surface is suspected to possess relatively low value of K_s[22] which may enable large-area uniform growth of h-BN sheet. (5) In addition, the flux of the radicals through boundary layer can be described by Fick's first law of diffusion as shown:

$$F_{\text{mass transport}} = h_g (C_g - C_S) = -D_g \nabla C = D_g (C_g - C_S)/\delta$$

$$\Leftrightarrow h_g = D_g/\delta \quad \textbf{Equation 3.4}$$

where D_g is diffusivity factor, and δ is the boundary layer thickness. Hence, the mass transport coefficient (h_g) can be further defined by the ratio of diffusivity factor (D_g) and thickness of boundary layer (δ). At low pressure operation, the collision of the active precursors is less, leading to a higher diffusivity factor ($D_g \propto 1/(\text{total pressure})$). In spite of the increase in the thickness of boundary layer at low pressure, the increase of D_g is much higher. Consequently, mass transport coefficient, h_g is high at low pressure, leading to enhance diffusion of the precursors through the boundary, making surface reaction the rate limiting step (as shown in equation 3.3). The oxygen-assisted nucleation of h-BN film is also apparent from the XPS spectra for B 1s, which is described next. The edge-attachment and lattice integration involves dehydrogenation at domain edges, the edge-attachment barrier is effectively reduced due to the strong binding energy between B and O.

The growth mechanism further is analyzed *via* the bonding state and the elemental composition of boron (B), oxygen (O), and nitrogen (N), which is obtained from XPS. The spectrum of each element is fit with Gaussian curve. As shown in **Figure 3.5a**, the B 1s spectrum is composed of two peaks at binding energy (BE) ~ 190.53 eV and ~ 191.59 eV, which are corresponding to B-N[25,26] and O-B-N[27,28] bonding, respectively. Furthermore, the convoluted peaks of the O 1s spectrum at 532.39 eV which is due to Si-O-Si binding and at 533.34 eV which

is to O-B-N binding[29]. In addition, another minor peak appears at 530.08 eV, which can be attributed to the adsorbed oxygen from the atmosphere. On the other hand, the spectrum of N 1s peak can be fit with only one Gaussian curve (centered at BE ~ 398.13 eV), which represents the N-B bonding[25,26] (**Figure 3.5c**). These evidences propose that the O of SiO_2 substrate act as nucleation sites for B of $(BN)_xH_y$ radical, which continues to connect to the adjacent of $(BN)_xH_y$ radical to form a uniform, and continuous h-BN film. Furthermore, as shown in **Figure 3.5b** the B-O peaks imply the presence of boron terminated edge of hBN film binding to SiO_2/Si substrate, where B is bound to O and possibly two Ns. The elemental stoichiometric analysis confirms the chemical composition of h-BN with an almost equal composition of B and N elements: B/N ratio = 1:1.16±0.03.

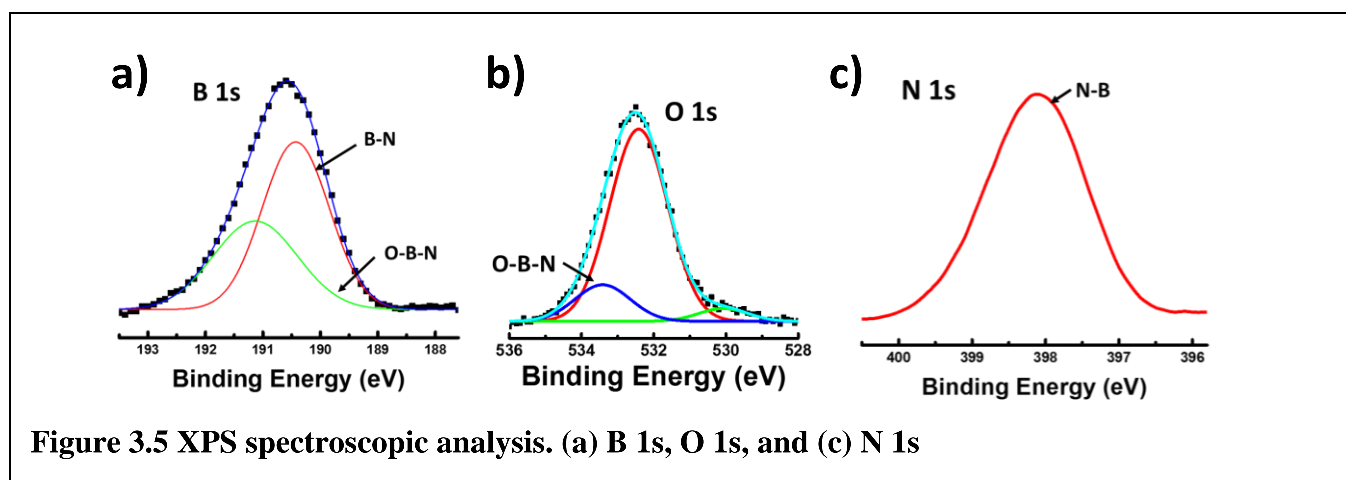

Figure 3.5 XPS spectroscopic analysis. (a) B 1s, O 1s, and (c) N 1s

Growth of the h-BN film on Si (the control experiment)

In order to confirm the importance of the oxide group on the surface, a silicon (Si) was placed inside the LPCVD, and underwent the same condition. The Raman spectrum and optical microscopic image for the post h-BN growth Si surface are shown in **Figure 3.6a-b**. As expected, there is no Raman signature of h-BN film or island on the surface of Si substrate.

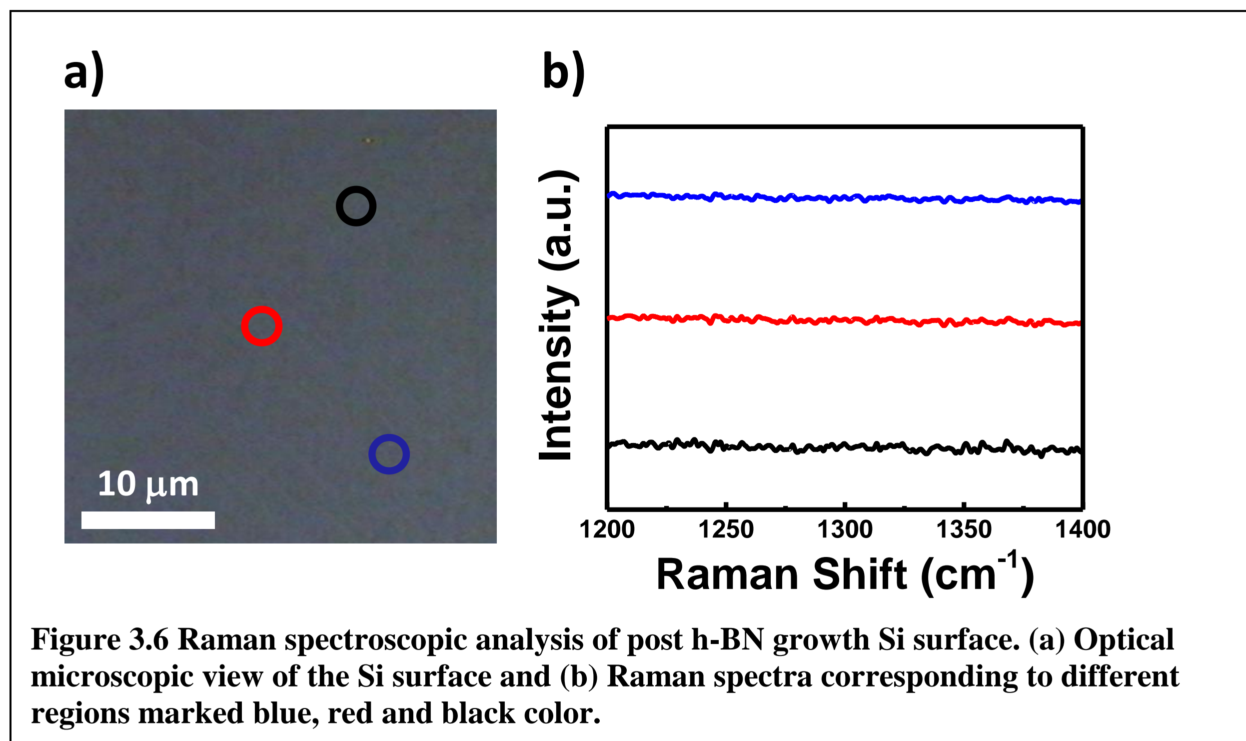

Figure 3.6 Raman spectroscopic analysis of post h-BN growth Si surface. (a) Optical microscopic view of the Si surface and (b) Raman spectra corresponding to different regions marked blue, red and black color.

Structural characterization of the h-BN film

The quality and uniformity of the grown h-BN film formed on SiO_2/Si substrates is characterized by Raman spectroscopy. The h-BN Raman signature peaks occurs at ≈ 1368 - 1370 cm^{-1} corresponding to E_{2g} phonon vibration represented in **Figure 3.7a**. The Raman spectral position mapping is presented in **Figure 3.7b** with the regions marked blue, red and black circle corresponds to Raman spectra in **Figure 3.7c**, and to the areas of optical image in inset of **Figure 3.7a**. The homogeneous color contrast of the optical image, and the Raman position mapping of E_{2g} peak, and the Raman intensity mapping of E_{2g} peak clearly show a continuous, and uniform h-BN film formation on SiO_2/Si substrate. In 1-minute growth, the-BN thickness is 7 nm as shown in **Figure 3.7d**. In our study, the Raman E_{2g} peak position shifts to higher frequency which could be attributed to 1) the formation of surface induced stress in the h-BN films[30][31]and 2) the adsorption/ binding of oxygen impurities in the grain boundaries (B dangling bond) of h-BN film

during the CVD growth, which is also suggested by XPS data (discussed above). Furthermore the average FWHM (~65 cm^{-1}) of the E_{2g} peak corresponds to crystal domain size (L_a) of ~2.5 nm through the following relationship[32]:

$$L_a(\text{Å}) = {}^{1417}\!/_{(FWHM - 8.7)} \quad \textbf{Equation 3.5}$$

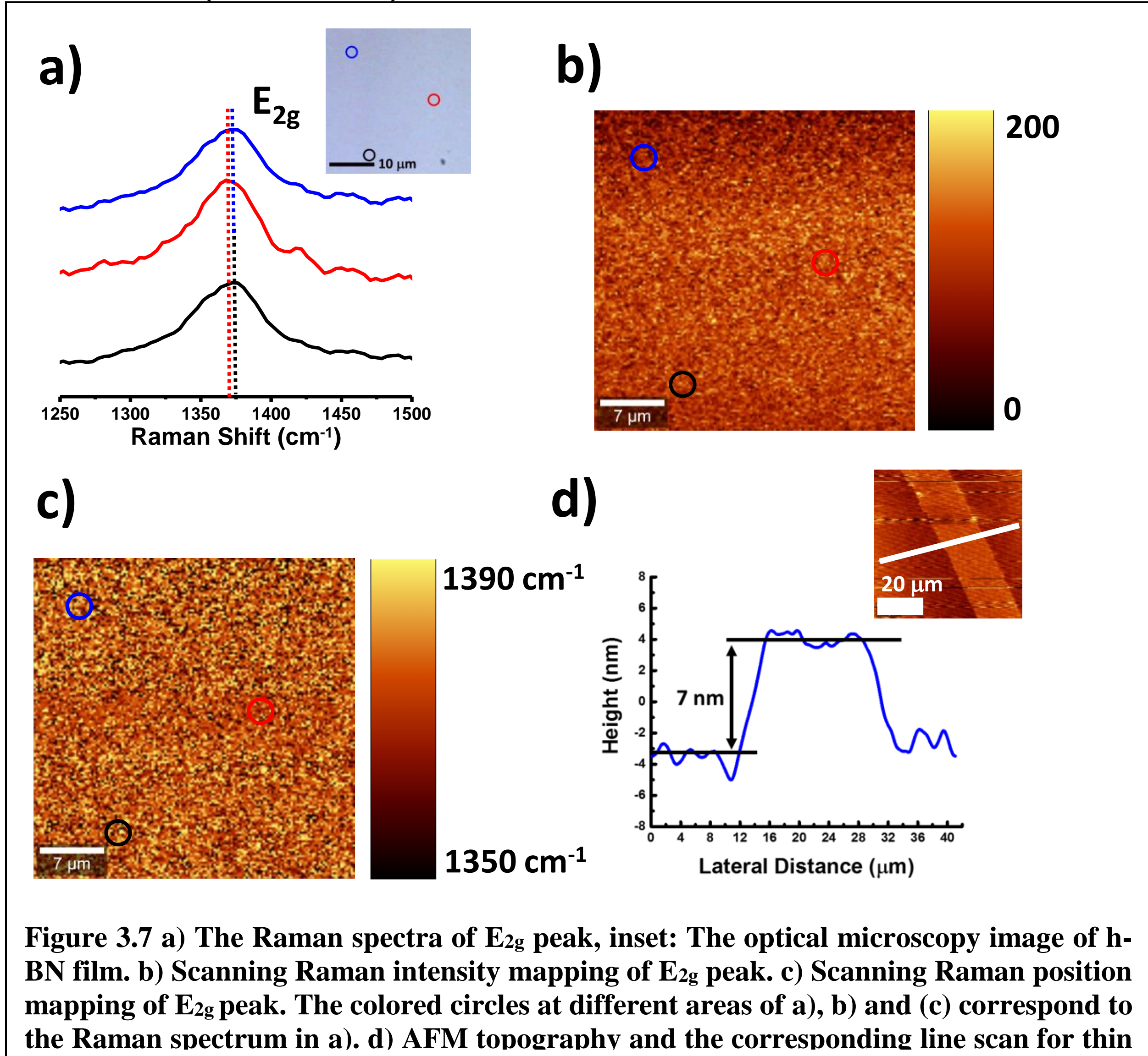

Figure 3.7 a) The Raman spectra of E_{2g} peak, inset: The optical microscopy image of h-BN film. b) Scanning Raman intensity mapping of E_{2g} peak. c) Scanning Raman position mapping of E_{2g} peak. The colored circles at different areas of a), b) and (c) correspond to the Raman spectrum in a). d) AFM topography and the corresponding line scan for thin

Due to a planar sp^2 hybridized bonds and weak out-of-plane van der Waals bonds, the h-BN possesses to a smooth surface, and a decreased density of absorbed impurities. **Figure 3.8a** presents the surface morphology for SiO_2/Si substrate and h-BN thin film grown on SiO_2/Si. Both

samples went under the same CVD process, consisting low pressure (10 Torr) and thermal treatment (1100ºC). The smoothness is depicted by the roughness histograms fitted by Gaussian distributions with roughness of 1.37 nm for the h-BN modified SiO_2/Si surface and 8.59 nm for the SiO_2/Si surface (~6-fold increase) as shown in **Figure 3.8b**. Furthermore, it is noted that wrinkle

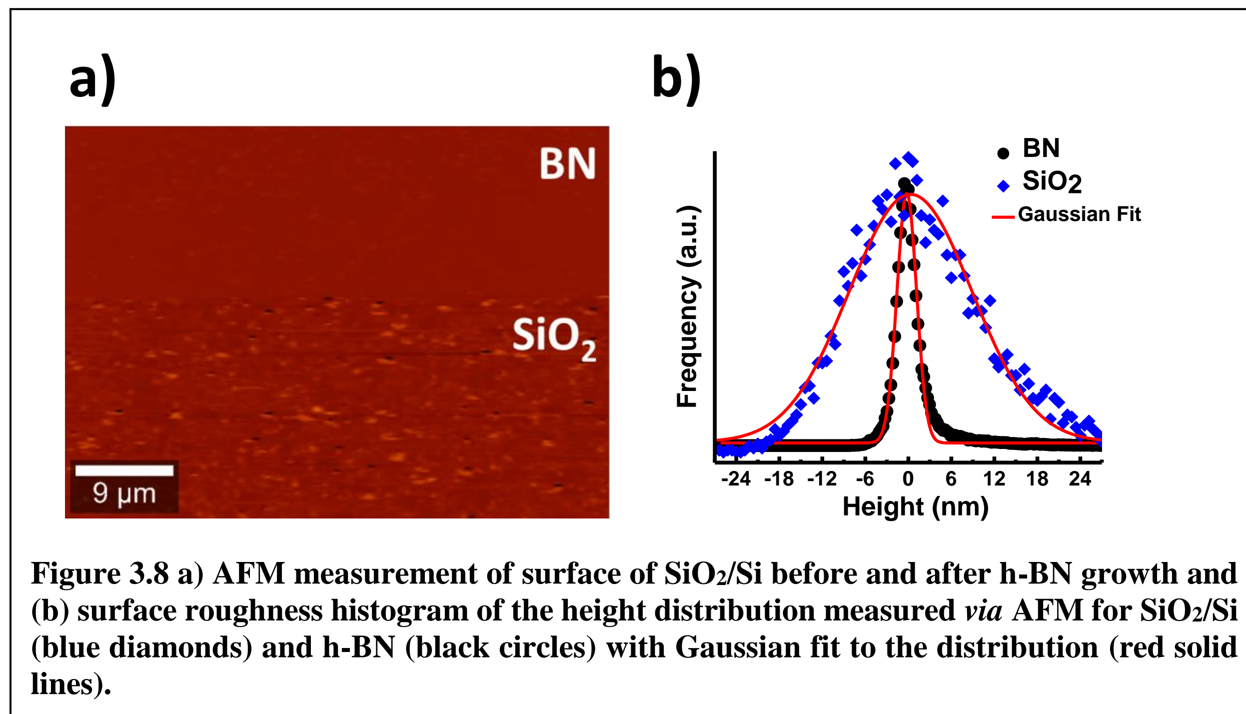

Figure 3.8 a) AFM measurement of surface of SiO_2/Si before and after h-BN growth and (b) surface roughness histogram of the height distribution measured *via* AFM for SiO_2/Si (blue diamonds) and h-BN (black circles) with Gaussian fit to the distribution (red solid lines).

like formation could not be found in our sample. In addition, because of its high energy surface optical phonon modes, the h-BN film reduces electronic scattering from electron–phonon interactions, which makes it an ideal substrate for thin 2D nanomaterials in electronic, and photonic applications[3].

Selective area electron diffraction (SAED) is employed to obtain the h-BN film's crystalline structure (as shown in **Figure 3.9a**). The six-fold symmetry is clearly found, indicating crystalline nature, and the hexagonal structure characteristic of the grown film. Due to lip-lip interaction between neighboring hBN layers[33], the h-BN layers are stacking in A-A structure. In addition, X-

ray diffraction (XRD) of h-BN film on SiO_2/Si substrate is displayed in **Figure 3.9b**, which clearly indicates the majority of crystal orientation are in the direction of (002) centered at $2\theta=24^{o}$[34]. According to Bragg's law, the estimated interlayer spacing ($2d\sin(\theta)=n\lambda$) is 0.37 nm for h-BN, which is closed to other studies[35,36].

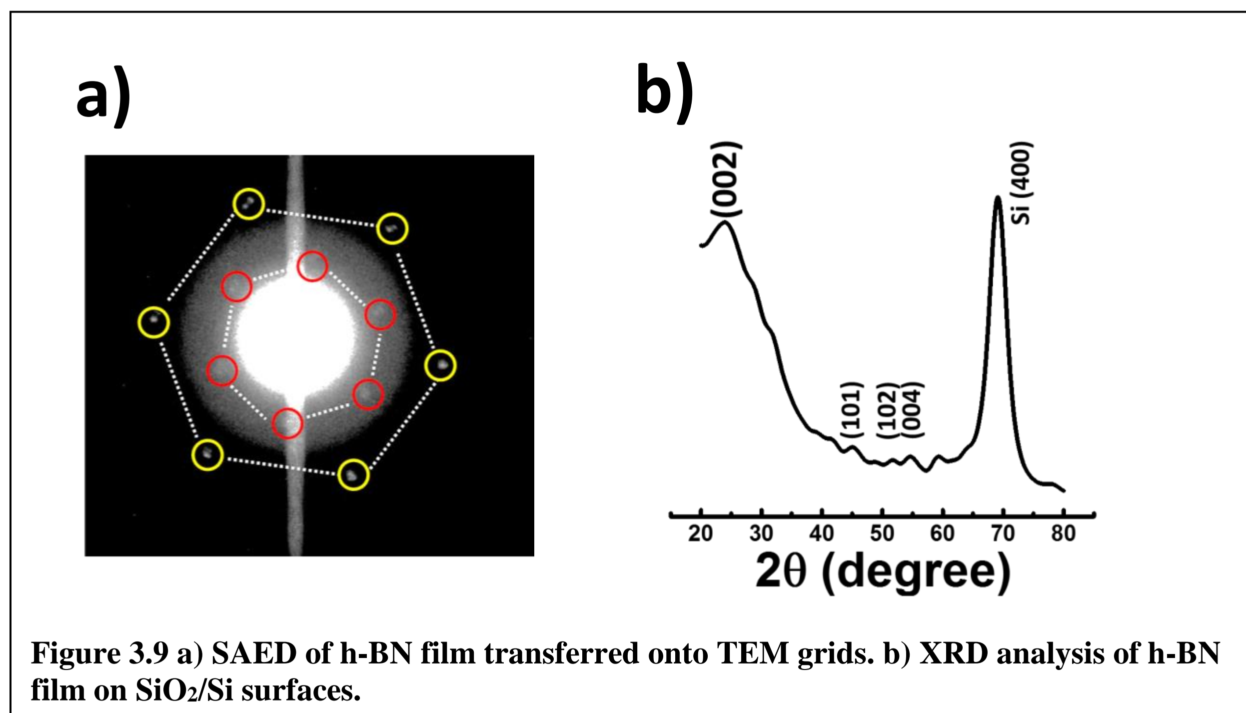

Figure 3.9 a) SAED of h-BN film transferred onto TEM grids. b) XRD analysis of h-BN film on SiO_2/Si surfaces.

Optical band gap analysis of the h-BN film

A large-area h-BN film was synthesized directly onto a quartz slide (2 cm x 1.5 cm area) *via* the same CVD process as performed for SiO_2/Si substrates (**Figure 3.10a**). The corresponding Raman peak of the grown h-BN is centered at ~1371 cm^{-1}, indicating the multi-layer structure as shown in **Figure 3.10b**. Furthermore, the UV-visible absorption spectrum of the h-BN/quartz film

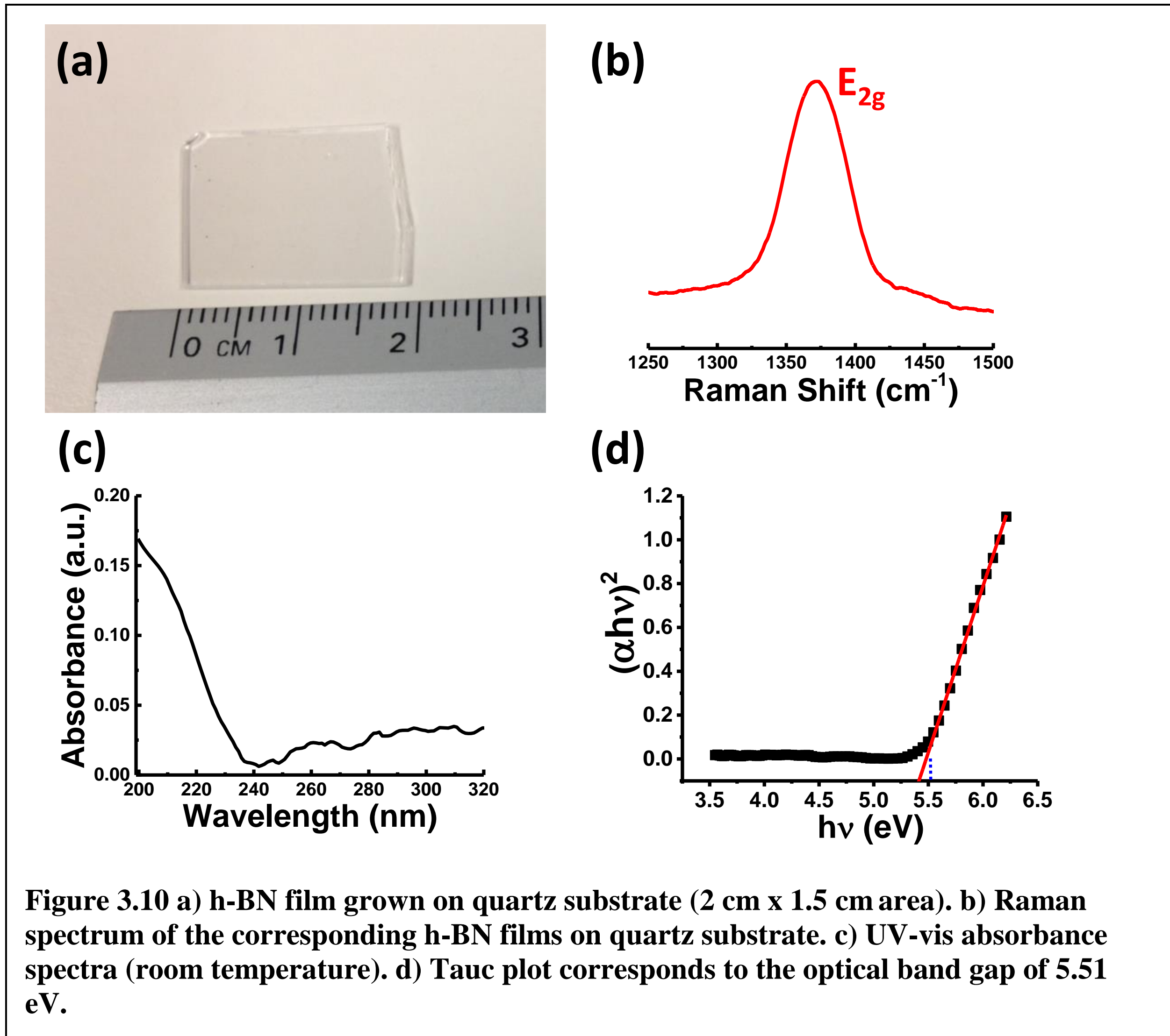

Figure 3.10 a) h-BN film grown on quartz substrate (2 cm x 1.5 cm area). b) Raman spectrum of the corresponding h-BN films on quartz substrate. c) UV-vis absorbance spectra (room temperature). d) Tauc plot corresponds to the optical band gap of 5.51 eV.

was obtained in order to evaluate the h-BN's optical energy gap based on its optically induced band transition. Despite being debated, our grown h-BN film is assumed to have indirect bandgap. Hence, the following Tauc's equation was used to determine the optical band gap E_g[37],

$$\alpha h\nu = A(\mathrm{h\nu} - \mathrm{E}_g)^{\frac{1}{2}} \quad \textbf{Equation 3.6}$$

where α is the optical absorbance obtained in 200 nm to 350 nm range, hν is the energy of incident photon, A is the proportionality constant and E_g is the optical energy band gap. The quartz background was subtracted using a blank quartz as the h-BN film is directly on the quartz surface.

Figure 3.10c shows the absorption spectrum of h-BN film on quartz substrate. On the basis of Tauc's formulation in equation 3.4, the linear relationship of $(\alpha h\nu)^2$ and $h\nu$ should be a straight line at the absorption range, and the intersection point with the hν-axis is the optical energy band gap, E_g as shown in **Figure 3.10d**. The estimated optical band gap is 5.51 eV, matching with previous report[26]. The theoretical calculations predict the energy band gap for single layer h-BN film to be 6 eV[38,39] because the equivalent bands do not cross each other. Furthermore, direct bandgap of h-BN crystal was reported with the band energy of ~5.9 eV[40–43]. The low optical band gap energy could be explained due to defects[44–46] causing by oxygen impurities in our grown h-BN film (previously discussed in XPS data).

Structural characterization of the MoS_2 grown on h-BN film

Recent reports indicate dramatic improvement in optical and electronic properties of TMD[47,48] layers stacked on h-BN dielectrics[49,50]. A substantial amount of previous work reports on mechanical exfoliation of at least one of the TMDs or h-BN materials to form both the lateral and vertical heterostructures[49,51,52]. In order to leverage the potential of our direct grown h-BN film, heterostructured films with MoS_2 is fabricated and characterized. The right inset of **Figure 3.11a** shows the optical image of synthesized MoS_2 surface.

Raman spectroscopy is a commanding technique to determine the presence of MoS_2 and its thickness through the measurement of E^1_{2g} and A_{1g} peak positions and their frequency difference[53]. In **Figure 3.11a**, E^1_{2g} and A_{1g} peaks of MoS_2 grown on h-BN are centered at ∼375.6 and ∼401.5 cm^{-1}, respectively. The E^1_{2g} mode represents the in-plane vibration (S atoms in opposite direction

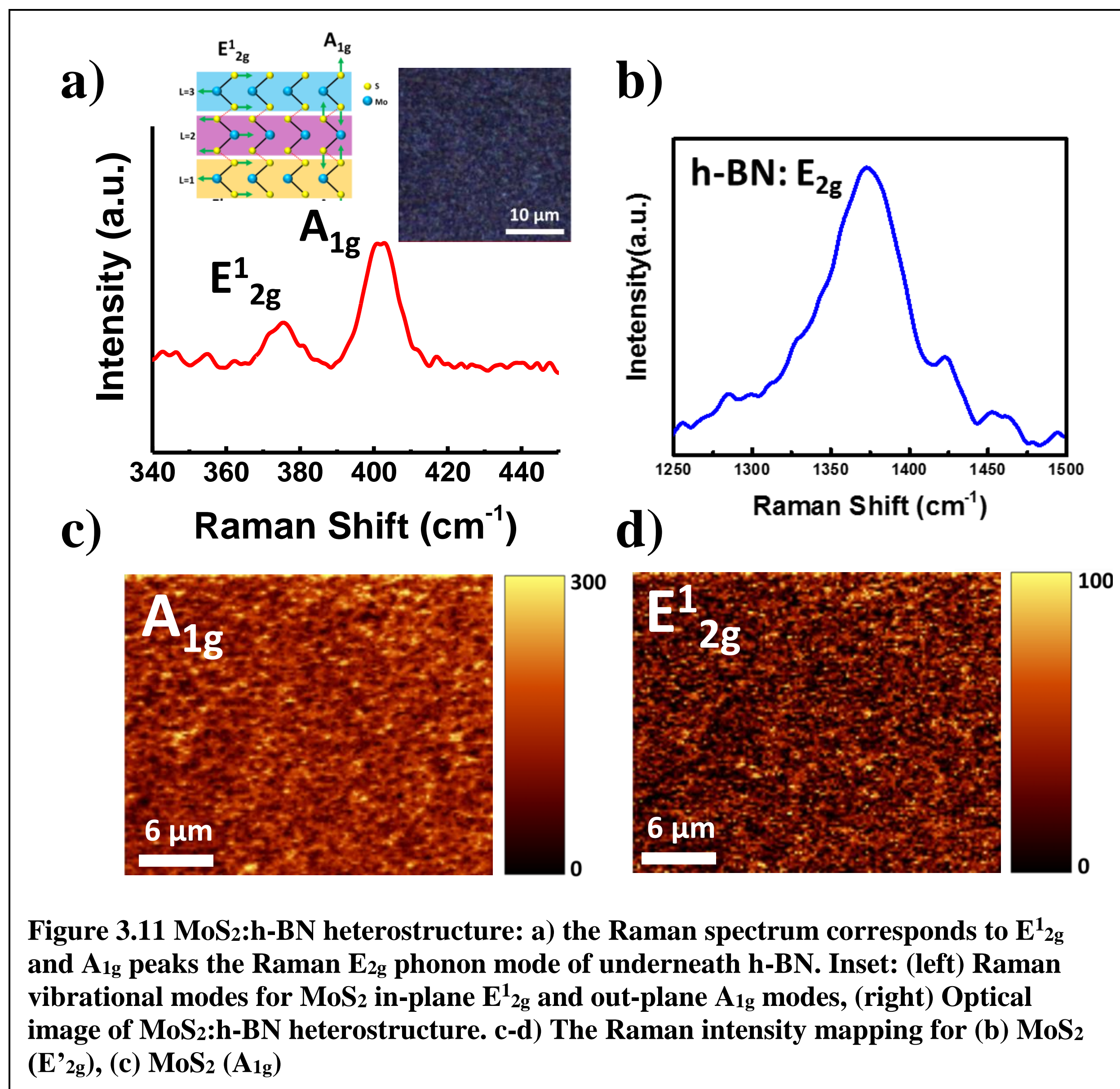

Figure 3.11 MoS_2:h-BN heterostructure: a) the Raman spectrum corresponds to E^1_{2g} and A_{1g} peaks the Raman E_{2g} phonon mode of underneath h-BN. Inset: (left) Raman vibrational modes for MoS_2 in-plane E^1_{2g} and out-plane A_{1g} modes, (right) Optical image of MoS_2:h-BN heterostructure. c-d) The Raman intensity mapping for (b) MoS_2 (E'_{2g}), (c) MoS_2 (A_{1g})

to the Mo atom), while the A_{1g} mode is related to the out-of-plane vibration (S atoms in opposite directions) (left inset of **Figure 3.11a**)[54]. The corresponding Raman mapping of E^1_{2g} and A_{1g} peaks indicates the MoS_2 formed over the entire surface of h-BN/SiO_2/Si substrate as shown in **Figure 3.11c-d**. The difference between E^1_{2g} and A_{1g} peaks are ~ 26 cm^{-1}, implying multilayer structure[55]. Furthermore, **Figure 3.11b** shows that the intensity of the h-BN peak (~1368 cm^{-1}) corresponds well with the MoS_2 peak intensities (i.e. the relative intensity of h-BN [E_{2g}] peak to

MoS_2 [A_{1g}] peak or [E^1_{2g}] peak remains constant through-out the Raman scanning area). Since the peak intensity is sensitive to the distance from the focal plane of the laser, this implies that the general distance between h-BN and the MoS_2 layers is consistent and thus governed by van der Waals interaction. Furthermore, the h-BN peak positions do not change after synthesis, which implies that the layers are expected to be electronically isolated.

The chemical composition of MoS_2 on h-BN was confirmed *via* XPS. **Figure 3.12a** shows the Mo 3d peaks at 229 eV and 232 eV corresponds to $3d_{5/2}$ and $3d_{3/2}$, respectively, whereas the S 2s peaks appears at 226 eV. The S $2p_{3/2}$ and S $2p_{1/2}$ peaks appear at 161.5 and 163 eV, respectively

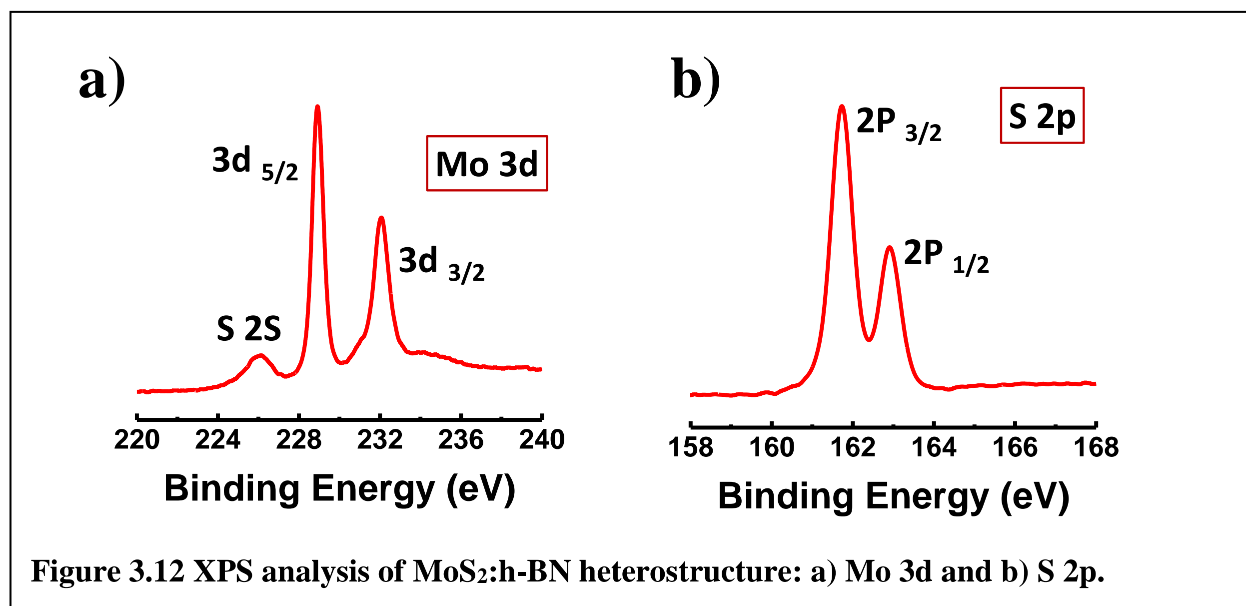

Figure 3.12 XPS analysis of MoS_2:h-BN heterostructure: a) Mo 3d and b) S 2p.

as displayed in **Figure 3.12b**. These are consistent with the peak positions from literature[56]. There is no evidence of bonding between h-BN and MoS_2 which further confirm electronic isolation between two layers. This is also attributed to the thermal stability of h-BN during the growth process.

Electrical analysis of the MoS_2 grown on h-BN film

The photoluminescence (PL) of direct growth MoS_2 on h-BN and SiO_2 samples were investigated by using 532 nm laser excitation. As bulk MoS_2 thinned to monolayer MoS_2, the indirect band gap increases, while the direct excitonic band structure at K point does not alter. Hence, the direct transition becomes more favorable, leading to a stronger photoluminescence signal in monolayer and few layer MoS_2, than in bulk MoS_2[57]. The PL spectrum comprises of the A peak, corresponding to neutral exciton emission from the direct transition at the K point and the B peak, corresponding to the exciton emission from another direct transition between the conduction and valence band[57]. The peaks were fit with Lorentzian curve. **Figure 3.13a-b** shows two pronounced PL peaks located at 1.85 eV (A) and 2.01 eV (B), which are in good agreement with the previous report[51] for both MoS_2 on SiO_2/Si substrate and that on h-BN/SiO_2/Si substrate.

The influence of h-BN on the electrical property of MoS_2 was characterized through current-voltage (I-V) measurements of MoS_2/h-BN sample as shown in the **Figure 3.13b**. The conductivity can be expressed as $\sigma = q\mu_p p + q\mu_n n$, where q is the elementary charge, μ_p, μ_n are hole and electron mobilities, and p, n are hole and electron concentrations. Since, these MoS_2 is n-type due to the pinning of the conduction band close to the Fermi level of metal contacts, this equation becomes: $\sigma = q\mu_n n$. Furthermore, MoS_2 on both h-BN sample and SiO_2 were grown in the same CVD tube (i.e. same process conditions) and the growth mechanism of MoS_2 film is similar to physical deposition (surface independent process), the thickness of MoS_2 on both sample are assumed to be similar. Furthermore, when the MoS_2 layers are placed on SiO_2 surfaces, these films are unintentionally negatively doped due to high level of trapped donors[58,59]. Hence, the electron concentration (n) in MoS_2/SiO_2 heterostructure is expected to be higher than on h-BN. On the other hand, placing MoS_2 layer on h-BN surfaces, provide an electronically clean platform with

limited doping as h-BN lacks trap charges. However, our results show that the current (I) of MoS_2/h-BN are 5 times higher than MoS_2/SiO_2. Since the electron density on h-BN is expected to decrease, the increase in total conductivity of MoS_2/h-BN implies an enhanced electron mobility (μ_n), attributed to the smooth h-BN substrate and reduced charged impurity scattering. This conclusively indicates that h-BN enhances the carrier/phonon transport in the interfaced MoS_2, and also potentially in graphene as shown in previous work[3].

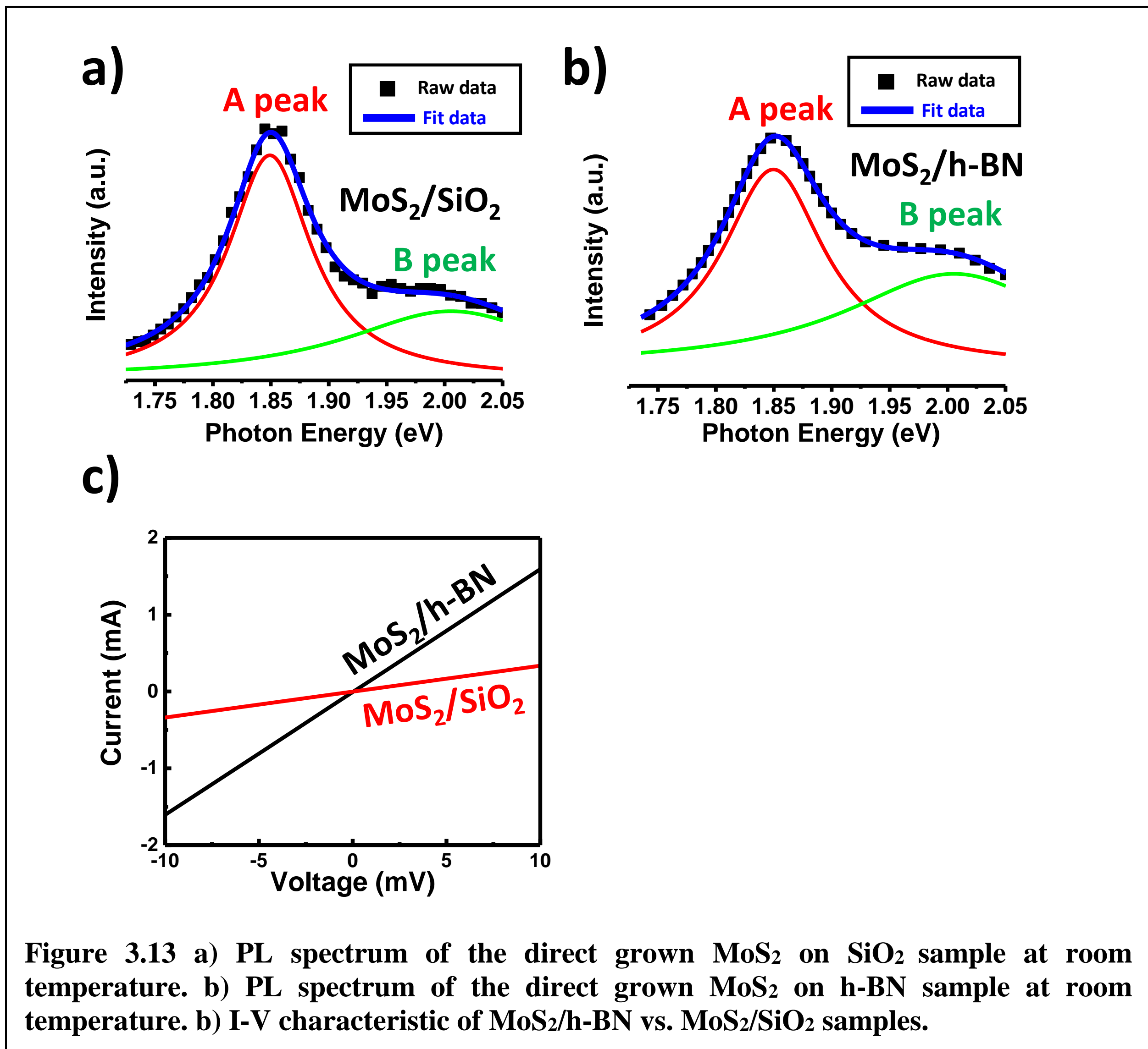

Figure 3.13 a) PL spectrum of the direct grown MoS_2 on SiO_2 sample at room temperature. b) PL spectrum of the direct grown MoS_2 on h-BN sample at room temperature. b) I-V characteristic of MoS_2/h-BN vs. MoS_2/SiO_2 samples.

Conclusion

In conclusion, this chapter demonstrate a facile, and robust method to grow uniform, large scale, controllable thickness of h-BN films on SiO_2 and quartz substrates. Such manufacturability will benefit several electronic, photonic, composite, and mechanical applications. This chapter also provide the details of the growth mechanism, where the oxygen on these surfaces binds with boron to produce nucleation sites for oxide-assisted growth of large-area and continuous films of h-BN. The nucleation density and domain sizes are highly dependent on the surface morphology and oxygen content. In addition, due to the increased surface oxygen on the SiO_2/Si and the strong binding between B and O, the edge-attachment energy barrier is reduced. Furthermore, the large-area, van der Waals bound, and electronically isolated MoS_2 heterostructures with h-BN were also grown. The grown h-BN has consistently exhibited its use for enhancing carrier mobility for electronic 2D nanomaterials by bringing electronic-isolation and providing ultra-smoothness platform. The results from this work provide avenue for large-area, scalable, directly-grown, contamination free, transfer/unloading free and heterostructure-ready h-BN, which is vital for high-performance 2D nanoelectronics, optoelectronics and nanothermionics, currently limited by physically exfoliated h-BN flakes or transferred h-BN. Furthermore, the atomically-precise placement achieved here can be extended to produce complex sandwiched and lateral architectures for ultrathin integrated 2D-circuitries.

Acknowledgements

The financial supports from National Science Foundation (Grants: CMMI-1503681 and CMMI-1030963) and University of Illinois at Chicago were acknowledged. This work made use of instruments in the Electron Microscopy Service (Research Resources Center, UIC). Donovan Briggs, Shikai Deng and Leonardo Marques were acknowledged for the valuable discussions on

MoS_2 growth. VB thank Prof. C. G. Takoudis and Mr. Arghya Bishal for help with the contact angle measurements.

References

1. Geim, A. K. et al. Van Der Waals Heterostructures. Nature 499, 419–25 (2013).
2. Qi, Z. J. et al. Electronic Transport In Heterostructures Of Chemical Vapor Deposited Graphene And Hexagonal Boron Nitride. Small 11, 1402–1408 (2015).
3. Dean, C. R. et al. Boron Nitride Substrates For High-Quality Graphene Electronics. Nature Nanotechnology 5, 722–726 (2010).
4. Tao, O. et al. Thermal Transport In Hexagonal Boron Nitride Nanoribbons. Nanotechnology 21, 245701 (2010).
5. Zhi, C. et al. Large-Scale Fabrication Of Boron Nitride Nanosheets And Their Utilization In Polymeric Composites With Improved Thermal And Mechanical Properties. Advanced Materials 21, 2889–2893 (2009).
6. Tamor, M. A. et al. Method Of Making Hard, Transparent Amorphous Hydrogenated Boron Nitride Films. U.S. Patent 5518780 A (1996).
7. Chen, Y. et al. Boron Nitride Nanotubes: Pronounced Resistance to Oxidation. Applied Physics Letters 84, 2430 (2004).
8. Liu, Z. et al. Ultrathin High-Temperature Oxidation-Resistant Coatings Of Hexagonal Boron Nitride. Nature Communications 4, 2541 (2013).
9. Li, L. H. et al. Strong Oxidation Resistance Of Atomically Thin Boron Nitride Nanosheets. ACS Nano 8, 1457–1462 (2014).
10. Kubota, Y., Watanabe, et al. Deep Ultraviolet Light-Emitting Hexagonal Boron Nitride Synthesized At Atmospheric Pressure. Science 317, 932–934 (2007).
11. Britnell, L. et al. Electron Tunneling Through Ultrathin Boron Nitride Crystalline Barriers. Nano Letters 12, 1707–1710 (2012).
12. Kim, K. K. et al. Synthesis And Characterization Of Hexagonal Boron Nitride Film As A Dielectric Layer For Graphene Devices. Acs Nano 6, 8583–8590 (2012).
13. Kim, K. K. et al. Synthesis Of Monolayer Hexagonal Boron Nitride On Cu Foil Using Chemical Vapor Deposition. Nano Letters 12, 161–166 (2012).

14. Yang, P. C. et al. The Formation Of Epitaxial Hexagonal Boron Nitride On Nickel Substrates. Journal Of Electronic Materials 34, 1558–1564 (2005).

15. Orofeo, C. et al. Growth And Low-Energy Electron Microscopy Characterization Of Monolayer Hexagonal Boron Nitride On Epitaxial Cobalt. Nano Research 6, 335–347 (2013).

16. Kim, G. et al. Growth Of High-Crystalline, Single-Layer Hexagonal Boron Nitride On Recyclable Platinum Foil. Nano Letters 13, 1834–1839 (2013).

17. Lu, G. et al. Synthesis Of Large Single-Crystal Hexagonal Boron Nitride Grains On Cu-Ni Alloy. Nature Communications 6, 6160 (2015).

18. Wang, M. et al. A Platform For Large-Scale Graphene Electronics – CVD Growth Of Single-Layer Graphene On CVD-Grown Hexagonal Boron Nitride. Advanced Materials 25, 2746–2752 (2013).

19. Paffett, M. T. et al. Borazine Adsorption And Decomposition At Pt(111) And Ru(001) Surfaces. Surface Science 232, 286–296 (1990).

20. Fazen, P. J. et al. Thermally Induced Borazine Dehydropolymerization Reactions. Synthesis And Ceramic Conversion Reactions Of A New High-Yield Polymeric Precursor To Boron Nitride. Chemistry Of Materials 2, 96–97 (1990).

21. Liu, B. et al. Importance Of Oxygen In The Metal-Free Catalytic Growth Of Single-Walled Carbon Nanotubes From SiO_x By A Vapor-Solid-Solid Mechanism. Journal Of The American Chemical Society 133, 197–199 (2011).

22. Chen, J. et al. Oxygen-Aided Synthesis Of Polycrystalline Graphene On Silicon Dioxide Substrates. Journal Of The American Chemical Society 133, 17548–17551 (2011).

23. Bhaviripudi, S. et.al. Role Of Kinetic Factors In Chemical Vapor Deposition Synthesis Of Uniform Large Area Graphene Using Copper Catalyst. Nano Letters 10, 4128–4133 (2010).

24. Tay, R. Y. et al. Growth Of Large Single-Crystalline Two-Dimensional Boron Nitride Hexagons On Electropolished Copper. Nano Letters 14, 839–846 (2014).

25. Shi, Y. et al. Synthesis Of Few-Layer Hexagonal Boron Nitride Thin Film By Chemical Vapor Deposition. Nano Letters 10, 4134–4139 (2010).

26. Song, L. et al. Large Scale Growth And Characterization Of Atomic Hexagonal Boron Nitride Layers. Nano Letters 10, 3209–3215 (2010).

27. Petravic, M. et al. Decoration Of Nitrogen Vacancies By Oxygen Atoms In Boron Nitride Nanotubes. Physical Chemistry Chemical Physics 12, 15349–15353 (2010).

28. Liu, D. et al. Template-Free Synthesis Of Functional 3D BN Architecture For Removal Of Dyes From Water. Scientific Reports 4, 4453 (2014).

29. Schild, D. et al. XPS Investigations Of Thick, Oxygen-Containing Cubic Boron Nitride Coatings. Solid State Sciences 12, 1903–1906 (2010).

30. Kuzuba, T. et al. Raman-Scattering Study Of High-Pressure Effects On The Anisotropy Of Force Constants Of Hexagonal Boron Nitride. Physical Review B 18, 4440–4443 (1978).

31. Gorbachev, R. V. et al. Hunting For Monolayer Boron Nitride: Optical And Raman Signatures. Small 7, 465–468 (2011).

32. Nemanich, R. J. et al. Light Scattering Study Of Boron Nitride Microcrystals. Physical Review B 23, 6348–6356 (1981).

33. Golberg, D. et al. Boron Nitride Nanotubes And Nanosheets. ACS Nano 4, 2979–2993 (2010).

34. Bhimanapati, G. R. et al. Large-Scale Synthesis And Functionalization Of Hexagonal Boron Nitride Nanosheets. Nanoscale 6, 11671–11675 (2014).

35. Xue, Y. et al. Excellent Electrical Conductivity Of The Exfoliated And Fluorinated Hexagonal Boron Nitride Nanosheets. Nanoscale Research Letters 8, 49 (2013).

36. Kim, S. M. et al. Synthesis Of Large-Area Multilayer Hexagonal Boron Nitride For High Material Performance. Nature Communications 6, 8662 (2015).

37. Tauc, J., et al. Optical Properties And Electronic Structure Of Amorphous Germanium. Physica Status Solidi (B) 15, 627–637 (1966).

38. Blase, X., et al. Quasiparticle Band Structure Of Bulk Hexagonal Boron Nitride And Related Systems. Physical Review B 51, 6868–6875 (1995).

39. Xia, F. et al. A. Two-Dimensional Material Nanophotonics. Nature Photonics 8, 899–907 (2014).

40. Shi, Y. et al. Synthesis Of Few-Layer Hexagonal Boron Nitride Thin Film By Chemical Vapor Deposition. Nano Letters 10, 4134–4139 (2010).

41. Stehle, Y. et al. Synthesis Of Hexagonal Boron Nitride Monolayer: Control Of Nucleation And Crystal Morphology. Chemistry Of Materials 27, 8041–8047 (2015).

42. Watanabe, K. et al. Direct-Bandgap Properties And Evidence For Ultraviolet Lasing Of Hexagonal Boron Nitride Single Crystal. Nature Materials 3, 404–409 (2004).

43. Edgar, J. H. et al. Characterization Of Bulk Hexagonal Boron Nitride Single Crystals Grown By The Metal Flux Technique. Journal Of Crystal Growth 403, 110–113 (2014).

44. Remes, Z. et al. The Optical Absorption And Photoconductivity Spectra Of Hexagonal Boron Nitride Single Crystals. Physica Status Solidi (A) 202, 2229–2233 (2005).

45. Tran, T. T. et al. Quantum Emission From Hexagonal Boron Nitride Monolayers. Nature Nanotechnology 11, 37–41 (2016).

46. Cassabois, G. et al. Hexagonal boron nitride is an indirect bandgap semiconductor. Nature Photonics 10, 262–266 (2016).

47. Behura, S. et al. Interfacial nondegenerate doping of MoS_2 and other two-dimensional semiconductors. ACS Nano 9, 2227–2230 (2015).

48. Sreeprasad, T. S. et al. Controlled, Defect-Guided, Metal-Nanoparticle Incorporation Onto MoS_2 *Via* Chemical And Microwave Routes: Electrical, Thermal, And Structural Properties. Nano Letters 13, 4434–4441 (2013).

49. Lee, G. H. et al. Flexible And Transparent Mos2 Field-Effect Transistors On Hexagonal Boron Nitride-Graphene Heterostructures. ACS Nano 7, 7931–7936 (2013).

50. Yin, Z. et al. Single-layer MoS2 phototransistors. ACS Nano 6, 74–80 (2012).

51. Wang, S. et al. All Chemical Vapor Deposition Growth Of MoS_2:H-BN Vertical Van Der Waals Heterostructures. ACS Nano 9, 5246–5254 (2015).

52. Okada, M. et al. Direct Chemical Vapor Deposition Growth Of WS_2 Atomic Layers On Hexagonal Boron Nitride. ACS Nano 8, 8273–8277 (2014).

53. Gong, Y. et al. Vertical And In-Plane Heterostructures From WS_2/Mos_2 Monolayers. Nature Materials 13, 1135–1142 (2014).

54. Liang, L. et al. First-Principles Raman Spectra Of MoS_2, WS_2 And Their Heterostructures. Nanoscale 6, 5394 (2014).

55. Li, H. et al. From Bulk To Monolayer MoS_2: Evolution Of Raman Scattering. Advanced Functional Materials 22, 1385–1390 (2012).

56. Lee, Y. H. et al. Synthesis Of Large-Area Mos2 Atomic Layers With Chemical Vapor Deposition. Advanced Materials 24, 2320–2325 (2012).

57. Splendiani, A. et al. Emerging Photoluminescence In Monolayer MoS_2. Nano Letters 10, 1271–1275 (2010).

58. Mao, N. et al. Solvatochromic Effect On The Photoluminescence Of Mos_2 Monolayers. Small 9, 1312–1315 (2013).

59. Lu, C. P. et al. Bandgap, Mid-Gap States, And Gating Effects In MoS_2. Nano Letters 14, 4628–4633 (2014).

Chapter 4 - Few layer graphene interfacing with reversible mechanical dipole-modulating molecules: A graphene interface-molecular machine

Abstract

Molecular dipole-moment plays a significant role in governing important phenomena like molecular interactions, molecular-configuration, and charge-transfer, which are important in several electronic, electrochemical and optoelectronic systems. This chapter demonstrates the effect of the change in the dipole moment of a tethered molecule on the carrier properties of (functionalized) trilayer graphene – a stack of three layers of single-atom-thick sheets of sp^2 hybridized carbon atoms. It is shown that due to the high carrier-confinement and large quantum capacitance, the trans to cis isomerisation of 'covalently-attached' azobenzene molecule with a change in dipole moment of 3D, leads to the generation of an effective gating voltage. Resultantly, 6 unit of holes are produced per azobenzene molecules (hole density increases by 2.44×10^{12} holes/cm^2). Based on the Raman and XPS data, a model for outer-layer, azobenzene-functionalized trilayer-graphene with current modulation in the inner sp^2 matrix is outlined. Here, 0.097 V is applied by the isomerisation of the functionalized azobenzene. Furthermore the measured large quantum-capacitance of 6.3 μF/cm^2 justifies the large Dirac point in the heavily doped system. The mechanism defining the effect of dipole-modulation of covalently-tethered molecules on graphene will enable future sensors and molecular-machine interfaces with graphene.

Introduction

Isomerizable molecules produce precise dipolar-modulation and nanoscale mechanics[1–8], which can be employed to build molecular-valves[2,9], molecular hydro-switches[8], molecular-cargo-lifting[10], and molecular-shuttles[4,11–13]. Similarly, several biosystems leverage molecular mechanics and dipolar behavior. For example, flagella strands (2 – 100 nm) on the outer cell-wall of bacteria rotate to propel bacteria in solutions. Amongst mechanically actuating molecules, the photo-switchable (photo-isomerizable) molecules are interesting since these systems can be switched optically. The mechanics of these molecules are characterized by modulation of dipole-moment, response at high frequencies and absence of heat-production. An extensively studied photo-switchable molecule is azobenzene, which photo-isomerizes between trans and cis states, where the two configurations assume different dipole moments (trans = 0D; cis = 3D). There are several examples of electron-tunneling-modulation through junctions with azobenzene[5–7,14]; however, studies on its "covalent interfacing" to apply dipole-induced potential to change the carrier properties of the interfaced substrate are limited. In 2011, Kim et al[12], showed that azobenzene molecules attached vertically on graphene *via* π–π interfacing between pyrene and graphene can induce a doping. However, noncovalent anchoring strategies (π–π interfacing, adsorption etc) are less robust at certain conditions required for cleaning graphenic surfaces such as annealing at high temperatures or joule heating under high vacuum.

In this contribution, top and bottom layers of trilayer graphene (which are functionalized) can be leveraged as a platform to covalently bind azobenzene molecules at the top sp^3 regime with epoxy, COOH-, and –OH groups. Futhermore, the functionalization process, structural/optoelectronic characterization, and conductivity modulation model are further dicussed. In this stable, covalently-functionalized azobenzene-trilayer-graphene (ATG) device, the

electric-field (and its polarity) from the molecular dipole-moment of azobenzene, their configuration and orientation (normal-component) as well as proximity with respect to graphene influences graphene's doping-density (and/or carrier-polarity). Hence, the devices exhibit robust and reversible carrier-doping *via* configuration change of azobenzene upon programmed UV/blue light exposure (top right in set of **Figure 4.1**).

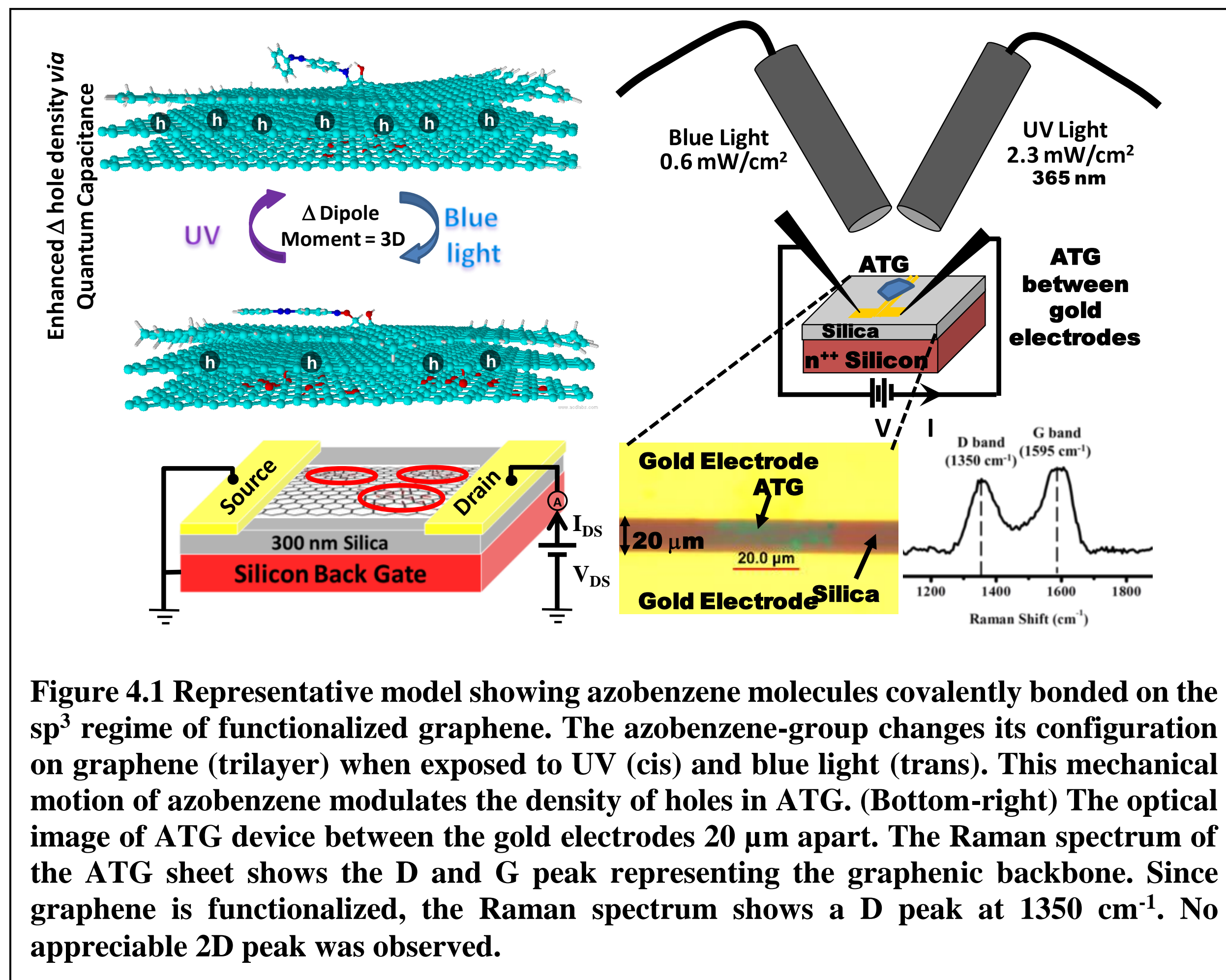

Figure 4.1 Representative model showing azobenzene molecules covalently bonded on the sp^3 regime of functionalized graphene. The azobenzene-group changes its configuration on graphene (trilayer) when exposed to UV (cis) and blue light (trans). This mechanical motion of azobenzene modulates the density of holes in ATG. (Bottom-right) The optical image of ATG device between the gold electrodes 20 µm apart. The Raman spectrum of the ATG sheet shows the D and G peak representing the graphenic backbone. Since graphene is functionalized, the Raman spectrum shows a D peak at 1350 cm^{-1}. No appreciable 2D peak was observed.

Experimental Section

In this part, a typical ATG device is comprised of three main components as shown in **Figure 4.2**: (1) Silica substrate (300 nm SiO_2/ n^{++} Si), (2) trilayer graphene platform, and (3) covalent binding azo-benzene molecule. The preparation of device, synthesizing of reduce

graphene oxide (RGO), and chemical functionalization route are described in the following sections:

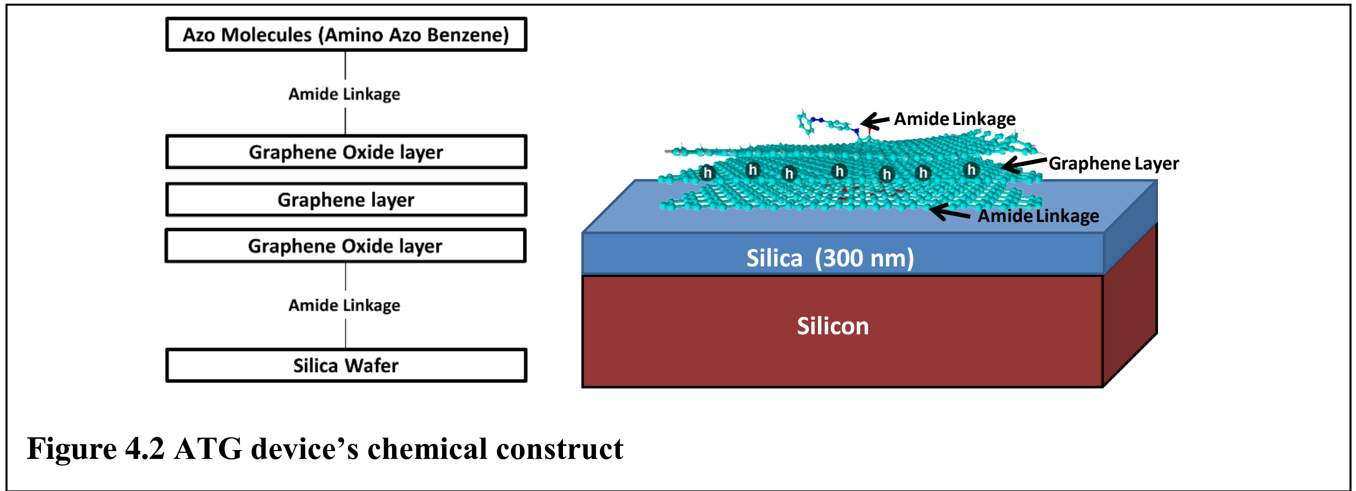

Figure 4.2 ATG device's chemical construct

Graphene oxide (GO) preparation

5 grams of Mesh 7 - graphite flakes were mixed with 33 ml of 68% nitric acid + 200 ml of 96% sulfuric acid and stirred continuously for 40 minutes in an ice bath. 30 grams of potassium permanganate ($KMnO_4$) was then added into the solution, while the temperature was slowly increased to 40°C, and kept at 400C for 30 minutes. Subsequently, the excess potassium permanganate was removed by treatment with 10% hydrogen peroxide (H_2O_2). Finally, the GO sheets were obtained by centrifuging this solution at 15,000 rpm for 30 minutes followed by repeated washing with DI water. The sample was then dialyzed (MWCO 2000D) for 24 hours and the subsequently stored as a suspension in DI water at room temperature.

The ATG device fabrication

The device construct consists of a 300 nm silica dielectric layer on heavily doped n-type silicon back-gate with ATG deposited between two gold electrodes 20 μm apart. Furthermore, a monolayer (3- Amino-propyl-triethoxy-silane (APTES) (Acros Organics) is used as a linker

between silica (silane chemistry) and the bottom layer of ATG (*via* amide bond). Briefly, to fabricate the device, the silica-substrate with gold electrodes is cleaned with water, acetone, ethanol, and isopropanol, dried and exposed to oxygen plasma for 5 min (700 mTorrs, 100 W). Subsequently, the substrate is submerged in 0.1 % APTES in ethanol for 10 min to introduce positively-charged amine groups on the silica surface. The chip is washed with 100% ethanol solution, dried and baked in the oven at 120 ^{0}C for 5 min to strengthen the bond between silane and silica. To deposit the trilayer graphene (TLG) sheets across the gold electrodes, the chip is submerged in the GO solution for 15 min. This covalently binds GO to the substrate *via* amide bonds. Finally, the 4-aminoazobenzene molecule is tethered to the GO sheet *via* amide linkage by incubating the chip in 4-aminoazobenzene solution (1% aqueous) in the presence of 2-(1H-7-Azabenzotriazol-1-yl)--1,1,3,3-tetramethyluronium hexafluorophosphate Methanaminium (HATU) reagent[15,16] for 12 hours.

Here, the carboxylic and hydroxyl groups on the GO's exposed surface and the amine group on the 4-aminoazobenzene form amide bonds in the presence of HATU catalyst (see section 2.3.1.2.A)[15,17,18]. Subsequently the unreacted oxy-groups are reduced *via* hydrazine treatment (see section 2.3.1.2.B) to produce ATG sheets spanning between electrodes. Finally, the device is washed thoroughly with copious amount of water, acetone and isopropanol to remove any residual hydrazine or adsorbed azobenzene. For subsequent calculation and analysis, the optimized orientation of the azobenzene molecule with respect to graphene was obtained from the ChemSketch program's molecular mechanics algorithm (**Figure 4.1** and **Figure 4.2**).

Amino azo benzene attachment

The 1% amino azo benzene solution was prepared by dissolving 0.2 g 4-amino azobenzen hydro chloride (TCI America, item number A0771) in 20 mL. Subsequently, the solution was

added with 5 mg Hatu (Novabiochem®, item number 8510130025) as a catalyst for the amide formation between the azo molecules and carboxylic group of chemical modified grapheme oxide.

The reduction of GO to RGO *via* hydrazine treatment

The GO samples were treated with hydrazine vapors in a closed chamber. In this chamber, liquid hydrazine is heated at a temperature of ~75°C. This results in the formation of vapors which reduces the GO sheets into RGO immobilized on the silica surface.

Instrumentations for chemical, physical and electrical characterization

Raman spectroscopy system

The Raman measurements were conducted using an Ocean Optics QE65000 spectrometer (50 micron slit) connected to an optical microscope (Olympus BX51) *via* a collimator. A 532 nm green laser with a beam diameter of 30 microns through a 50X objective was used as an excitation source at 50 mW. The data acquisition time for each scan was kept at 100 second.

X-ray photoelectron spectroscopy (XPS) system

XPS data were recorded with a Perkin–Elmer PHI 5400 electron spectrometer using acrochromatic Al Kα radiation (1486.6 eV). Analysis was carried out under a vacuum less than 5×10^{-9} Torr. The XPS binding energies were measured with a precision of 0.025 eV. The analyzer pass energy was set to 17.9 eV, the contact time was 50 ms, and the area scanned was 4 mm^2. The spectrometer was calibrated by setting the binding energies of Au $4f_{7/2}$ and Cu $2p_{3/2}$ to 84.0 and 932.7 eV, respectively. Spectra were referenced to C1s peak at 284.8 eV.

Cryostat electrical system

The setup is similar to that described in chapter 2, and chapter 3 (Experimental section). The electrical measurements of ATG samples were carried out in Janis ST100 cryogenic probe

station. Edwards E2M5 rotary vane pump, and Edward turbo molecular pump were connected in series to chamber to provide high vacuum (<5 × 10^{-6} Torr). Lakeshore temperature controller (model 336) provided the control of the temperature of sample. The Keithley 2612 dual-channel system source meter connected to a computer *via* a GPIB/IEEE-488 interface card. Gating was performed by keeping the source-drain voltage constant and measuring the change in conductivity with the gate voltage, which was applied to the heavy-doped silicon backgate.

Results and Discussion

Structural and chemical characterization of ATG

A typical device (**Figure 4.1**) consists of ~ 35 x 20 μm^2 ATG between gold electrodes. The Raman spectrum of a typical ATG sheet shows the D and the G peak at 1350 and 1595 cm^{-1}, respectively. This indicates the presence of the graphenic backbone in ATG (as shown in figure **Figure 4.1**). No appreciable peak for 2D band was observed, as expected for functionalized graphene[19]. AFM analysis of the ATG devices gave a total thickness of 3.6 nm (as shown **Figure 4.3a**). Considering the height of the azobenzene-group (0.31 nm), the remaining thickness corresponds to 3 graphene layers with two outer functionalized sheets and 1 inner graphene sheet.

In the XPS analysis, the bulk density of azobenzene molecules is analyzed from carbon and nitrogen peaks. Furthermore, the carbon peaks are contributed approximately from the carbon atoms of tri layer graphene sheet, azobenzene molecules, and silane molecules. In addition, the nitrogen peaks are deliberated comparably from the nitrogen atoms of azobenzene molecules and silane molecules. From the deconvolution of N 1s, for the ATG, the XPS analysis reveals the N 1s peak for the amide bond (O=C-N) and the -(N=N)- azo bond of azobenzene molecules and silane (containing only amide bond) appearing around 401.5 eV and 400.5 eV respectively[20]; while for

the trilayer graphene (TLG, without azobenzene) the peak for the amide linkage with silica appears at around 401.5 eV as shown in **Figure 4.3b-c**[21].

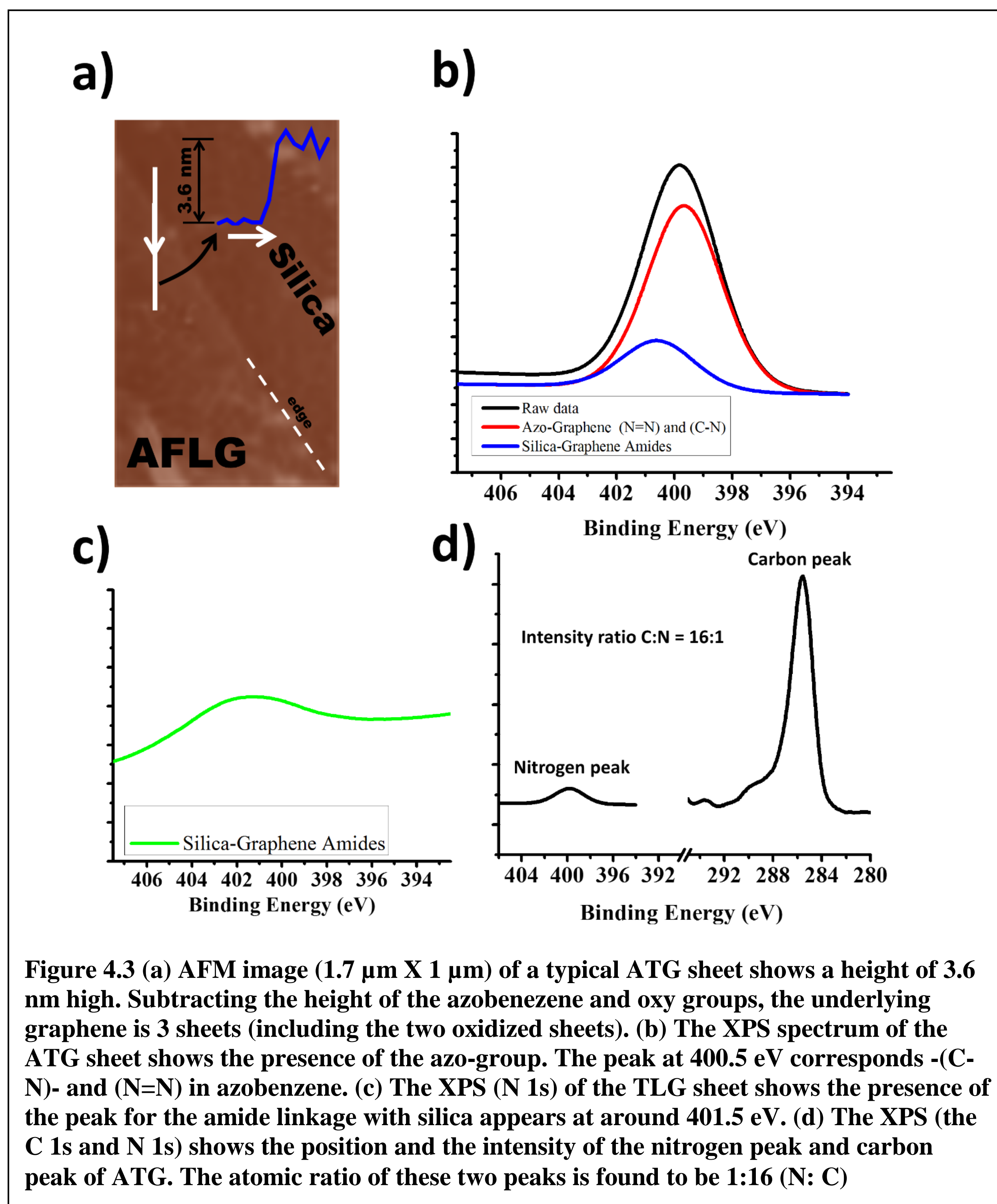

Figure 4.3 (a) AFM image (1.7 μm X 1 μm) of a typical ATG sheet shows a height of 3.6 nm high. Subtracting the height of the azobenezene and oxy groups, the underlying graphene is 3 sheets (including the two oxidized sheets). (b) The XPS spectrum of the ATG sheet shows the presence of the azo-group. The peak at 400.5 eV corresponds -(C-N)- and (N=N) in azobenzene. (c) The XPS (N 1s) of the TLG sheet shows the presence of the peak for the amide linkage with silica appears at around 401.5 eV. (d) The XPS (the C 1s and N 1s) shows the position and the intensity of the nitrogen peak and carbon peak of ATG. The atomic ratio of these two peaks is found to be 1:16 (N: C)

For every azobenzene molecule, there are 2 nitrogen atoms in -(N=N)- bond and 1 nitrogen atom in -(C-N)- bond. Moreover, there are 12 carbon atoms from the two benzene rings. Meanwhile, for every silane molecule, there is 1 nitrogen atom in -(C-N)- bond. Also after silanation, (APTES) has 7 carbons atom. Finally, in every nm^2 of mono layer of graphene sheet, there are 36 carbon atoms (108 carbon atoms for tri layers).

In detail, for 1 nm^2 of area, there are:

a = # N atoms in N=N azobenzene molecules per nm^2,

(6a) = # C atoms in azobenzene molecules per nm^2,

b = # N atoms in C-N azobenzene molecules per nm^2 ($b = \frac{a}{2}$),

c = # N atoms in C-N silane molecules per nm^2,

(7c) = # C atoms in silane molecules per nm^2,

108 = # C atoms in trilayer graphene per nm^2,

Ratio of # N atoms: # C atoms = 1:16 (calculated from XPS data as shown **Figure 4.3d**),

Ratio of # N atoms (azobenzene molecule): # N atoms (silane attachment) = 1:4 (calculated from XPS data).

Therefore,

$$\frac{\#\,N}{\#\,C} = \frac{1}{16} = \frac{a + b + c}{108 + 6a + 7c}$$

$$\frac{\#\,N}{\#\,C} = \frac{1}{16} = \frac{a + \frac{a}{2} + c}{108 + 6a + 7c}$$

$\frac{\#\,N}{\#\,C} = \frac{1}{16} = \frac{\frac{3a}{2} + c}{108 + 6a + 7c}$ **Equation 4.1**

In addition,

$$\frac{\#\,N\text{ in (azo molecule)}}{\#\,N\text{ in (silane attachment)}} = \frac{4}{1} = \frac{a + b}{c}$$

$$\frac{\#\ \mathbf{N\ in\ (azo\ molecule)}}{\#\ \mathbf{N\ in\ (silane\ attachment)}} = \frac{\mathbf{4}}{\mathbf{1}} = \frac{\frac{\mathbf{3}}{\mathbf{2}}\mathbf{a}}{\mathbf{c}} \quad \textbf{Equation 4.2}$$

From system of equation 4.1 and equation 4.2, number of nitrogen atoms (a = 5.0) corresponding to (N=N) bond is solved. For one azobenzene molecule there are two nitrogen atoms of (N=N) bond. Therefore, number of azobenzene molecules is ~2.5 molecules /nm^2. Furthermore, the area of the azobenezene molecule is 0.27 nm^2 (or 1/0.27= 3.7 per nm^2 of packed density). Hence fractional coverage of azobenezene molecule (f) is 0.625 (ratio of azobenzene packed density over azobenzene experimental density = 2.5/3.7 = 0.625)

Opto-electronic characterization

After confirming the anchoring of azobenzene on TLG, a study the ATG device's opto-electronic behavior under UV/Blue light exposure was conducted. As discussed earlier, graphene surface is ultrasensitive to the interfacial events and two primary explanations are discussed in the literature for this phenomenon[23]. (A) Graphene possesses a high quantum capacitance (for monolayer: $C_q = \left(4e\pi^{1/2}/h\vartheta_F\right)\left(n_l + n_g\right)^{1/2}$, where e is the electron charge, h is Planck constant, ϑ_F is the Fermi velocity of the Dirac electron, and n_g and n_l are the carrier concentrations from the gate potential and the intrinsic carrier concentration of graphene, respectively[17]; for bilayer and trilayer: $C_q = e^2 g_v g_s / 2\pi\hbar^2 \vartheta_F{}^2$, if Fermi energy (ε_F) is higher than the interlayer coupling (γ_1); for trilayer: $C_q = \left(e^2 g_v g_s / 4\pi\hbar^2 \vartheta_F{}^2\right)\left(4\varepsilon_F + \sqrt{2}\gamma_1\right)$, if $\varepsilon_F < \gamma_1$. The quantum-coupling of the interfacial molecules with graphene enhances the effective electric-field due to the dipole moment of the molecules[24]. The effective gating potential (ΔV_G), therefore, translates from a change in dipole voltage (ΔV_d) of the molecule to $\Delta V_G = f\left(C_q/C_{tot}\right)\Delta V_d$, where f is the fraction of sp^2 area which is gated by the azobenzene molecules. This was calculated using the equation, $f = \frac{2\pi r^2}{\sqrt{3}a^2} = \rho_{bulk} A_{azo} = 2.5 \times 0.27 = 0.675$, where the bulk density of azobenzene ρ_{bulk} = 2.5 azo/nm^2

(calculated from XPS section) and the area of one azobenzene molecule (A_{azo} = 0.27 nm^2). Also, $C_{tot} = \left(C_q^{-1} + C_g^{-1}\right)^{-1}$ and C_g is the gate capacitance. (B) Confined Doping: The change in the carrier concentration of graphene due to the change in the dipole-moment of the molecule is amplified as a result of the confinement of the doped carriers within its ultrathin structure. The consortium of these properties makes graphene an ideal candidate for detecting interfacial molecular events.

Before the optoelectronic measurements, care was taken to remove adsorbed/non-bonded molecules (including any residual azobenzene, which can bind on graphene[25,26]. All the ATG devices were electrically annealed (Joule heating = IVt; 3 V for 5 min). Since high vacuum is not effective to avoid molecular desorption/adsorption[27], the device's optoelectronic response was characterized under helium-pressurized (19 psia) probe-station with quartz optical-windows (He adsorption on graphene surface is negligible[28]). The gold electrodes spanning ATG (source-drain) and silicon (back-gate) were connected to a dual-source meter (Keithley 2612). Each device was again electrically annealed (3 V for 30 min) under high He pressure to remove residual adsorbed impurities if any. The quartz-optical-ports were connected with UV (365 nm, power = 2.3 mW/cm^2) and Blue (420 nm, power = 0.6 mW/cm^2) lamps to study the effect of UV and blue light exposures and dark (**Figure 4.1**). The UV light isomerizes the azobenzene into its cis form (benzene rings closer to one-another and Dipole moment = 3D), while blue light (or dark at room temperature) brings the azobenzene back to its trans form (benzene rings are opposite one-another and Dipole moment = 0D).

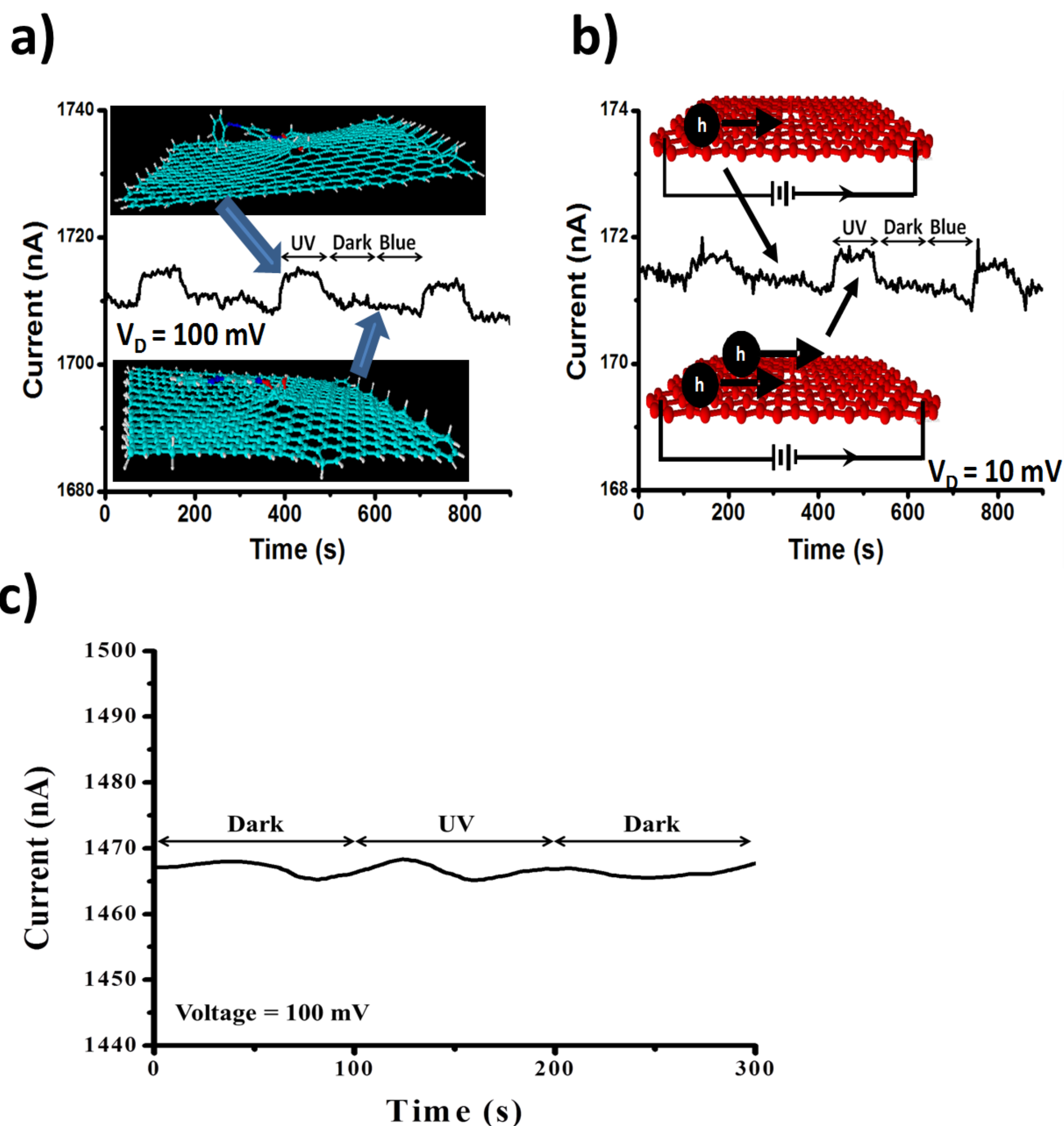

Figure 4.4 a) The figure shows the response of the ATG device (under 19 psia pure He environment at room temperature) exposed to UV, Blue and Dark for 90 sec each at 100 mV source-drain voltage. b) The same response (as (a)) is measured at 10 mV source-drain voltage. The current axis has been rescaled to better represent the change. Also, the azobenzene's trans configuration can be achieved *via* blue light exposure and temperature. Since, the rate of decrease of conductivity was not significantly more than that in dark environment; the room temperature is high enough to favor the trans state in the absence of UV. Further, it is known that the azobenzene could readily fluctuate between cis and trans configuration[22], leading to fluctuation in current as observed in electrical measurements. c) The response in conductivity of the functionalized TLG (without azobenzene attachment) on 300 nm silica substrate exposed to UV and Dark for 100 sec each at 100 mV source-drain voltage is shown as control sample.

The optoelectrical measurements (**Figure 4.4a-b**) show that the conductivity of the ATG device increases with exposure to UV, and reverts back to the original value with exposure to blue light (420 nm) or in dark (UV/Blue off), where the exposure time was 90 seconds each. The change in current for 100 mV and 10 mV source-drain voltage were 0.5 and 5 nA, which are directly scaled with the voltage. This change in conductivity is attributed to doping of charge-carriers in graphene due to a change in the dipole-moment of the azobenzene. Here, the increase in dipole-potential (due to 3D change in dipole moment) leads to hole-doping in the cis configuration on the p-type (shown later) device. Furthermore, the direct scaling of current-modulation with voltage implies that the change in conductivity is not caused by desorption, the rate of which must increase with voltage due to Joule heating induced desorption. A reduced-graphene-oxide device (without azobenzene) did not show any discernible response to UV/Blue exposure under similar conditions (**Figure 4.4c**). The noise observed in the current measurements are expected to be a result of fluctuation in the configuration of the azobenzene, as has been discussed in several studies[22].

The carrier mobility and polarity in the ATG device were measured from back-gating studies using silicon as the back-gate and 300 nm silicon-oxide as the gate-oxide (**Figure 4.5a**). The negative differential of the I_{DS} with V_G indicates that holes are the majority carriers (p-type device). In figure **Figure 4.5b**, the (average) slope of -2.22 X 10^{-2} nA/V implies a hole mobility of 0.195 $cm^2/V/s$ calculated *via*:

$$\mu = \frac{d_{SiO_2} \cdot l}{(\overline{W}) \cdot \varepsilon \cdot \varepsilon_o \cdot V_D} \cdot \left(\frac{\Delta I_D}{\Delta V_G}\right)$$ **Equation 4.3**

Here, μ is the hole mobility, d_{SiO_2} is the thickness of silicon wafer, l is the channel length (20 mm), $\overline{W}$ is the average channel width (40 μm), ε is the relative static permittivity of SiO_2 (~4), ε_o is the

permittivity of free space, V_D is the source-drain voltage, and $\left(\frac{\Delta I_D}{\Delta V_G}\right)$ is the absolute value of the linear slope of the back-gating curve.

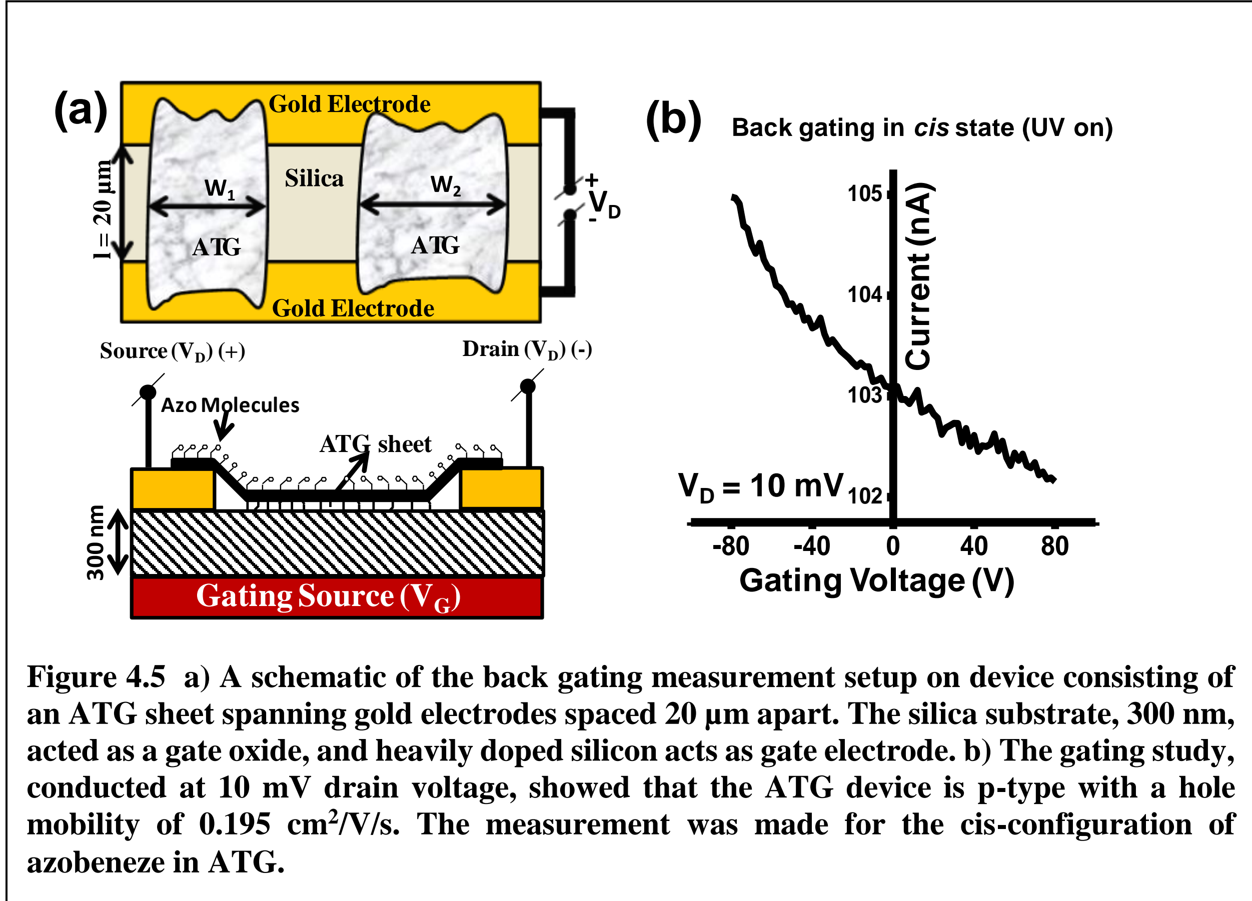

Figure 4.5 a) A schematic of the back gating measurement setup on device consisting of an ATG sheet spanning gold electrodes spaced 20 µm apart. The silica substrate, 300 nm, acted as a gate oxide, and heavily doped silicon acts as gate electrode. b) The gating study, conducted at 10 mV drain voltage, showed that the ATG device is p-type with a hole mobility of 0.195 $cm^2/V/s$. The measurement was made for the cis-configuration of azobeneze in ATG.

Based on the carrier-mobility and hole dominant transport, the change in hole concentration due to the configuration change of the azobenzene-molecule was approximated. Here, the gating voltage ($|\Delta V_G|$) which induces the same change in current as the azobenzene mechanics (0.5 nA) is 36 V. This gating voltage provides the change in carrier density *via* the gate-capacitance equation: $\Delta q = {C_{SiO_2}|\Delta V_G|}/{e}$. Here, Δq is the carrier surface density created due to azobenzene isomerization, and e is the elementary charge (1.60×10^{-19} C). This equation provides a value of ~ 2.44×10^{12} holes/cm^2 generated due to the molecular-gating from UV-induced change of the azobenzene-molecule's configuration from trans to cis. With an azobenzene density of 2.5 nm^{-2},

this implies that mechanics of ~ 100 azobenzene molecule produces 1 holes. This corresponds to 3 quanta of hole generated per 100 nm^2 of the base ATG. Also, the total carrier concentration at zero gate voltage is 1.6 x 10^{14} cm^{-2} ($n_{Total} = \frac{L}{W}\frac{I}{\mu e V_{DS}}$).

To explain the mechanism of isomerization-induced doping in ATG, a simple model was developed as followed: chemically exfoliated trilayer graphene comprises of two outer (top and bottom) functionalized (sp^3) and one middle graphene (sp^2) layer. In this system, the top layer is assumed to have a homogenous distribution of covalently bonded azobenzene and bottom is assumed to have oxy-groups. Therefore, the electronic transport is dominant in the middle graphene layer with azobenzenes on the top layer acting as molecular gates. Although, the charge mobility is high in sp^2 region was observed as a low value, which is attributed to the presence of large-density of charge-traps from the functionalized groups in the top and bottom layers.

The dipole voltage induced on the middle graphene layer by azobenzene molecules *via* the change in dipole moment of the molecules (from cis to trans forms) is calculated by $\Delta V_d = [(\Delta\mu)\sin(\theta)/(4\pi\varepsilon_o r^2)][4\sum[i^2(\xi/r_{Azo\text{-}Graphene})^2 - 1]^{-3/2} + 3(i\text{-}1)\sum[3i^2/4(\xi/r_{Azo\text{-}Graphene})^2 - 1]^{-3/2}$ where $\Delta\mu$ is the change in the dipole moment of azobenzene, i is the index (representing the distance of the dipole of the azobenzene and the point of interest), $r_{Azo\text{-}Graphene}$ is the distance between a dipole and middle-layer graphene, $\rho_{packed\text{-}azo}$ is the density of azobenzene molecules packed in top layer graphene oxide (3.7 azobenzene/nm^2), and θ is the angle of inclination of the cis-azobenzene with respect of graphene (θ=17.5). The $\Delta\mu$ is calculated to be 3D (3sin(θ) D = 0.92 D), which yields an induced dipole voltage (ΔV_d) of 0.097 V.

The gating experiment shows that the change in conductivity *via* azobenzene's isomerization (0.5 nA at 10 mV V_{DS}) is also brought by 36 V of gating potential (as shown in **Figure 4.6**). This implies that the change in the charge carriers for azobenezene-isomerization

through graphene's quantum capacitance is the same as that produced by gating: $\Delta V_G = f(C_q/C_{tot})\Delta V_d$, where f is the fraction of sp^2 area which is gated by the azobenzene molecules as defined above. This provides a quantum capacitance value of 6.3 $\mu F/cm^2$. Furthermore, since the mobility of carriers in TLG is not expected to change with doping,[31] our approximation of constant mobility with azobenzene-actuation is justified and consistent with earlier results on molecular-interfacing of few layer graphene with molecular moieties[15,28–31]. The quantum capacitance of 4.3 provides a measure of the total carrier concentration ($fC_Q = \left(4e\pi^{1/2}/h\vartheta_F\right)(n_{Total})^{1/2}$, $n_{Total} = 2.9 \times 10^{12}$ cm^{-2}.

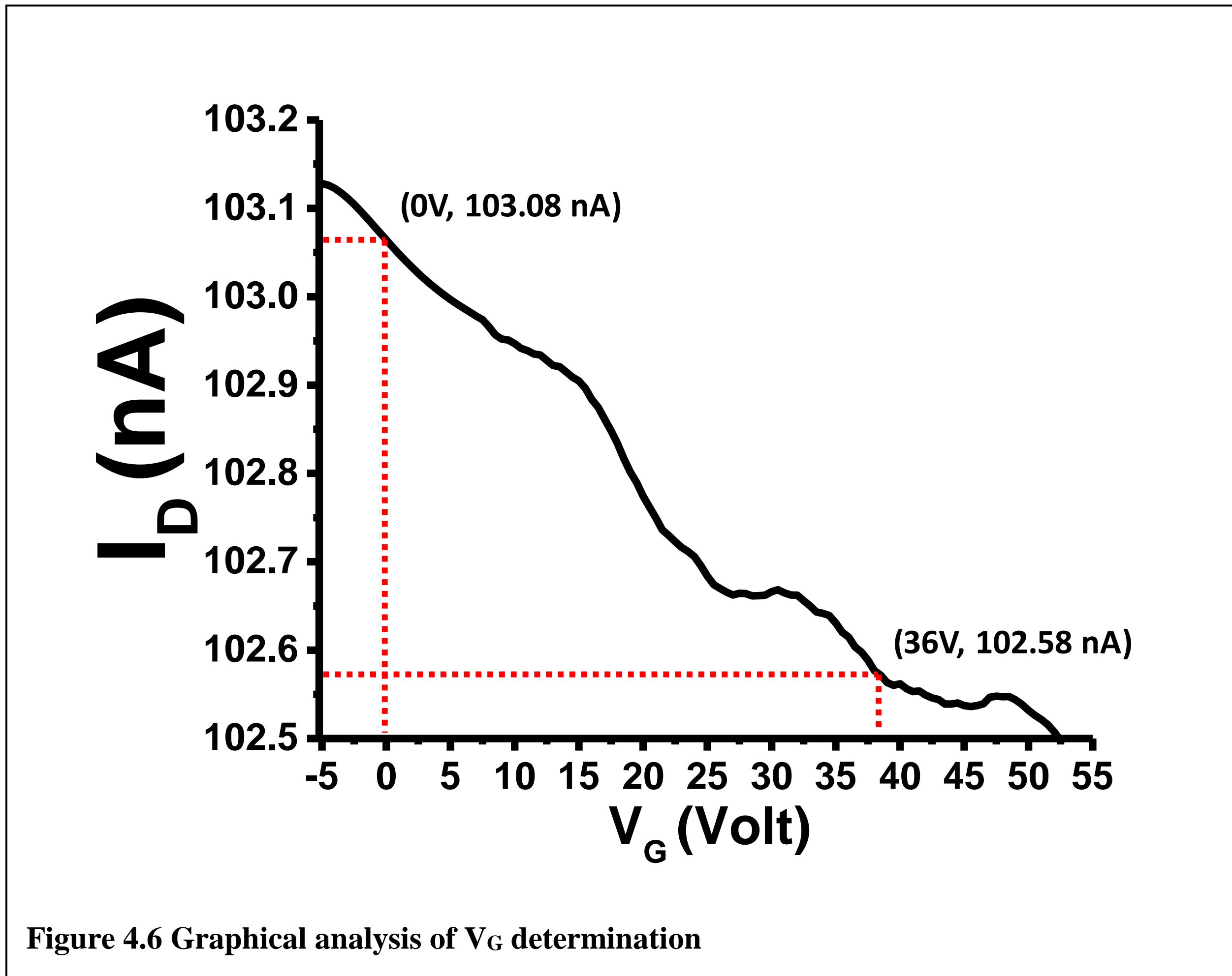

Figure 4.6 Graphical analysis of V_G determination

Conclusion

In summary, this chapter demonstrated that molecular mechanics (trans to cis configuration) of covalently anchored azobenzene (density = 2.5 nm^{-2}) on trilayer graphene (37.5% sp^2 coverage) can sensitively and reversibly modulate its carrier density (2.44 x 10^{12} holes/cm^2). Here, the change of 3D in the molecular dipole-moment produces 0.097 V of dipole voltage, which leads to production of 1 quanta of hole per 100 azobenzene molecule. The sensitivity evolves from the high quantum capacitance of 6.3 μF/cm^2. The total carrier density calculated from gating was consistent with that from quantum capacitance. We envision that this work will generate interest in applying graphene's sensitivity to molecular actuation and dependence on original orientation to develop rational interfaces with molecular-machines (for example, rotaxane) and biomolecules for advanced applications in molecular switches, electromechanics and protein-folding. Futuristically, graphene nanoribbons devices interfaced with actuable molecules (proteins or molecular machines) could exhibit enhanced sensitivity.

Acknowledgements

The financial support from NSF (CMMI-1054877, CMMI-0939523 and CMMI-1030963), Office of Naval Research (grant-N000141110767), Terry C. Johnson Center for Basic Cancer Research, and KSU start-up were acknowledged.

References

1. Anelli, P. L. et al. A Molecular Shuttle. Journal Of The American Chemical Society 113, 5131–5133 (1991).
2. Angelos, S. et al. Photo-Driven Expulsion Of Molecules From Mesostructured Silica Nanoparticles. The Journal Of Physical Chemistry C 111, 6589–6592 (2007).
3. Badjic, J. D. et al. A Molecular Elevator. Science 303, 1845–9 (2004).

4. Brouwer, A. M. et al. Photoinduction Of Fast, Reversible Translational Motion In A Hydrogen-Bonded Molecular Shuttle. Science 291, 2124–8 (2001).

5. Choi, B-Y. et al. Conformational Molecular Switch Of The Azobenzene Molecule: A Scanning Tunneling Microscopy Study. Physical Review Letters 96, 156106 (2006).

6. Collier, C. P. et al. Molecular-Based Electronically Switchable Tunnel Junction Devices. Journal Of The American Chemical Society 123, 12632–12641 (2001).

7. Comstock, M. J. et al. Reversible Photomechanical Switching Of Individual Engineered Molecules At A Metallic Surface. Physical Review Letters 99, 038301 (2007).

8. Delorme, N., et al. Azobenzene-Containing Monolayer With Photoswitchable Wettability. Langmuir 21, 12278–12282 (2005).

9. Liu, N. et al. Photoregulation Of Mass Transport Through A Photoresponsive Azobenzene-Modified Nanoporous Membrane. Nano Letters 4, 551–554 (2004).

10. Ferri, V. et al. Light-Powered Electrical Switch Based On Cargo-Lifting Azobenzene Monolayers. Angewandte Chemie International Edition 47, 3407–3409 (2008).

11. Green, J. E. et al. A 160-Kilobit Molecular Electronic Memory Patterned At 10^{11} Bits Per Square Centimetre. Nature 445, 414–417 (2007).

12. Kim, M. et al. Light-Driven Reversible Modulation Of Doping In Graphene. Nano Letters 12, 182–187 (2012).

13. Feringa, B. L. et al. Light-Driven Monodirectional Molecular Rotor. Nature 401, 152–155 (1999).

14. Donhauser, Z. J. et al. Conductance Switching In Single Molecules Through Conformational Changes. Science 292, 2303–7 (2001).

15. Mohanty, N. et al. Graphene-Based Single-Bacterium Resolution Biodevice And DNA Transistor: Interfacing Graphene Derivatives With Nanoscale And Microscale Biocomponents. Nano Letters. 8, 4469–4476 (2008).

16. Mohanty, N. et al. Impermeable Graphenic Encasement Of Bacteria. Nano Letters. 11, 1270–1275 (2011).

17. Nguyen, P. et al. Graphene Interfaced With Biological Cells: Opportunities And Challenges. Journal Of Physical Chemistry Letters 3, 1024–1029 (2012).

18. Mohanty, N. et.al. High-Throughput, Ultrafast Synthesis Of Solution- Dispersed Graphene *Via* A Facile Hydride Chemistry. Small 6, 226–231 (2010).

19. Kaniyoor, A. et al. A Raman Spectroscopic Investigation Of Graphite Oxide Derived Graphene. AIP Advances 2, 032183 (2012).

20. Sharma, L. et al. Investigation Into The Surface Relief Grating Mechanism *Via* XPS In New Azobenzene Based Optical Material. Polymers For Advanced Technologies 13, 481–486 (2002).

21. Metwalli, E. et al. Surface Characterizations Of Mono-, Di-, And Tri-Aminosilane Treated Glass Substrates. Journal Of Colloid And Interface Science. 298, 825–831 (2006).

22. Yasuda, S. et al. Phase Switching Of A Single Isomeric Molecule And Associated Characteristic Rectification. Journal Of The American Chemical Society 125, 16430–16433 (2003).

23. Sreeprasad, T. S. et al. How Do The Electrical Properties Of Graphene Change With Its Functionalization? Small 9, 341–350 (2013).

24. Xia, J. et al. Measurement Of The Quantum Capacitance Of Graphene. Nature Nanotechnology 4, 505–509 (2009).

25. Peimyoo, N. et al. Photocontrolled Molecular Structural Transition And Doping In Graphene. ACS Nano 6, 8878–8886 (2012).

26. Peimyoo, N. et al. Thickness-Dependent Azobenzene Doping In Mono- And Few-Layer Graphene. Carbon 50, 201–208 (2012).

27. Lin, J. et al. Molecular Absorption And Photodesorption In Pristine And Functionalized Large-Area Graphene Layers. Nanotechnology 22, 355701 (2011).

28. Schedin, F. et al. Detection Of Individual Gas Molecules Adsorbed On Graphene. Nature Materials 6, 652–655 (2007).

29. Lu, G. et al. Gas Detection Using Low-Temperature Reduced Graphene Oxide Sheets. Applied Physics Letters 94, 083111 (2009).

30. Jung, I. et al. Effect of Water Vapor on Electrical Properties of Individual Reduced Graphene Oxide Sheets. The Journal Of Physical Chemistry C 112, 20264–20268 (2008).

31. Fowler, J. D. et al. Practical Chemical Sensors From Chemically Derived Graphene. ACS Nano 3, 301–306 (2009).

Chapter 5 - Molybdenum disulfide (MoS_2) for metal-nanoparticles interfacing: An avenue for the modification electrical, thermal, and structural Properties

Abstract

Ultrathin (0.3 – 3 nm) metal dichalcogenides exhibit confinement of carriers, evolution of band-structure and photophysical properties with thickness, high on/off rectification (in MoS_2, WS_2 etc) and high thermal absorption. This chapter shows the leveraging of the stable sulfur/nobel-metal binding for the incorporation of highly-capacitive gold nanoparticles (Au NPs) onto MoS_2 in order to raise the effective gate-voltage by an order of magnitude. Functionalization is achieved *via* both diffusion limited aggregation and instantaneous reaction arresting (using microwaves) with selective deposition on crystallographic edges (with 60^0 displacement). The electrical, thermal and Raman studies show a highly capacitive interaction between Au NP and MoS_2 flakes ($C_{Au\text{-}MoS2} = 2.17\ \mu F/cm^2$), a low Schottky barrier (14.52 meV), a reduced carrier-transport thermal-barrier (253 to 44.18 meV after Au NP functionalization), and increased thermal conductivity (from 15 W/mK to 23 W/mK post NP deposition). The process could be employed to attach electrodes to heterostructures of graphene and MoS_2, where a gold film could be grown to act as an electron-tunneling gate-electrode connected to MoS_2.

Introduction

Elimination of interfacial influences and evolution of confinement by isolating sheets from layered materials has led to the realization of a wide variety of phenomena and extraordinary applications. This outcome was first observed in graphene, where due to the emergent electronic

structure with massless Dirac fermions, ballistic carrier transport was achieved[1]. As a semiconducting analog of two-dimensional (2D) graphene, MoS_2 monolayer is a three-atom-thick layered transition-metal dichalcogenide, composed of a stratum of molybdenum atom sandwiched between two layers of sulfur atoms in a trigonal prismatic (or antiprismatic) lattice. The relatively weak interlayer interaction between the MoS_2 sheet allows their monolayer crystals (thickness 0.65 nm) to be cleaved mechanically and chemically[2]. Furthermore, the electrical and optical properties of MoS_2 changes dramatically with number of layers: bulk MoS_2 exhibits an indirect band-gap of 1.2 eV, while monolayer MoS_2 has a direct band-gap of ~1.8 eV[3] with enhanced photoluminescence[4]. Single layer MoS_2 field effect transistor (FET) exhibits a mobility of 0.5 – 15 $cm^2/(Vs)$ with a high on/off current ratio (10^3 to 10^8)[5]. Recent studies show that MoS_2 can be applied effectively in sensing[6,7], energy harvesting[8], and photo-electronic application[9].

To incorporate MoS_2 into rational applications, it is imperative to functionalize it with chemical moieties, which can enable its interface with other nano- or micro- systems. Nano-interfacing can provide an avenue for controlling MoS_2's electrical and thermal properties; while metal functionalization can provide contacts for MoS_2-graphene heterostructure-devices. Other applications that will be impacted include plasmonic devices, catalytic substrates, Raman active surfaces, controlled photoluminescence, and selective sensing. Furthermore, anchoring gold nanoparticles (Au NP) on heterostructures can enhance photophysical properties for improved optoelectronic application.[10] This chapter reports the solution-based metal functionalization of few layer MoS_2, the metal-interfacing mechanism and its influence on the electrical, thermal and structural properties of MoS_2.

Experimental Section

Metal nanostructures were incorporated on chemically (liquid-dispersed-phase) and physically (solid-phase) exfoliated MoS_2 crystals (from SPI supplies). This was achieved by reduction of metal salt by chemical, microwave, and thermal routes, and establishing sulfur-metal linkage on MoS_2.

MoS_2 incorporation with metal-nanoparticles *via* chemical route

Procedure for mechanical exfoliation MoS_2

Physically exfoliated MoS_2 sheets were produced *via* scotch-tape method[5] and transferred onto a silica chip (300 nm silica on n-doped silicon substrate) with (or without) pre-deposited electrodes (300 nm gold, with 5 or 10 μm gap) for electrical studies. The chip was washed with copious amount of water and IPA, dried in N_2 flow for Furthermore characterization. For functionalization of this pre-immobilized MoS_2, the MoS_2-substrate was immersed in the metal ion solution (10 mL, 1 mM), followed by adding NH_2OHz (50 wt%, 15 μL) and keeping the solution undisturbed for 10 h. The substrate was later removed from the solution and washed thoroughly with water and IPA, dried in N_2 flow, and kept for structural and electrical characterization.

Procedure for solution-based exfoliation MoS_2

The liquid phase exfoliation and dispersal of MoS_2 (10 mg) was carried out in N-methyl-pyrrolidinone (NMP, 10 mL in a 20 mL glass container)[2] *via* 2 hr sonication and 10 min centrifugation (5000 rpm). Furthermore, a silica chip (300 nm silica on n-doped silicon substrate) was immersed in this solution for 2 to 24 h at ambient conditions (Figure 1). The chip was then taken out of the solution, washed and dried in N_2 flow for further characterization. For MoS_2

dispersed in NMP, the metal salt ($HAuCl_4$ (10 mL, 1 mM) or $AgNO_3$ (10 mL, 1 mM)) was added and stirred for 5 mins. A mild reducing agent, hydroxyl amine (NH_2OH, 50 wt%, 15 µL) was then added to reduce the metal ions in the solution (10 min). To immobilize the resultant MoS_2–metal structure, a bare silica chip was introduced into the mixture and kept undisturbed for a set period of time.

MoS_2 incorporation with metal-nanoparticles *via* microwave route

Metal NP incorporation onto MoS_2 sheets can also be induced by microwave (MW) aided instantaneous reduction and incorporation. Here, local dielectric heating from MW exposure (1.05 kW, 2450 MHz) is applied on an aqueous solution of metal salt (0.1 mM of $HAuCl_4$, or $AgNO_3$) and MoS_2 (solvent assisted exfoliation, 500 µL of parent solution in 10 ml) for 2 to 15 seconds. Furthermore, to deposit the resultant MoS2–metal structure, a bare silica chip was submerged into the mixture and kept undisturbed for a set period of time.

MoS_2 incorporation with metal-nanoparticles *via* physical deposition (DC sputtering)

A MoS_2 (mechanical exfoliated) device was sputtered with Au/Pd (cold sputtering) for 2 and 4 second (35 mTorr Ar atmosphere, 45 mA current). This control sample is for comparison of the interaction between chemical functionalization route and physical deposition route, which is shown in section 3.4.3.3)

Instrumentations for chemical, physical and electrical characterization

Raman spectroscopy system

The data for Raman spectroscopy was obtained using Horiba spectrometer (iHR550 f/6.4, 50 micron slit) connected to an optical microscope (Olympus BX51) *via* a collimator. A

thermoelectric cooled Synapse CCD camera (SYN-1024x256- BIDD) (-75ºC) used to collect Raman signal. Furthermore, a laser excitation wavelength of 532 nm (power of 20 mW) was used with spot size of 1 μm. The focal length of Horiba spectrometer is 550 mm, which was connected to a collimator *via* 100 μm optical fiber cable. The 100X objective (NA =0.9), the integration time of 0.1 s, and 600 l/mm grating were used to examine all MoS_2 and Au-MoS_2 samples. The SiO_2/Si substrate (~520 cm^{-1}) was used as a reference to calibrate the Raman instrument.

Thermal conductivity measurement set-up

Raman spectroscopy provides an indirect route to measure thermal conductivity of nanomaterials. It is essential to measure the Raman shift as respect to reflected laser power, and as respected to sample temperature (as discussed later in the result and discussion section). The 2400 l/mm grating was used here to provide high spectral resolution. The contact time is 0.5 s to increase the intensity of the peak.

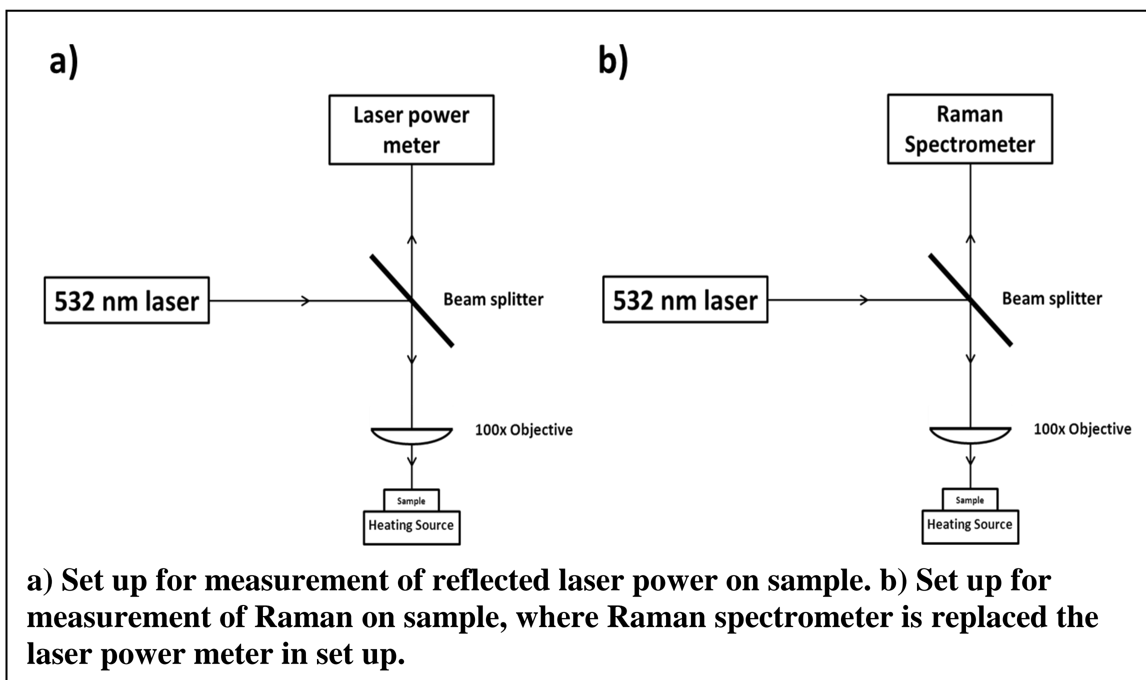

a) Set up for measurement of reflected laser power on sample. b) Set up for measurement of Raman on sample, where Raman spectrometer is replaced the laser power meter in set up.

The reflected laser power is varied by inserting a 532 nm laser power filter (50%, 90%, and 99.5%). The reflected laser power was measured using laser power meter (as shown in above figure a). Using the current set up or the Raman data (above figure b), the at the minimal power (99.5% inserted power filter), the temperature of the sample is varied (25^oC, 40^oC, and 55^oC), and the Raman signals are measured. In the other hand, at room temperature, the reflected power laser (100%, 50%, 10%, and 0.5%), is varied, and the Raman signals are measured. Furthermore, this thermal conductivity was setup for the measurement for both bare and gold functionalized (*via* microwave process) trilayer MoS_2 supported on 300 nm SiO_2 (mechanical exfoliation)[10].

Field emission scanning electron microscope (FESEM)

The FESEM image was collected using FEI Company Nova NanoSEM 430. The acceleration voltage was used as 10-30 kV with ETD detector, and spot size of 3.5.

Transmission electron microscope (TEM)

The TEM image was collected using FEI-CM100 TEM. The acceleration voltage was 100 kV.

Cryostat electrical system

The setup is similar to that described in the experimental section of pervious chapters. The electrical measurements of MoS_2 and Au-MoS_2 samples were carried out in Janis ST100 cryogenic probe station under high vacuum ($<5 \times 10^{-6}$ Torr). Lakeshore temperature controller (model 336) provided the control of the temperature of sample. The Keithley 2612 dual-channel system source meter connected to a computer *via* a GPIB/IEEE-488 interface card. The I-V characteristic was measured by varying the current, and measured the voltage. Gating was performed by keeping the

source-drain voltage constant and measuring the change in conductivity with the gate voltage, which was applied to the heavy-doped silicon backgate.

Results and Discussion

The mechanism of Au incorporation into MoS_2 *via* chemical route functionalization and the corresponding structural characterization structural characterization

The formation of these nanostructures commence with creation of metal nuclei *via* nanoscale-crystallization of chemically reduced metal ions. **Figure 5.1a** is the mechanistic representation of this functionalization process, where the hydroxyl amine reduces Au^{3+} (Ag^{+}) to Au^{0} (Ag^{0}) ($HAuCl_4 + NH_2OH \rightarrow Au + 4\ HCl + NO$). The defects and edges on MoS_2 contain partially-unbound sulfur, which binds with Au or Ag and act as sites for metal nuclei seeding and their subsequent growth into bigger nanostructures *via* Au^{0} (Ag^{0}) crystal-incorporation. The Au (or Ag) radicals can also incorporate onto the gold nanostructures (GNs) in solution[11,12] and may later anchor onto MoS_2[13–15]. Furthermore, oxygen can dissociate the Mo-S-Mo bond, resulting in increased defects[16] with reaction time: 2h (**Figure 5.1d**), 6h (**Figure 5.1f**) and 24 h (**Figure 5.1e**) of reaction shows increase in the functionalization density with time.

Here, the rate of nucleation, J (i.e. the number of nuclei formed per unit time per unit volume), can be expressed in the form of the Arrhenius reaction velocity equation[17] ($J = A \exp[\frac{(\Delta E_{des} - \Delta E_d - \Delta G_{crit})}{kT}]$), where ΔG_{crit} is the critical excess free energy (nucleation); ΔE_{des} is the atomic activation energy of desorption, ΔE_d is the surface diffusion activation energy, k is the Boltzmann constant, and T is the temperature[17]. These nuclei grow to form highly faceted seed particles. It is known that heterogeneous nucleation (on a suitable surface (like MoS_2)) occurs with lesser change in free energy compared to the spontaneous nucleation process in super-saturated

homogeneous systems[17]. The strong affinity of metal nuclei towards valency-deficient sulfur on MoS_2 surface leads to its anchoring on MoS_2, which acts as the heterogeneous substrate. Furthermore, these seed-particles moving randomly in solution stick onto MoS_2 with specific lattice facets depending on their chemical potential (υ). Since the sulfur atoms at the edge of the sheets as well as those on surface defects are valency deficient, the gold nuclei get preferentially incorporated during the initial phase of the reaction (as shown in **Figure 5.2**). The phenomenon is more pronounced in microwave based instantaneous gold nucleation and incorporation process, which will be discussed in next section (**Figure 5.4a**).

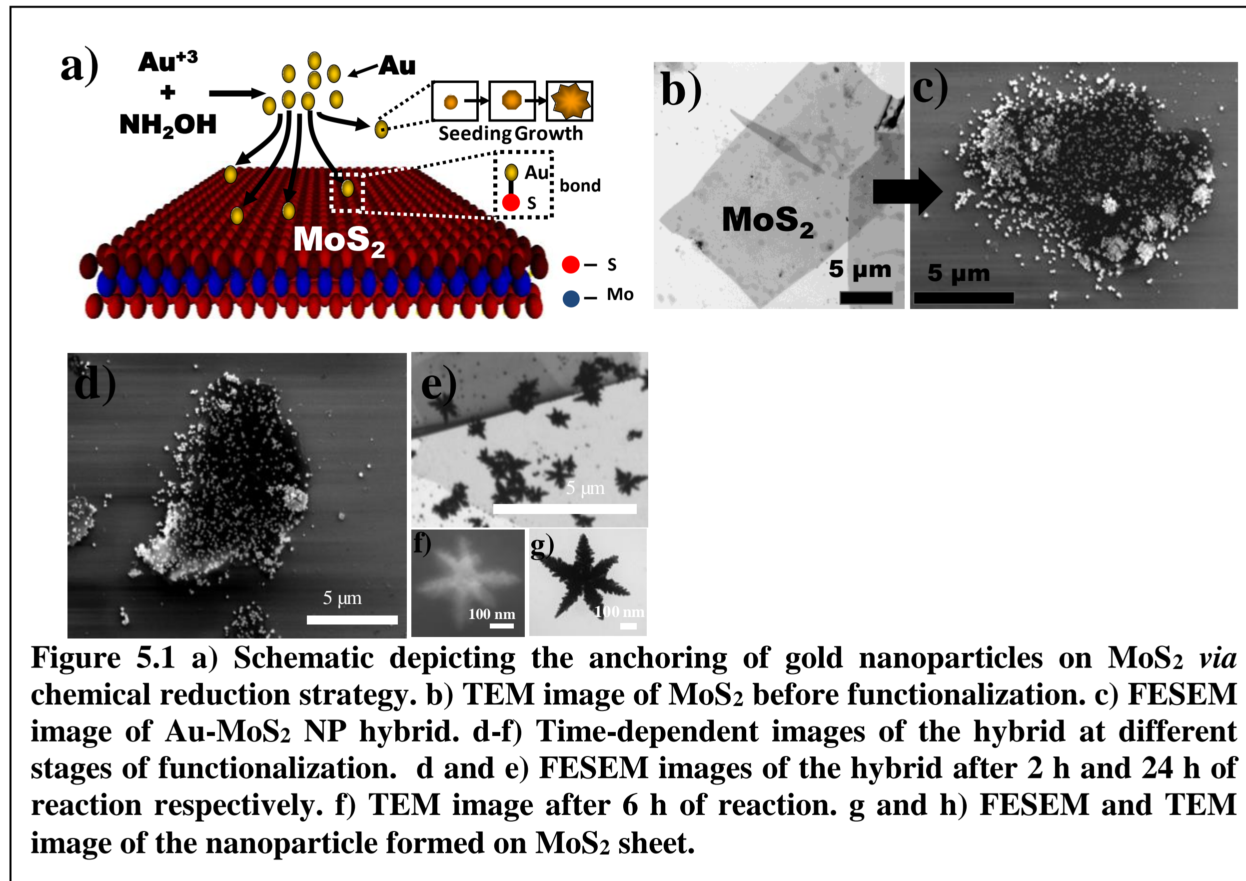

Figure 5.1 a) Schematic depicting the anchoring of gold nanoparticles on MoS_2 *via* chemical reduction strategy. b) TEM image of MoS_2 before functionalization. c) FESEM image of Au-MoS_2 NP hybrid. d-f) Time-dependent images of the hybrid at different stages of functionalization. d and e) FESEM images of the hybrid after 2 h and 24 h of reaction respectively. f) TEM image after 6 h of reaction. g and h) FESEM and TEM image of the nanoparticle formed on MoS_2 sheet.

Chemically exfoliated[2], substrate-immobilized MoS_2 sheet functionalized with Au NP (**Figure 5.1e**, FESEM) show star-shaped GNs (SGNs) and dendritic structures with anisotropically rough arms embedded on the MoS_2 sheet (see **Figure 5.1g**). The dendritic

structure formation involves the surface catalyzed seeded growth of nanoparticles on MoS_2, which is based on diffusion limited growth[11]. The total rate of formation of GNs (r_F) is governed by the rates of diffusion of Au^{3+} onto the MoS_2 surface (r_D) and the rate of Au incorporation into a growing dendritic structure (r_G); $r_F^{-1} = r_D^{-1} + r_G^{-1}$. Here, $r_G >> r_D$, since metal incorporation is catalytic. Therefore, the dendritic structure is governed by rate of diffusion (r_D), which has a strong dependence on temperature. Consistently, our reaction at the room temperature exhibited the SGNs, at 4 ^{0}C the process yielded comparatively smaller particles with lower density and at higher temperature of 60 ^{0}C a larger density of irregular fractal structures of NPs was produced (as shown in **Figure 5.2b-d**).

At lower temperature, the resistance for diffusion (k_D^{-1} α $T^{-1.5}$) and particle incorporation (k_G^{-1} α $\exp(E_A/(RT))$) increases leading to a smaller particle size and lower density. At room temperature, k_D (< k_G) is believed to increase more than k_G and will result in the formation of dendritic structures. Moreover, due to the difference in the surface chemical potential (υ) induced by small deformations, anisotropic growth occurs. As suggested by Mullins-Sekereka instability[18,19], irregular surfaces with high υ grow more preferentially than blunt surfaces with low υ. Furthermore, high mass-transfer rates and the chemical potentials at higher temperatures result in a nanoparticle-cluster formation on MoS_2 surfaces. Since this is diffusion limited process conducted over a large time-scale, the selectivity with respect to edge is low. Micrographs of Ag NPs functionalization can be found in **Figure 5.2e**.

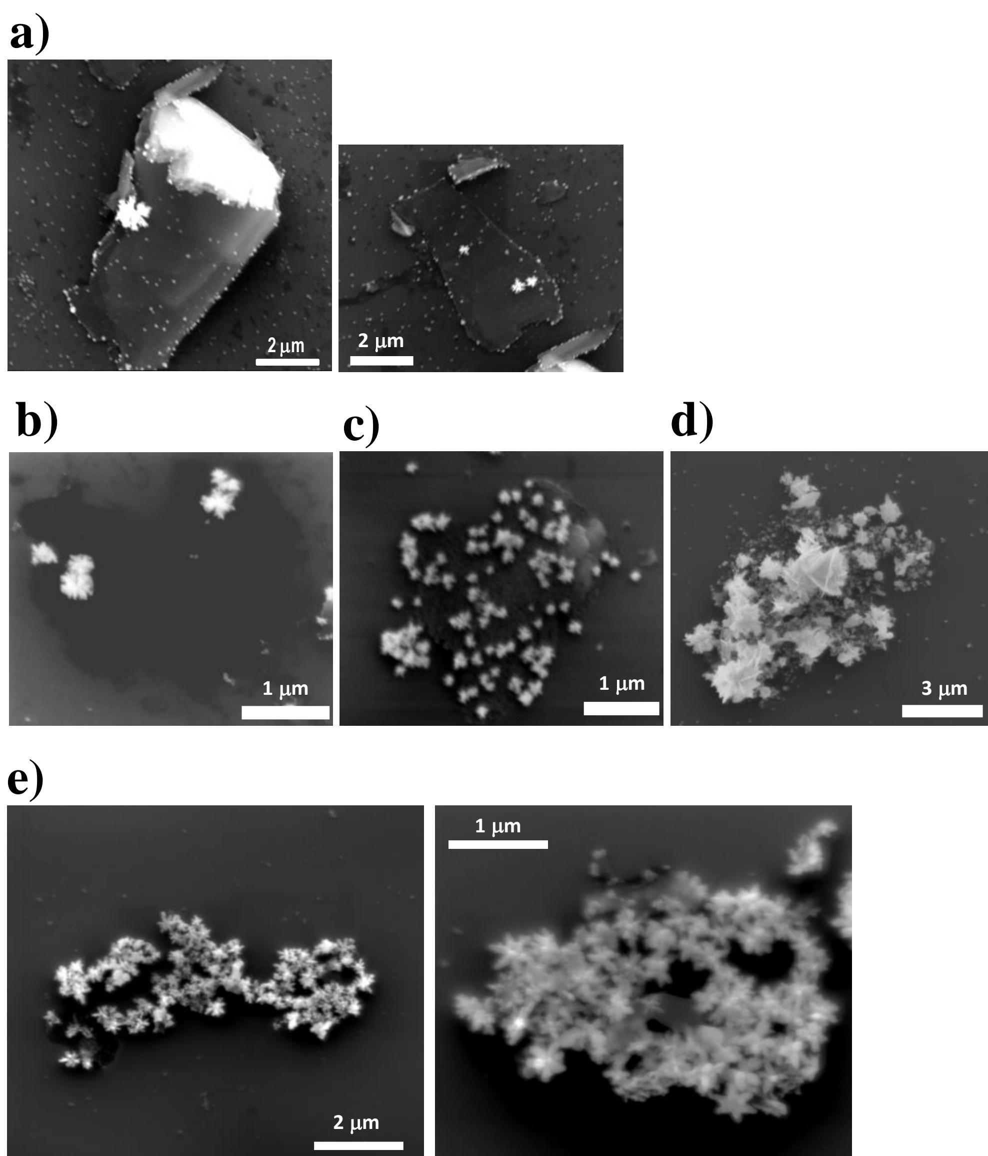

Figure 5.2 a) FESEM images of multilayered MoS_2 preferentially functionalized at the edges during the initial phases of the chemical reduction reaction. b-d) FESEM images of Au-MoS_2 composite prepared using chemical reduction route done at different temperatures, b) 4 °C, c) 25 °C and d) 60 °C. e) FESEM images of Ag-MoS_2 composite prepared using chemical reduction route.

It is important to mention that MoS_2 acts as a stabilizing agent for the GNs, since in the absence of MoS_2 the NPs settle down to the container floor. As shown in **Figure 5.3**, The formed composite was analyzed using energy dispersive spectroscopy (EDS), and the elemental maps and the EDS spectrum validating the formation of proposed hybrid structure.

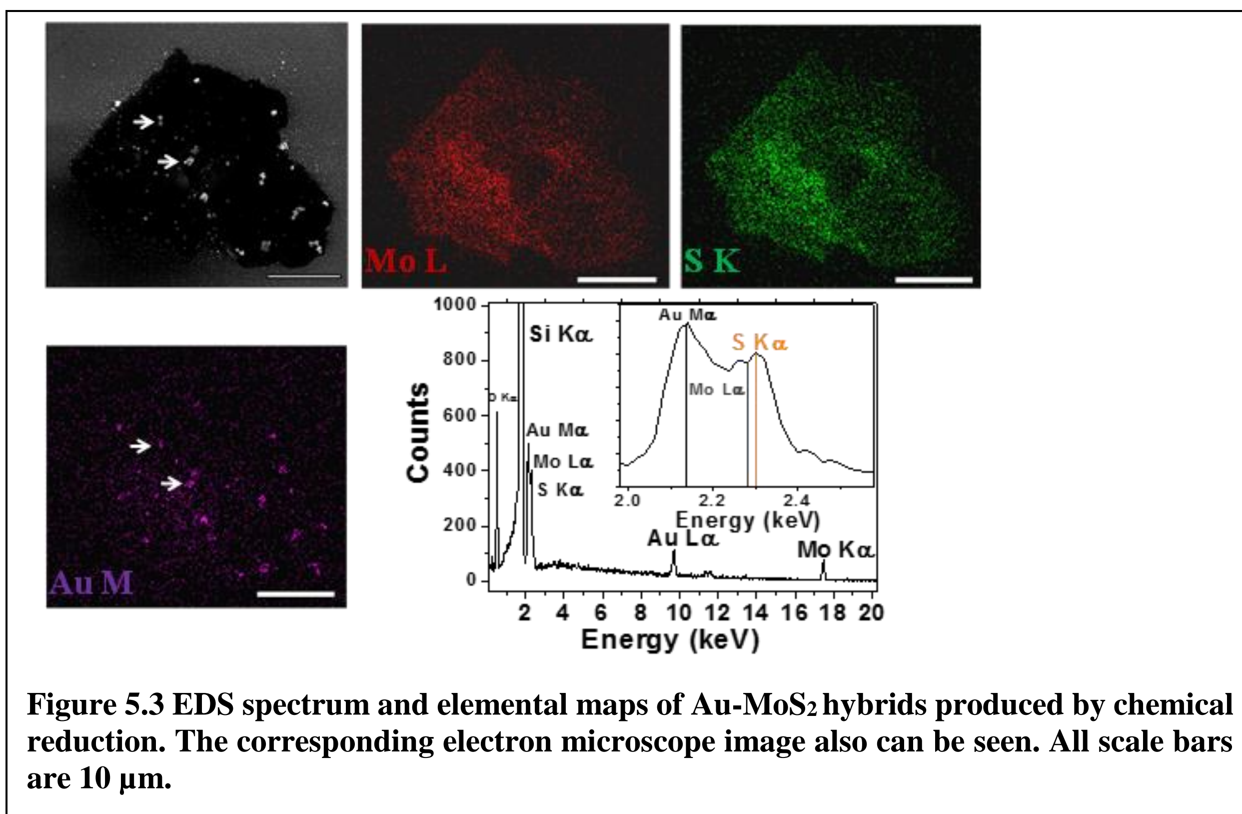

Figure 5.3 EDS spectrum and elemental maps of Au-MoS_2 hybrids produced by chemical reduction. The corresponding electron microscope image also can be seen. All scale bars are 10 µm.

The mechanism of Au incorporation into MoS_2 *via* microwave route functionalization and the corresponding structural characterization

Metal NP incorporation onto MoS_2 sheets can also be induced by microwave (MW) aided instantaneous reduction and incorporation (**Figure 5.4a**). The mechanism of attachment is similar to that for chemically reduced Au, where the valency deficient sulfur atoms in the matrix act as nucleating and anchoring sites (**Figure 5.4b-c**) for Au NP hybrids; however, the process of nucleation, implantation, stabilization on the MoS_2 sheets and nuclei growth is simultaneous and expeditious. This is due to high local temperatures, which eliminates diffusion limited growth and dendritic structure formation, while ensuring that large density of nanoparticles is embedded onto the sheets. Here, microwave induces space-confined heating given by $E = f\varepsilon'(\tan \delta)P^2$, where P is the microwave power, f is the frequency of the microwave, ε' is the dielectric constant of the

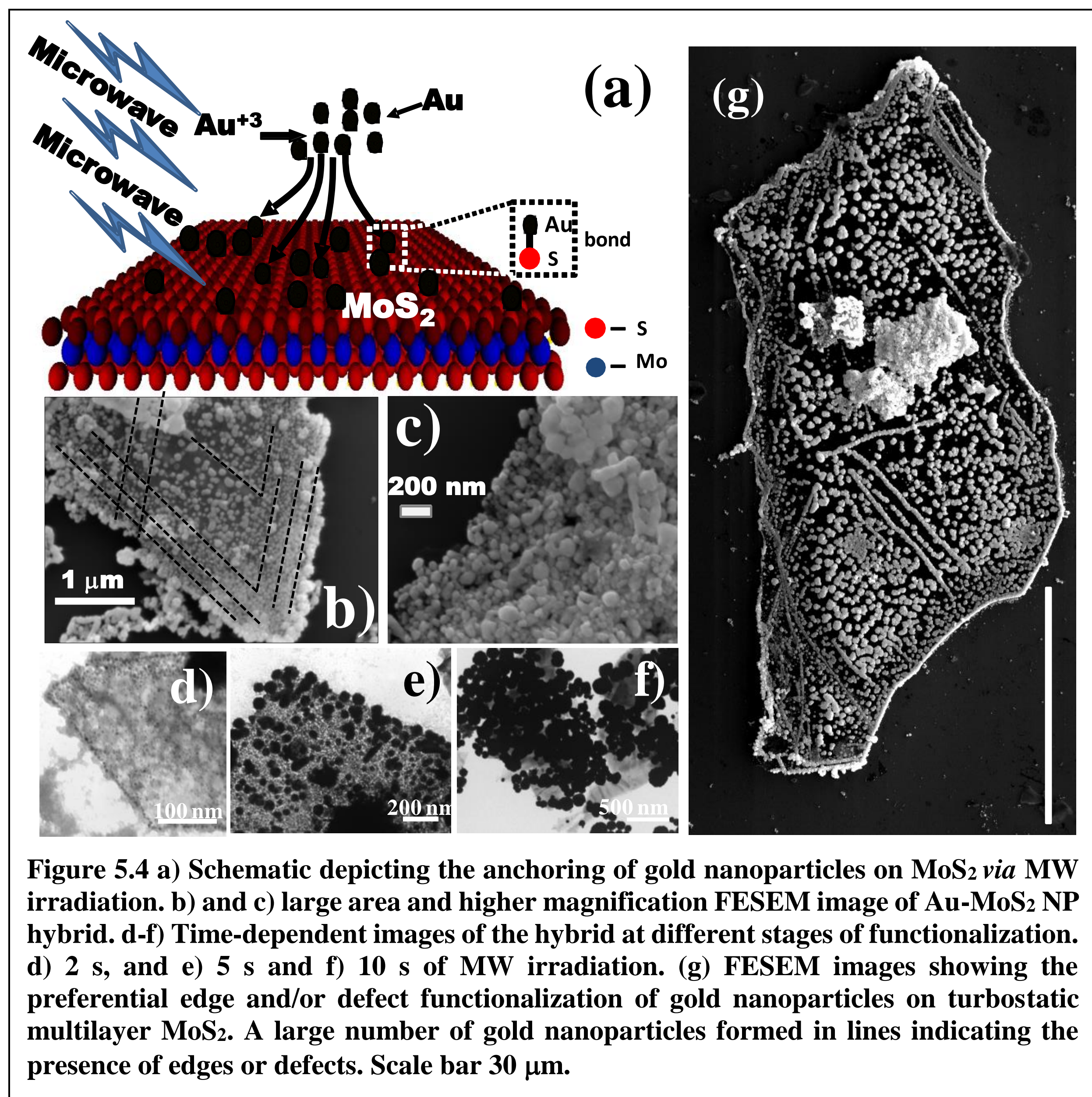

Figure 5.4 a) Schematic depicting the anchoring of gold nanoparticles on MoS_2 *via* MW irradiation. b) and c) large area and higher magnification FESEM image of Au-MoS_2 NP hybrid. d-f) Time-dependent images of the hybrid at different stages of functionalization. d) 2 s, and e) 5 s and f) 10 s of MW irradiation. (g) FESEM images showing the preferential edge and/or defect functionalization of gold nanoparticles on turbostatic multilayer MoS_2. A large number of gold nanoparticles formed in lines indicating the presence of edges or defects. Scale bar 30 μm.

solvent, and δ is the loss factor. In high dielectric solvents such as water the rapid dipolar rotations of the polarized water molecules creates local heating and regions of high kinetic energy. This reduces the barrier and duration of ion reduction, nucleation, and incorporation, leading to formation of NPs on MoS_2 (Note: Total time of MW is 2 – 15 s). Here, reduction and nucleation are independent, while incorporation process is dependent on the interaction between the metal and sulfur, which is higher at the edges even for small duration of MW exposure. It is for this

reason that the gold nanoparticle deposition on MoS_2 edges is clearly evident (**Figure 5.4b** and **Figure 5.4g**).

This was verified further by using a multilayered MoS_2, where functionalization occurs preferentially on the edges on the multilayer structures, indicated by the formation of NPs in straight lines (**Figure 5.5**) with angular displacement of 60°, evidence of crystallographic

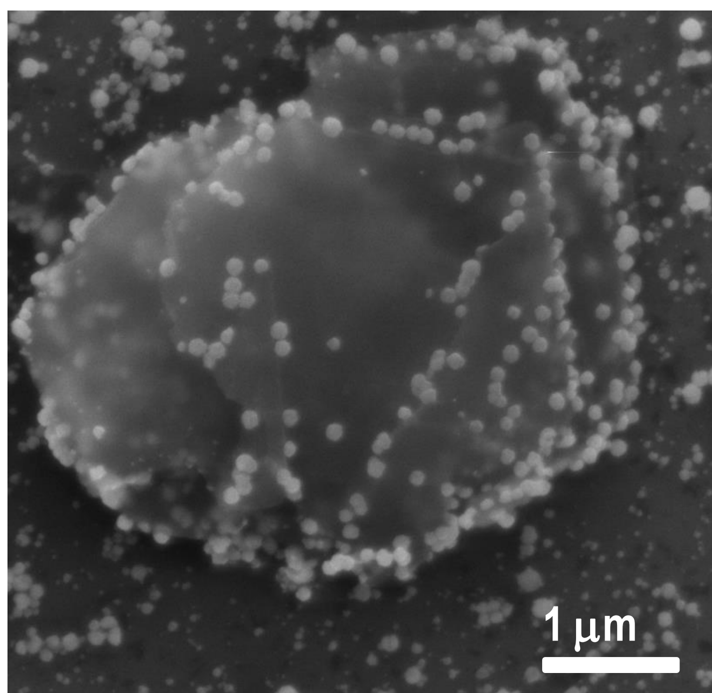

Figure 5.5 FESEM images of multilayered MoS_2 preferentially functionalized at the edges during the initial phases of microwave irradiation.

deposition of metal nanostructures. On turbostatic crystals, the angle can be variable; however, the NP deposition on straight lines is still observed (**Figure 5.4b**). Consistently, the selectivity of functionalization on the edges is higher at smaller durations of MW irradiation (2 s) (as shown in **Figure 5.4d** and **Figure 5.5**), while the number-density and size of the nanoparticles formed is higher for longer irradiation times (**Figure 5.4d-f**). Furthermore, the density of GNs produced on physically exfoliated MoS_2 (on substrate) was lesser than for solution dispersed MoS_2. This is

attributed to a low degree of surface defects on physically exfoliated MoS_2. Furthermore, the lack of capping molecule on the anchored gold nanoparticles implying their high catalytic efficiency[12].

The structural characterization is further confirmed through the transmission electron microscopy (TEM). Similar to the observed images of FESEM, the selectivity of NPs at the edge is favorable due the excessive dangling bond of sulfur. As shown in **Figure 5.6**, the TEM images further confirms an intimate contact between MoS_2 and Au NPs in the hybrid.

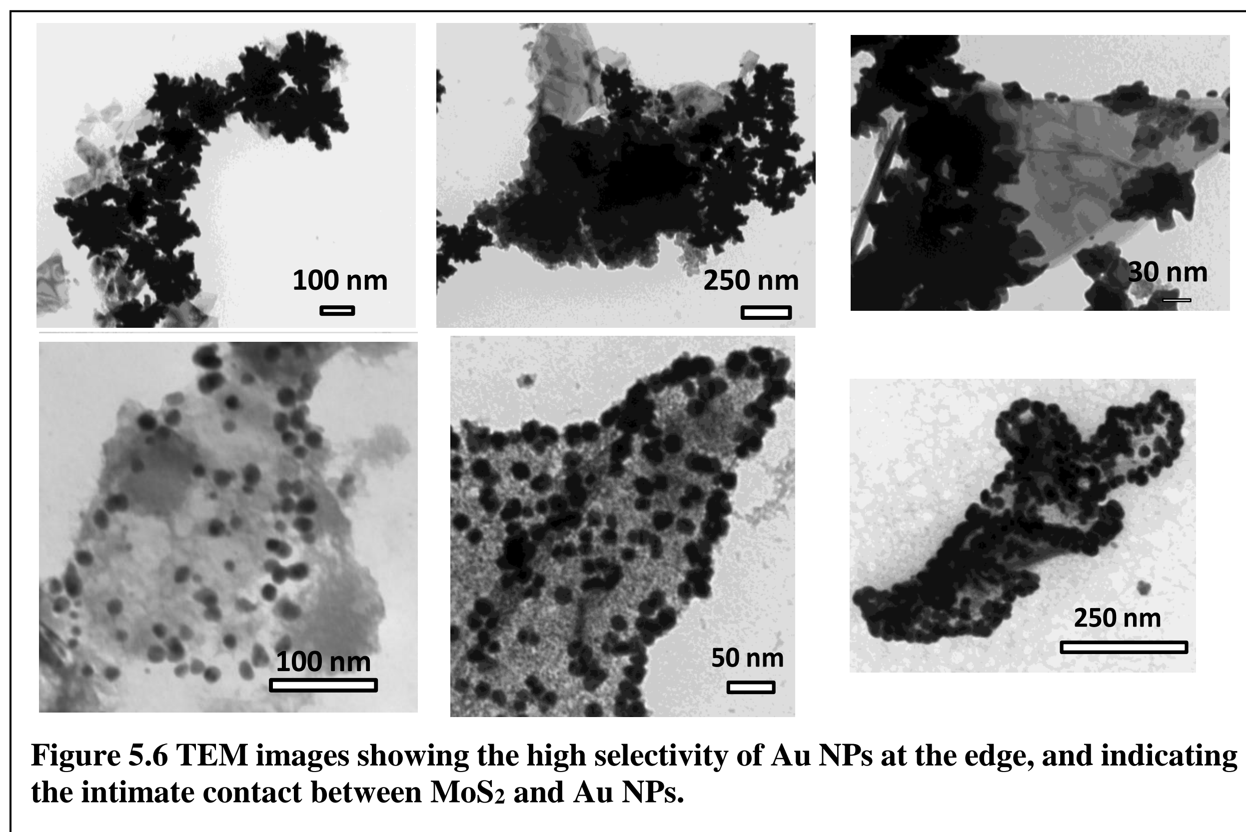

Figure 5.6 TEM images showing the high selectivity of Au NPs at the edge, and indicating the intimate contact between MoS_2 and Au NPs.

Raman characterization for metal-nanoparticles incorporated MoS_2

The effect of formation of such a hybrid on the lattice of MoS_2 was analyzed using Raman spectroscopy. The pristine MoS_2 and MoS_2-gold NP hybrid were analyzed using Raman spectroscopy (**Figure 5.7a-b**), which shows the E^1_{2g} (~391 cm^{-1}) and A_{1g} (~417 cm^{-1}) peaks corresponding to the in plane (2 S atoms in opposite direction to the Mo atom) and out of plane (S

atoms in opposite directions) vibrations for bulk MoS_2 (**Figure 5.7c**)[20]. The difference in the peak positions, Δ (difference between the E^1_{2g} and A_{1g} peak positions), is known to be an indicator of the number of layers[3]. Here, when the number of layers increases, the van der Waals force between MoS_2 sheets results in a higher force constant for atomic vibration. This affects the E^1_{2g} peak predominantly and results in its blue shift. On the other hand, stacking-induced long-range Coulombic interlayer interactions result in a redshift of atomic vibrations, predominantly observed in A_{1g}. As a combined effect, the energy gap (Δ) between E^1_{2g} and A_{1g} decreases with reduction in

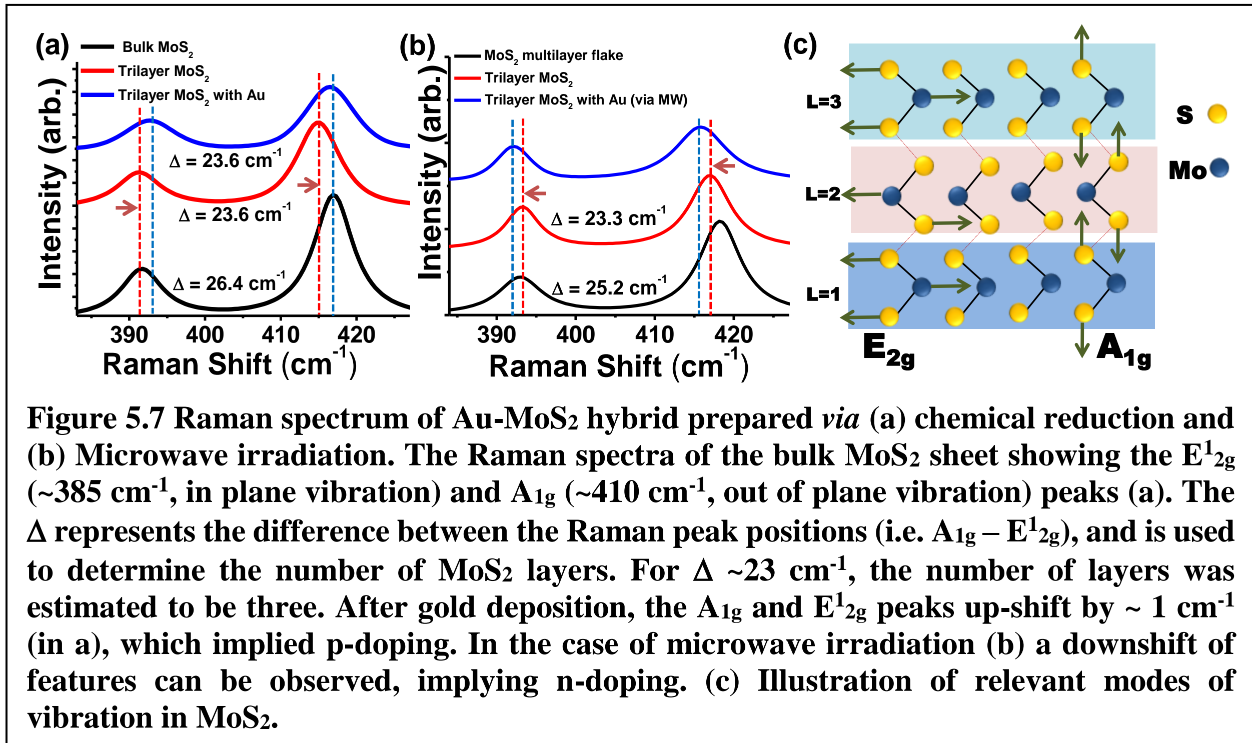

Figure 5.7 Raman spectrum of Au-MoS_2 hybrid prepared *via* (a) chemical reduction and (b) Microwave irradiation. The Raman spectra of the bulk MoS_2 sheet showing the E^1_{2g} (~385 cm^{-1}, in plane vibration) and A_{1g} (~410 cm^{-1}, out of plane vibration) peaks (a). The Δ represents the difference between the Raman peak positions (i.e. $A_{1g} – E^1_{2g}$), and is used to determine the number of MoS_2 layers. For Δ ~23 cm^{-1}, the number of layers was estimated to be three. After gold deposition, the A_{1g} and E^1_{2g} peaks up-shift by ~ 1 cm^{-1} (in a), which implied p-doping. In the case of microwave irradiation (b) a downshift of features can be observed, implying n-doping. (c) Illustration of relevant modes of vibration in MoS_2.

number of layers[10,16]. Bulk MoS_2 shows a Δ value of 26 cm^{-1}. Our sample after exfoliation exhibited a Δ value 23.6 cm^{-1} suggesting that they are trilayer MoS_2 sheets. Furthermore, the line width for our trilayer samples also increased in comparison to the bulk MoS_2. This is because for bulk MoS_2, the inner layers dominate the Raman intensity resulting in a reduced line width. Thinning down of MoS_2 and the associated structural changes results in the development of

varying force constants between the inner and outer layers of the material inducing an increased line width with decrease in the number of layers[10].

After attachment of Au nanoparticles *via* chemical functionalization, the Raman showed a distinct up-shift of features indicating p-type doping of MoS_2 sheets[21], consistent with recent studies (**Figure 5.7a**)[22]. However, MW assisted functionalization showed a small down-shift of features pointing towards n-type doping as shown in **Figure 5.7b**. Several experiments confirm this trend and indicate the importance of the mode of bonding on the polarity of doping. It is important to mention that MW process did not have hydroxylamine and exhibited higher edge-selectivity, which might have a role to play in doping MoS_2. More studies are required to identify the cause of the difference in doping polarity.

Electrical characterization for metal-nanoparticles incorporated MoS_2

The influence of the metal functionalization (chemical) on the electrical properties of mechanically exfoliated layered-MoS_2 between electrodes (gold, 20 μm channel width) was characterized for the Schottky barrier, gate capacitance of MoS_2, and Au-MoS_2, thermal-barrier, carrier concentration and field effect mobility. Each device was washed in acetone and isopropanol mixture (3:1), dried in N_2 and placed in a cryostat chamber at 10^{-4} Torr. The device was thermally annealed at 120 ^{0}C, followed by electric Joule heating (2V, 2 μA) for 3 hours to remove adsorbates and to reduce contact resistance between MoS_2 and Au contact.

The Schottky-barrier analysis

Due to the mismatched work-function between MoS_2 flakes (~25 nm thick, confirmed by atomic force microscopy (AFM of **Figure 5.8a**) of 5 μm channel,) and metal contacts, a Schottky barrier is introduced at the interface between source/drain electrodes and MoS_2. Here, as the source-drain bias voltage increases, the carrier hopping through the Schottky barrier increases[23].

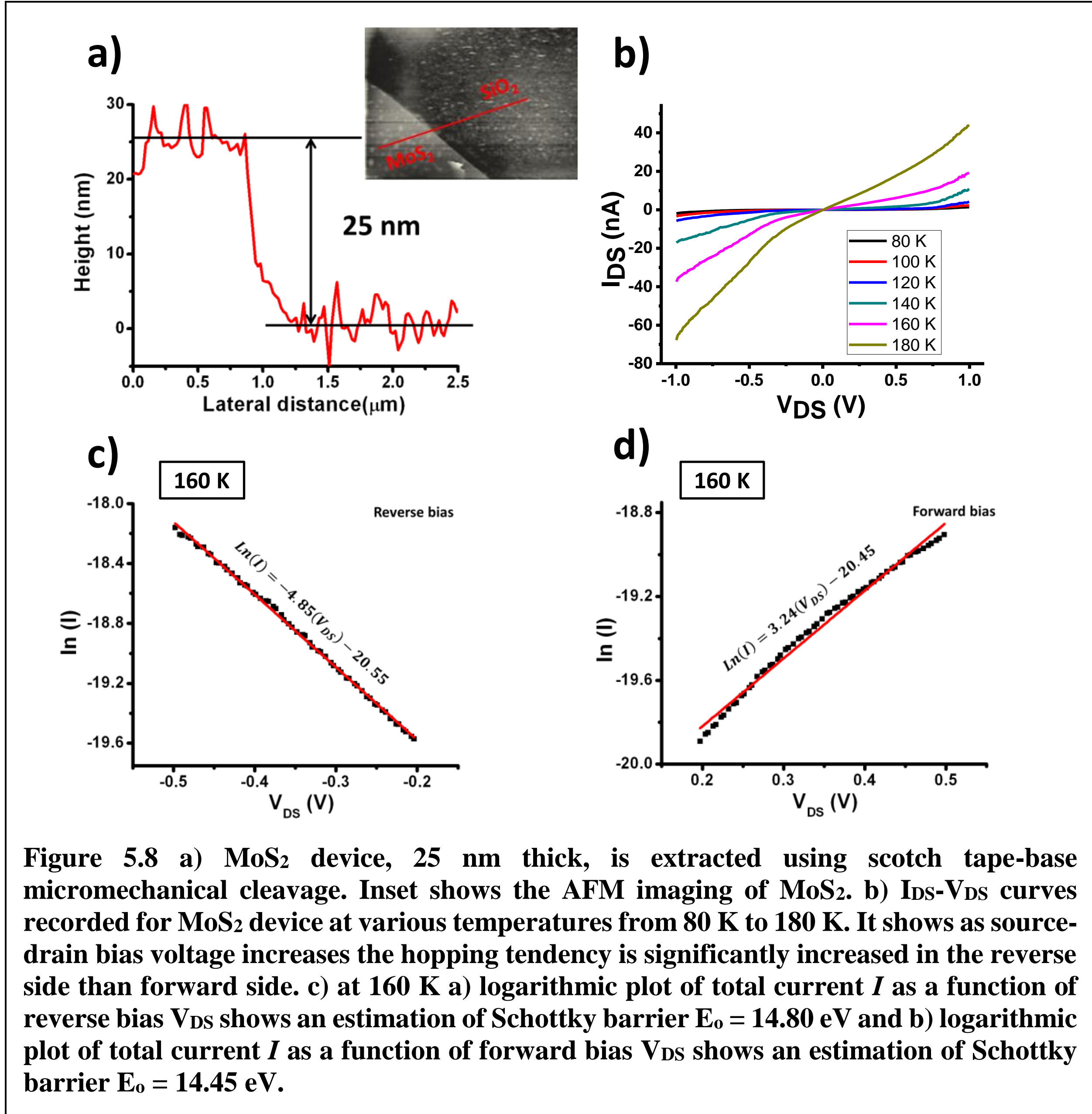

Figure 5.8 a) MoS_2 device, 25 nm thick, is extracted using scotch tape-base micromechanical cleavage. Inset shows the AFM imaging of MoS_2. b) I_{DS}-V_{DS} curves recorded for MoS_2 device at various temperatures from 80 K to 180 K. It shows as source-drain bias voltage increases the hopping tendency is significantly increased in the reverse side than forward side. c) at 160 K a) logarithmic plot of total current *I* as a function of reverse bias V_{DS} shows an estimation of Schottky barrier E_o = 14.80 eV and b) logarithmic plot of total current *I* as a function of forward bias V_{DS} shows an estimation of Schottky barrier E_o = 14.45 eV.

This phenomenon translates into an increase in current at high source-drain voltage in the IV curve as shown in **Figure 5.8b**. Furthermore, at intermediate bias voltage, the total current *I* is governed by the Schottky barrier according to the following equation[24,25]:

$$I = SJ_s \exp\left[V_{DS}\left(\frac{q}{kT} - \frac{1}{E_0}\right)\right] \quad \textbf{Equation 5.1}$$

Linear relationship equation is derived as shown:

$$\ln(I) = \left[\left(\frac{q}{kT} - \frac{1}{E_o}\right)\right] V_{DS} + \ln(SJ_s)$$ **Equation 5.2**

Where J_s is a slowly varying function of applied bias, S is contact area associated with the Schottky barrier, V_{DS} is the source-drain bias voltage, q is magnitude of electron charge, k is the Boltzmann constant, T is the absolute temperature, and E_o is the Schottky barrier, which is estimated to be 14.62 meV (average) is obtained from slope of logarithmic plot of total current I versus V_{DS} (**Figure 5.8c-d**). The carrier density, n (evaluated to be 1.39 x 10^{15} cm^{-3}), carrier concentration of MoS_2 sample, was found from $E_o = E_{oo}\coth\left(\frac{qE_{oo}}{kT}\right)$ with $E_{oo} = \frac{qh}{4\pi}\sqrt{\frac{n}{m^*\varepsilon_r\varepsilon_o}}$, where E_{oo} is the Padovani-Stratton parameter, m^* is effective electron-mass in MoS_2, ε_r is the relative permittivity of MoS_2, ε_o is vacuum permittivity, and h is the Planck's constant. From the calculated carrier concentration, the average electron mobility is estimated to be 3.11 $cm^2V^{-1}s^{-1}$ using the equation $\mu = \frac{1}{nq\rho}$ where ρ is the resistivity of MoS_2 sample. This mobility value is consistent with previous measurements from other groups[26]. The Schottky-barrier analysis cannot be applied on the Au-MoS_2 device due to the added capacitance between MoS_2 and the Au NP islands (discussed in later section).

MoS_2 field effect mobility analysis

Figure 5.9a shows the current-voltage (I_{DS}-V_{DS}) behavior of a 5 μm channel of MoS_2 flake before and after gold NP deposition. Post Au NP incorporation, the device exhibits 3 orders of magnitude increase in conductivity at 80 K. From the V_{BG} versus I_{DS} at 160 K (as shown in **Figure 5.9b**), the field-effect mobility was estimated as ~ 3.71 cm^2 $V^{-1}s^{-1}$ for MoS_2 device using the equation:

$$\mu = \left(\frac{L}{W}\right)\left(\frac{dI_{DS}}{dV_{BG}}\right)\left(\frac{V_{DS}}{C_{BG}}\right)$$ **Equation 5.3**

where L/W ~ 70 is the ratio between channel length and width, V_{DS} is the source-drain voltage, and $\left(\frac{dI_{DS}}{dV_{BG}}\right)$ is the absolute value of the linear slope of the back-gating curve. At a voltage bias of V_{DS} = 500 mV, the current on/off ratio: I_{on}/I_{off} is ~10^3 for the ± 20 V range of V_{BG}, with the off-

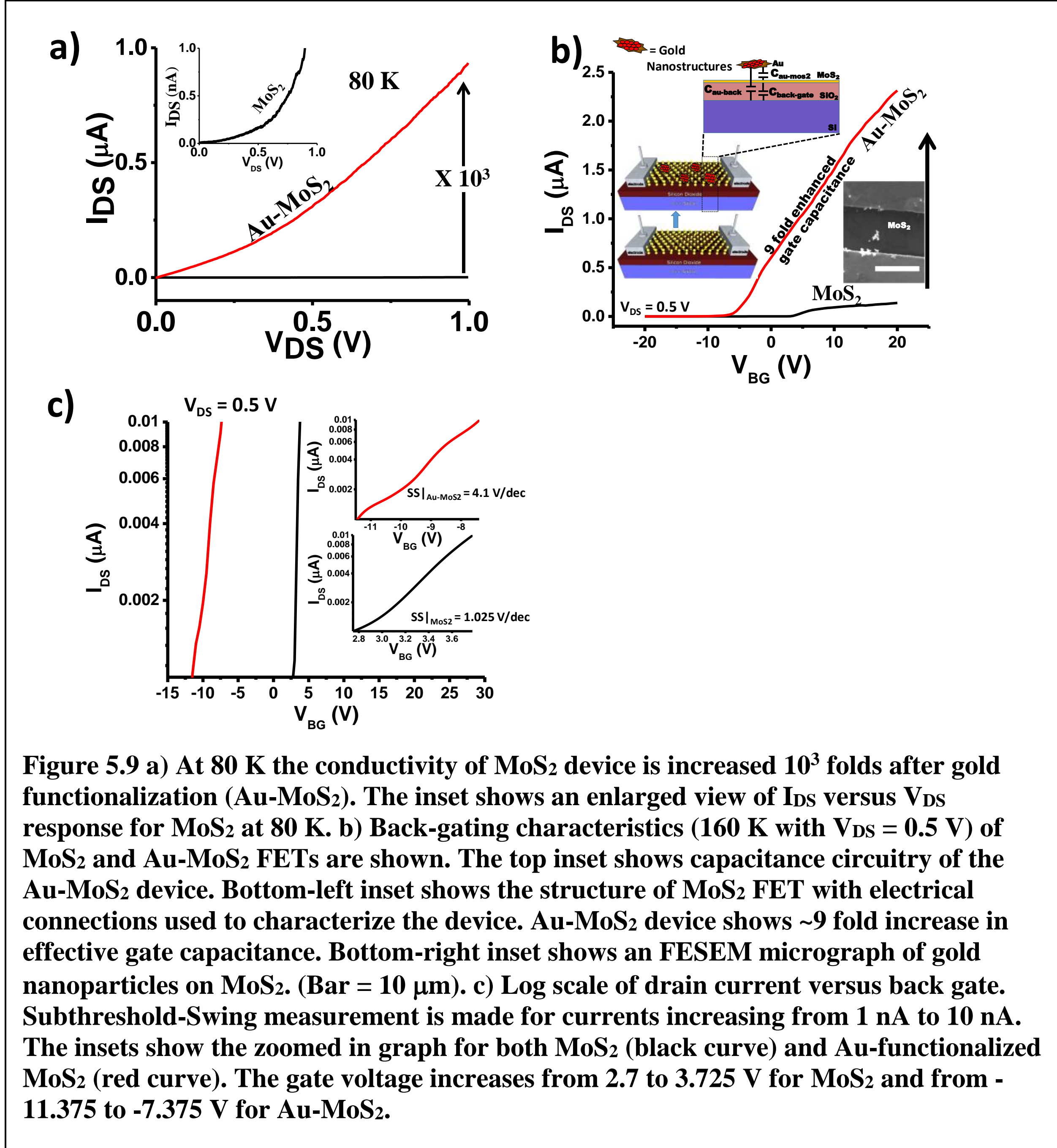

Figure 5.9 a) At 80 K the conductivity of MoS_2 device is increased 10^3 folds after gold functionalization (Au-MoS_2). The inset shows an enlarged view of I_{DS} versus V_{DS} response for MoS_2 at 80 K. b) Back-gating characteristics (160 K with V_{DS} = 0.5 V) of MoS_2 and Au-MoS_2 FETs are shown. The top inset shows capacitance circuitry of the Au-MoS_2 device. Bottom-left inset shows the structure of MoS_2 FET with electrical connections used to characterize the device. Au-MoS_2 device shows ~9 fold increase in effective gate capacitance. Bottom-right inset shows an FESEM micrograph of gold nanoparticles on MoS_2. (Bar = 10 μm). c) Log scale of drain current versus back gate. Subthreshold-Swing measurement is made for currents increasing from 1 nA to 10 nA. The insets show the zoomed in graph for both MoS_2 (black curve) and Au-functionalized MoS_2 (red curve). The gate voltage increases from 2.7 to 3.725 V for MoS_2 and from -11.375 to -7.375 V for Au-MoS_2.

state current smaller than 100 fA (as shown in **Figure 5.9b**). **Figure 5.9c** shows the subthreshold

voltage, which is estimated as the gate-voltage per current-decibels from the gating data for currents increasing from 1 nA to 10 nA or 1 decibel. The sub-threshold swing for MoS_2 increases from 1.025 to 4.1 V/dec after Au-functionalization in our device.

The enhancement in gate capacitance

It is known that a top gate electrode (disconnected) along with a bottom gate enhances the net gate capacitance; implying that at lower gate voltage a higher change in source-drain current (I_{DS}) can be achieved[27]. The Au NP deposition on MoS_2 is proposed as an unconnected top gate with very high capacitance ($C_{Au\text{-}MoS2}$), which leads to an enhanced effective gate capacitance ($C_{effective}$), when the back gate is applied ($C_{back\text{-}gate}$). Therefore, $C_{effective} = C_{back\text{-}gate} + f(C_{Au\text{-}MoS2}^{-1} + C_{Au\text{-}back}^{-1})^{-1}$, where $C_{Au\text{-}back}$ is the capacitance between gold and silicon and f is the fraction of MoS_2 area with Au NP. Since $C_{Au\text{-}back} > C_{Au\text{-}MoS2} > C_{back\text{-}gate}$, $C_{effective} \approx fC_{Au\text{-}MoS2}$. This implies that the effective capacitance becomes $C_{Au\text{-}MoS2}$, which is higher than the $C_{back\text{-}gate}$. For MoS_2 with gold nanostructures acting as gate enhancers, the slope $\left(\frac{dI_S}{dV_{BG}}\right)$ shows a 9.04 fold increase (as shown in figure 3.9b), implying that effective capacitance increases from 12 nF/cm^2 (= $C_{back\text{-}gate}$) to 108.48 nF/cm^2 (= $C_{effective} \approx fC_{Au\text{-}MoS2}$ = 108.48 nF/cm^2) for an Au NP coverage of ~ 5 %. This implies that the $C_{Au\text{-}MoS2}$ ~ 2.17 μF/cm^2, a value similar to the quantum capacitance for graphene[28–30]. This capacitance coupled with gate electrode provides an enhanced pseudo-mobility[27] of 33.5 cm^2/V/s. It is important to mention that interfacing MoS_2 with high-k dielectric material can cause dielectric suppression of the Coulomb scattering and modification of the acoustic phonon spectrum[5,31,32]. However, that requires higher (complete) coverage of the dielectric. Furthermore, Fuhrer and Hone[27] showed that capacitive interfacing on relatively thicker dielectric produces a two-orders of magnitude higher pseudo-mobility than dielectric suppression. Therefore, capacitive coupling is conjectured as the primary mechanism behind the modified gating behavior of our device.

The analysis of gate capacitance of Au deposition *via* functionalization route and one *via* physical deposition

The strong interaction of chemically deposited Au NP on MoS_2 was compared with sputter deposited Au on MoS_2 *via* analyzing the respective capacitance between deposited Au and MoS_2.

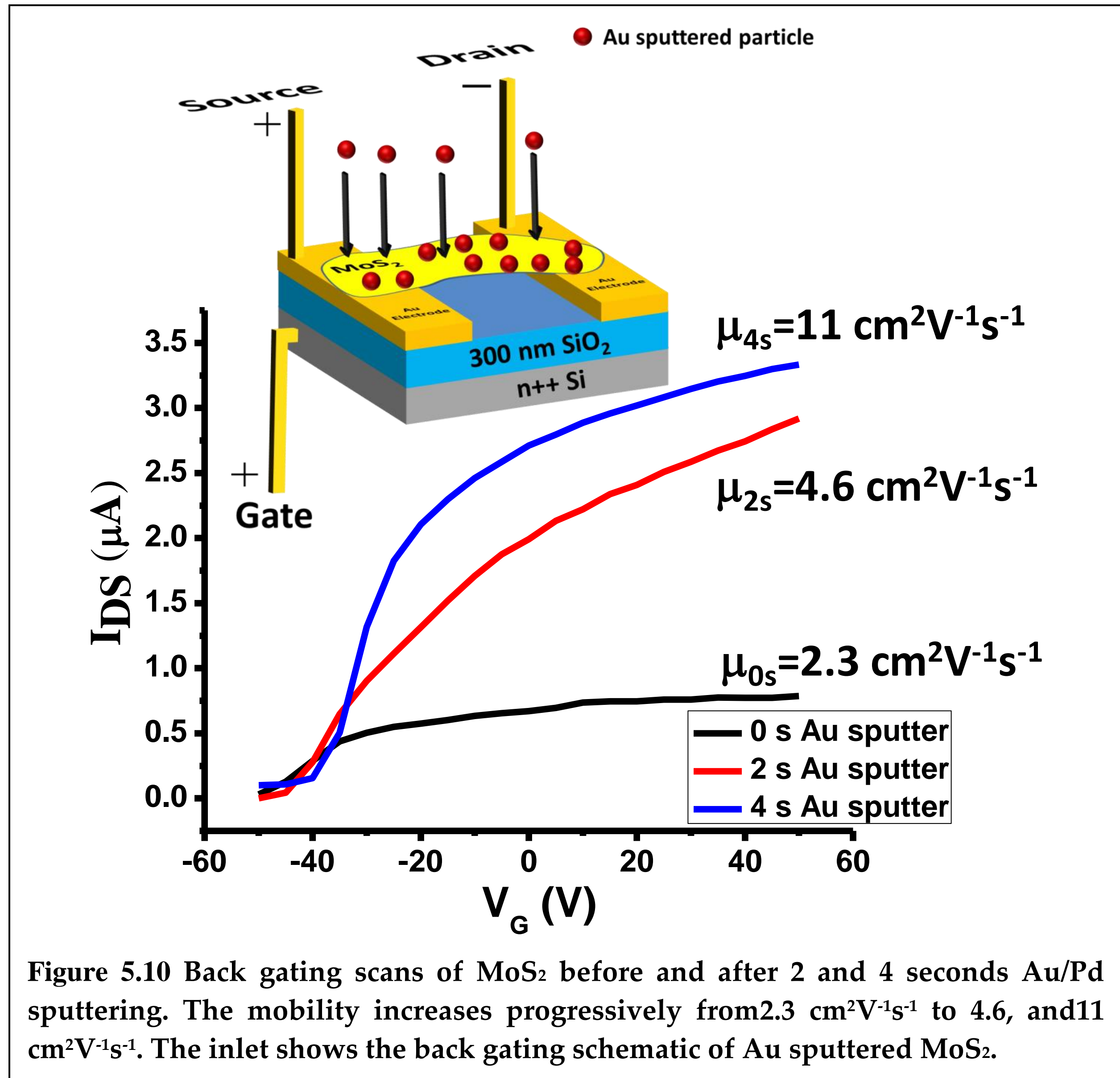

Figure 5.10 Back gating scans of MoS_2 before and after 2 and 4 seconds Au/Pd sputtering. The mobility increases progressively from2.3 $cm^2V^{-1}s^{-1}$ to 4.6, and11 $cm^2V^{-1}s^{-1}$. The inlet shows the back gating schematic of Au sputtered MoS_2.

Figure 5.10 shows the evolution of response in the form of back gating scans of sputtered Au-MoS_2 . After each sputter (0 s, 2 s, and 4s), the back gating mobility of device increased to 2.3,

4.6, and 11 $cm^2V^{-1}s^{-1}$, respectively. At 4 sec sputtering and a 4.78 fold increase in mobility, the capacitance between sputtered gold and MoS_2 was estimated, assuming there is no damage to MoS_2 during sputtering. Here, the $C_{effective} \approx fC_{Au\text{-}MoS2} = 57.39$ nF/cm^2. Hence, the capacitance between sputtered gold and MoS_2 was ~ 3 folds less than $C_{gold\text{-}MoS2}$. This confirms a more intimate contact between MoS_2 and Au deposited *via* chemical process than physical process, as expected. Moreover, gold-sputtered on MoS_2 exhibits lesser n-doping.

The effect of loading density on the I-V behavior

As mentioned above, the final deposition density of gold NP on MoS_2 is dependent on the defect-density on MoS_2. For long duration of functionalization, the device shows ohmic and high

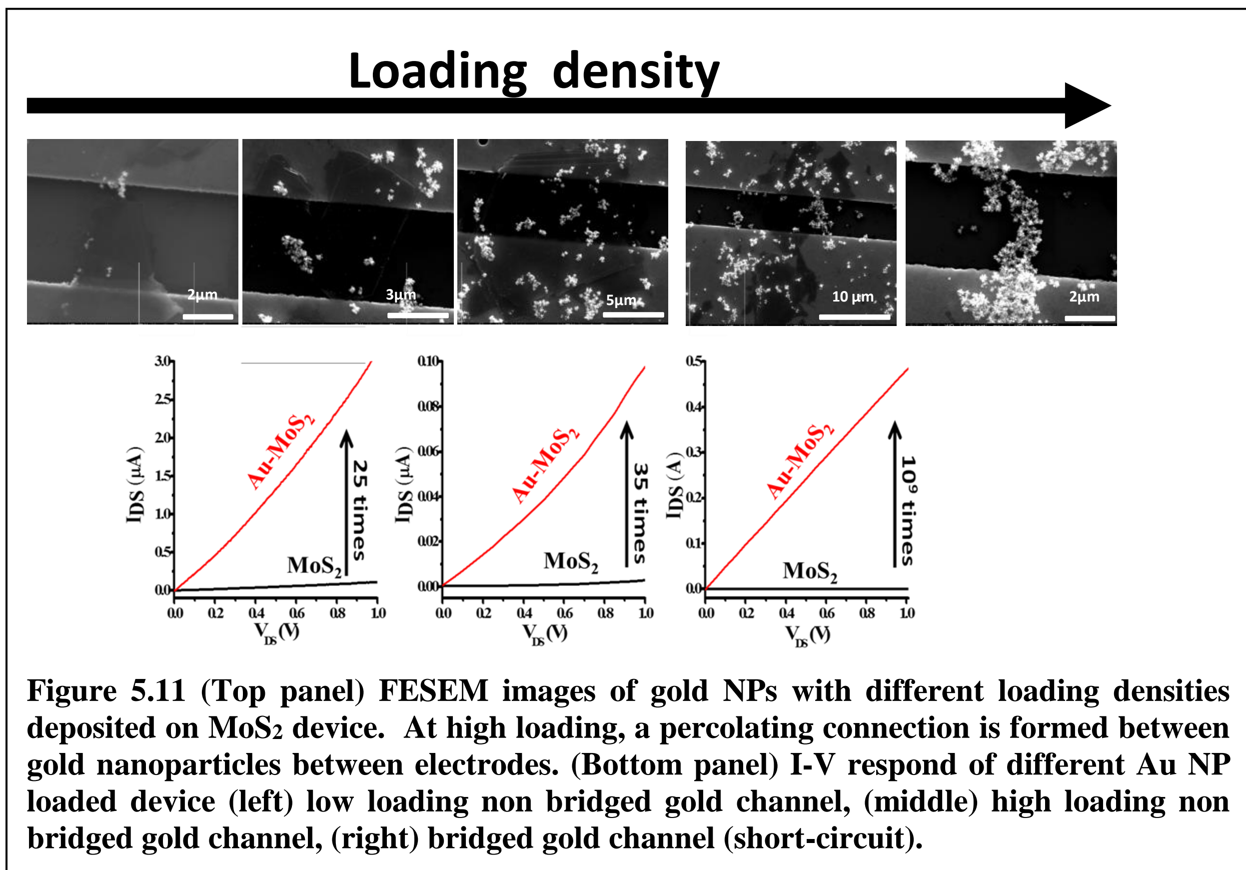

Figure 5.11 (Top panel) FESEM images of gold NPs with different loading densities deposited on MoS_2 device. At high loading, a percolating connection is formed between gold nanoparticles between electrodes. (Bottom panel) I-V respond of different Au NP loaded device (left) low loading non bridged gold channel, (middle) high loading non bridged gold channel, (right) bridged gold channel (short-circuit).

conductivity, attributed to connected gold channels (leakage). As shown in **Figure 5.11** (top panel), as the loading density increase, the deposit Au NP starts to form islands of NPs, to a

percolating network, and finally a connecting bridge between the electrode. At such high loading, The Au NPs tends to make conductive channels between the source and drain, which is indicating by the linearlity of current-voltage curve as shown in **Figure 5.11** (bottom panel).

The effect of the metal's work function on the doping polarity on MoS_2

The polarity of doping induced by metals on MoS_2 strongly depends on the work function (ϕ) of the metal as well as MoS_2. MoS_2 work function (ϕ_{MoS2}) is reported to vary from 4.48 eV to 5.2 eV depending on the layer thickness[33–36]. The same for gold (ϕ_{Au}) is reported to be 5.1 eV. Hence, thin flakes of MoS_2 (multilayer) are known to get n-doped[37] when in contact with gold. Interaction of ultrathin MoS_2 (1-3 layers) can also modulate the work function. In the present study, anchoring of Au NP on trilayer MoS_2 induces a p-doping as verified by Raman spectroscopy (**Figure 5.7a**). This implies that trilayer MoS_2 on silica has work function (and Fermi level position) which allows the electron to flow from MoS_2 to Au, resulting in p-doping. However, our electrical gating measurements show an increase in saturation current after anchoring of Au NPs. The increase in saturation current in n-type MoS_2 implies n-type doping.

The difference in polarity between the Raman (shown in Raman analysis section above) and electrical measurement is due to two things. (1) The MoS_2 sample used for electrical studies are thicker (25 nm, multilayer) compared to the sample used for Raman measurements (trilayer). This in turn translates into a lesser work function. (2) While the sample for Raman measurement was supported on SiO_2, the electrical measurements were done on SiO_2 chips with pre-deposited Au electrodes. The interaction of MoS_2 with Au electrodes modulates the Fermi level of MoS_2 (*via* n-doping[37]) to facilitate the transfer of electron from Au NP to MoS_2 after Au NP deposition as shown in **Figure 5.12**. To verify this, Raman spectra was taken from the sample on Au electrode

before and after Au NP anchoring. The Raman spectra clearly showed a downshift, implying n-doping, consistent to the electrical measurement and the theory.

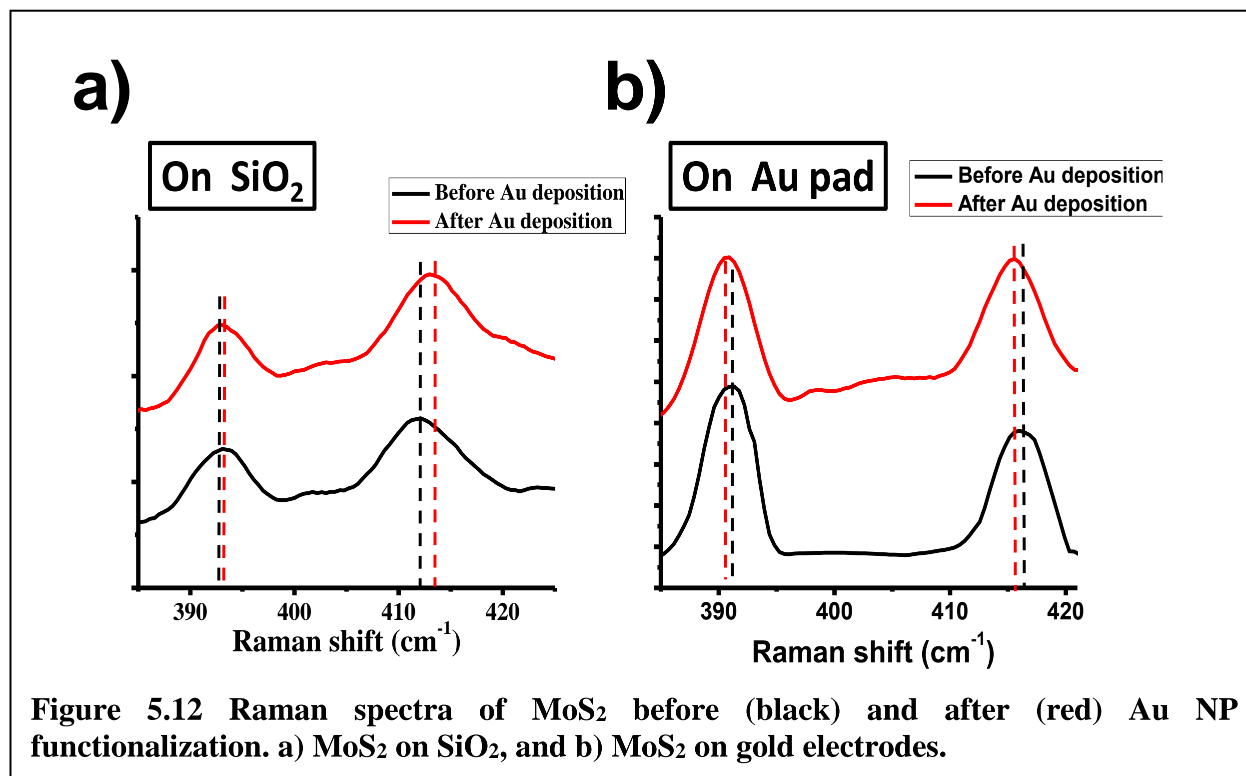

Figure 5.12 Raman spectra of MoS_2 before (black) and after (red) Au NP functionalization. a) MoS_2 on SiO_2, and b) MoS_2 on gold electrodes.

The effect of MoS_2 defects on the electrical behavior

The MoS_2 devices' conductivity scans (I-V), and back gate responses were measured before and after water exposure at 25°C for 24-hour period. In contrast to the Au incorporation, exposing the MoS_2 device with only water for 24 h without gold source causes a reduction a reduction in 4-point probe conductivity (~ 10 folds) and field effect mobility (~ 2.33 folds) are shown in **Figure 5.14a-b**. The observed result can be explained by generation of defects on MoS_2 *via* water interaction (oxidized or thiolated sites), which act as nucleation sites on MoS_2 for incorporation/growth of gold nanoparticles. This observation is consistent with an earlier study on oxidation and hydrolysis of MoS_2 in water[38].

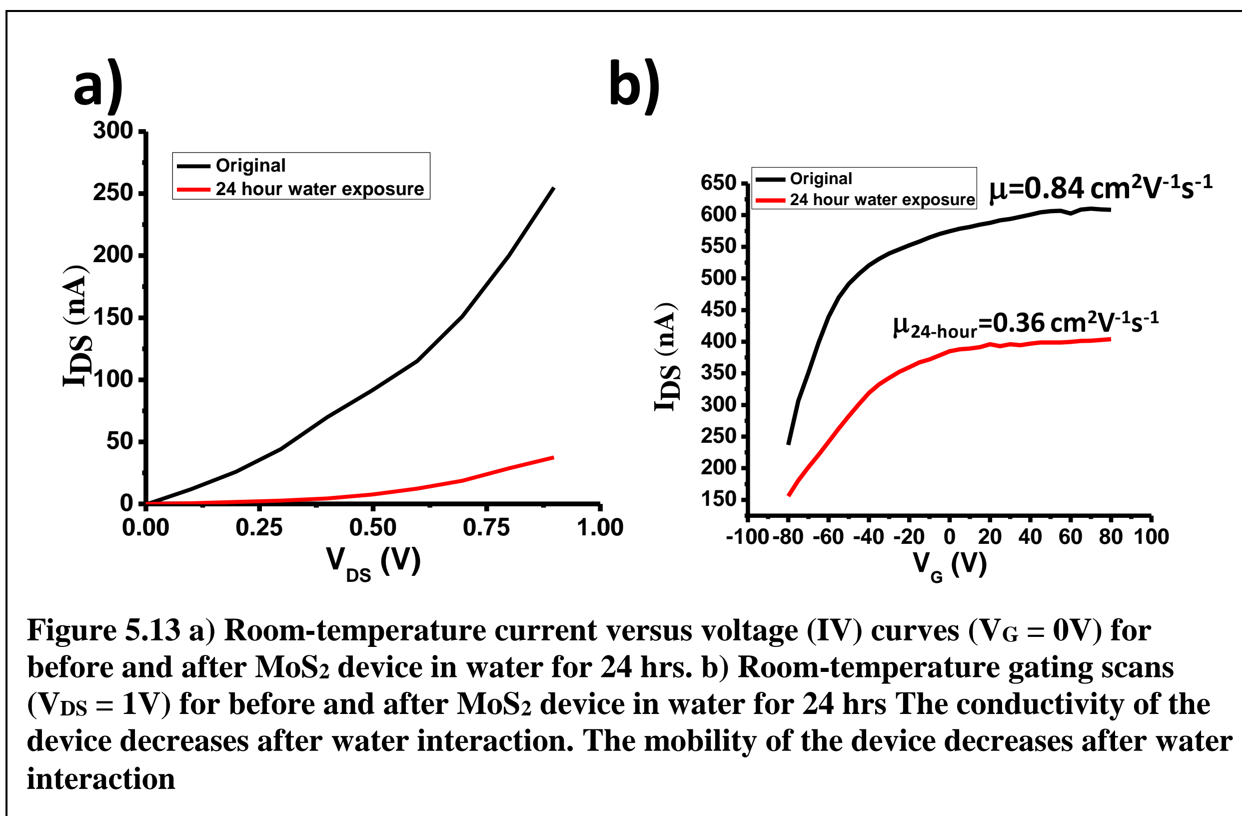

Figure 5.13 a) Room-temperature current versus voltage (IV) curves (V_G = 0V) for before and after MoS_2 device in water for 24 hrs. b) Room-temperature gating scans (V_{DS} = 1V) for before and after MoS_2 device in water for 24 hrs The conductivity of the device decreases after water interaction. The mobility of the device decreases after water interaction

In the other hand, a lesser reduction in conductivity was observed for device exposed to microwave (device immersed in water, under microwave for 5s) as shown in **Figure 5.14a-b**. Here the interaction of MoS_2 and water happens at elevated temperature but for significantly lower interval (5s). Hence the resultant defect formation might be minimal. Furthermore, the presence of metal centers could cause local hotspots, which can create highly elevated temperatures and hence more defects leading to more functionalization. Here, in the absence of metal NPs, only minimal defects might be getting formed indicated by the lesser extent of reduction in conductivity and field effect mobility.

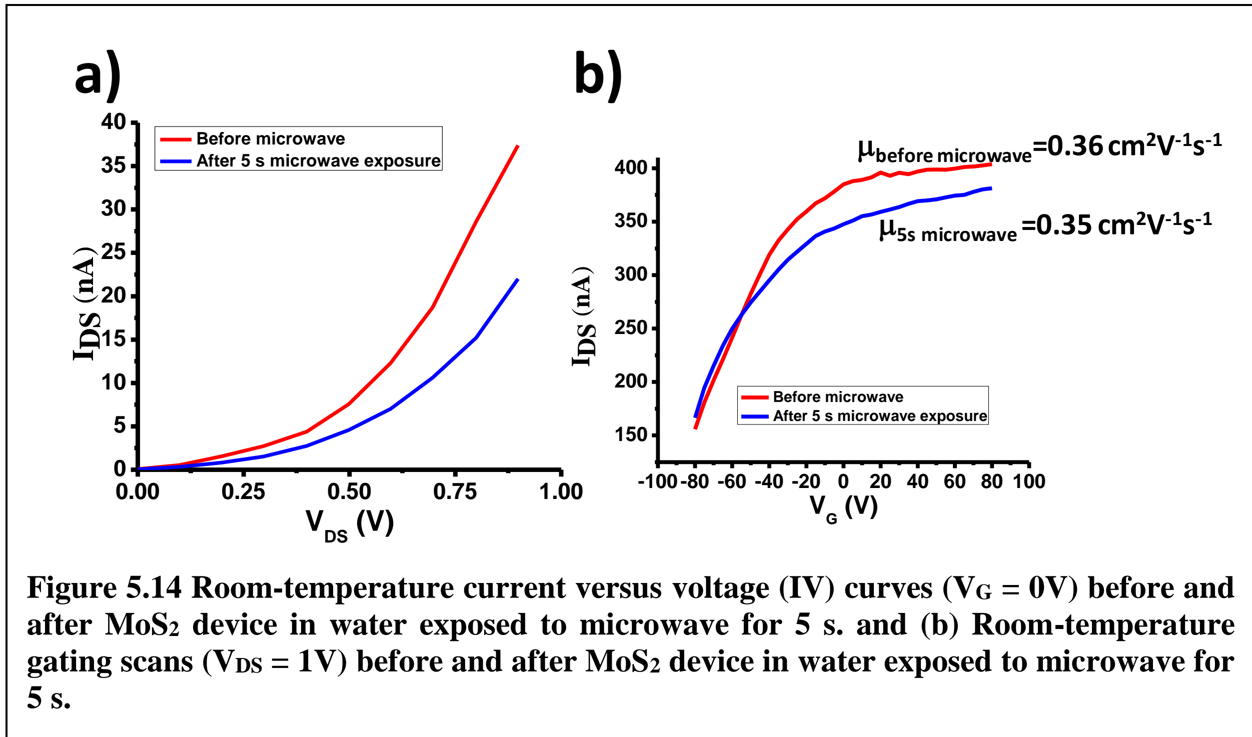

Figure 5.14 Room-temperature current versus voltage (IV) curves (V_G = 0V) before and after MoS_2 device in water exposed to microwave for 5 s. and (b) Room-temperature gating scans (V_{DS} = 1V) before and after MoS_2 device in water exposed to microwave for 5 s.

The carrier transport mechanism in metal incorporated MoS2 device

Variable temperature measurements were carried out to investigate the carrier transport mechanism in the Au-MoS_2 device (**Figure 5.15a**). With a decrease in temperature, both Au-MoS_2 and MoS_2 exhibited a decrease in conductivity and an increase in V_{DS}-I_{DS} non-linearity (as shown in **Figure 5.8b**). This suggested a finite total thermal barrier for both devices, which can be described as Arrhenius equation $I_{sat} = Ce^{(\frac{-\varnothing_{th}}{k_BT})}$, where I_{sat} is current saturation at V_{BG} = 20 V (in our experiment), C is a constant, $\varnothing_{th}$ (eV) is the thermal barrier, k_B is Boltzmann constant (8.617 x 10^{-5} eV K^{-1}), and T (K) is temperature. From the ln(I_{sat}) versus 1/T plot, it is observed that Au-MoS_2 and MoS_2 exhibit linear dependence, consistent with the equation. Thermal barrier heights $\varnothing_{th}$ (eV), estimated from the slope of these curve are 253 meV and 44.18 meV for MoS_2, and Au-MoS_2 respectively as shown in **Figure 5.15b**. Furthermoremore, the carrier transport in Au-MoS_2 and MoS_2 can be classified as variable range hopping mechanism due to the linear

relationship in ($\ln I_{DS} \propto T^{\frac{-1}{3}}$) plot (inset of **Figure 5.15b**), which involves inelastic tunneling dominantly in 2 dimensions (in plane and between the layer)[11,12,39].

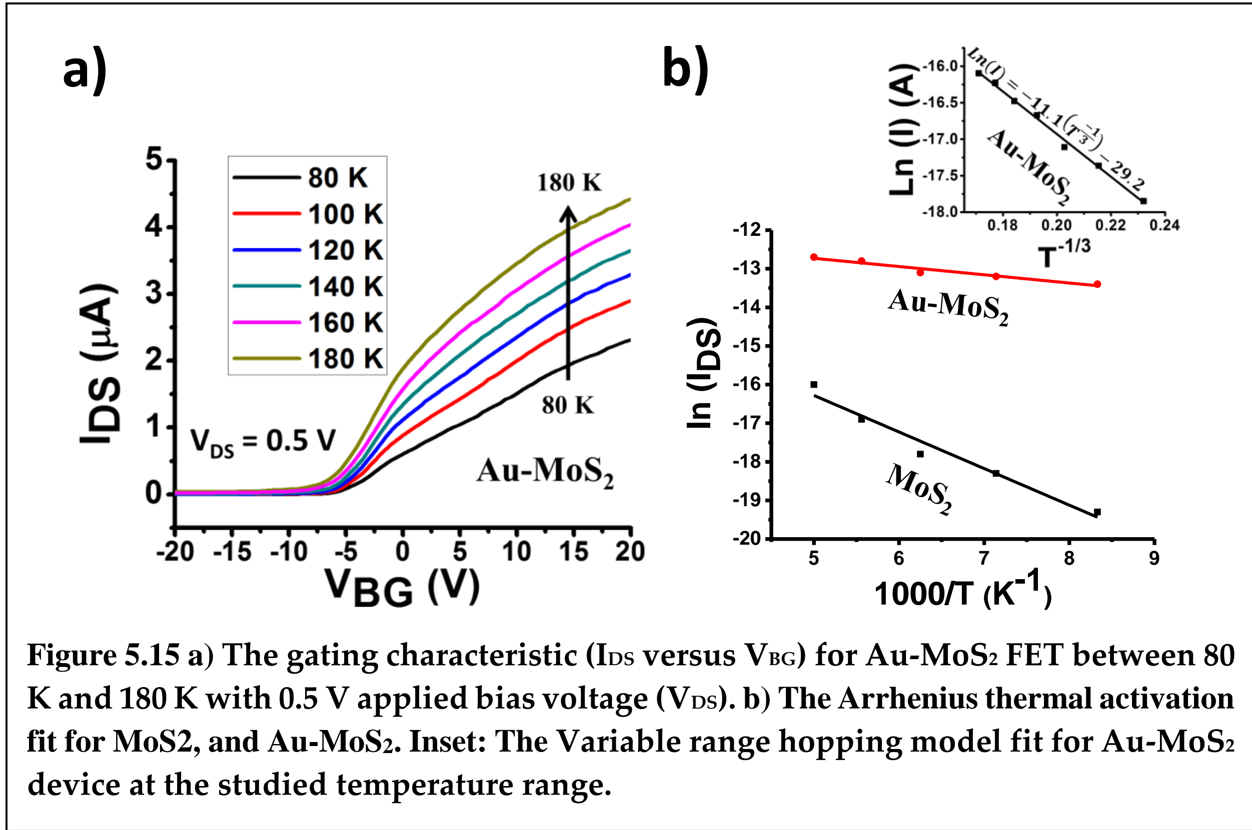

Figure 5.15 a) The gating characteristic (I_{DS} versus V_{BG}) for Au-MoS_2 FET between 80 K and 180 K with 0.5 V applied bias voltage (V_{DS}). b) The Arrhenius thermal activation fit for MoS2, and Au-MoS_2. Inset: The Variable range hopping model fit for Au-MoS_2 device at the studied temperature range.

The thermal conductivity analysis of MoS2 and metal incorporated MoS_2

Since the electrical properties of MoS_2 are sensitive to its temperature, it is important to study the heat transport properties in these structures for comprehensive device analysis. This analysis was conducted for both bare and gold functionalized (*via* microwave process) trilayer MoS_2 supported on 300 nm SiO_2 (mechanical exfoliation)[10]. Raman spectroscopy provides an indirect route to measure thermal conductivity of nanomaterials, while its accuracy is dependent on the frequency of the Raman peaks. Lower thickness MoS_2 provides higher sensitive Raman signal; therefore, trilayer MoS_2 was used to study its thermal conductivity before and after gold functionalization (a sufficiently large monolayer was not observed even after extensive search).

High flux and intensity laser exposure can etch MoS_2 and thus can interfere with the thermal measurements[40]. The maximum laser power used in our measurements was 20 μW, which is 500 times lesser than the power used by Castellanos-Gomez *et al*[40] to etch MoS_2. Control experiment was conducted to study the change in Raman features from exposure to the maximum laser power (20 μW) for 15 s (as shown in **Figure 5.16b**). Absence of any noticeable change in Raman peaks indicates that the thermal conductivity measurements are negligibly affected by laser interaction with the samples. Here, a 532 nm laser beam (~1 μm diameter) was focused at the center of trilayer MoS_2 and the generated heat propagates laterally and steadily through the thin layer, presumably due to low thermal conductivity of air (0.025 W/mK) (**Figure 5.16a**)[10]. The intensities of the

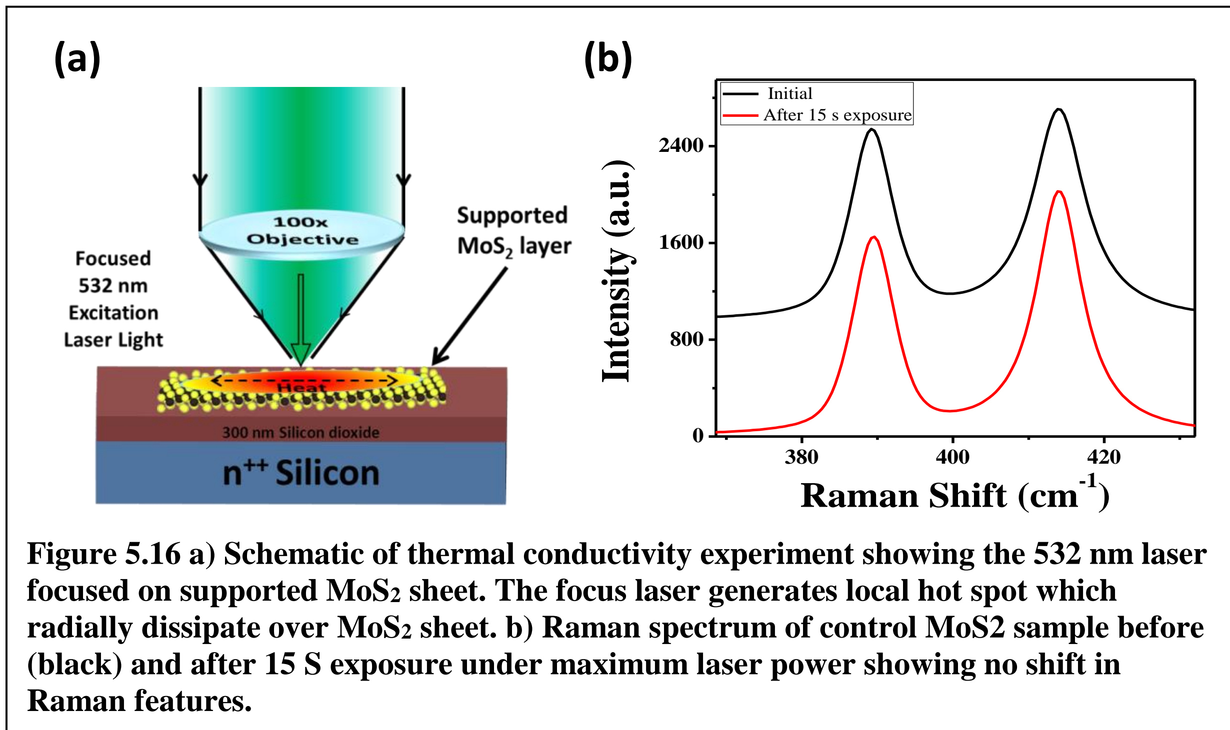

Figure 5.16 a) Schematic of thermal conductivity experiment showing the 532 nm laser focused on supported MoS_2 sheet. The focus laser generates local hot spot which radially dissipate over MoS_2 sheet. b) Raman spectrum of control MoS2 sample before (black) and after 15 S exposure under maximum laser power showing no shift in Raman features.

reflected beam from MoS_2 and from bare silica were measured by a laser power meter to obtain the power absorbed by MoS_2 given by P. The radial heat conduction through the surface of cross-sectional area A can be evaluated from the following equation

$$\frac{\delta Q}{\delta t} = -k\oint \nabla T \cdot dA$$ **Equation 5.4**

where Q is the amount of heat transferred over time t, T is the absolute equilibrium temperature, k is the thermal conductivity. The steady-state, average solution of this equation provides the thermal conductivity: $k = \frac{1}{2}\pi d \frac{\delta P}{\delta T}$ where, d is the thickness of MoS_2 layer (2 nm). Here, T is the equilibrium temperature for a given power, P.

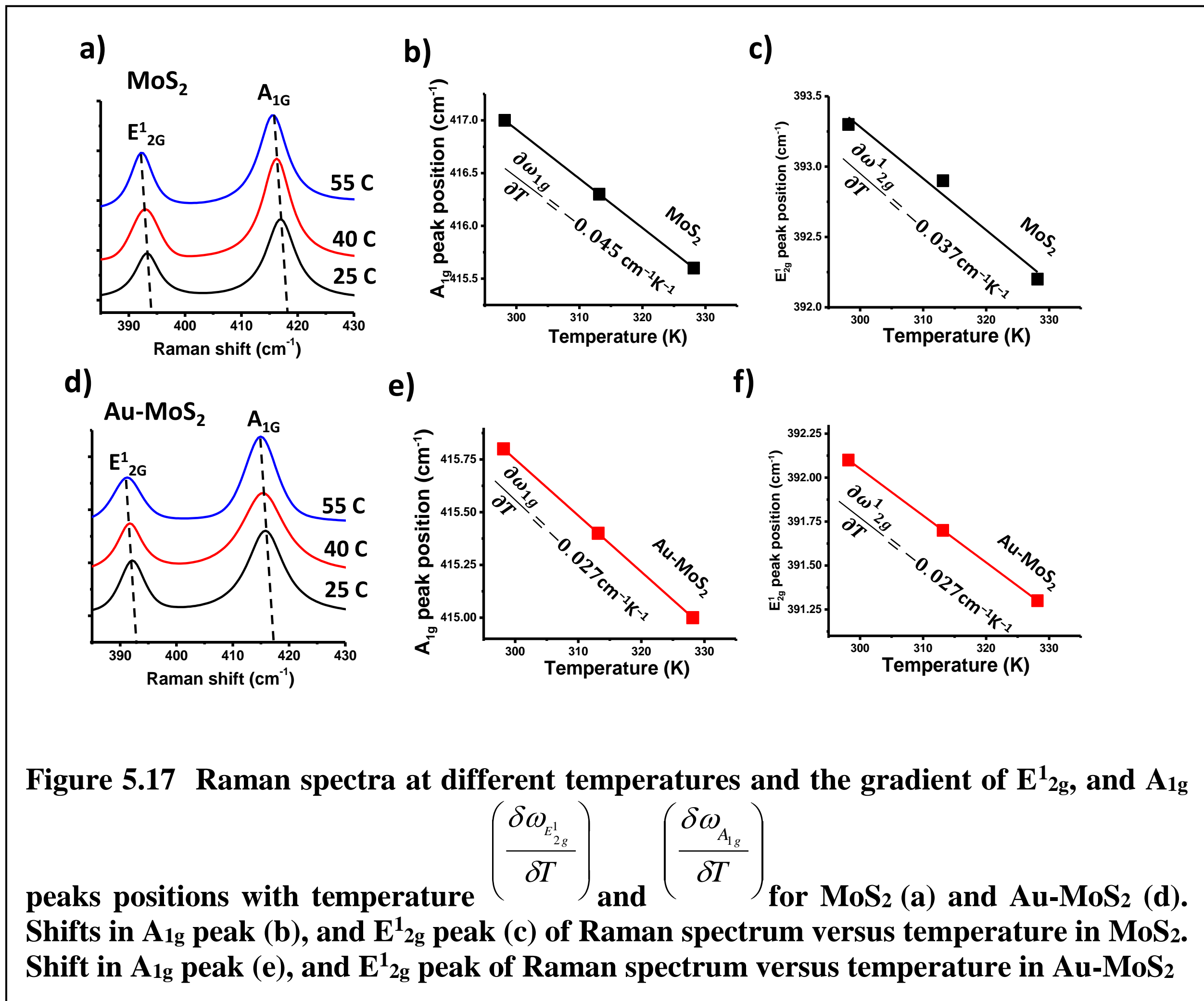

Figure 5.17 Raman spectra at different temperatures and the gradient of E^1_{2g}, and A_{1g} peaks positions with temperature $\left(\frac{\delta\omega_{E^1_{2g}}}{\delta T}\right)$ and $\left(\frac{\delta\omega_{A_{1g}}}{\delta T}\right)$ for MoS_2 (a) and Au-MoS_2 (d). Shifts in A_{1g} peak (b), and E^1_{2g} peak (c) of Raman spectrum versus temperature in MoS_2. Shift in A_{1g} peak (e), and E^1_{2g} peak of Raman spectrum versus temperature in Au-MoS_2

To measure k, $\frac{\delta P}{\delta T}$ or the relationship between power and temperature was required. This interplay is evaluated indirectly *via* Raman by correlating the Raman peak position with temperature (controlled externally) and with laser power, then combining them to find k:

$$k = \frac{1}{2}\pi d \frac{\delta P}{\delta T} = \frac{1}{2}\pi d \left(\frac{\delta \omega}{\delta T}\right)\left(\frac{\delta \omega}{\delta P}\right)^{-1} \qquad \textbf{Equation 5.5}$$

where, $\left(\frac{\delta \omega}{\delta T}\right)$ is the gradient in the A_{1g} or E^1_{2g} Raman peak positions with sample temperature (as shown in **Figure 5.18**), and $\left(\frac{\delta \omega}{\delta P}\right)$ is the gradient in the A_{1g} or E^1_{2g} with laser power (as shown in **Figure 5.19**)[41]. From these gradients, the thermal conductivity of MoS_2 and Au-MoS_2 are averaged to be 16.2 W/mK and 21.3 W/mK respectively. The increase in thermal conductivity is attributed to the high thermal conductivity of gold islands (~300 W/mK), which enhances phonon transport on MoS_2 platform.

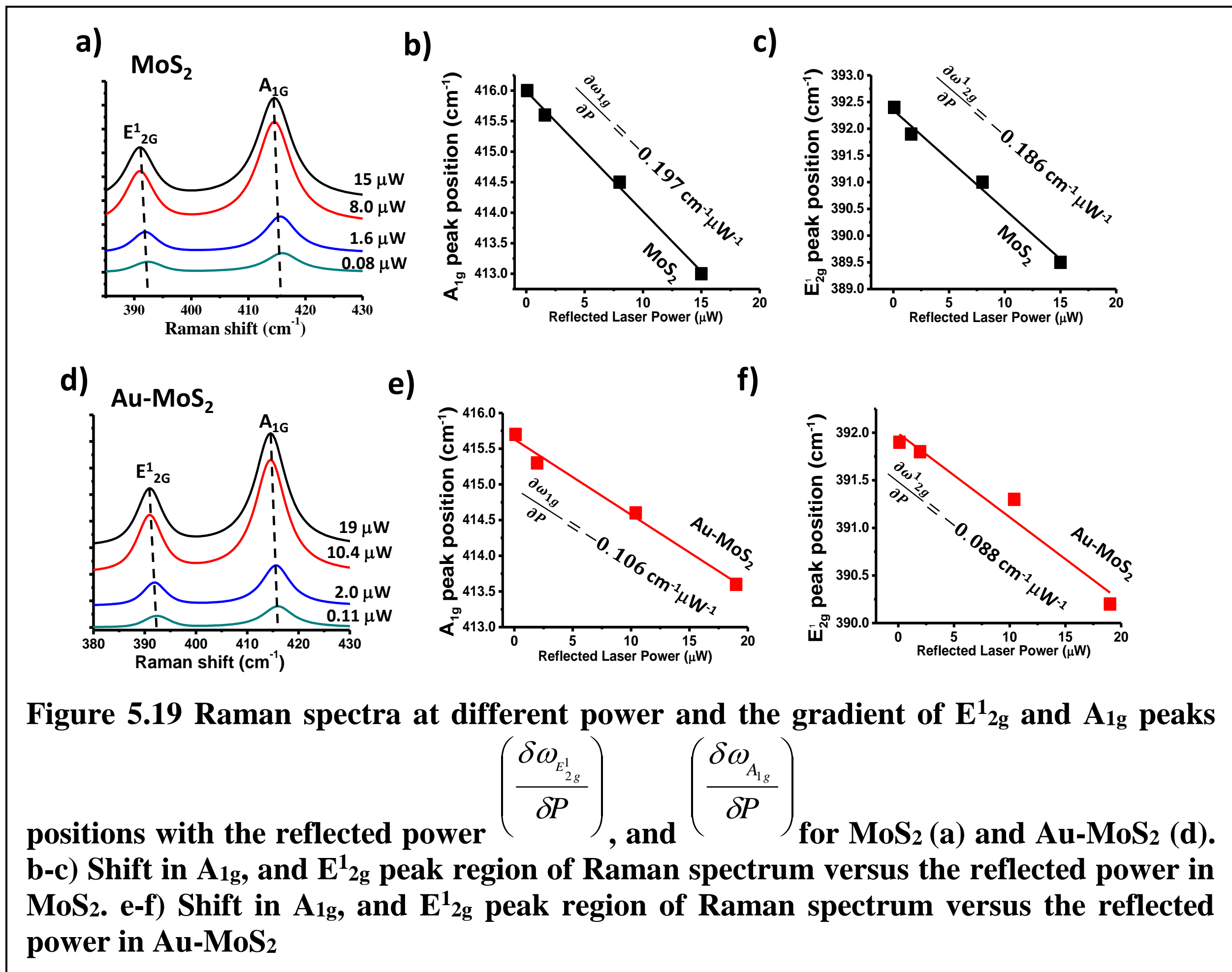

Figure 5.19 Raman spectra at different power and the gradient of E^1_{2g} and A_{1g} peaks positions with the reflected power $\left(\frac{\delta \omega_{E^1_{2g}}}{\delta P}\right)$, and $\left(\frac{\delta \omega_{A_{1g}}}{\delta P}\right)$ for MoS_2 (a) and Au-MoS_2 (d). b-c) Shift in A_{1g}, and E^1_{2g} peak region of Raman spectrum versus the reflected power in MoS_2. e-f) Shift in A_{1g}, and E^1_{2g} peak region of Raman spectrum versus the reflected power in Au-MoS_2

Conclusion

In conclusion, this chapter has shown chemical and MW routes to incorporate Au and Ag nanoparticles on MoS_2, which results in significant modulation of its electrical, thermal and structural properties, and increased effective gate capacitance by 9 folds. Here, a facile sulfur-metal interaction is leveraged to achieve functionalization of metal nanostructures on MoS_2 *via* both diffusion limited aggregation and instantaneous reaction arresting. The NP deposition occurs preferentially on the edges and defects, and exhibits 60^0 displacements on certain crystallographic edges. The Raman measurements show that the polarity of doping is dependent on the functionalization route and electrical analysis indicated that the interaction between gold nanoparticles and MoS_2 flakes is highly capacitive ($C_{Au\text{-}MoS2} = 2.17\ \mu F/cm^2$). Through Schottky model analysis, a barrier of 14.52 meV and a mobility of 3.11 $cm^2/V/s$ (and 3.71 $cm^2/V/s$ from gating) is evaluated; while the thermal transport barrier reduces from 253 to 44.18 meV after gold nanoparticle functionalization. The thermal conductivity of MoS_2 was found to increase from 15 W/mK to 23 W/mK post nanoparticle deposition. Furthermore, the deposition of highly capacitive gold nanostructures on MoS_2 can be employed to increase the effective gating by orders of magnitude. Futuristically, this versatile process can provide access to a wide range of functionalized metal dichalcogenides for development of fundamental theories on the optical/Raman[42]/electrical/thermal/structural properties/correlations and novel 2D heterostructures and applications.

Acknowledgements

The financial support from Terry C. Johnson Center for Basic Cancer Research, and partial support from NSF (CMMI-1054877, CMMI-0939523 and CMMI-1030963) and Office of Naval Research (grant-N000141110767) were acknoledged. Daming Wei and Dr. James Edgar were

acknowledged for their support with the AFM measurement. Donovan Briggs and Cody Fager were acknowledged for help with exfoliating MoS_2.

References

1. Novoselov, K. S. et al. Two-Dimensional Gas Of Massless Dirac Fermions In Graphene. Nature 438, 197–200 (2005).

2. Coleman, J. N. et al. Two-Dimensional Nanosheets Produced By Liquid Exfoliation Of Layered Materials. Science 331, 568–71 (2011).

3. Mak, K. F. et al. Atomically Thin MoS_2: A New Direct-Gap Semiconductor. Physical Review Letters 105, 136805 (2010).

4. Splendiani, A. et al. Emerging Photoluminescence In Monolayer Mos 2. Nano Letters. 10, 1271–1275 (2010).

5. Radisavljevic, B. et al. A. Single-Layer MoS_2 Transistors. Nature Nanotechnology. 6, 147–150 (2011).

6. Li, H. et al. Fabrication Of Single- And Multilayer MoS_2 Film-Based Field-Effect Transistors For Sensing NO At Room Temperature. Small 8, 63–67 (2012).

7. Perkins, F. K. et al. Chemical Vapor Sensing With Monolayer MoS_2. Nano Letters. 13, 668–673 (2013).

8. Gourmelon, E. et al. MS_2 (M = W, Mo) Photosensitive Thin Films For Solar Cells. Sol. Energy Mater. Sol. Cells 46, 115–121 (1997).

9. Buscema, M. et al. Large And Tunable Photothermoelectric Effect In Single-Layer Mos 2. Nano Lett. 13, 358–363 (2013).

10. Lee, C. et al. Anomalous Lattice Vibrations Of Single- And Few-Layer MoS_2. ACS Nano 4, 2695–2700 (2010).

11. Jasuja, K. et al. Implantation And Growth Of Dendritic Gold Nanostructures On Graphene Derivatives: Electrical Property Tailoring And Raman Enhancement. ACS Nano 3, 2358–2366 (2009).

12. Jasuja, K. et.al. Microwave-Reduced Uncapped Metal Nanoparticles On Graphene: Tuning Catalytic, Electrical, And Raman Properties. The Journal of Physical Chemistry Letters 1, 1853–1860 (2010).

13. Lin, J. et.al. Plasmonic Enhancement Of Photocurrent In Mos2 Field-Effect-Transistor. Applied Physics Letters 102, 203109 (2013).

14. Govinda Rao, B. et al. Decoration Of Few-Layer Graphene-Like Mos_2 And $Mose_2$ By Noble Metal Nanoparticles. Journal of Cluster Science 23, 929–937 (2012).

15. Chu, X. et al. Size-Tunable Au Nanoparticles On Mos_2(0001). Nanotechnology 23, 375603 (2012).

16. Li, H. et al. From Bulk To Monolayer MoS_2: Evolution Of Raman Scattering. Advanced Functional Materials 22, 1385–1390 (2012).

17. Zhuo, R. F. et al. Multistep Synthesis, Growth Mechanism, Optical, And Microwave Absorption Properties Of Zno Dendritic Nanostructures. The Journal of Physical Chemistry C 112, 11767–11775 (2008).

18. Mullins, W. W. et al. Stability of a Planar Interface During Solidification of a Dilute Binary Alloy. Journal of Applied Physics 35, 444 (1964).

19. Langer, J. S. Instabilities And Pattern Formation In Crystal Growth. Reviews of Modern Physics 52, 1–28 (1980).

20. Bertrand, P. A. Surface-Phonon Dispersion Of MoS_2. Physical Review B 44, 5745–5749 (1991).

21. Chakraborty, B. et al. Symmetry-Dependent Phonon Renormalization In Monolayer MoS_2 Transistor. Physical Review B 85, 161403 (2012).

22. Shi, Y. et al. Selective Decoration Of Au Nanoparticles On Monolayer MoS_2 Single Crystals. Scientific Reports 3, 183–191 (2013).

23. Lee, K. et al. Electrical Characteristics Of Molybdenum Disulfide Flakes Produced By Liquid Exfoliation. Advanced Materials 23, 4178–4182 (2011).

24. Zhang, Z. et al. Quantitative Analysis Of Current–Voltage Characteristics Of Semiconducting Nanowires: Decoupling Of Contact Effects. Advanced Functional Materials 17, 2478–2489 (2007).

25. Padovani, F. A. et al. Field And Thermionic-Field Emission In Schottky Barriers. Solid State Electronics 9, 695–707 (1966).

26. Novoselov, K. S. et al. Two-Dimensional Atomic Crystals. Proceedings of the National Academy of Sciences 102, 10451–10453 (2005).

27. Fuhrer, M. S.et al. Measurement Of Mobility In Dual-Gated Mos2 Transistors. Nature Nanotechnology 8, 146–147 (2013).

28. Mohanty, N. et al. Graphene-Based Single-Bacterium Resolution Biodevice And DNA Transistor: Interfacing Graphene Derivatives With Nanoscale And Microscale Biocomponents. Nano Letters. 8, 4469–4476 (2008).

29. Nguyen, P. et al. Graphene Interfaced With Biological Cells: Opportunities And Challenges. Journal Of Physical Chemistry Letters 3, 1024–1029 (2012).

30. Sreeprasad, T. S. et al. How Do The Electrical Properties Of Graphene Change With Its Functionalization? Small 9, 341–350 (2013).

31. Jena, D. et al. Enhancement Of Carrier Mobility In Semiconductor Nanostructures By Dielectric Engineering. Physical Review Letters 98, 136805 (2007).

32. Wang, H. et al. Integrated Circuits Based On Bilayer MoS_2 Transistors. Nano Letters. 12, 4674–4680 (2012).

33. McMenamin, J. C. et al. Photoemission Studies Of Layered Transition-Metal Dichalcogenides: MoS_2. Physical Review B 16, 5474–5487 (1977).

34. McGovern, I. T. et al. Electronic Properties Of Cleaved Molybdenum Disulphide Surfaces. Surface Science 46, 427–440 (1974).

35. Schlaf, R. et al. Band Lineup Of Layered Semiconductor Heterointerfaces Prepared By Van Der Waals Epitaxy: Charge Transfer Correction Term For The Electron Affinity Rule. Journal of Applied Physics 85, 2732 (1999).

36. Kamaratos, M. et al. Adsorption Studies On Ar+ -Sputtered MoS_2 (0001). Surface Science 178, 865–871 (1986).

37. Fontana, M. et al. Electron-Hole Transport And Photovoltaic Effect In Gated MoS_2 Schottky Junctions. Scientific Reports 3, 666–669 (2013).

38. Cannon, P. et al. Reaction Between Molybdenum Disulphide And Water. Nature 203, 750–751 (1964).

39. Mohanty, N. et al. Nanotomy-Based Production Of Transferable And Dispersible Graphene Nanostructures Of Controlled Shape And Size. Nature Communications 3, 844 (2012).

40. Castellanos-Gomez, A. et al. Laser Thinning Of MoS_2: On Demand Generation Of A Single-Layer Semiconductor. Nano Letters. 12, 3187–3192 (2012).

41. Balandin, A. A. et al. Superior Thermal Conductivity Of Single-Layer Graphene. Nano Letters. 8, 902–907 (2008).

42. Sajanlal, P. R. et al. A New Class Of Highly Efficient Surface-Enhanced Raman Active And Infrared-Absorbing Materials. Nano Research 2, 306–320 (2009).

Chapter 6 - Conclusion

In this dissertation, this dissertation successfully addressed the challenges associated with the incorporation of 2D nanomaterial into practical applications. Chapter 1 presented a brief overview of the wondrous class of 2D nanomaterials (graphene, MoS_2, and hBN), and the 2D nanomaterial current synthesis technique. Such backgrounds of these materials provided insights of motivation, and an attempt to contextualize the results in chapters 2 – 5 in perspective view of the overall landscape of 2D nanomaterial science

By leveraging the carbon diffusion through copper grain, the direct formation of large area, high quality, and thin layer graphene on SiO_2 substrate was enabled. This growth mechanism was discussed in detail in chapter 2. Furthermore, the growth parameters ($T=900^{o}C$, and $F_{H2}/F_{CH4}\sim1/5$) are optimized to robustly form turbostratic stacking, and low defect thin graphene film ($L_a\sim140$ nm), with a field effect mobility of 277 $cm^2V^{-1}s^{-1}$, and 233 $cm^2V^{-1}s^{-1}$ for holes and electrons respectively. The electronic transport in thin film graphene was described by an overlapping band of 2.3±0.4 meV (STB model), a thermal activation energy of 2.0±0.2 meV (Arrhenius thermal activation model), and 2-D hopping conduction (VRH model).

Chapter 3 provided a novel method to growth of uniform, large area, continuous h-BN films on SiO_2. In our understanding, the oxygen on the SiO_2 substrate plays a crucial role as a nucleation sites by bonding with B of boron nitride active radical, which is confirmed by XPS data. The domain size of h-BN film was estimated to be 10 μm in diameter. Furthermore, the h-BN film was 6 fold smoother than SiO_2 substrate, which played a dominant role in affecting the electrical performance of other 2D nanomaterial placed on its surface, such as MoS_2. Through the study of the electrical behavior of MoS_2 on the grown h-BN, the h-BN film possesses a smooth platform, which also provides an electronic isolation to MoS_2. Consequently, this resulted in

enhanced carrier mobility for electronic 2D metal chalcogenides, leading to an improvement of the electrical conductivity (5 folds).

Chapter 4 showed the study of nano-molecular actuation on the surface of trilayer graphene (37.5% sp^2 coverage). These photo-switchable azobenzene were covalently incorporated into graphene lattice with a density of 2.5 nm^{-2}. Due to trilayer graphene's high quantum capacitance of 6.3 $\mu F/cm^2$, and its quantum confinement, the trans to cis configuration of azobenzen (the change of 3D in molecular dipole moment) generates a hole carrier density of 2.44×10^{12} in graphenic platform, corresponding to 1 quanta of hole per 100 azobenzene molecules. Remarkably, the total carrier density calculated from gating was consistent with that from quantum capacitance. We believe that this work leads to the development of graphene interface with other molecular electronic systems such as molecular-machines (for example, rotaxane) and molecular switches, and photo-detector, MEMS and protein-folding.

Chapter 5 demonstrated a controlled functionalization and/or covalently interfacing of MoS_2 with noble metal nanoparticles (Au, and Ag). The stable sulfur/noble metal functionalization was enhanced *via* both diffusion limited aggregation (chemical functionalized route) and instantaneous reaction arresting (microwave assisted route). The gold nanoparticles were incorporated selectively on MoS_2 crystallographic directions (with 60° displacement). Such incorporation can significantly modulate that the electrical and thermal properties of MoS_2 material. *Via* electrical measurement, the interface between MoS_2 and gold nanoparticles led to a 9-fold increase in effective gate capacitance, ($C_{Au\text{-}MoS2}$ = 2.17 mF/cm^2), and a vastly reduced carrier-transport thermal-barrier (253 to 44.18 meV). *Via* Raman data analysis, the polarity of doping can be altered by switching the functionalization method. Furthermore, by modifying the Raman spectroscopy system, the thermal conductivity values were evaluated at 15 W/mK for

MoS_2, and 23 W/mK for Au-MoS_2. We envision that this versatile process provides an avenue to interface 2D metal dichalcogenides with the class of metal nanoparticles leading to the development of various potential advanced thermionic, and electrical systems, such as electrode-attachment to the hetero-structures of graphene and MoS_2, where the gold nanostructure could be grown to act as an electron-tunneling gate-electrode connected to MoS_2.

Chapter 7 - Future outlook

This dissertation reports key discoveries in the growth mechanism and interfacial chemistries of 2D nanomaterials; resulting in several high impact publications. Although these findings have made an impact in the field, there is research required to expand the applications of 2D nanomaterials and expand the scope of interfaces that can be achieved. Further, the research can be applied to other 2D nanomaterials. Some of essential points that we would contribute to a further understanding of the growth mechanism, and the structure of the materials are discussed below:

In the case of the growth of multilayer graphene on SiO_2 substrate, the complete growth mechanism can be understood by studying: 1) the chemistry, and the kinetic of the graphene formation at the interface, 2) the effect of underlying SiO_2/Si <111> and SiO_2/Si <100> substrates substrate on the crystallization of capped Cu layer at elevated temperature, and 3) the transport of the carbon radicals (C_xH_y) through Cu grain boundaries. We suggest that a study of sequential dosing of isotope methane ($^{12}CH_4$ and $^{13}CH_4$) should further explain the growth formation of graphene at the interface. By leveraging the separation of the ^{12}C and ^{13}C Raman modes, Raman G band position mapping will reveal the spatial distribution of graphene domains at different growth time, i.e. whether the graphene islands, strings of graphene, and the graphene film consist of ^{12}C local regions and ^{13}C ones. Further, the surface chemistry of interface between Cu and SiO_2 on Si<111>, and on Si<100> should provide information on the crystallizing process of Cu film at elevated temperature. Lastly, the comprehension of the transport of carbon radical through the copper grain boundaries could be determined by either an in-situ study *via* TEM with heating stage.

For the growth of h-BN on SiO_2 substrate, the comprehension of the growth mechanism can be accomplished by elucidating (1) the role of oxygen on SiO_2 surface on the formation of h-

BN film, and (2) the kinetic growth model for multilayer h-BN film. In the first case, whether oxygen has influence on the adsorption step or on the surface reaction, there should be a study of surface chemistry of SiO_2 film interacting with $(BN)_x(H)_y$ radical at high temperature. In the latter case, we suggest another study on the growth of h-BN film with respect to the growth time, and dielectric substrates such as silicon nitride (SiN), and sapphire (Al_2O_3).

In order to further realize the electronic applications of directly grown h-BN film, and directly grown multilayer graphene film, there should be a research on their structural defects including point defects (holes, atomic vacancies), line defect (grain boundaries, Stone-Wales defects), and sp^3 defects, which introduced by oxidation during CVD process. In case of multilayer graphene film, these defects are major limiting factors in the charge mobility in the grown graphene. On the other hand, these defects in h-BN film not only influence the dispersion of electronic bands, but also the spatial charge inhomogeneity in 2D nanomaterial interfacing the surface of h-BN film. The structural characterization of these directly grown materials could be accomplished by employing high resolution TEM, and scanning tunneling electron microscopy (STM) techniques. Although, the grown h-BN film was shown as a clean electronic platform for 2D nanomaterial electronic applications in our study, we recommend a study of the electronic charge distribution in 2D nanomaterials such as graphene, and MoS_2 placed on h-BN film. Because the electronic local density of states of 2D nanomaterials is proportional to the tunneling current of STM, the profile of electronic charge puddles can be mapped *via* scanning tunneling electron microscopy (STM) technique.